



HAL
open science

Pump-probe spectroscopy of vibronic dynamics using high-order harmonic generation: general theory and applications to SO₂

Camille Lévêque

► **To cite this version:**

Camille Lévêque. Pump-probe spectroscopy of vibronic dynamics using high-order harmonic generation: general theory and applications to SO₂. Condensed Matter [cond-mat]. Université Pierre et Marie Curie - Paris VI; Ruprecht-Karls-Universität (Heidelberg, Allemagne), 2014. English. NNT: 2014PA066513. tel-01165076

HAL Id: tel-01165076

<https://theses.hal.science/tel-01165076>

Submitted on 18 Jun 2015

HAL is a multi-disciplinary open access archive for the deposit and dissemination of scientific research documents, whether they are published or not. The documents may come from teaching and research institutions in France or abroad, or from public or private research centers.

L'archive ouverte pluridisciplinaire **HAL**, est destinée au dépôt et à la diffusion de documents scientifiques de niveau recherche, publiés ou non, émanant des établissements d'enseignement et de recherche français ou étrangers, des laboratoires publics ou privés.

Thèse de Doctorat de l'Université Pierre et Marie Curie

Spécialité :

P2MC : La Physique de la particule à la Matière condensée

Inaugural-Dissertation

zur Erlangung der Doktorwürde der
Naturwissenschaftlich-Mathematischen Gesamtfakultät der
Ruprecht-Karls-Universität Heidelberg

Pump-probe spectroscopy of vibronic dynamics using High Order Harmonic Generation: General Theory and applications to SO₂

vorgelegt von

Camille Lévêque, M.Sc. in Physical Chemistry
Aus Paris (Frankreich)

Pr. R. Vuilleumier
Pr. M. Lein
Pr. R. Marquardt
Pr. H.-R. Volpp
Dr. A. Zaïr
Pr. H. Köppel
Dr. R. Taïeb

President
Referee
Referee
Examiner
Examiner
Referee, Examiner, Supervisor
Referee, Examiner, Supervisor

Tag der mündlichen Prüfung:
31. October 2014

Abstract

The SO₂ molecule is long known in the literature for its complex UV absorption spectrum, which is caused by a variety of strong couplings - not properly understood - between the electronic states involved. This long and rich history was augmented recently by new time-dependent spectroscopic methods, namely, Time-Resolved Photoelectron Spectroscopy (TRPES) and High-order Harmonic Generation (HHG). Additional open questions emerged immediately, e.g., what was the role of the different known electronic states, which were the relevant couplings and also the timescales of the different relevant processes.

To resolve some of these issues theoretically, we start by considering the electronic ground state together with the two lowest singlet excited states. The latter interact through strong non-adiabatic couplings leading to a complex photoabsorption spectrum. Our results were particularly accurate, especially concerning the so-called Clements bands, and provide the first comprehensive theoretical description of the photoabsorption spectrum. When further including the spin-orbit coupling, relevant for the weak long-wavelength absorption system, the three-states model turns into a 12 coupled-states system, which in turn can be reduced into two subsystems by the use of symmetry. Analysis of the different couplings gives insight into the different mechanisms leading to the intersystem crossing. Three main points have been shown: (i) the preponderant role of a 3B_2 state, (ii) the possibility of quantum interferences during the process and (iii) a new interpretation of the "forbidden" band.

The TRPES and the HHG spectroscopies have been used experimentally to probe the time-dependent dynamics in all these states. With the aid of first-principles simulations we show that the TRPES method is sensitive to the dynamics in the singlet and in the triplet states. The time profile of the photoelectron yield provides information on the time scales of the intersystem crossing and non-adiabatic transitions. The simulation of the HHG required first the development of a model, which includes explicitly the quantum nature of the nuclei. Then we show that this experiment is sensitive only to the intersystem crossing, but not to the dynamics in the singlet states. Good agreement between theory and experiment has been achieved both for TRPES and HHG spectra.

Kurzfassung

Das SO_2 Molekül ist in der Literatur seit langem bekannt für sein komplexes UV Absorptionsspektrum, welches durch eine Vielzahl von starken und nicht ausreichend verstandenen Kopplungen zwischen den beteiligten elektronischen Zuständen bestimmt wird. Kürzlich wurden die zur Verfügung stehenden experimentellen Methoden zur Untersuchung von SO_2 um die Time-Resolved Photoelectron Spectroscopy (TRPES) und High-order Harmonic Generation (HHG) Methoden erweitert. Die Untersuchungsergebnisse werfen eine Reihe von Fragen bezüglich der Rolle der elektronischen Zustände, der relevanten Kopplungen und der Zeitskala der unterschiedlichen relevanten Prozesse auf.

Zur Beantwortung dieser Fragen mittels theoretischer Methoden betrachten wir zunächst den elektronischen Grundzustand sowie die zwei niedrigsten angeregten Singulett-Zustände. Die letzteren wechselwirken miteinander durch starke nicht-adiabatische Kopplungen, wodurch ein komplexes optisches Absorptionsspektrum entsteht. Unsere Ergebnisse sind besonders genau, speziell im Bezug auf die sogenannten Clements-Banden und liefern die erste umfassende theoretische Beschreibung des optischen Absorptionsspektrums. Die Hinzunahme der Spin-Bahn Kopplung, relevant für das System mit schwacher Absorption im langwelligen Bereich, verwandelt das Drei-Zustands-Modell in ein Modell mit 12 gekoppelten Zuständen, welches seinerseits durch Anwendung von Symmetrierauswahlregeln in zwei Teilsysteme aufgeteilt werden kann. Die Analyse der unterschiedlichen Kopplungen gewährt einen Einblick in den Mechanismus, der zum sog. Intersystem Crossing führt. Drei wichtige Aspekte wurden herausgearbeitet: (i) die beherrschende Rolle des 3B_2 Zustandes, (ii) die Möglichkeit des Auftretens von Quanteninterferenzen während des Prozesses und (iii) die neuartige Interpretation der "verbotenen" Bande.

Die Methoden der TRPES- und HHG-Spektroskopie wurden bereits eingesetzt, um die zeitabhängige Kerndynamik in allen drei genannten Zuständen experimentell zu studieren. Mit Hilfe von ab-initio Simulationen konnten wir zeigen, dass die TRPES-Methode empfindlich gegenüber Kerndynamik in den Singulett- und Triplett-Zuständen ist. Das zeitabhängige Profil der Photoelektronenausbeute liefert Informationen bezüglich der Zeitskala des Intersystem Crossing und der nicht-adiabatischen Übergänge. Zur Simulation von HHG war die Entwicklung eines Modells notwendig, welches die quantenmechanische Natur der Atomkerne explizit berücksichtigt. Mittels dieses Modells konnten wir zeigen, dass das Experiment empfindlich ausschließlich gegenüber Intersystem Crossing und nicht gegenüber der Kerndynamik in den Singulett-Zuständen ist. Gute Übereinstimmung zwischen Theorie und Experiment konnte sowohl für TRPES als auch für HHG-Spektren erzielt werden.

Résumé

Le spectre d'absorption dans l'ultra-violet (UV) de la molécule de dioxyde de soufre (SO_2) est bien connu dans la littérature scientifique pour sa complexité résultante de forts couplages, pas encore entièrement élucidés, entre les états électroniques impliqués. Cette longue et riche histoire a récemment été complétée par de nouvelles études spectroscopiques permettant le suivi de l'évolution temporelle du système utilisant la spectroscopie de photoémission résolue en temps (TRPES) et la génération d'harmonique d'ordre élevé (HHG). Immédiatement, de nouvelles questions sans réponse interpellent les expérimentateurs à propos du rôle des différents états électroniques, des différents mécanismes de couplage entre ces derniers ainsi que les temps caractéristiques des différents processus.

Pour répondre théoriquement à certaines de ces questions, nos recherches ont, dans un premier temps, inclus l'état électronique fondamental de la molécule ainsi que ses deux premiers états excités. Ces derniers interagissent au travers d'un fort couplage, dit non-adiabatique, qui se traduit par une complexité accrue du spectre de photoabsorption. Les résultats ainsi obtenus se montrent précis, en particulier pour les dénommées bandes de Clements, fournissant ainsi la première explication théorique complète du spectre de photoabsorption. Le pas suivant fut d'inclure les couplages spin-orbites permettant une interaction entre les états singulets et triplets de spin, ces derniers jouant un rôle essentiel pour la partie de faible énergie du spectre. Le modèle qui jusqu'alors comportait trois états en est augmenté de neuf, mais découplé équitablement en deux sous-groupes par symétrie. L'analyse des différents couplages permet de mieux comprendre les mécanismes de conversion inter-système. Trois principaux résultats ont été obtenus : (i) une population forte (comparable aux états singulets) d'un état 3B_2 , (ii) la possibilité d'interférences quantiques lors du processus de conversion inter-système et (iii) une nouvelle interprétation de la bande dite "interdite", à faible énergie.

Les spectroscopies mentionnées ci-dessus, i.e. TRPES et HHG, ont été mise en œuvre expérimentalement pour étudier la dynamique temporelle du système complet. Grâce à des méthodes, dites ab-initio, de simulation numérique, nous avons pu démontrer la sensibilité de la spectroscopie TRPES quant à la dynamique nucléaire dans les états singulets et triplets. L'évolution temporelle du taux de photoémission permet d'extraire des expériences les temps caractéristiques des transition non-adiabatiques et de la conversion inter-système. Pour étudier la spectroscopie HHG, nous avons, en premier lieu, développer un modèle permettant de tenir compte explicitement de la nature quantique des noyaux. Ensuite il fut possible de montrer que cette méthode n'est sensible qu'à la dynamique de conversion inter-système alors que la dynamique des états singulets demeure inaccessible. Nos résultats sont appuyés par un très bon accord avec les différentes expériences.

Acknowledgements

First of all I would like to acknowledge the members of the jury, who gave me the opportunity to defend this work. The president, Prof. Rodolphe Vuilleumier, the two referees Prof. Roberto Marquardt and Prof. Manfred Lein, and the two examiners, Dr. Amelle Zair and Prof. Hans-Robert Volpp. I am very grateful that you accepted to be part of my jury and I sincerely appreciate your valuable comments and your interest in my work.

I am also indebted to my two extraordinary Ph.D. supervisors, Richard and Horst. I do not know how I could, with just a few words, thank you for these last three years. It has been a pleasure to work with both of you and I have felt at each time your continuous support and interest in my project. Working and discussing with you has been a pleasure and I find that you are wonderful people. For all these moments that we have shared together, I thank you.

This project has been carried out in two different institutes: the Theoretical-Chemistry Group of the University of Heidelberg and the LCPMR. Therefore, I am very honoured to thank their two directors, Lorentz Cederbaum and Alain Dubois, respectively, for welcoming me in them. Moreover, there are many people in both groups I would like to thank so I will thank them globally. I always felt very welcomed during my stays. It has always been a pleasure to discuss and spent time with all of you, exchanging our vision of science and of the world.

Moving every six months is not easy and I would like to thank Annette and David for their efficient work and help with the different administration tasks, for making my life much simpler in both countries. François and Tsveta, it has been a pleasure to share with you offices and for the countless discussions that we have had! Adrian, thank you for your help with my paper work issues at the end of my Ph.D. and François thank you for your support until the very last minute (and for feeding me the last days)! I would like to thank the climbing group of Heidelberg and Daniel for supporting always my ideas, discussing science, and for all the good times that we have had together.

I would like to specially thank Iain Wilkinson for having shared with me the nice experiments he performs, as well as Albert Stolow, David Villeneuve and Hans-Jakob Wörner. I sincerely appreciate your interest in my work and all the discussions concerning this fascinating topic.

To conclude these acknowledgements, I would like to thank my family, my mother for her support and love during the past 26 years and more in particular this last three. Nadège and her little family, Jules and Louise, for reminding me how funny it is to play with some "pâte à modeller". And, of course, Florian, for your endless curiosity concerning my work and your advices when my computer crashed. And Sophie thank you for sharing with me all these years and for your support.

It is because of all of you that I can write this few lines today.

Contents

1	Introduction	1
2	Theoretical Methods and Algorithms	9
2.1	Introduction	9
2.2	Quantum treatment of the nuclear motion	10
2.2.1	The Born-Huang expansion and Born-Oppenheimer approximation	11
2.2.2	The Breakdown of the Born-Oppenheimer approximation	15
2.2.3	Diabatic states	16
2.2.4	Conical intersection and regularized diabatic states	18
2.2.5	Electronic properties from adiabatic to diabatic basis	25
2.3	Numerical Methods	28
2.3.1	Numerical formulation of the TDSE	28
2.3.2	Numerical solution of the TDSE	32
2.3.3	Numerical integration of the equation of motion	37
2.4	Eigenenergies and eigenfunctions for the electronic problem	41
2.4.1	Solving the electronic problem	41
2.4.2	MCSCF and CI methods	48
2.5	Spectroscopy as an important experimental probe	51
2.5.1	One photon absorption spectroscopy: Weak field regime	51
2.5.2	Time resolved photoelectron spectra	53
2.5.3	High-order Harmonic Generation	55

3	Electronic Structure Results	69
3.1	Introduction	69
3.2	Adiabatic potential energy surfaces	69
3.2.1	Active space and primitive basis	69
3.2.2	Adiabatic electronic ground state 1^1A_1 and singlet excited states 1^1B_1 and 1^1A_2 . . .	70
3.2.3	Adiabatic triplet excited states 1^3B_1 , 1^3A_2 and 1^3B_2	76
3.2.4	Adiabatic ionic doublet states 1^2A_1 , 1^2B_2 and 1^2A_2	80
3.3	Diabatization of the adiabatic states coupled through conical intersection	83
3.3.1	Diabatization of the 1^1B_1 and 1^1A_2 adiabatic states	83
3.3.2	Diabatization of the $1^3B_1/1^3A_2$ and $1^2A_1/1^2B_2$ adiabatic states	88
3.3.3	Grid for quantum dynamics	90
3.4	Spin-orbit Coupling and Transition dipole moment	95
3.4.1	Spin-orbit Coupling	95
3.4.2	Transition Dipole Moment	103
3.4.3	Recombination matrix element in the SFA approximation	104
4	Weak field spectroscopy: Photoabsorption and photoelectron spectra	107
4.1	Introduction	107
4.2	Photoabsorption: the Clements band	108
4.2.1	Time dependent wavepacket propagation	108
4.2.2	Quantum attribution of the lowest part of the photoabsorption spectrum	116
4.3	Including the triplet states	121
4.3.1	Intersystem crossing to the $1^3B_1(-)$ and $1^3A_2(-)$ states	125
4.3.2	Intersystem crossing to the $1^3B_2(+)$ state	128
4.3.3	Intersystem crossing to the $1^3B_2(0)$ state	129
4.3.4	Quantum Interferences	131
4.3.5	The "Forbidden band"	133
4.3.6	General discussion about the intersystem crossing	141
4.4	Photoelectron spectra	143

<i>CONTENTS</i>	XI
5 Strong field spectroscopy: Following time-dependent dynamics	149
5.1 Introduction	149
5.2 multiphoton ionisation: Following wavepacket dynamics	149
5.2.1 The dynamics of the singlet states in the Clements bands	151
5.2.2 Intersystem crossing and experimental evidence of 1^3B_2	158
5.3 Strong field spectroscopy: towards attosecond resolution using HHG	162
5.3.1 SO_2 in the vibrational ground state: "Classical" vs "Quantum" description of the molecule for HHG	164
5.3.2 Tracking vibrational dynamics: the case of the electronic ground state	169
5.3.3 Probing singlet excited state dynamics	175
6 Conclusions and Perspectives	189
Bibliography	195
List of Publications	211
Résumé	213

Chapter 1

Introduction

The interaction between light and matter is one of the few ways to probe and understand the organisation of atoms, molecules and solids. Over the last century spectroscopy, has been widely developed to probe the time independent quantum nature of the molecules. With the recent advent in laser technology, following different ways such as increasing intensity, reducing the time of the laser pulse, controlling delay between two laser pulses on the femtosecond time scale, fixing its phase, provides to chemists and physicists the tools to probe dynamically the motion of nuclei and electrons in molecules and/or atoms. The theoretical description of experiment is in many cases the state of the art of the ab-initio study, the development of theoretical tools to simulate new experimental setups is a major task to carry on with a deeper understanding of quantum systems on new time scale or field regime.

Particularly, since 2001, with the first generation of attosecond light pulses [1], impressive progresses concerning the generation and the characterisation [2, 3, 4] of these attosecond pulses, such that one can speak about "attosecond technology" and "attosecond science". Two principal types of applications are currently investigated, first the attosecond pulses are used in order to excite or ionise a medium of interest, to either initialise or probe an ultra-fast dynamics. This approach has been successfully applied in the case of atomic Auger decay [5], solid photoemission from core states [6], atomic tunnelling ionisation [7] or electron wavepackets interferences [8]. The second approach uses the mechanism of the attosecond emission as a signature of the generating medium itself. Thus the attosecond electronic wavepacket, released by the

strong interaction between the laser and the medium, is driven back to the core by the laser field half a cycle later, emitting an ultrashort XUV pulse. This self-probing scheme can then be analysed by collecting the emitted light and provides, thanks to its inherent coherent nature, a quantum imaging of the system [9, 10]. Unprecedented insights are possible thanks to the knowledge of amplitude and phase of the wavefunction with respect to time and space [11]. This new piece of information has been successfully exploited in order to achieve a tomographic reconstruction of the molecular orbitals [12]. The High-order Harmonic Generation (HHG) also reveals its sensitivity to nuclear motion in the ionic states evolving during the excursion time of the ionised electron in the continuum, and applied in the case of H_2 [13] or nuclear vibration in SF_6 [14] and N_2O_4 [15], opening the way of a new time scale in molecular dynamics.

The high-order harmonic spectroscopy, demonstrated its sensitivity to the electronic structure of a molecule as well as to the molecular dynamics. It becomes the ideal candidate to probe chemical reactions, in which large amplitude nuclear motion occurs accompanied by a fast and important modification of the electronic wavefunction, particularly in the valence shell. The extraction of these simultaneous pieces of information, encoded in the XUV emission of the process, has been already achieved in the last years but only for the electronic ground state of the molecules [16]. The extension to the study of the nuclear dynamics, for instance after a photoexcitation, has been experimentally achieved only at the beginning of our project, with the successful study of the Br_2 molecule [17], followed by the case of NO_2 [18]. The former established the possibility to follow the bond cleavage in the molecule, while the latter studied the case of the nuclear dynamics in the vicinity of a conical intersection. While speaking of *chemical reaction* seems exaggerated in these cases, these studies have to be seen as prototype of such process with the bond breaking and the fast nuclear motion and modification of the electronic structures in the case of NO_2 .

The case of the conical intersection is not simply interesting for hypothetical future applications in chemical reactions, but it is primordial by itself. It is a well-known situation for which the Born-Oppenheimer approximation fails because of a strong correlation between the nuclear motion and the electronic configuration, leading to an important non-adiabatic coupling. The nuclei in such situation exhibit a fast motion accompanied by an electronic configuration mixing, leading to a coherent superposition of them. Because of their presence in almost all the molecular systems with more than two atoms, they received a considerable

attention in the literature over the last decades and continue to be intensively studied nowadays. Their consideration in photophysics, photochemistry and photo-initiated reactions is mandatory to understand the complex photoabsorption and photoelectron spectra of many molecules [19]. But their role goes beyond these fields with their implication in systems of biological interest. More specifically their role can explain the stability of the DNA molecule [20, 21] with respect to radiation as well as the mechanism of the vision thanks to the study of the retinal [22]. The theoretical treatment of the conical intersection remains a complex task. Various quantal and classical approaches have been developed to deal with the inherent strong non-adiabatic coupling effects, and required an approximate treatment [19]. Most of the methods keep the concept of the Potential Energy Surfaces (PES), which are approximated or obtained from an ab-initio evaluation, and an approximate evaluation of the non-adiabatic coupling terms is done. One of these approaches, known as the linear vibronic coupling model, developed at the University of Heidelberg [23], rests on the Taylor-series expansion of the electron-nuclear interaction and has been successfully applied in numerous systems. Nonetheless, its harmonic approximation of the PES remains drastic to study small molecules for which accurate evaluation of the adiabatic PES can be performed. Thus a recent diabatization scheme [24, 25] has been proposed in order to keep the anharmonic shape of the PES. This method, known as the regularised diabatic scheme, provides accurate results and treats the nuclear motion on a fully quantal basis.

The simultaneous theoretical study of nuclear dynamics, conical intersection and HHG required the choice of a small system. Unfortunately, conical intersection does not occur in diatomic systems, for which the only vibrational degree of freedom leads to avoiding crossing between the potential energy curves. Thus triatomic molecules must be investigated. In the large panel of triatomic systems, the sulfur dioxide (SO_2) particularly raises our curiosity by its implication in various fields of research and an intensive production in the literature. The study of electronic excited states of SO_2 started as an academic problem in the 30's, after the extensive investigation of diatomic systems, in which great advances have been achieved thanks to the development of quantum theory. The ground state properties of SO_2 were just investigated by infrared and Raman spectroscopy [26], and Watson and Parker paved the way to the molecular excited state spectroscopy [27]. With the resolution and intensity available at this time, the so-called "first allowed band" was observed, and because of its complicated structures it opened a large debate over a decade for its vibrational assignment as well as the nature of the electronic state(s) [28, 29, 30], but remained unsolved.

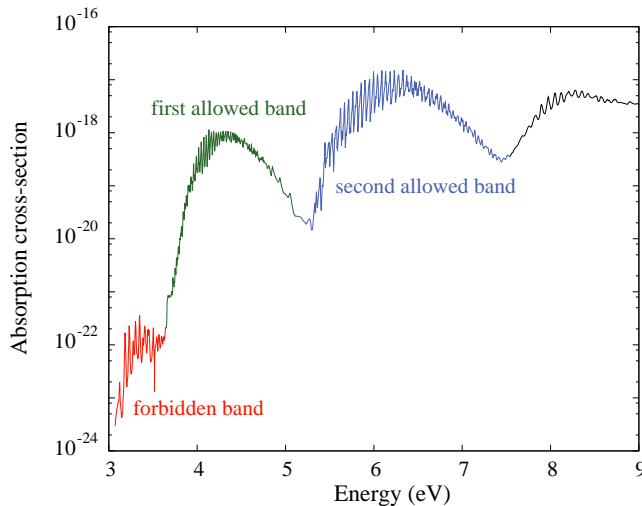


Figure 1.1: Photoabsorption spectrum of the sulfur dioxide in the near- vacuum UV domain between 3 – 9 eV. The three absorption bands discussed in the text are indicated, in red for the so-called "forbidden band", in green for the "first allowed" band and in blue for the "second allowed" band. The spectrum has been recorded by S. Manatt and A. Lane [31] in the gas phase at 293 ± 10 K.

Sulfur dioxide is then established as a major atmospheric pollutant in the middle of the 60's, and the reactivity of the excited electronic states is widely considered and established to play a role in acid rains, respiratory difficulties, damage to vegetation and materials [32]. While its presence in the air was already under survey, large efforts have been deployed to study the photochemistry of the molecule and its reactivity with atmospheric compounds, such as O_2 [33], CO [34], hydrocarbons [35] etc., summarized by Calver and Pitts [36]. During the same time, new experimental methods were used to unravel the first allowed band of the molecule, and using strong magnetic field Douglas [37] observed a Zeeman effect and assigned the "forbidden band" to electronic triplet state, later rotationally demonstrated to be of B_1 symmetry by Merer [38]. This first assignment of electronic excited states of the molecule is supported by the first ab-initio calculation of SO_2 in 1971 by Hillier and Saunders [39]. The theoretical prediction of the different electronic states in this energy range make possible the rotational attribution of the "first allowed" band (Fig. 1.1), which concluded that the band is a transition to an excited state of A_2 symmetry [40]. Interestingly, the transition is dipole-forbidden but can borrow through vibronic coupling with the electronic state of B_1 symmetry predicted a non-vanishing transition dipole moment [41]. This short introduction to the photophysics and photochemistry of SO_2 has been nicely reviewed for the photophysics by Herzberg [42], then Hecklen

et al. [43] and for the atmospheric photochemistry by Calvert and Pitts [36], then Heicklen [44] and Calvert *et al.* [45] and thus for the considerable work performed from 1930 to 1975.

In a period of thirty years, the electronic attribution of the "first allowed band" has been established. Interestingly, the "second allowed band" does not puzzle much, and has been assigned to an electronic state of B_2 symmetry by Brand *et al.* [46, 47], theoretically confirmed later [48]. To our knowledge, no recent review on SO_2 has been published, but the interest remains starting by the first observation in interstellar space [49] in 1975, followed by its detection on Venus [50, 51, 52], Mars [53] and Io [54, 55, 56, 57] and its participation to the photochemistry of their atmospheres and in comets [58, 59]. The molecule became relevant for astrophysics and accurate photoabsorption measurement for its detection continue to be an active research area [60, 61]. And the molecule continues to catch interest in many fields, with the study of volcano emission [53], and climate palaeontology with the first observation of Sulfur mass-independent fraction in Archean sediments [62, 63, 64, 65], which increase greatly the interest in the molecule.

Because of the pertinence of SO_2 in these different fields, theoretical investigations have also been carried out [66, 67, 68] and provided single point calculation and cuts in the PES with a good overview of the pertinent potential energy surfaces of both the singlet and triplet states. While the molecule has been widely study over almost one century, only few studies have been performed, concerning the photo absorption spectrum [69] and the dynamics [70] and do not provide enough information for the total understanding of the photophysics taking place in the 3.1 – 5.5 eV range.

The specific choice of SO_2 for this thesis has been greatly motivated by the recent experimental work carried out by I. Wilkinson, A. Stolow and D. Villeneuve from the university of Ottawa and H-J. Wörner at the ETH in Zürich [71]. They performed two different pump-probe schemes in order to study the dynamics initiated by an excitation into the two first singlet excited states. One experiment used Time-Resolved Photo-Electron Spectroscopy (TRPES), method in which the probe ionised the molecular system after a controllable delay with the pump, and the yield of photoelectron is monitored as a function of the time. This method, in the same way as high-order harmonic spectroscopy, its sensitive to both the nuclei and valence-electron dynamics, which derives from the ionisation-matrix [72]. Using this probe, they have been able to track the signature of the dynamics of the wavepacket in the neutral excited states. The second set of experiment makes

use of the HHG spectroscopy after a prior excitation with the same pump as before. While this method is established for unprecedented sensitivity to both nuclear and electron motion, no clear signature of dynamics is observed, while features similar to the case of NO_2 were expected. It shows that the HHG spectroscopy applied to molecular dynamics required theoretical investigation in order to understand its applicability and why it does not work for any kind of system.

The aim of our work is to answer to the previous interrogation and try to understand the limits of application of the HHG spectroscopy to study correlated electron-nuclear dynamics. In order to achieve this goal, two main points have to be studied. First we need an accurate description of the photophysics of SO_2 occurring after the excitation in the first absorption band. The singlet electronic states are known to be relevant, but a clear interpretation of the role of the triplet states is also required. This first step is mandatory before the consideration of the HHG in the molecule. The second point is the methodological development of a model to take into account the nuclear dynamics during the HHG process. A direct resolution for a system as SO_2 is beyond the scope of any work nowadays, a set of approximations has to be used, and our model will be based on the Strong-field approximation which has been successfully applied to atoms [73] and extended to molecules [74], but not for time-dependent dynamics.

The present document collects the results of the last three years to try to unravel the mentioned issues. The first part of the manuscript presents the theoretical framework that has been used to solve the problem. The separation of the electronic and nuclear degrees of freedom in order to solve separately the electronic and nuclear problem is presented, with the consideration of the coupling terms which, in the case of a conical intersection, breaks down the Born-Oppenheimer approximation. Then the concept of diabatic states is introduced and how quasi-diabatic states are obtained. It is followed by the introduction to the methods to solve the time-independent electronic Schrödinger equation, and the time-dependent one for the nuclear dynamics. This part is closed by the introduction of methods used to compute photoabsorption and photoelectron spectra in the time-dependent formalism as well as the methods used for the Time-resolved photoelectron spectra and our model for HHG with a quantum description of the nuclei.

The second part is dedicated to the results of the methodological section. The ab-initio potential energy

surfaces of the different states considered are presented and discussed. Then the states coupled through a conical intersection have been diabaticized. An important point of the work is the extension of the diabaticization to take into account the geometry dependence of the spin-orbits coupling elements. The results of the method are detailed, and a brief summary of the diabaticization of the transition dipole moment is proposed. The second part will be ended by the results concerning the diabaticization of the recombination matrix element required to describe the HHG in the molecule.

The results concerning the physics of the system are exposed in the third and fourth part of the manuscript. Starting by the dynamics in the singlet excited states and the analysis of the photoabsorption spectrum. Next the role of the triplet states is presented and the mechanisms of the intersystem conversion analysed as well as the low energy part experimentally assigned to them. A similar work has been carried out of the ionic states of the system, required to describe the TRPES and HHG processes. The TRPES simulations are presented with a different model in order to get information regarding the experiment carried out at his time. The HHG is studied, first with a comparison of the wavepacket formulation and the classical description. Then a wavepacket dynamic in the electronic ground state is proposed to understand the role of the different mechanisms with a simple system before the consideration of the dynamics in the excited states, and the comparison with the experiments.

Chapter 2

Theoretical Methods and Algorithms

2.1 Introduction

In this chapter the different methods and approximations that have been used in this thesis are presented. In the field of atoms and molecules interacting with electro-magnetic fields the problem of a theoretician can be conveniently presented, it is just contained in one general equation:

$$i\hbar \frac{d}{dt} |\Psi(t)\rangle = \hat{H}(t) |\Psi(t)\rangle, \quad (2.1)$$

the time dependent Schrödinger equation [75]. Without going into further details, this equation is the basis of quantum mechanics, describing the physical law of the dynamics on the particle scale. It describes the time evolution of the wavefunction $|\Psi(t)\rangle$, the representation of a quantum state of a system, under the influence of a Hamiltonian operator $\hat{H}(t)$. Solving this equation gives us the possibility to follow, from a set of initial conditions, the evolution in time of the system. Unfortunately analytical solutions are only possible for textbook examples and such solutions are generally not available for physical systems such as multi-electron atomic or molecular systems. The goal of this methodological part is to highlight how we solved the Schrödinger equation for our system, the different approximations we chose for the different physical processes we were interested on.

Even if we will try to be as general as possible, one should keep in mind that the final goal of this work

is to study the sulfur dioxide molecule, composed of one sulfur atom and two oxygen atoms with a total of 32 electrons. In principle all the methods discussed here can be applied to any system, but the choice of approximation and methods always have to be chosen for a particular system.

2.2 Quantum treatment of the nuclear motion

Starting from the general form of the Schrödinger equation (2.1), let us have a look on its different terms that compose it. We want to describe a molecular system in empty space without interaction with the rest of the universe. The molecule is composed of a finite number N of nuclei that can be labelled k , with $k = 1, 2, 3, \dots, N$. Each atom k has a number n_k of electrons leading to a total of electron $n = \sum_i^N n_k$ in the system. Introducing a three-dimension orthonormal frame in space, we can attribute to each of the particles of our system a set of three Cartesian coordinates and define a position vector that we call \mathbf{R}_k for the nuclei and \mathbf{r}_i for the electrons. Projecting our quantum state $|\Psi(t)\rangle$ onto the basis formed by the position of the $(N + n)$ particles we obtain a representation of the wavefunction (*wf*) of the system $\Psi(\mathbf{R}, \mathbf{r}, t)$ in this particular basis where we introduced \mathbf{R} and \mathbf{r} the vector collecting the positions of all nuclei and electrons, respectively.

The Hamiltonian $\hat{H}(t)$ describes all the interactions in the system and can be expressed as the sum of two terms:

$$\hat{H}(\mathbf{R}, \mathbf{r}, t) = \hat{T}(\mathbf{R}, \mathbf{r}) + U(\mathbf{R}, \mathbf{r}, t) \quad (2.2)$$

where we have introduced the kinetic energy operator $\hat{T}(\mathbf{R}, \mathbf{r})$ and a general potential energy operator $U(\mathbf{R}, \mathbf{r}, t)$. The latter can be decomposed in a time dependent and a time independent terms:

$$U(\mathbf{R}, \mathbf{r}, t) = V(\mathbf{R}, \mathbf{r}) + f(\mathbf{R}, \mathbf{r}, t). \quad (2.3)$$

In the purpose of this section we will drop the time dependent part, $f(\mathbf{R}, \mathbf{r}, t)$, of the potential function, because we will only study the molecular system. We will reintroduce it to deal with the interaction of the

molecule with an external electric field later. Then our working Hamiltonian reads:

$$\hat{H}(\mathbf{R}, \mathbf{r}) = \hat{T}(\mathbf{R}, \mathbf{r}) + V(\mathbf{R}, \mathbf{r}). \quad (2.4)$$

In the following the atomic unit system will be used [76]. In the Cartesian basis that we introduced, the kinetic energy operator can be written,

$$\hat{T}(\mathbf{R}, \mathbf{r}) = \sum_i^n -\frac{1}{2} \nabla_{e,i}^2 + \sum_k^N -\frac{1}{2M_k} \nabla_k^2. \quad (2.5)$$

In the above equation $\nabla_{e,i}^2$ and ∇_k^2 represent the Laplacian of the electron and of the k^{th} nucleus, respectively. M_k is the ratio of the mass of nucleus k to the mass of an electron. The potential function $V(\mathbf{R}, \mathbf{r})$ describes all the electrostatic interactions between the particles of the systems, and can be written as:

$$V(\mathbf{R}, \mathbf{r}) = - \sum_i^n \sum_k^N \frac{Z_k}{|\mathbf{R}_k - \mathbf{r}_i|} + \sum_{i>j}^n \frac{1}{|\mathbf{r}_i - \mathbf{r}_j|} + \sum_{k>l}^N \frac{Z_k Z_l}{|\mathbf{R}_k - \mathbf{R}_l|}, \quad (2.6)$$

where we introduced Z_k the nuclear charge of the k^{th} nucleus. Reading the above equation from left to right, we have the electron-nucleus attractive interaction, the electron-electron and the nucleus-nucleus repulsive interactions. Our system is composed of two different particles, the electrons and nuclei, with different properties, so in the following we will rewrite Eq. (2.5) and (2.6) to concentrate on the electronic part of the Hamiltonian.

2.2.1 The Born-Huang expansion and Born-Oppenheimer approximation

The main idea of the Born-Oppenheimer (BO) approximation [77] is based on the mass ratio of the electrons and nuclei. The nuclei are composed by the nucleons (protons and neutron) and have masses ~ 1836 times heavier than the electron one. The resulting stronger inertia of the nuclei compare to the electron allows to consider that the electrons move in the field of fixed nuclei. In addition, the Hamiltonian does not depend on the time variable and we can proceed with the time-independent Schrödinger equation (TISE) [78, 79],

$$\hat{H}(\mathbf{R}, \mathbf{r})\Psi(\mathbf{R}, \mathbf{r}) = E\Psi(\mathbf{R}, \mathbf{r}), \quad (2.7)$$

where we used the Hamiltonian from Eq. (2.4), and E the total energy of the system. The BO approximation results in the definition of the electronic wavefunction $\phi_e(\mathbf{r}; \mathbf{R})$, where the inclusion of the semi-colon indicates that the electronic wavefunction depends parametrically of the nuclei positions \mathbf{R} . Collecting only the electronic part of the Hamiltonian (2.4), we define the time-independent *electronic* Schrödinger equation:

$$\hat{H}_e(\mathbf{r}; \mathbf{R})\phi_e^l(\mathbf{r}; \mathbf{R}) = E_e^l(\mathbf{R})\phi_e^l(\mathbf{r}; \mathbf{R}), \quad (2.8)$$

where the electronic energy $E_e^l(\mathbf{R})$ depends on the position of nuclei and $\hat{H}_e(\mathbf{r}; \mathbf{R})$,

$$\hat{H}_e(\mathbf{r}; \mathbf{R}) = \sum_i^n -\frac{1}{2}\nabla_{e,i}^2 - \sum_i^n \sum_k^N \frac{Z_k}{|\mathbf{R}_k - \mathbf{r}_i|} + \sum_{i>j}^n \frac{1}{|\mathbf{r}_i - \mathbf{r}_j|} \quad (2.9)$$

is the electronic Hamiltonian. The set of eigenfunctions $\{\phi_e^l(\mathbf{r}; \mathbf{R})\}$ forms a complete basis of the electronic space, spanning every value of \mathbf{R} and we will detail later (see Sec. 2.4) how the $\phi_e^l(\mathbf{r}; \mathbf{R})$ are obtained. We can use this complete basis to expand the full wavefunction of the system $\Psi(\mathbf{r}, \mathbf{R})$ [19],

$$\Psi(\mathbf{r}, \mathbf{R}) = \sum_i \phi_e^i(\mathbf{r}; \mathbf{R})\chi_i(\mathbf{R}), \quad (2.10)$$

where $\chi_i(\mathbf{R})$ is the vibrational nuclear wavefunction. Inserting this ansatz (2.10) in the Schrödinger equation Eq. (2.7), multiplying on the left by $\phi_e^{j*}(\mathbf{r}; \mathbf{R})$ and integrating over the electronic coordinates leads to a set of coupled differential equations for the nuclear wavefunction $\chi_j(\mathbf{R})$,

$$(E_e^j(\mathbf{R}) + V_N(\mathbf{R}))\chi_j(\mathbf{R}) + \sum_i \int d\mathbf{r} \phi_e^{j*}(\mathbf{r}; \mathbf{R}) \hat{T}_N(\mathbf{R}) \phi_e^i(\mathbf{r}; \mathbf{R}) \chi_i(\mathbf{R}) = E \chi_j(\mathbf{R}). \quad (2.11)$$

Note that the coupling term $[\sum_i \dots]$ comes from the action of the nuclear kinetic energy operator on the parametrized electronic *wf*. The resolution of the Schrödinger equation is cumbersome because of this coupling term. Using the explicit form of $\hat{T}_N(\mathbf{R})$ expressed in Eq. (2.5) we obtain,

$$\begin{aligned} & \sum_i \int d\mathbf{r} \phi_e^{j*}(\mathbf{r}; \mathbf{R}) \hat{T}_N(\mathbf{R}) \phi_e^i(\mathbf{r}; \mathbf{R}) \chi_i(\mathbf{R}) = -\frac{1}{2M} \sum_i \int d\mathbf{r} \phi_e^{j*}(\mathbf{r}; \mathbf{R}) \nabla_{\mathbf{R}}^2 [\phi_e^i(\mathbf{r}; \mathbf{R}) \chi_i(\mathbf{R})] \\ = & \delta_{ij} \hat{T}_N(\mathbf{R}) \chi_i(\mathbf{R}) + \left[-\frac{1}{2M} \sum_i \left(\int d\mathbf{r} \phi_e^{j*}(\mathbf{r}; \mathbf{R}) \nabla_{\mathbf{R}}^2 \phi_e^i(\mathbf{r}; \mathbf{R}) + 2 \int d\mathbf{r} \phi_e^{j*}(\mathbf{r}; \mathbf{R}) \nabla_{\mathbf{R}} \phi_e^i(\mathbf{r}; \mathbf{R}) \cdot \nabla_{\mathbf{R}} \right) \right] \chi_i(\mathbf{R}) \end{aligned} \quad (2.12)$$

In this expression, the term in square brackets is known as the non-adiabatic coupling operator and acts on the nuclear wavefunction. The first aspect to emphasise is that this operator is composed of one scalar component, i.e.

$$\int d\mathbf{r} \phi_e^{j*}(\mathbf{r}; \mathbf{R}) \nabla_{\mathbf{R}}^2 \phi_e^i(\mathbf{r}; \mathbf{R}), \quad (2.13)$$

and a vectorial one,

$$\int d\mathbf{r} \phi_e^{j*}(\mathbf{r}; \mathbf{R}) \nabla_{\mathbf{R}} \phi_e^i(\mathbf{r}; \mathbf{R}) \cdot \nabla_{\mathbf{R}}. \quad (2.14)$$

Noting \mathbf{G} and \mathbf{F} the matrices of $\nabla_{\mathbf{R}}^2$ and $\nabla_{\mathbf{R}}$ onto the adiabatic electronic basis set, their matrix elements read,

$$G_{ji} = \langle \phi_e^{j*}(\mathbf{R}) | \nabla_{\mathbf{R}}^2 | \phi_e^i(\mathbf{R}) \rangle, \quad F_{ji} = \langle \phi_e^{j*}(\mathbf{R}) | \nabla_{\mathbf{R}} | \phi_e^i(\mathbf{R}) \rangle. \quad (2.15)$$

We can rewrite the non-adiabatic coupling operator as:

$$\sum_i -\frac{1}{2M} (G_{ji} + 2F_{ji} \cdot \nabla_{\mathbf{R}}). \quad (2.16)$$

Thus, by expressing the nuclear wavefunction as a vector $\chi = (\chi_1(\mathbf{R}), \dots, \chi_m(\mathbf{R}))^\dagger$, the Schrödinger equation can be expressed in a matrix form:

$$\mathbf{E}_e \chi + (\hat{T}_N + V_N) \mathbf{1} \cdot \chi - \frac{1}{2M} (\mathbf{G} + 2\mathbf{F} \cdot \nabla) \chi = E \chi \quad (2.17)$$

where \mathbf{E}_e is the diagonal electronic energy matrix, see Eq. (2.8), $\mathbf{1}$ is the unitary matrix and the gradient ∇ is a vector in the nuclear space. It is instructive at this point to have a look on the characteristics of the scalar and vectorial coupling terms, starting with the latter, and using the orthogonality relation $\langle \phi^j(\mathbf{R}) | \phi^i(\mathbf{R}) \rangle = \delta_{ij}$ one gets

$$\begin{aligned} \nabla_{\mathbf{R}} \langle \phi_e^j(\mathbf{R}) | \phi_e^i(\mathbf{R}) \rangle &= \langle \nabla_{\mathbf{R}} \phi_e^j(\mathbf{R}) | \phi_e^i(\mathbf{R}) \rangle + \langle \phi_e^j(\mathbf{R}) | \nabla_{\mathbf{R}} \phi_e^i(\mathbf{R}) \rangle = 0 \\ \text{and } F_{ji} &= -F_{ij}^*. \end{aligned} \quad (2.18)$$

Thus \mathbf{F} is anti-Hermitian, and if the electronic wavefunction are chosen to be real, its diagonal is null, i.e. $F_{ii} = 0$. The gradient of \mathbf{F} is

$$\nabla_{\mathbf{R}} F_{ji} = \langle \phi_e^j(\mathbf{R}) | \nabla_{\mathbf{R}}^2 \phi_e^i(\mathbf{R}) \rangle + \langle \nabla_{\mathbf{R}} \phi_e^j(\mathbf{R}) | \nabla_{\mathbf{R}} \phi_e^i(\mathbf{R}) \rangle \quad (2.19)$$

leading to

$$G_{ji} = \nabla_{\mathbf{R}} F_{ji} - \langle \nabla_{\mathbf{R}} \phi_e^j(\mathbf{R}) | \nabla_{\mathbf{R}} \phi_e^i(\mathbf{R}) \rangle, \quad (2.20)$$

which, when introducing the closure relation, $\sum_k |\phi_e^k(\mathbf{R})\rangle \langle \phi_e^k(\mathbf{R})| = 1$, becomes

$$G_{ji} = \nabla_{\mathbf{R}} F_{ji} - \sum_k F_{jk} F_{ki}. \quad (2.21)$$

It turns out that the non-adiabatic coupling is fully defined by the knowledge of \mathbf{F} only, and Eq. (2.17) is rewritten as

$$[(\mathbf{E}_e + V_N \cdot \mathbf{1}) - \frac{1}{2M} (\nabla + \mathbf{F})^2 - E] \chi = 0 \quad (2.22)$$

with the help of

$$(\nabla + \mathbf{F})^2 = \nabla^2 + \mathbf{F} \cdot \nabla + \nabla \cdot \mathbf{F} + \mathbf{F} \cdot \mathbf{F} = \nabla^2 + \mathbf{F} \cdot \nabla + \mathbf{G}. \quad (2.23)$$

It is important to keep in mind that this relation results from the closure relation, and then is truly satisfied in a complete electronic basis only. This situation is impossible to obtain, but Eq.(2.22) is a convenient form to introduce the approximations that may be done to simplify and solve the problem [19]. (i) The problem can be simplified by setting $\mathbf{F} = \mathbf{0}$ in Eq. (2.22), which leads to a set of *uncoupled* equations. Each of them can be solved separately for an individual electronic solution $\chi_i(\mathbf{R})$, and actually describes the nuclei wavefunction of the adiabatic Potential Energy Surface (PES) $E_e^i(\mathbf{R})$ associated to $\phi_e^i(\mathbf{r}; \mathbf{R})$. This approximation is the so-called Born-Oppenheimer approximation. (ii) A second possibility to simplify the resolution of Eq. (2.22), known as the Born-Huang approximation, is to neglect only the off diagonal elements of \mathbf{F} . In the case of real electronic wavefunction, it is equivalent to consider the diagonal matrix element of \mathbf{G} , i.e. G_{ii} , because of the anti-hermiticity of \mathbf{F} , see Eq. 2.18, and leads also to a set of uncoupled equations. These approximations have been suggested because of the non-adiabatic coupling is inversely proportional to the nuclei masses and have been shown to be accurate in some situation (for example in our case it is perfectly suitable for the

electronic ground state). But in some situations these approximation gives disastrous results, which we will discuss in the following.

2.2.2 The Breakdown of the Born-Oppenheimer approximation

To understand why neglecting the non-adiabatic coupling can lead to disastrous results, we have to come back to \mathbf{F} , and particularly on the action of the nuclear gradient on the parametrized electronic wavefunctions and Hamiltonian $H_e(\mathbf{R})$. As \mathbf{F} is anti-hermitian, only the case $\phi_e^j(\mathbf{r}; \mathbf{R})$ and $\phi_e^i(\mathbf{r}; \mathbf{R})$ with $i \neq j$ has to be considered, i.e.

$$\begin{aligned} \nabla_{\mathbf{R}} \langle \phi_e^j(\mathbf{R}) | H_e(\mathbf{R}) | \phi_e^i(\mathbf{R}) \rangle &= E_e^i(\mathbf{R}) \langle \nabla_{\mathbf{R}} \phi_e^j(\mathbf{R}) | \phi_e^i(\mathbf{R}) \rangle + \langle \phi_e^j(\mathbf{R}) | \nabla_{\mathbf{R}} H_e(\mathbf{R}) | \phi_e^i(\mathbf{R}) \rangle + E_e^j(\mathbf{R}) \langle \phi_e^j(\mathbf{R}) | \nabla_{\mathbf{R}} \phi_e^i(\mathbf{R}) \rangle \\ \Leftrightarrow F_{ji} &= \frac{\langle \phi_e^j(\mathbf{R}) | \nabla_{\mathbf{R}} H_e(\mathbf{R}) | \phi_e^i(\mathbf{R}) \rangle}{(E_e^i(\mathbf{R}) - E_e^j(\mathbf{R}))} \end{aligned} \quad (2.24)$$

This relation is often called in the literature "non-diagonal" form of the Hellman-Feynman theorem [19]. In the denominator appears the energy difference between the two electronic states, which means that neglecting \mathbf{F} is only possible for electronic states which are well separated in energy. This approximation breaks down in the case of electronic states with similar energies, and becomes worse for two degenerate electronic states, i.e. with the same energy. As only electronic states with close energies are coupled, the idea has been proposed to restrict the infinite set of coupled Eq. (2.22) to a subgroup of strongly coupled states. We call $\{\alpha\}$ this subgroup and we assume their coupling with the complementary manifold weak enough to be neglected. The Schrödinger equation can then be expressed for the subgroup $\{\alpha\}$ as:

$$\left[\left(\mathbf{E}_e^{\{\alpha\}}(\mathbf{R}) + V_N \cdot \mathbf{1} \right) - \frac{1}{2M} (\nabla + \mathbf{F})^{2\{\alpha\}} - E \right] \chi^{\{\alpha\}} = 0 \quad (2.25)$$

using the expanded form of $(\nabla + \mathbf{F})^{2\{\alpha\}}$ of Eq. (2.23). The derivative coupling $\mathbf{F}^{\{\alpha\}}$ is well defined in this subgroup of electronic states, but \mathbf{G} contains a global interaction term Eq. (2.21),

$$G_{ji} = \nabla_{\mathbf{R}} F_{ji} - \sum_k \langle \nabla_{\mathbf{R}} \phi_e^j(\mathbf{R}) | \phi_e^k(\mathbf{R}) \rangle \langle \phi_e^k(\mathbf{R}) | \nabla_{\mathbf{R}} \phi_e^i(\mathbf{R}) \rangle \quad (2.26)$$

where the index k is running over the complete electronic basis. The truncation of the sum into the subspace $\{\alpha\}$ introduces an error that can be estimated by making used of the same relation as Eq. (2.24) considering

the diagonal and off-diagonal matrix elements,

$$G_{ji} = \begin{cases} \nabla_{\mathbf{R}} \left(\frac{\langle \phi_e^j(\mathbf{R}) | \nabla_{\mathbf{R}} H_e(\mathbf{R}) | \phi_e^i(\mathbf{R}) \rangle}{(E_e^i(\mathbf{R}) - E_e^j(\mathbf{R}))} \right) - \sum_k \frac{\langle \phi_e^j(\mathbf{R}) | \nabla_{\mathbf{R}} H_e(\mathbf{R}) | \phi_e^k(\mathbf{R}) \rangle \langle \phi_e^k(\mathbf{R}) | \nabla_{\mathbf{R}} H_e(\mathbf{R}) | \phi_e^i(\mathbf{R}) \rangle}{(E_e^k(\mathbf{R}) - E_e^j(\mathbf{R})) (E_e^i(\mathbf{R}) - E_e^k(\mathbf{R}))} & \text{if } i \neq j \\ -\langle \phi_e^j(\mathbf{R}) | \nabla_{\mathbf{R}} H_e(\mathbf{R}) | \phi_e^i(\mathbf{R}) \rangle & \text{if } i = j. \end{cases} \quad (2.27)$$

An error is introduced in the off-diagonal terms of \mathbf{G} , where the sum over k is restricted to the subspace $\{\alpha\}$. The terms which are neglected present in the denominator the inverse of the energy difference between electronic states of $\{\alpha\}$ and the complementary ones. As we assumed that the states of $\{\alpha\}$ are energetically well separated to the other, these terms are small. The approximated Schrödinger equation in the subspace of electronic states $\{\alpha\}$ is,

$$[(\mathbf{E}_e^{(\alpha)} + V_N \cdot \mathbf{1}) - \frac{1}{2M} (\nabla + \mathbf{F}^{(\alpha)})^2 - E] \chi^{(\alpha)} = 0, \quad (2.28)$$

which is the expression of the nuclear function in a restricted space of electronic states. The subspace $\{\alpha\}$ can include an arbitrary number of states, and Eq. (2.28) is exact when $\{\alpha\}$ includes all of them.

2.2.3 Diabatic states

Once the problem reduced to the subspace $\{\alpha\}$, the singularity of \mathbf{F} , in the case of degenerate electronic states, still remains. It is interesting to note that this difficulty to solve the nuclear dynamics results from our way to handle the electronic calculation. By using adiabatic electronic states (obtained by setting $T_N = 0$) to uncouple the nuclear motion from the electronic one, we introduced a coupling into the equation of the nuclear motion, which leads to a coupling between the different electronic states. Nevertheless, nowadays this method is certainly the most used for large set of system and the most practical one and then we have to deal with it. Coming back to our problem, the non-adiabatic coupling will be strongly reduced if the electronic functions have a smooth variation according to the nuclear displacement, or even vanishing if they do not depend of them. The method to handle the non-adiabatic coupling is to find a more suitable electronic basis to express the total wavefunction. Such basis are called diabatic basis and will be denoted in the following as $\{\phi_i^{(d)}(\mathbf{r}; \mathbf{R})\}$ where we have dropped the subscript "e" for electron. In the same idea we rename the adiabatic electronic basis $\{\phi_i^{(a)}(\mathbf{r}; \mathbf{R})\}$ in the following discussion. The idea of the diabatization is to find a unitary transformation $\mathbf{U}(\mathbf{R})$, which minimises the non-adiabatic coupling, in the following we use the notation:

$\mathbf{U}_{\mathbf{R}} \equiv \mathbf{U}(\mathbf{R})$. The diabatic electronic functions are defined as [80]

$$\phi^{(d)} = \mathbf{U}_{\mathbf{R}}^\dagger \phi^{(a)}, \quad (2.29)$$

where $\phi^{(a)} = (\phi_1^{(a)}(\mathbf{r}; \mathbf{R}), \dots, \phi_m^{(a)}(\mathbf{r}; \mathbf{R}))$ and $\phi^{(d)} = (\phi_1^{(d)}(\mathbf{r}; \mathbf{R}), \dots, \phi_m^{(d)}(\mathbf{r}; \mathbf{R}))$ are row vectors collecting all the diabatic and adiabatic wavefunctions, respectively. The total wavefunction, which does not depend on the basis, can be expressed in the two basis as,

$$\Psi(\mathbf{R}, \mathbf{r}) = \phi^{(d)} \cdot \chi^{(d)} = \phi^{(a)} \cdot \chi^{(a)} \quad (2.30)$$

where $\chi^{(d)}$ and $\chi^{(a)}$ collect the vibrational wavefunction in the diabatic and adiabatic basis, respectively with the notation introduced in Sec. 2.2.1. From the definition in Eq.(2.29), we obtain:

$$\chi^{(a)} = \mathbf{U}_{\mathbf{R}} \chi^{(d)} \text{ and } \chi^{(d)} = \mathbf{U}_{\mathbf{R}}^\dagger \chi^{(a)}, \quad (2.31)$$

where we used the properties of an unitary matrix, i.e. $\mathbf{U}_{\mathbf{R}}^{-1} \mathbf{U}_{\mathbf{R}} = \mathbf{U}_{\mathbf{R}}^\dagger \mathbf{U}_{\mathbf{R}} = \mathbf{1}$. The diabatic vibrational wavefunctions can then be used in Eq. (2.22),

$$\begin{aligned} & \left[(\mathbf{E}_e(\mathbf{R}) + V_N \cdot \mathbf{1}) - \frac{1}{2M} (\nabla + \mathbf{F})^2 - E \right] \mathbf{U}_{\mathbf{R}} \chi^{(d)} = 0 \\ \Leftrightarrow & \quad [\mathbf{E}_e(\mathbf{R}) + V_N \cdot \mathbf{1} - E] \mathbf{U}_{\mathbf{R}} \chi^{(d)} - \frac{1}{2M} [\nabla^2 \mathbf{U}_{\mathbf{R}} + \mathbf{G} \mathbf{U}_{\mathbf{R}} + 2\mathbf{F} \nabla \mathbf{U}_{\mathbf{R}}] \chi^{(d)} \\ & - \frac{1}{M} [\nabla \mathbf{U}_{\mathbf{R}} + \mathbf{F} \mathbf{U}_{\mathbf{R}}] \nabla \chi^{(d)} - \frac{1}{2M} \mathbf{U}_{\mathbf{R}} \nabla^2 \chi^{(d)} = 0 \end{aligned} \quad (2.32)$$

If we now assume that $\mathbf{U}_{\mathbf{R}}$ is chosen that

$$\nabla \mathbf{U}_{\mathbf{R}} + \mathbf{F} \mathbf{U}_{\mathbf{R}} = 0 \quad (2.33)$$

Eq. (2.32) not becomes only more simple but leads to another interesting property, when evaluating the gradient of Eq. (2.33) using Eq. (2.21)

$$0 = \nabla (\nabla \mathbf{U}_{\mathbf{R}} + \mathbf{F} \mathbf{U}_{\mathbf{R}}) = \nabla^2 \mathbf{U}_{\mathbf{R}} + \mathbf{G} \mathbf{U}_{\mathbf{R}} + 2\mathbf{F} \nabla \mathbf{U}_{\mathbf{R}}. \quad (2.34)$$

Thus Eq. (2.32) becomes

$$[\mathbf{E}_e(\mathbf{R}) + V_N \cdot \mathbf{1} - E] \mathbf{U} \boldsymbol{\chi}^{(d)} - \frac{1}{2M} \mathbf{U} \mathbf{R} \nabla^2 \boldsymbol{\chi}^{(d)} = 0, \quad (2.35)$$

that, when multiplying on the left by \mathbf{U}^\dagger , leads to the more attractive equation

$$[\mathbf{E}_e^{(d)}(\mathbf{R}) + V_N \cdot \mathbf{1} - E] \boldsymbol{\chi}^{(d)} + \hat{T}_N \mathbf{1} \cdot \boldsymbol{\chi}^{(d)} = 0. \quad (2.36)$$

However, it is still a set of coupled equations but now the coupling is transferred to the diabatic potential matrix $\mathbf{E}_e^{(d)}(\mathbf{R})$, given by

$$\mathbf{E}_e^{(d)}(\mathbf{R}) = \mathbf{U}_R^\dagger \mathbf{E}_e(\mathbf{R}) \mathbf{U}_R. \quad (2.37)$$

The price to pay is that potential matrix is no longer diagonal and the off-diagonal terms of $\mathbf{E}_e^{(d)}(\mathbf{R})$ is a signature of the derivative coupling in the diabatic basis, which is not diagonal anymore. Eq. (2.33) could be difficult to fulfill (and often impossible), but it gives the condition to obtain an exact diabatic basis, which totally removes the non-adiabatic coupling. It is worth making a complete description of the different schemes that have been proposed to obtain an approximate solution for \mathbf{U}_R and obtain a set of quasi-diabatic states. Many approaches have been suggested within the last 40 years, and in the following we will focus on the one that we chose to perform in our work. We will highlight its advantage and its inconvenience.

2.2.4 Conical intersection and regularized diabatic states

Particular attention has been carried in the case when \mathbf{F} becomes singular, i.e. when two adiabatic electronic states are energetically degenerate. The intersection of the adiabatic states is strongly related to symmetry properties of the states within the point group of the molecular system. Defining the latter gives us the possibility of labelling the different electronic states according to the irreducible representation in which they belong. The symmetry condition which are needed to have an intersection between two adiabatic electronic states can be easily understood from a general form of the diabatic potential matrix [80, 19], that we can write,

$$\mathbf{E}_e^{(d)}(\mathbf{R}) = \begin{pmatrix} E_{11}^{(d)}(\mathbf{R}) & E_{12}^{(d)}(\mathbf{R}) \\ E_{12}^{(d)}(\mathbf{R}) & E_{22}^{(d)}(\mathbf{R}) \end{pmatrix} \quad (2.38)$$

We know that the diagonalisation of the diabatic potential (2.37) leads to the adiabatic potential

$$E_e^\pm(\mathbf{R}) = \frac{1}{2} \left[E_{11}^{(d)}(\mathbf{R}) + E_{22}^{(d)}(\mathbf{R}) \pm \sqrt{(E_{11}^{(d)}(\mathbf{R}) - E_{22}^{(d)}(\mathbf{R}))^2 + 4(E_{12}^{(d)}(\mathbf{R}))^2} \right]. \quad (2.39)$$

The energy separation between the two adiabatic states $\Delta E_e(\mathbf{R})$ is given by

$$\begin{aligned} \Delta E_e(\mathbf{R}) &= E_e^+(\mathbf{R}) - E_e^-(\mathbf{R}) \\ &= \sqrt{(E_{11}^{(d)}(\mathbf{R}) - E_{22}^{(d)}(\mathbf{R}))^2 + 4(E_{12}^{(d)}(\mathbf{R}))^2}. \end{aligned} \quad (2.40)$$

Both squared terms in the square root are positive quantities and to have a degeneracy ($\Delta E_e(\mathbf{R}) = 0$) the matrix elements must satisfy simultaneously two conditions:

$$E_{11}^{(d)}(\mathbf{R}) = E_{22}^{(d)}(\mathbf{R}) \quad (2.41)$$

$$\text{and } E_{12}^{(d)}(\mathbf{R}) = 0. \quad (2.42)$$

For a system with only one degree of freedom (e.g. diatomic molecule), if the two electronic states belong to the same irreducible representation both conditions cannot be fulfilled and the well-known non-crossing rules of von Neumann and Wigner stands [81]. In the case of two electronic states, which belong to two different irreducible representations, then the numerator of Eq. (2.24) vanishes, i.e. $E_{12}^{(d)}(\mathbf{R}) = 0$ by symmetry, and the two states do not interact with each other and may freely cross. Generalizing these considerations for a N-dimension system, two coordinates are required to define the intersection point. In the space spanned by both coordinates, any variation of them lifts the degeneracy with a shape of a double-cone (Eq. (2.40)). Due to this geometric particularity, these intersections are known as *conical intersections*.

According to the symmetry of the electronic states and nuclear vibrations, different kinds of conical intersections can be classified [19]. (i) Conical intersections between electronic states of the same symmetry are called, *same-symmetry conical intersection*. This intersection can occur in a subspace of N-2 dimensions, with N the number of internal degree of freedom in the system. (ii) Conical intersections are called *symmetry-required* when two electronic states belong the same degenerate irreducible representation, and thus are energetically degenerate. A small asymmetric distortion of the system will lift the degeneracy, leading to the

popular example of the Jahn-Teller effect. (iii) The last type of is the so-called *symmetry-allowed* conical intersections. It take place in a system that can be describe in a high-symmetric point group, but has one (or more) asymmetric *dof* that can lower its symmetry losing one (or more) symmetry elements. Thus, if in the high-symmetry representation two electronic states with different symmetry cross each other but belong to the same irreducible representation of the low symmetry group, a *symmetry-allowed* conical intersection appears. In the high-symmetry subspace, the condition $E_{12}^{(d)}(\mathbf{R}) = 0$ is fulfilled for any \mathbf{R} . Defining N_g as the number of symmetric *dof* and N_u the number of asymmetric ones, the second condition of Eq. (2.60) is fulfilled in an hyperplane of $N_g - 1$ dimensions, where the two electronic state scan cross freely. because s fulfilled from symmetry reason. This type of conical intersection will take place in our system.

The important point in conical intersection is that symmetry plays a *primordial* role, and can be used to construct the diabatic basis. To continue the discussion on the construction of such basis, as proposed by H. Köppel *et al.* [82, 24, 25], we limit the study into a subspace of two electronic states, i.e. $\alpha = 2$ in Eq. (2.28). A general form of the two-state diabatic Hamiltonian, can be expressed as, according to Eq. (2.36),

$$\mathbf{H}_{dia}(\mathbf{R}) = (\hat{T}_N(\mathbf{R}) + \Sigma(\mathbf{R}))\mathbf{1} + \mathbf{W}(\mathbf{R}) \quad (2.43)$$

$$= (\hat{T}_N(\mathbf{R}) + \Sigma(\mathbf{R}))\mathbf{1} + \begin{pmatrix} d(\mathbf{R}) & c(\mathbf{R}) \\ c(\mathbf{R}) & -d(\mathbf{R}) \end{pmatrix}. \quad (2.44)$$

Diagonalizing the diabatic potential $\Sigma(\mathbf{R})\mathbf{1} + \mathbf{W}(\mathbf{R})$ with an unitary transformation $\mathbf{U}_{\mathbf{R}}$ leads (Eq. (2.37)) to the adiabatic potential,

$$\mathbf{E}_e(\mathbf{R}) = \Sigma(\mathbf{R})\mathbf{1} + \mathbf{U}_{\mathbf{R}} \mathbf{W}(\mathbf{R}) \mathbf{U}_{\mathbf{R}}^\dagger. \quad (2.45)$$

Moreover, diagonalizing the potential matrix $\mathbf{W}(\mathbf{R})$ and introducing the Pauli matrix σ_z ,

$$\sigma_z = \begin{pmatrix} 1 & 0 \\ 0 & -1 \end{pmatrix} \quad (2.46)$$

permits to express Eq.(2.45) as,

$$\mathbf{E}_e(\mathbf{R}) = \Sigma(\mathbf{R})\mathbf{1} + \Delta(\mathbf{R})\sigma_z \quad (2.47)$$

where $\Delta(\mathbf{R}) = \sqrt{d^2(\mathbf{R}) + c^2(\mathbf{R})}$ is the absolute value of the eigenvalue of $\mathbf{W}(\mathbf{R})$. By identifying the matrix elements of the adiabatic basis and with the ones of the diagonalised diabatic one, $\Sigma(\mathbf{R})$ and $\Delta(\mathbf{R})$ can be expressed as a function of the adiabatic states:

$$\Sigma(\mathbf{R}) = \frac{1}{2}(E_e^1(\mathbf{R}) + E_e^2(\mathbf{R})) \quad (2.48)$$

$$\Delta(\mathbf{R}) = \frac{1}{2}(E_e^1(\mathbf{R}) - E_e^2(\mathbf{R})). \quad (2.49)$$

The unitary matrix $\mathbf{U}_{\mathbf{R}}$ can be expressed for a two-state problem, without loss of generality, as a rotation matrix

$$\mathbf{U}_{\mathbf{R}} = \begin{pmatrix} \cos \theta_{\mathbf{R}} & -\sin \theta_{\mathbf{R}} \\ \sin \theta_{\mathbf{R}} & \cos \theta_{\mathbf{R}} \end{pmatrix}, \quad (2.50)$$

with $\theta_{\mathbf{R}} \equiv \theta(\mathbf{R})$ depends on the nuclear coordinates and is defined as the adiabatic-to-diabatic mixing angle.

Explicitly writing the diagonalisation of $\mathbf{W}(\mathbf{R})$ with the used of $\mathbf{U}_{\mathbf{R}}$ leads to,

$$\mathbf{U}_{\mathbf{R}}^\dagger \mathbf{W}(\mathbf{R}) \mathbf{U}_{\mathbf{R}} = \begin{pmatrix} (\cos^2 \theta_{\mathbf{R}} - \sin^2 \theta_{\mathbf{R}})d(\mathbf{R}) + 2 \sin \theta_{\mathbf{R}} \cos \theta_{\mathbf{R}} c(\mathbf{R}) & (\cos^2 \theta_{\mathbf{R}} - \sin^2 \theta_{\mathbf{R}})c(\mathbf{R}) - 2 \sin \theta_{\mathbf{R}} \cos \theta_{\mathbf{R}} d(\mathbf{R}) \\ (\cos^2 \theta_{\mathbf{R}} - \sin^2 \theta_{\mathbf{R}})c(\mathbf{R}) - 2 \sin \theta_{\mathbf{R}} \cos \theta_{\mathbf{R}} d(\mathbf{R}) & (\sin^2 \theta_{\mathbf{R}} - \cos^2 \theta_{\mathbf{R}})d(\mathbf{R}) - 2 \sin \theta_{\mathbf{R}} \cos \theta_{\mathbf{R}} c(\mathbf{R}) \end{pmatrix}. \quad (2.51)$$

This latter becomes diagonal, when equalizing the off-diagonal term to 0. This leads to the expression of the mixing angle $\theta_{\mathbf{R}}$,

$$\begin{aligned} (\cos^2 \theta_{\mathbf{R}} - \sin^2 \theta_{\mathbf{R}} c(\mathbf{R}) - 2 \sin \theta_{\mathbf{R}} \cos \theta_{\mathbf{R}} d(\mathbf{R})) &= 0 \\ \Leftrightarrow \theta_{\mathbf{R}} &= \frac{1}{2} \arctan \left(\frac{c(\mathbf{R})}{d(\mathbf{R})} \right). \end{aligned} \quad (2.52)$$

As the singularity of \mathbf{F} arises at the degeneracy point and raises numerical problems, the starting point to construct the diabatic basis is the degeneracy point of geometry \mathbf{R}_0 . At this geometry both adiabatic states are energetically equal, and it results that

$$\Delta(\mathbf{R}_0) = \sqrt{d^2(\mathbf{R}_0) + c^2(\mathbf{R}_0)} = 0 \Rightarrow c(\mathbf{R}_0) = d(\mathbf{R}_0) = 0 \quad (2.53)$$

or in other words, $\mathbf{W}(\mathbf{R}_0) = 0$. From this relevant geometry it is possible to expand $\mathbf{W}(\mathbf{R})$ in a Taylor series

around \mathbf{R}_0 , i.e.

$$\mathbf{W}(\mathbf{R}) = \mathbf{W}^{(n)}(\mathbf{R}) + \mathbf{W}^{(n+1)}(\mathbf{R}) + \dots \quad (2.54)$$

where the different orders n with respect to the nuclear displacements are collected in $\mathbf{W}^{(n)}(\mathbf{R})$. Considering only the first term of the Taylor expansion, the authors of Ref. [82] have shown that this leading term, $\mathbf{W}^{(n)}(\mathbf{R})$, determines the singular part of the derivative coupling. It can be demonstrate by: (i) the diabaticization of the electronic states and (ii) a back-transformation into the adiabatic basis to ensure that the singularity remained [82]. Using the mixing angle $\theta_{\mathbf{R}}^{(n)}$ defined from $\mathbf{W}^{(n)}(\mathbf{R})$ the unitary transformation $\mathbf{U}_{\mathbf{R}}^{(n)}$ removes totally the singularity in the diabatic basis. This transformation diagonalises the diabatic potential matrix \mathbf{W}^n ,

$$\mathbf{U}_{\mathbf{R}}^{(n)\dagger} \mathbf{W}^{(n)}(\mathbf{R}) \mathbf{U}_{\mathbf{R}}^{(n)} = \Delta^{(n)}(\mathbf{R}) \sigma_z \quad (2.55)$$

Applying the inverse of the above transformation on the adiabatic potential matrix yields the expression of the diabatic one

$$\mathbf{W}_{reg}(\mathbf{R}) = \mathbf{U}_{\mathbf{R}}^{(n)} \mathbf{E}_e(\mathbf{R}) \mathbf{U}_{\mathbf{R}}^{(n)\dagger} = \Sigma(\mathbf{R}) \mathbf{1} + \Delta^{(n)}(\mathbf{R}) \mathbf{U}_{\mathbf{R}}^{(n)} \sigma_z \mathbf{U}_{\mathbf{R}}^{(n)\dagger}. \quad (2.56)$$

From Eq. (2.55) the transformation of the Pauli matrix can be expressed as

$$\mathbf{U}_{\mathbf{R}}^{(n)} \sigma_z \mathbf{U}_{\mathbf{R}}^{(n)\dagger} = \frac{\mathbf{W}^{(n)}(\mathbf{R})}{\Delta^{(n)}(\mathbf{R})}, \quad (2.57)$$

which leads to the final expression of the diabatic potential,

$$\mathbf{W}_{reg}(\mathbf{R}) = \Sigma(\mathbf{R}) \mathbf{1} + \frac{\Delta(\mathbf{R})}{\Delta^{(n)}(\mathbf{R})} \mathbf{W}^{(n)}(\mathbf{R}). \quad (2.58)$$

It is important to notice that the Taylor expansion is only used to define the mixing angle $\theta_{\mathbf{R}}^{(n)}$, and subsequently to $\Delta^{(n)}(\mathbf{R})$ and $\mathbf{W}^{(n)}(\mathbf{R})$, but $\Sigma(\mathbf{R})$ and $\Delta(\mathbf{R})$ are defined from the ab-initio calculations of the adiabatic states. Furthermore, we can see from Eq. (2.43) that when the non-adiabatic coupling term is weak (or vanishes), i.e. $c(\mathbf{R}) \sim 0$, the diabatic potentials is similar (or equal) to the adiabatic ones. It happens in the C_{2v} subspace, but also far from the locus of the conical intersection, when the adiabatic picture is a good approximation (see Sec. 3.3).

Until now, no approximation has been done in the construction of the diabatic states. The singular part of the derivative coupling is the one that leads the dynamics of the system nearby the conical intersection. Thus in this work we consider *only* the leading part of the Taylor expansion. Moreover, we *assume* that in the resulting diabatic basis the nuclear kinetic energy operator (\hat{T}_N) is diagonal, which is the approximation of the model.

Nevertheless, the regularized diabaticization scheme does not define univocally the transformation from adiabatic to diabatic states yet, because the definition of $c(\mathbf{R})$ and $d(\mathbf{R})$ is only given by *one* equation,

$$\Delta(\mathbf{R}) = \sqrt{c^2(\mathbf{R}) + d^2(\mathbf{R})}. \quad (2.59)$$

The symmetry consideration of the conical intersection presented in the beginning of this section will help to solve this problem. In our case we want to deal with a symmetry allowed conical intersection between two electronic states. We call Γ_1 and Γ_2 the irreducible representation of the first and second electronic state, respectively. The two states will interact through a vibrational mode of symmetry Γ_v if,

$$\Gamma_1 \otimes \Gamma_v \otimes \Gamma_2 \supset \Gamma_A, \quad (2.60)$$

is fulfilled. This means that the direct product of the electronic and vibrational irreducible representations must include the totally symmetric representation Γ_A . As mentioned above, a symmetry allowed conical intersection results from a free crossing of the electronic states of two different irreducible representations, i.e. $\Gamma_1 \neq \Gamma_2$. Thus, only an asymmetric vibration can fulfill the condition of Eq. (2.60) in this case. To discuss the vibrational degree of freedom of the molecular system the cartesian coordinates \mathbf{R} , used until now, is not convenient. It is more suitable to introduce a set of coordinate \mathbf{Q} , which describes molecule in term of vibrational modes, for instance the normal coordinates. We collect the symmetric vibrational modes in the subspace \mathbf{Q}^g and the asymmetric ones in \mathbf{Q}^u . In the case where the leading term of the Taylor expansion (Eq. (2.54)) is linear ($n = 1$), the symmetric coordinates do not couple the electronic states and thus are involved in the diagonal elements of the diabatic potential. It is the opposite for the asymmetric ones, which

induced the coupling and thus are involved as off-diagonal elements. The diabatic potential reads,

$$\mathbf{W}^{(1)}(\mathbf{Q}) = \begin{pmatrix} \sum_i^{N_g} \kappa_i Q_i^g & \sum_j^{N_u} \lambda_j Q_j^u \\ \sum_j^{N_u} \lambda_j Q_j^u & -\sum_i^{N_g} \kappa_i Q_i^g \end{pmatrix}, \quad (2.61)$$

where the index i runs over the N_g symmetric displacement and the index j runs over the N_u asymmetric displacement of the molecule. The displacements Q_i^g and Q_j^u are defined from the point of degeneracy Q_0 . From the explicit form of the matrix elements of the diabatic potential, Eq. (2.59) can be rewritten as

$$\Delta(\mathbf{Q}) = \sqrt{\left(\sum_i^{N_g} \kappa_i Q_i^g\right)^2 + \left(\sum_j^{N_u} \lambda_j Q_j^u\right)^2}. \quad (2.62)$$

Differentiating the above equation with respect to the asymmetric displacement Q_j^u at the point of degeneracy leads to

$$\left. \frac{\partial \Delta(\mathbf{Q})}{\partial Q_j^u} \right|_{Q_0} = \lambda_j \quad \Leftrightarrow \quad \lambda_j = \frac{1}{2} \left. \frac{\partial (E_e^1(\mathbf{Q}) - E_e^2(\mathbf{Q}))}{\partial Q_j^u} \right|_{Q_0}. \quad (2.63)$$

The same holds for the symmetric displacement Q_i^g

$$\kappa_i = \frac{1}{2} \left. \frac{\partial (E_e^1(\mathbf{Q}) - E_e^2(\mathbf{Q}))}{\partial Q_i^g} \right|_{Q_0}. \quad (2.64)$$

This means that the quantities needed to fully define the diabatic states can be evaluated from the knowledge of the adiabatic states *only*. As pointed out by the authors, the strength of the method is that no additional ab-initio calculations are requested to diabaticize the electronic states. To determine the coupling constants using Eq. (2.63) and (2.64) the differentiation has to be done at the intersection point Q_0 , but in the case of N_g symmetric displacements the hyperplane of intersections has to be determined, which is not a straightforward task. Thus, this evaluation of the coupling constant is only manageable for small molecular systems. The authors of Ref. [24] proposed a clever idea resulting from symmetry consideration, which consists of taking the adiabatic and diabatic states equal in the high symmetry subspace. This makes sense because the seam of conical intersections fully belongs to this subspace and the adiabatic states do not interact with each other. In this subspace $\mathbf{W}^{(1)}(\mathbf{Q})$ is diagonal, and by identifying the diagonal elements to the adiabatic

potential we obtain,

$$\mathbf{W}^{(1)}(\mathbf{Q}) = \begin{pmatrix} \Delta_0(\mathbf{Q}^g) & \sum_j^{N_u} \lambda_j Q_j^u \\ \sum_j^{N_u} \lambda_j Q_j^u & -\Delta_0(\mathbf{Q}^g) \end{pmatrix} \quad (2.65)$$

Where we introduced the notation $\Delta_0(\mathbf{Q}^g)$ to describe the evaluation of $\Delta(\mathbf{Q})$ in the sub-space \mathbf{Q}^g . Finally, the diabatic Hamiltonian becomes,

$$\mathbf{H}_{dia}(\mathbf{Q}) = (\hat{T}_N + \Sigma(\mathbf{Q}))\mathbf{1} + \frac{\Delta(\mathbf{Q})}{\sqrt{\Delta_0^2(\mathbf{Q}^g) + \sum_j^{N_u} \lambda_j^2 (Q_j^u)^2}} \begin{pmatrix} \Delta_0(\mathbf{Q}^g) & \sum_j^{N_u} \lambda_j Q_j^u \\ \sum_j^{N_u} \lambda_j Q_j^u & -\Delta_0(\mathbf{Q}^g) \end{pmatrix}. \quad (2.66)$$

The system that we consider (SO_2) is small enough to determine the seam of conical intersections and use the above diabatic Hamiltonian. But for larger system, Mahapatra *et al.* [24] proposed to determine the coupling constants of the asymmetric motions, in a similar way than the one used for symmetric displacements,. The $\{\lambda_j\}$ can be computed by differentiating $\Delta(\mathbf{Q})$ with respect to the asymmetric displacement at all point of the high-symmetry subspace,

$$\lambda'_j = \left[\frac{1}{2} \frac{\partial^2 \Delta(\mathbf{Q})}{\partial (Q_j^u)^2} \right]_{Q_j^u=0}^{1/2}. \quad (2.67)$$

Both methods to determine the coupling constants (λ and λ') will be discussed later in this thesis (see Sec. 3.3.1). Now the unitary matrix to transform the adiabatic basis into the diabatic one is well defined.

2.2.5 Electronic properties from adiabatic to diabatic basis

The Quantum Chemistry packages, and more generally the solution of the electronic Schrödinger equation provides the adiabatic electronic wave functions, but these latter is not suitable to solve the nuclear Schrödinger equation. Then the different properties such as the transition and the dipole moments, the spin-orbit couplings and any other electronic properties are computed with the adiabatic wavefunction(s). In other words, these properties are the matrix elements of a mono- or multi-electronic operator \hat{O} in the adiabatic basis. Thus, they must be suitably transformed into the diabatic one. Considering a two-state problem, the matrix representation of $\mathbf{O}^{(a)}$ in the adiabatic basis reads,

$$\mathbf{O}^{(a)} = \begin{pmatrix} O_{11}^{(a)} & O_{12}^{(a)} \\ O_{21}^{(a)} & O_{22}^{(a)} \end{pmatrix}. \quad (2.68)$$

As the electronic wavefunction depends parametrically on \mathbf{R} , the same stands for the matrix representation of the electronic operator. In this section, the electronic *wf* and the matrix elements depend on \mathbf{R} but it will not be mention explicitly. Each matrix element is expressed as,

$$O_{ij}^{(a)} = \langle \phi_e^{i(a)} | \hat{O} | \phi_e^{j(a)} \rangle \quad (2.69)$$

one can also express the diabatic electronic wavefunction as a linear combination of the adiabatic ones by applying the transformation \mathbf{U} , as

$$\begin{pmatrix} \phi_e^{1(d)} \\ \phi_e^{2(d)} \end{pmatrix} = \mathbf{U}^\dagger \begin{pmatrix} \phi_e^{1(a)} \\ \phi_e^{2(a)} \end{pmatrix} = \begin{pmatrix} U_{11}\phi_e^{1(a)} + U_{21}\phi_e^{2(a)} \\ U_{12}\phi_e^{1(a)} + U_{22}\phi_e^{2(a)} \end{pmatrix}. \quad (2.70)$$

The matrix element of $\mathbf{O}^{(d)}$ in the diabatic matrix can be expressed thanks to the matrix elements in the adiabatic basis,

$$O_{11}^{(d)} = \langle \phi_e^{1(d)} | \hat{O} | \phi_e^{1(d)} \rangle \quad (2.71)$$

$$= U_{11}^2 O_{11}^{(a)} + U_{21}^2 O_{22}^{(a)} + U_{11}U_{21}O_{12}^{(a)} + U_{11}U_{21}O_{21}^{(a)} \quad (2.72)$$

equivalently, if we use the matrix notation,

$$\mathbf{O}^{(d)} = \mathbf{U}^\dagger \mathbf{O}^{(a)} \mathbf{U}. \quad (2.73)$$

All the methodology that is needed to deal with a two-state problem with a symmetry-allowed conical intersection has been reviewed at this point. Nevertheless, in our study we investigate the interaction between singlet and triplet electronic states through the Spin-Orbit Coupling (SOC). In the perturbation theory and thanks to the Breit-Pauli operator, it is possible to compute the latter. The resulting potential matrix is not diagonal, and contains the SOC as off-diagonal elements. If we diagonalise this potential matrix, a new basis of electronic states is obtained, with functions that are mixed configuration of singlet and triplet states. In this basis, the physical character of the electronic states is lost and the dynamics of the intersystem conversion is difficult to understand. The choice here is to keep the non-mixed basis function, even if the potential is not diagonal, to simplify the interpretation of the physical process during the nuclear dynamics. To be accurate,

we have to take into account the SOC as a function of the nuclear geometry. Thus, all the SOC elements resulting from the ab-initio calculations must be transformed into the diabatic basis. It is reminiscent to the transformation discussed above, but now we have to deal with more than two electronic states. In the following, we discuss the diabatization of the SOC, in two different basic cases. First we can consider two singlet states coupled by a conical intersection and both interacting through the SOC with a third state, triplet of spin. The adiabatic potential matrix of the system reads,

$$\mathbf{E}^{(a)} = \begin{pmatrix} E_1^{(a)} & 0 & S^1/T \\ 0 & E_2^{(a)} & S^2/T \\ (S^1/T)^\dagger & (S^2/T)^\dagger & E_T^{(a)} \end{pmatrix}, \quad (2.74)$$

where $E_{1,2}^{(a)}$ stands for the adiabatic PES of the two singlet states and $E_T^{(a)}$ for the one of the triplet state T . We also introduced S^i/T the SOC between the singlet state i and T . Note that each element of Eq. (2.76) depends on the nuclear coordinates. Since there is a conical intersection between the singlet states, they can be diabatized using the unitary transformation \mathbf{U}_S , construct exclusively in the singlet subspace. This transformation leaves unchanged the triplet state, and its general expression reads,

$$\mathbf{U}_{tot} = \begin{pmatrix} \mathbf{U}_S & \mathbf{0} \\ \mathbf{0}^t & 1 \end{pmatrix}. \quad (2.75)$$

where \mathbf{U}_S is defined by Eq. (2.50), and $\mathbf{0}^\dagger = (0 \ 0)$. This transformation matrix is easy to understand, applied on the total adiabatic potential matrix, it diabatizes the singlet states thanks to \mathbf{U}_S and leaves unchanged the adiabatic triplet state. Applying the transformation matrix, \mathbf{U}_{tot} , on the full adiabatic potential matrix (i.e. with off-diagonal elements), leads to the diabatic potential matrix and transform the adiabatic SOC onto the diabatic one.

In the second case we consider two singlet states coupled with a conical intersection and two triplet states also coupled by a conical intersection. These four electronic states interact with each other through the SOC,

and the adiabatic potential matrix reads,

$$\mathbf{E}^{(a)} = \begin{pmatrix} E_1^{(a)} & 0 & S^1/T^1 & S^1/T^2 \\ 0 & E_2^{(a)} & S^2/T^1 & S^2/T^2 \\ (S^1/T^1)^\dagger & (S^2/T^1)^\dagger & E_{T_1}^{(a)} & 0 \\ (S^1/T^2)^\dagger & (S^2/T^2)^\dagger & 0 & E_{T_2}^{(a)} \end{pmatrix}, \quad (2.76)$$

where we introduced a new triplet state T_2 , with its adiabatic PES on the diagonal and its coupling with the two singlet states as off-diagonal terms. Proceeding in the same way than above, we can diabaticize separately the singlet and triplet states. From this diabaticization, we determine the transformation matrix to diabaticize the singlet states \mathbf{U}_S and the triplet states \mathbf{U}_T . Thus, the total transformation matrix, which acts on the total adiabatic basis, reads,

$$\mathbf{U}_{tot} = \begin{pmatrix} \mathbf{U}_S & \mathbf{0} \\ \mathbf{0} & \mathbf{U}_T \end{pmatrix}, \quad (2.77)$$

where $\mathbf{0}$ stands now for 4x4 null matrix. Again applying this transformation on the full adiabatic matrix, the diabatic potential is obtained, with the correct diabaticization of the SOC elements. These two cases can then be combined to study more complex situations, and will be detailed in Sec. 3.4.1 for the case of SO_2 .

2.3 Numerical Methods

2.3.1 Numerical formulation of the TDSE

To be numerically solved, the TDSE has to be formulated in a suitable set of equations. First we need a basis, equivalent to the primitive basis function discussed in the electronic problem (see Sec. 2.4). Two methods exist to formulate the wf and thus the Hamiltonian in a basis. One is known as the collocation method rewrites the wavefunction and the Hamiltonian on a set of discretized points along each coordinates. In a discrete basis, the derivative operators can be approximated using finite difference methods and the TDSE rewrites as a matrix problem. This approach is used, for instance, in the Crank-Nicholson scheme [83]. Due to the finite difference approximation of the spatial or temporal derivatives, the step between basis point must be small to avoid a too large numerical error. For a multidimensional systems such description becomes not efficient or often impossible. The second method is known as spectral method. It considers that

the nuclear wavefunction can be exactly expanded in any arbitrary basis of square-integrable functions:

$$\Psi(\mathbf{R}, t) = \sum_i a_i(t) \phi_i(\mathbf{R}). \quad (2.78)$$

In this basis the Hamiltonian can be expressed in a matricial form, with matrix elements,

$$\begin{aligned} H_{ij} &= \langle \phi_i | H | \phi_j \rangle \\ &= \langle \phi_i | T | \phi_j \rangle + \langle \phi_i | V | \phi_j \rangle \\ &= T_{ij} + V_{ij}. \end{aligned} \quad (2.79)$$

To be expressed numerically the set of functions $\{\phi_i\}$ must be truncated up to a finite number N . The use of this finite representation is referred in the literature [84] as the *Variational Basis Representation* or shortly noted "VBR". To discuss the effect of such a truncation on the TSDE, it is useful to introduce the projector, P_N onto the subspace of the N basis functions [80],

$$P_N = \sum_{j=1}^N |\phi_j\rangle\langle\phi_j|. \quad (2.80)$$

Using orthogonal basis functions, the projection of the exact (or total) wavefunction Ψ onto the subspace reads then,

$$\begin{aligned} P_N \Psi &= \sum_{j=1}^N \sum_i a_i |\phi_j\rangle\langle\phi_j|\phi_i\rangle \\ &= \sum_{j=1}^N a_j |\phi_j\rangle = \Psi_N \end{aligned} \quad (2.81)$$

$$(2.82)$$

The complementary part of Ψ_N , noted Ψ_{\perp} , to describe the total wavefunction, can be obtained by applying $(1 - P_N)$,

$$\Psi_{\perp} = (1 - P_N)\Psi = \sum_{i=N+1} a_i |\phi_i\rangle. \quad (2.83)$$

As the total wavefunction can be expressed as the direct sum of Ψ_N and its complementary,

$$\Psi = \Psi_N + \Psi_{\perp} \quad (2.84)$$

it is easy to show that Ψ_N is a variational representation of the exact wavefunction. In order to have an accurate description of Ψ in the subspace, the latter must ensure that Ψ_{\perp} is negligible. This can be done by smartly choosing the basis functions to ensure fast convergence of the truncation or consider a large subspace N . The basis functions are not subject to any constraint for the moment, and can be chosen to have an analytical expression for evaluating the kinetic energy matrix elements and the position operator. A simple choice of such basis functions is the consideration of the eigenfunction of the kinetic energy operator. The matrix elements then read,

$$X_{ij} = \langle \phi_i | x | \phi_j \rangle \quad (2.85)$$

$$T_{ij}^{(1)} = \langle \phi_i | \frac{\partial}{\partial x} | \phi_j \rangle \quad (2.86)$$

$$T_{ij}^{(2)} = \langle \phi_i | \frac{\partial^2}{\partial x^2} | \phi_j \rangle. \quad (2.87)$$

The problem of the spectral method is the evaluation of the potential matrix elements,

$$V_{ij} = \langle \phi_i | V | \phi_j \rangle, \quad (2.88)$$

as in general, these matrix elements do not have analytical form. Their evaluation have to be done numerically over the range of the nuclear coordinates, because the basis functions are delocalised. In the general case it is even worst because the potential is obtained from ab-initio calculations and are known only for a discrete number of nuclear geometries, which make the evaluation not accurate. But the potential operator can be expressed as a function of the nuclear coordinates and then its matrix can be expressed as a function of the position matrix,

$$\mathbf{V}^{FBR} = V(\mathbf{X}) \quad (2.89)$$

where the superscript stands for *Finite Basis Representation*. This expression is an *approximation* of potential matrix \mathbf{V}^{VBR} in the VBR. The potential evaluated at a discrete set of nuclear coordinates $\{x_k\}_{k=1}^n$ can be

expressed analytically as a polynomial function $L_n(x)$ by the Lagrange polynomial interpolation, such as,

$$\forall x_i \in \{x_k\}, L_n(x_i) = V(x_i), \quad (2.90)$$

which interpolates the potential V between two consecutive points x_k and x_{k+1} . From Lagrange interpolation theory, we know that L_n is a polynomial of degree $n - 1$ or smaller, and can be formally rewritten as,

$$L_n(x) = l_0 + l_1x + l_2x^2 + \dots + l_{n-1}x^{n-1} = \sum_{i=0}^{n-1} l_i x^i. \quad (2.91)$$

We do not care about the evaluation of the coefficient l_i , the knowledge of this analytical expression of V is enough, and can be used to compare the VBR and FBR potential,

$$V^{VBR} \equiv P_N V P_N = P_N \left(\sum_{i=0}^{n-1} l_i x^i \right) P_N \quad (2.92)$$

and

$$P_N V^{FBR} P_N = V(P_N X P_N) = \sum_{j=0}^{n-1} l_j (P_N x P_N)^j = \sum_{j=0}^{n-1} l_j (P_N x)_j P_N, \quad (2.93)$$

where we used the projector property, $P^2 = P$. Even if V^{FBR} and V^{VBR} look different, when the basis set is complete, the projector is then equal to the identity and both potentials are equal. Thus, the VBR and FBR representations are equivalent in a complete basis set but not in the case of the truncated one. Note that the FBR is not variational anymore. Due to the simplified expression of the potential in the FBR, this latter is used and to evaluate the potential, the position matrix can be diagonalised using the unitary transformation \mathbf{U} ,

$$\mathbf{X} = \mathbf{U} \mathbf{X}^{diag} \mathbf{U}^\dagger. \quad (2.94)$$

Noting $\{x_\alpha\}$ the set of eigenvalues of \mathbf{X}^{diag} , the potential matrix can be easily evaluated in this new basis and can be transformed back to the FBR, through

$$V_{jk}^{FBR} = \sum_{\alpha=1}^N U_{j\alpha} V(x_\alpha) U_{k\alpha}^* \quad (2.95)$$

This procedure has been introduced by Harris *et al.* [85] and they built the full Hamiltonian in the FBR. An important step has been done by Dickson and Certain [86], who showed that if the position operator is tridiagonal in the basis, which is the case for the classical orthogonal polynomials (Hermite, Legendre, etc.), then the FBR approximation turns to be a Gaussian quadrature approximation, with its well known quality. The *discrete variable representation* (DVR) has then be introduced on the idea that the unitary matrix U used to diagonalise the position operator can actually be used to define a new basis, the DVR, to express the TDSE. In this basis the position operator is diagonal per construction, and the potential matrix easily computed Eq. (2.95).

2.3.2 Numerical solution of the TDSE

We introduced previously the DVR basis to represent the wavefunction, and its description by a collection of coefficients on the DVR grid points. As the TDSE and the TISE do not have an analytical solution, it requires the use of numerical methods to solve them. It seems thus primordial to think about the system, for which we need to solve the TDSE and how it is expressed on a computer. One of the goals of theoretical chemistry is to study polyatomic molecules. The nuclear wavefunction used to describe the latter is a function of the coordinates of all the atoms which composed it, that we call in the following N_{at} . In our case we are interested at the molecular vibrations, and we can remove translational and rotational degree of freedom. The dimension of the wf remains to $N_{at} - 5$ or $N_{at} - 6$ vibrational degree of freedom, depending if the molecule is linear or not, respectively. Then to study molecule with a large number of atoms, the wavefunction has to be construct on a DVR grid, which is the product of the DVR used for each dof . The general form of the wf reads [84, 87],

$$\Psi(q_1, \dots, q_f, t) = \sum_{j_1=1}^{n_1} \sum_{j_2=1}^{n_2} \dots \sum_{j_f=1}^{n_f} C_{j_1, \dots, j_f}(t) \prod_{\alpha=1}^f \chi_{j_\alpha}^{(\alpha)}(q_\alpha) \quad (2.96)$$

where we introduce q_i as the coordinate of the dof i , n_i the number of DVR functions used to describe the i^{th} dof and f the total number of dof . The $\chi_{i\alpha}^\alpha$ are the DVR functions which are used as a basis to represent the wf and $C(t)$ the time dependent coefficient of the wf in this former. The total number n_{tot} of DVR functions use to describe the system is,

$$n_{tot} = \prod_{i=1}^f n_i. \quad (2.97)$$

To simplify, we consider that the same number DVR functions is used for each *dof*, i.e. $n_i = n \forall i$, and we get $n_{tot} = n^f$. The coefficients of the wavefunction are complex numbers and to be accurately described in the computation each of them is stored on 16 bytes. Moreover, to have an efficient calculation, the wavefunction must be stored in the RAM of the computer. Then the quantity of RAM needed is given by $16 \times n_{tot}$ bytes. As a simple example, we can estimate the RAM required considering 50 points for each *dof*, the results are reported in Tab. 2.1. [84]

It appears clearly that in this description of the wavefunction is not manageable for more than $\sim 5 - 6$

Table 2.1: Memory requirement for the storage of the wavefunction

f	1	2	3	4	5	6	7
Memory	100 octet	4.88 ko	244.14 ko	11.92 Mo	596.05 Mo	29.10 Go	1.42 To

dofs, which represents triatomic molecules on one electronic state. The memory requirement depends also of the number of electronic states included in the calculation, as well as the integration scheme of the TDSE, etc. In our case, for the triatomic molecule SO_2 this method can be applied and has been actually used, except for the study of the multiphoton ionisation (see Sec. 2.5.2 and 5.2), for which we use an extra *dof* to describe the ionised electron. But generally speaking it is not suitable to study systems of chemical interest. Hans-Dieter Meyer *et al.* [84], proposed an alternative *ansatz* for the wavefunction in the method called Multi-Configuration Time Dependent Hartree (MCTDH), which is able to deal with molecules including six atoms with 12 active *dofs*, and even larger. The "Hartree" in MCTDH comes from the description of the *wf* as an Hartree Product (HP),

$$\Psi^{HP}(q_1, \dots, q_f, t) = c(t) \prod_{\alpha=1}^f \phi_{\alpha}(q_{\alpha}, t) \quad (2.98)$$

This *ansatz* for the electronic problem is incorrect due to the Pauli principle for fermions (see Sec. 2.4.1) but is suitable for the nuclear *wf*. The ϕ_{α} are the single-particle functions (*spf*), and now depend of the time t . These latter are expressed in the primitive basis, the DVR basis, which is time independent,

$$\phi_{\alpha}(q_{\alpha}, t) = \sum_{j=1}^{n_{\alpha}} c_j(t) \chi_j^{(\alpha)}(q_{\alpha}). \quad (2.99)$$

In the same way that the Hartree-Fock (HF) approximation, the total wavefunction Ψ^{HP} describes the multidimensional *wf* as a product of uncorrelated function of each *dof*. In the same manner, the equation

of motions of MCTDH method can be derived thanks to a variational principle, and the Hamiltonian is composed of one part acting on one *spf* and a potential part, which describes the interaction between the different *dof* thanks to a mean field approximation. Then the HP *wf* will suffer the same problem as the HF *wf*, with a lack of correlation. But this ansatz strongly reduces the size of the wavefunction,

$$n_{tot}^{HP} = \sum_{i=1}^f n_i \quad (2.100)$$

and if we consider same $n_i = n$ for each *dof*, $n_{tot} = f \times n$. While the full expansion of the *wf* had an exponential scaling according the number of *dof*, the HP *wf* has a linear dependency on the former. The MCTDH method, which belongs to the class of MC-TDSCF methods, has exactly the same spirit that the MCSCF method (see Sec. 2.4.2). To bridge the HP *wf* and the full one, we consider a multiconfigurational *wf*, defined by a linear combination of HP to obtain the total *wf*,

$$\Psi^{MCTDH}(q_1, \dots, q_f, t) = \sum_{j_1=1}^{n_1^{spf}} \dots \sum_{j_f=1}^{n_f^{spf}} A_{j_1, \dots, j_f}(t) \prod_{\alpha=1}^f \phi_{j_\alpha}^{(\alpha)}(q_\alpha, t). \quad (2.101)$$

where $A_{j_1, \dots, j_f}(t)$ are the time dependent coefficients of the HP and n_i^{spf} is the number of *spf* used to describe the i^{th} *dof*. If the *spf* are not optimised, the MCTDH *wf* is equivalent to the *wf* of the configuration-interaction method in electronic calculation (see Sec. 2.4.2), but has the goal is also to optimise the *spf*, it is equivalent to the MCSCF method. One can notice that if all the n_i^{spf} are taken to one, then the MCTDH *wf* is equivalent to the HP *wf*, and monotonically converges to the "exact" *wf* when n_i^{spf} approaches n_i . Now looking at the memory requirement of Ψ^{MCTDH} , and to simplify, keeping equal the number of *spf* per *dof*, i.e. $n_1^{spf} = \dots = n_f^{spf} = n^{spf}$ and also an identical number of DVR points $n_1 = \dots = n_f = n$ and noting that the number of different A_{j_1, \dots, j_f} grows as $(n^{spf})^f$,

$$n_{tot}^{MCTDH} = n^{spf} \times n_{tot}^{HP} + (n^{spf})^f = n^{spf} \times f \times n + (n^{spf})^f. \quad (2.102)$$

To compare with the exact *wf*, we can estimate the memory requirement of the MCTDH *wf* considering 50 DVR functions and 7 *spfs* for each *dof*. It is clear, see Tab. 2.2, that MCTDH *wf* is adapted to deal with larger systems. This definition of the *wf* was also introduced to solve the TISE, but this method revealed to be quite poor in this case. This comes from the inherent nature of the mean field approximation, which

Table 2.2: Memory requirement for the storage of the MCTDH wavefunction

f	1	2	3	4	5	6	7
Memory	714 octet	1.46 ko	2.7 ko	7.4 ko	36 ko	233 ko	1.5 Mo

will be more efficient on localised wavefunction. It is the case for time-dependent calculation of wavepacket propagation but not for the eigenfunctions of the system which are largely delocalised.

Now the TDSE has to be solved, and to this end the equations of motion (*gom*) have to be established, i.e. transforming the formal TSDSE into a suitable set of equations that are possible to solve. The MCTDH package makes use of the time-dependent variational principle of Dirac-Frenkel [88, 89], expressed as,

$$\langle \delta\Psi | H - i\partial_t | \Psi \rangle = 0 \quad (2.103)$$

where ∂_t is the time derivative. Let's start with the *gom* for the exact expansion of the wavefunction Eq. (2.96) and look at its variation according to its coefficients C_{j_1, \dots, j_f} turns to be the partial derivative,

$$\begin{aligned} \delta\Psi &\equiv \frac{\partial\Psi}{\partial C_{j_1, \dots, j_f}} \\ &= \sum_{j_1=1}^{n_1} \cdots \sum_{j_f=1}^{n_f} \partial C_{j_1, \dots, j_f}(t) \prod_{\alpha=1}^f \chi_{j_\alpha}^{(\alpha)}(q_\alpha) \end{aligned} \quad (2.104)$$

because the primitive basis is fixed. We also can look at the derivative of Ψ with respect to time:

$$\partial_t \Psi = \sum_{j_1=1}^{n_1} \cdots \sum_{j_f=1}^{n_f} \dot{C}_{j_1, \dots, j_f}(t) \prod_{\alpha=1}^f \chi_{j_\alpha}^{(\alpha)}(q_\alpha). \quad (2.105)$$

Using Eqs. (2.104) and (2.105) the Dirac-Frenkel variational principle reads,

$$\begin{aligned} &\langle \delta\Psi | H - i\partial_t | \Psi \rangle = 0 \\ \Leftrightarrow &\left\langle \sum_{j_1=1}^{n_1} \cdots \sum_{j_f=1}^{n_f} \delta C_{j_1, \dots, j_f}(t) \prod_{\alpha=1}^f \chi_{j_\alpha}^{(\alpha)}(q_\alpha) \middle| H \right\rangle \sum_{j_1=1}^{n_1} \cdots \sum_{j_f=1}^{n_f} C_{j_1, \dots, j_f}(t) \prod_{\alpha=1}^f \chi_{j_\alpha}^{(\alpha)}(q_\alpha) \\ &= i \left\langle \sum_{j_1=1}^{n_1} \cdots \sum_{j_f=1}^{n_f} \delta C_{j_1, \dots, j_f}(t) \prod_{\alpha=1}^f \chi_{j_\alpha}^{(\alpha)}(q_\alpha) \middle| \sum_{j_1=1}^{n_1} \cdots \sum_{j_f=1}^{n_f} \dot{C}_{j_1, \dots, j_f}(t) \prod_{\alpha=1}^f \chi_{j_\alpha}^{(\alpha)}(q_\alpha) \right\rangle \end{aligned} \quad (2.106)$$

which is true for any arbitrary $\delta C_{j_1, \dots, j_f}$, and also for the particular case where $\delta C_{j_1, \dots, j_f} = 1 \forall j_i = 1$, and $\delta C_{j_1, \dots, j_f} = 0 \forall \{j_i\} \in \llbracket 2, f \rrbracket$, this simplifies Eq. (2.106) to:

$$\begin{aligned}
& \langle \prod_{\alpha=1}^f \chi_{j_\alpha}^{(\alpha)}(q_\alpha) | H | \sum_{j_1=1}^{n_1} \cdots \sum_{j_f=1}^{n_f} C_{j_1, \dots, j_f}(t) \prod_{\alpha=1}^f \chi_{j_\alpha}^{(\alpha)}(q_\alpha) \rangle \\
&= i \langle \prod_{\alpha=1}^f \chi_{j_\alpha}^{(\alpha)}(q_\alpha) | \sum_{j_1=1}^{n_1} \cdots \sum_{j_f=1}^{n_f} \dot{C}_{j_1, \dots, j_f}(t) \prod_{\alpha=1}^f \chi_{j_\alpha}^{(\alpha)}(q_\alpha) \rangle \\
\Leftrightarrow & i \dot{C}_{j_1=1, \dots, j_f=1}(t) = \sum_{j_1=1}^{n_1} \cdots \sum_{j_f=1}^{n_f} \langle \prod_{\alpha=1}^f \chi_{j_\alpha}^{(\alpha)}(q_\alpha) | H | \prod_{\alpha=1}^f \chi_{j_\alpha}^{(\alpha)}(q_\alpha) \rangle \quad (2.107)
\end{aligned}$$

where we have used the orthogonality of the DVR functions. Introducing the global index $J = \{j_1 \cdots j_f\}$ and the compact notation, $\chi_J = \prod_{\alpha=1}^f \chi_{j_\alpha}^{(\alpha)}(q_\alpha)$, Eq.(2.107) is simplified to

$$i \dot{C}_K = \sum_J \langle \chi_K | H | \chi_J \rangle C_J, \quad \forall K \quad (2.108)$$

which is a set of $\prod_{i=1}^f n_i$ coupled differential equations with initial condition which can be formally integrated as,

$$\mathbf{C}(t) = e^{-i\mathbf{H}t} \mathbf{C}(0). \quad (2.109)$$

The *eom* of the exact wavefunction are easily obtained, but are far too large to be solved for any systems. For this latter the MCTDH approximation becomes advantageous, or often mandatory. The *eom* for the MCTDH *wf* has been already subject to many pedagogic reviews and will not be expressed here, further information can be found in Refs. [84, 87].

In the case of wavepacket propagation methods, the knowledge of an initial state $\Psi(t=0)$ is required to solve the TDSE, as seen in Eq. (2.109). The initial state depends on the physical process considered. In our case we only deal with transition from the electronic ground state of the system to electronic excited states. Thus, the nuclear *wf* of the electronic ground state must be determined and to obtain it two different methods can be used. First, as it is an eigenfunction of the GS Hamiltonian, it can be obtained by diagonalizing it. This method is discussed in Sec. 2.3.3, but can only be applied for small systems and is time consuming. An second possibility is to perform a *relaxation*, which is a propagation of a guess function using a imaginary

time $t = -i\tau$ [90]. The guest function, $\psi(t)$, can be expressed as a linear combination of the eigenstates of the GS Hamiltonian $\{\phi_j\}$ of energy $\{E_j\}$, as

$$\psi(t) = \sum_j a_j e^{-iE_j t} \phi_j. \quad (2.110)$$

The introduction of an imaginary time in Eq. (2.110) transforms the imaginary exponent $(-iE_j t)$ to a real one $(-E_j \tau)$. Thus each eigenfunction is damped to zero with a rate proportional to its eigenvalue. Thus, the ground state, of lowest energy, relaxes slower than the other eigenstates and for a time τ long enough, it is the only one remaining.

2.3.3 Numerical integration of the equation of motion

The derivation of the *eoms* in the case of the exact and MCTDH wavefunction have been discussed in the previous section and they have now to be solved. Different methods can be employed in order to solve them as discussed and compared in Ref. [91]. In our case the Short Iterative Lanczos algorithm (SIL) and the Runge-Kutta at the eighth order (RK8) have been used. Both methods are already implemented in the MCTDH package. We choose to discuss only the SIL integration scheme and information concerning RK method can be found in Ref. [92]. We have to solve Eq. (2.109), assuming that we know the initial conditions, i.e. the wf at time $t = 0$. This equation is simple to be solved if we know how to apply the exponential of the Hamiltonian. It is the goal of the SIL method, which has been introduced in the field of quantum chemistry by Park and Light in 1986 [93]. This method belongs to the general class of polynomial approximations, for which the propagator is approximated by a polynomial expansion

$$e^{i\mathbf{H}t} \sim \sum_n a_n P_n(\mathbf{H}), \quad (2.111)$$

where P_n is a polynomial function. The SIL method is based on the iterative Lanczos reduction method [94], which uses the concept of the Krylov-subspace [95]. The latter is mathematically defined as an invariant subspace of a linear operator. Denoting the Krylov-subspace as K_m , its definition reads

$$HK_m = \{Hk \mid k \in K_m\} \subseteq K_m. \quad (2.112)$$

One typical example of such subspace is the space spanned by m eigenfunctions of H . But the problem here is that the eigenfunctions of H are unknown and tedious or not possible to compute. The strength of the method is the possibility to build an approximate Krylov-subspace by successively applying the Hamiltonian on one arbitrary vector Ψ_0 ,

$$K_m^{\Psi_0} = \{\Psi_0, H\Psi_0, H^2\Psi_0, \dots, H^{m-1}\Psi_0\}. \quad (2.113)$$

The Krylov-subspace constructed in this way depends on the vector Ψ_0 used. It is an approximation of an exact Krylov-subspace because the last vector $H^{m-1}\Psi_0$ is not contained in K_m , i.e. if the Hamiltonian acts on it

$$H(H^n\Psi_0) = H^{n+1}\Psi_0 \subseteq K_m, \quad \text{if } n \neq m-1 \quad (2.114)$$

$$H(H^{m-1}\Psi_0) = H^m\Psi_0 \notin K_m. \quad (2.115)$$

The vector basis obtained are not orthogonal but can be orthogonalised during the construction thanks to a Gram-Schmidt procedure. If we call q_i the resulting orthogonal vectors, the construction reads,

$$q_0 = \Psi_0 \quad (2.116)$$

$$Hq_0 = \alpha_0 q_0 + \beta_0 q_1 \quad (2.117)$$

because Hq_0 is not orthogonal to q_0 , it can be expressed as a linear combination of two orthogonal vector q_0 and q_1 . The coefficients are then obtained by projecting Hq_0 on both of them giving,

$$\alpha_0 = \langle q_0 | H | q_0 \rangle, \quad \beta_0 = \langle q_1 | H | q_0 \rangle. \quad (2.118)$$

The third vector is obtained by applying H on q_1 ,

$$Hq_1 = \beta_0 q_0 + \alpha_1 q_1 + \beta_1 q_2 \quad (2.119)$$

Again, the coefficients come from the projection of Hq_1 on the orthogonal vectors and read,

$$\alpha_1 = \langle q_1 | H | q_1 \rangle, \quad \beta_0 = \langle q_1 | H | q_0 \rangle, \quad \beta_1 = \langle q_1 | H | q_2 \rangle. \quad (2.120)$$

We could imagine to continue like this until the basis is built, but the evaluation of higher vectors imply projection of the kind,

$$\gamma_0 = \langle q_2 | H | q_0 \rangle, \langle q_2 | \alpha_0 q_0 + \beta_0 q_1 \rangle, = 0, \quad (2.121)$$

because of the orthogonality of the vectors q_i . Then the general construction is a three-term recurrence, expressed as,

$$Hq_j = \beta_{j-1}q_{j-1} + \alpha_jq_j + \beta_jq_{j+1}. \quad (2.122)$$

The α_i and β_i are the matrix elements of the Hamiltonian in the orthogonal Krylov-subspace. It is tridiagonal and reads,

$$H_m = \begin{pmatrix} \alpha_0 & \beta_0 & & & 0 \\ \beta_0 & \alpha_1 & \beta_1 & & \\ & \ddots & \ddots & \ddots & \\ 0 & & & \beta_{m-2} & \alpha_{m-1} \end{pmatrix},$$

and can be efficiently diagonalised numerically [92]. An important point of the method is that the Krylov-subspace is constructed for both the Hamiltonian and the initial vector, thus the polynomial expansion is different for different initial vector. If Ψ_0 is chosen to be the initial wavefunction, $\Psi_0 = \Psi(t=0)$, then the polynomial expansion tailors the Hamiltonian as well as the wavefunction and is a good approximation of the evolution in the near future of the system. It is then convenient to solve the TDSE in the Krylov-subspace thanks to the tridiagonal shape of the Hamiltonian. However the wf has also to be expressed in this basis as well and the TDSE in this basis is expressed as function of the coefficients in the Krylov-subspace \mathbf{d} , and satisfies

$$\mathbf{d}(t) = e^{-i\mathbf{H}_m t} \mathbf{d}(0). \quad (2.123)$$

The initial condition is $\mathbf{d}(0) = (1, 0, \dots, 0)^t$ because $q_1 = \Psi(t=0)$, and it always satisfies (even for $\Psi(t \neq 0)$) if the wavefunction at time t is used to construct the Krylov-subspace. Diagonalizing \mathbf{H}_m with the unitary matrix \mathbf{U}_m such as,

$$\mathbf{H}_m = \mathbf{U}_m^{-1} \mathbf{H}_m^{diag} \mathbf{U}_m \quad (2.124)$$

we obtain the diagonal form of the Hamiltonian, this can be used to easily evaluate the propagator and solve Eq.(2.123),

$$\mathbf{d}(t) = \mathbf{U}_m^{-1} e^{-i\mathbf{H}_m^{diag}t} \mathbf{U}_m \mathbf{d}(0). \quad (2.125)$$

We obtain the time evolution of the coefficients in the Krylov-subspace, which can be transformed back to the initial basis.

Concerning the accuracy of the method, errors are introduced at two different stages of the method. The first one, which is numerical, arises during the orthogonalisation of the Krylov vectors and the second is inherent to the construction scheme of the Krylov-subspace. While the first suggests that a small Krylov-subspace should be used to avoid an increasing error in the vectors, the second requires a large space to avoid that the coefficient of the last Krylov vector plays a role in the dynamic, because we neglect its interaction with the complementary space. Actually this two antagonist effects can be used to realise a robust integration scheme in the SIL. As we do not need to use the same Krylov-subspace to propagate the initial wf until time t , it is possible to slice the propagation in shorter time τ , for which the polynomial expansion is accurate, i.e. $|d_{m-1}(\tau)|^2 \leq \epsilon$, with ϵ the error tolerance wished. Then, a small Krylov-subspace ($m \sim 20$) is used and minimises errors in the orthogonalisation process. At the next time step the same scheme is applied but the construction of the Krylov-subspace is done with $\Psi(\tau)$.

We present now the formalism to obtain the solutions of the TISE, which helped us to attribute the different structures in the photo-absorption spectrum, or studied some aspects of the singlet-triplet interaction. We have used the Lanczos diagonalisation implemented in the MCTDH package, which computes the eigenvalues of an Hamiltonian, but as we were also interested in the eigenfunctions, we had to modify it. The idea behind the Lanczos diagonalisation is exactly the same as the one used in the SIL integrator. This method has been widely spread in numerical diagonalisation for two interesting characteristics: first to compute the eigenvalues almost no storage is required (only 2 vectors of the dimensionality of the system), second the extrema of the Hamiltonian spectrum converges first, which is an advantage as we want to study the lowest ones. Using the construction scheme of the Krylov-subspace, the new matrix shares with the Hamiltonian the same set of eigenvalues, in addition its tridiagonal expression allows to use efficient algo-

gorithms to diagonalise it. The number of Lanczos vectors is identical to the number of iterations used in the Lanczos algorithm, one vector being constructed at each iteration, and the length of each vector is the same than Ψ_0 used to construct the Krylov-subspace. Even if the Lanczos matrix is a square matrix with the dimension of the number of iterations N , usually the number of physical eigenvalues is smaller because the algorithm leads to spurious ones that can be discarded, see for instance [92]. Furthermore the eigenvectors of the Hamiltonian, required in our work, are not the same as the ones of the Lanczos matrix. It can be shown that the eigenfunctions of the Hamiltonian are linear combination of the Lanczos vectors with their respective coefficient being the eigenvectors of the Lanczos matrix. It is not possible for large systems as the one we consider to store the Lanczos vectors but manageable for the eigenvectors. Then we have used twice the Lanczos algorithm, first to generate the Lanczos eigenvectors, then to construct the eigenvectors of the Hamiltonian during the construction of the Lanczos vectors without storing them.

2.4 Eigenenergies and eigenfunctions for the electronic problem

2.4.1 Solving the electronic problem

We present here the methods used in this thesis to solve the electronic wave equation problems. Even though these methods are already well known, we wanted to briefly review them for the self-consistency of the manuscript. The electronic Hamiltonian reads [78],

$$\hat{H}_e = \sum_i^n \frac{-\nabla_i^2}{2} - \sum_i^n \sum_I^N \frac{Z_I}{|r_i - R_I|} + \sum_i^n \sum_{j>i}^n \frac{1}{|r_i - r_j|} \quad (2.126)$$

we are looking for the n -electron wavefunction $|\Psi_0\rangle$ such that:

$$\hat{H}_e |\Psi_0\rangle = E_0 |\Psi_0\rangle, \quad (2.127)$$

which is the lowest eigenfunction of the electronic Hamiltonian with the associated energy (eigenvalue) E_0 . The presence in \hat{H}_e of the $e^- - e^-$ interaction makes the problem not solvable analytically. Let's first discard

this term, and write an approximate form of the Hamiltonian:

$$\hat{H}_e^{app} = \sum_i^n \hat{h}(i) \quad (2.128)$$

where we define the one-electron operator $\hat{h}(i)$ by:

$$\hat{h}(i) = -\frac{\nabla_i^2}{2} - \sum_I^N \frac{Z_I}{|r_i - R_I|}. \quad (2.129)$$

$\hat{h}(i)$ describes the interaction of a single electron i in the field of the N nuclei. The wavefunction associated to this electron can be obtain from:

$$\hat{h}(i)\chi_a(i) = \epsilon_a\chi_a(i), \quad (2.130)$$

i.e. the time-independent one-electron Schrödinger equation. $\hat{h}(i)$ is an hermitian operator, then an infinite set of $\{\chi_a\}$ wavefunctions satisfy Eq. (2.130). We are interested to the approximate solution of the total approximate Hamiltonian:

$$\hat{H}_e^{app}|\Psi_0^{app}\rangle = E_0^{app}|\Psi_0^{app}\rangle. \quad (2.131)$$

Then from the separability of \hat{H}_e^{app} , it is possible to construct $|\Psi_0\rangle$ as a product of the one particle function $\{\chi_a\}$,

$$\Psi_0^{app}(r_1, r_2, \dots, r_n) = \chi_a(r_1)\cdot\chi_b(r_2)\cdot\cdots\chi_k(r_n), \quad (2.132)$$

with a total energy E_0^{app} ,

$$E_0^{app} = \sum_{l=a}^k \epsilon_l. \quad (2.133)$$

This approximation of the multi-electron wavefunction has been originally introduced by Hartree, and is known as an Hartree Product (HP). This wavefunction, due to its definition, represents n uncorrelated electrons in the field of fixed nuclei. Slater [96] has noted that this definition of the total *wf* does not satisfy the antisymmetry or Pauli principle, and proposed an alternative wavefunction to satisfy it, based on the

HP,

$$|\Psi_0^{SD}\rangle = |\chi_a \cdots \chi_k\rangle = \frac{1}{\sqrt{N!}} \begin{vmatrix} \chi_a(x_1) & \chi_b(x_1) & \cdots & \chi_k(x_1) \\ \cdot & \cdot & & \cdot \\ \cdot & \cdot & & \cdot \\ \cdot & \cdot & & \cdot \\ \chi_a(x_n) & \chi_b(x_n) & \cdots & \chi_k(x_n) \end{vmatrix}. \quad (2.134)$$

Here the superscript *SD* stands for Slater Determinant, which is the usual name of this wavefunction. The Hartree-Fock (HF) method, which is presented in the following, is an extension of the original Hartree method, with the used of SD as multi-electron wavefunction. Even if we do not know the solution the electronic problem, because \hat{H}_e is a Hermitian operator, we know that a set of eigenfunctions $\{\Psi_a\}$ and eigenvalues $\{E_a\}$ must satisfy the relation:

$$\hat{H}_e|\Psi_a\rangle = E_a|\Psi_a\rangle. \quad (2.135)$$

Then any function f of the electronic coordinates can be exactly written as a linear combination of the $\{\Psi_a\}$,

$$|f\rangle = \sum_a c_a |\Psi_a\rangle = \sum_a |\Psi_a\rangle \langle \Psi_a | f \rangle, \quad (2.136)$$

and its energy can be obtained as,

$$E_f = \langle f | \hat{H}_e | f \rangle \quad (2.137)$$

$$= \sum_a c_a c_a^* E_a \langle f | \Psi_a \rangle \langle \Psi_a | f \rangle. \quad (2.138)$$

The Rayleigh-Ritz variational principle [78] demonstrates that E_f is an upper bound of the lowest eigenvalue of \hat{H}_e , with equality only if $f = \Psi_0$. The combination of the SD function and the variational principle is the corner stone of the Hartree-Fock method, for which the goal is to optimise thanks to the variational principle

a SD to lower its energy in order to converge to Ψ_0 . The energy of a SD can be expressed as,

$$\begin{aligned}
E_{SD} &= \langle \Psi^{SD} | \hat{H}_e | \Psi^{SD} \rangle \\
&= \langle \Psi^{SD} | \sum_{i=1}^n \hat{h}(i) + \sum_{i=1}^n \sum_{j>i}^n r_{ij}^{-1} | \Psi^{SD} \rangle \\
&= \sum_{i=1}^n \langle \chi_i | \hat{h} | \chi_i \rangle \\
&\quad + \frac{1}{2} \sum_{i=1}^n \sum_{j=1}^n [\langle \chi_i \chi_j | r_{12}^{-1} | \chi_i \chi_j \rangle - \langle \chi_i \chi_j | r_{12}^{-1} | \chi_j \chi_i \rangle].
\end{aligned} \tag{2.139}$$

The above equation is derived using the Slater rules [78] to evaluate matrix elements with SD wavefunctions.

The two last terms arise from the $e^- - e^-$ interaction, the first one,

$$\langle \chi_i \chi_j | r_{12}^{-1} | \chi_i \chi_j \rangle = \int dx_1 dx_2 \chi_i^*(x_1) \chi_j^*(x_2) \frac{1}{r_{12}} \chi_i(x_1) \chi_j(x_2) \tag{2.140}$$

is the Coulomb repulsion between the two electrons, and can be used to define the Coulomb operator:

$$\hat{J}_j = \int dx_1 |\chi_j(x_1)|^2 r_{12}^{-1}. \tag{2.141}$$

The second term results from the fact that the electrons are indistinguishable and this term decreases the energy of the SD by exchanging the electron orbitals for electrons with the same spin. We can define the exchange operator \hat{K}_j thanks to its action on one spin orbital χ_i :

$$\hat{K}_j \chi_i(x_1) = \left[\int dx_2 \chi_j^*(x_2) r_{12}^{-1} \chi_i(x_2) \right] \chi_j(x_1). \tag{2.142}$$

It is then possible to rewrite the energy of the SD by making use of the Coulomb and exchange operators:

$$E_{SD} = \sum_{i=1}^n \langle \chi_i | \hat{h} | \chi_i \rangle + \sum_{j=1}^n \langle \chi_i | \hat{J}_j - \hat{K}_j | \chi_i \rangle \tag{2.143}$$

and define the Fock operator \hat{F} from the above expression as:

$$\hat{F}(i) = \hat{h}(i) + \sum_{j=1}^n (\hat{J}_j - \hat{K}_j). \tag{2.144}$$

The Fock operator is a mono-electronic operator, i.e. it acts on one electron orbital only. But the Coulomb and exchange operators are defined thanks to the remaining orbitals, it is self-consistent, which means that we need the knowledge of all the $\{\chi_j\}$ to defined it. Inherently to its definition, the $e^- - e^-$ repulsion is treated as a mean field, i.e. the electron i will experience the mean field of the remaining $n - 1$ electrons. To find the best SD in the variational sense, we can use the flexibility on the choice of the spin-orbitals, which composed the SD, with the constraint that they remain orthogonal,

$$\langle \chi_a | \chi_b \rangle = \delta_{ab}. \quad (2.145)$$

An elegant way to minimise the SD energy, with the above constraints, is to use once again the Lagrange multiplier method, which allows to minimise a functional under constraints. In this case the Langrangian reads:

$$\mathcal{L}(x_1 \cdots x_n, \lambda_{ij}) = E[\Psi^{SD}] - \sum_{i,j} \lambda_{ij} \langle \chi_i | \chi_j \rangle, \quad (2.146)$$

where the λ_{ij} are the Lagrange multipliers. The goal is to find the minimum of the energy $E_{SD} = E[\Psi^{SD}]$, which is a functional of the SD wavefuntion. Mathematically, the minimum is obtained when the variation of \mathcal{L} is null, i.e.

$$\delta \mathcal{L} = 0 \Leftrightarrow \delta \{E[\Psi^{SD}]\} + \delta \left\{ \sum_{i,j} \lambda_{ij} \langle \chi_i | \chi_j \rangle \right\}. \quad (2.147)$$

The differentiation of the energy functional can be write:

$$\begin{aligned} \delta E[\Psi^{SD}] &= \delta \left[\langle \Psi^{SD} | \hat{H}_e | \Psi^{SD} \rangle \right] \\ &= \sum_{i=1}^n \langle \delta \chi_i | \hat{F} | \chi_i \rangle + c.c. \end{aligned} \quad (2.148)$$

with *c.c.* standing for complex conjugate. The second term of Eq. (2.147), can be expressed as:

$$\delta \left\{ \sum_{i,j} \lambda_{ij} \langle \chi_i | \chi_j \rangle \right\} = \sum_{i,j} \lambda_{ij} (\langle \delta \chi_i | \chi_j \rangle + \langle \chi_i | \delta \chi_j \rangle) \quad (2.149)$$

$$= \sum_{i,j} \lambda_{ij} \langle \delta \chi_i | \chi_j \rangle + c.c. \quad (2.150)$$

Injecting the above relation into eq. (2.147) gives:

$$\sum_{i=1}^n \langle \delta\chi_i | \hat{F} | \chi_i \rangle - \sum_{i,j}^n \lambda_{ij} \langle \delta\chi_i | \chi_j \rangle + c.c. = \sum_{i=1}^n \langle \delta\chi_i | \left[\hat{F} | \chi_i \rangle - \sum_j^n \lambda_{ij} | \chi_j \rangle \right] + c.c. = 0. \quad (2.151)$$

The above equation must be fulfilled for any $\delta\chi_i$, which means that we obtain a system of n equations of a coupled eigenvalue problem for each spin-orbital

$$\hat{F} | \chi_i \rangle = \sum_j^n \lambda_{ij} | \chi_j \rangle, \quad (2.152)$$

known as the Hartree-Fock equations. It can be shown that the λ_{ij} are equal to the matrix elements $F_{ij} = \langle \chi_i | \hat{F} | \chi_j \rangle$ of the Fock operator and then is Hermitian, and can be diagonalised by the use of an unitary transformation. The new basis of orbital $\{\chi'_a\}$ in which the Fock operator is diagonal are known as the canonical orbitals and the Hartree-Fock equation expressed in this basis reads,

$$\hat{F} | \chi'_i \rangle = \lambda'_i | \chi'_i \rangle \quad (2.153)$$

and are now uncoupled. The HF theory defines the problem that we have to solve. Using an initial function, which can be arbitrary chosen, it is possible to approach the exact solution of the electronic Hamiltonian H_e , supposing that the initial function is defined up to a set of variable parameters. A general form of the parametrized initial wavefunction has been developed by Roothan and Hall in 1951 [97, 98] and established an efficient framework to numerically solve the HF equations, which remains nowadays the basis of most of the Quantum Chemistry calculations. Their idea is to rewrite the HF equations, which are a set of integro-differential equations with respect to the spatial coordinates of the electron, starting from an *a priori* known basis functions of the electronic coordinates, which are called primitive basis functions $\{\phi_i\}$. The spatial orbitals $\{\chi_a\}$ can be expanded exactly in the primitive basis, as far as the basis set is complete:

$$\chi_a(r) = \sum_i^{\infty} c_{ia} \phi_i(r). \quad (2.154)$$

Here c_{ia} are the coefficient of χ_a in the primitive basis, i.e. the projection of χ_a on the set of $\{\phi_i\}$. The infinite summation prohibit numerical treatment, but supposing that the primitive basis is chosen such as a

finite expansion describes correctly the orbitals, one obtains:

$$\chi_a(r) \approx \sum_i^{n_b} c_{ia} \phi_i(r), \quad (2.155)$$

where n_b stand for the finite number of primitive functions needed to get correct accuracy. This expression gives a set of parameters $\{c_{ia}\}$ which can be optimised thanks to the HF procedure. Concretely, the expansion of the orbitals is optimised for any given set of primitive functions which are known, we will discuss later about their choice. Using this definition the HF equations can be rewritten as:

$$F|\chi'_a\rangle = \lambda'_{aa}|\chi'_a\rangle \Leftrightarrow F \sum_i^{n_b} c_{ia} \phi_i(r) = \lambda'_{aa} \sum_i^{n_b} c_{ia} \phi_i(r) \quad (2.156)$$

multiplying on the left by ϕ_j^* and integrating over electronic coordinates,

$$\begin{aligned} \sum_i^{n_b} c_{ia} \int dr \phi_j^*(r) F \phi_i(r) &= \lambda'_{aa} \sum_i^{n_b} c_{ia} \int dr \phi_j^*(r) \phi_i(r) \\ \Leftrightarrow \sum_i^{n_b} c_{ia} F_{ji} &= \lambda'_{aa} \sum_i^{n_b} c_{ia} S_{ji} \end{aligned} \quad (2.157)$$

where the F_{ji} are the matrix element of the Fock operator between the primitive basis function j and i , and S_{ji} the overlap matrix,

$$S_{ji} = \int dr \phi_j^*(r) \phi_i(r). \quad (2.158)$$

The latter is different to δ_{ij} element because we did not impose orthogonality for the primitive functions. The Roothan-Hall formulation Eq. (2.154) and subsequent can be rewritten more compactly in the matrix notation:

$$\mathbf{FC} = \mathbf{SC}\boldsymbol{\lambda}. \quad (2.159)$$

The introduction of a known primitive basis, totally defines the equations and the HF procedure can be applied. Nevertheless the HF method suffers of the loss of correlation between the electrons, principally due to the use of a mean field for the Coulomb repulsion. This overestimates the electrostatic repulsion, because the probability of finding two electrons of different spin in the same elementary space volume is not null. An additional limitation is the use of one SD, which strongly restricts the configuration space that the

system may explore. An improvement on both issues can be obtained by considering a multi-determinant wavefunction, in the so-called post-HF methods that we propose to introduce below.

2.4.2 MCSCF and CI methods

Configuration Interaction method

The draw back of the HF method, concerning the correlation of the electron, has been partially corrected by the introduction of the configuration interaction (CI) method. The problem of HF method is the consideration of the mean-field operator to take into account the electron-electron repulsion. It overestimates this energy because the electron can be too close to each other. The idea of the CI method is to give more flexibility to the electronic wavefunction to remove this unphysical behaviour. From the HF solution, a set of molecular orbitals (same number as primitive basis function used) is obtained. This latter can be divided in a subset of occupied orbitals and one of virtual orbitals (with no electron). Let's label the occupied orbitals with Latin letters (a,b,...) and the virtual ones with Greek letters (α,β,\dots). Introducing the so-called second quantisation formalism,

$$\Psi_a^\alpha = \hat{a}_a \hat{a}_\alpha^\dagger \Psi_0 \quad (2.160)$$

we can describe electron excitation from the occupied orbitals to the virtual ones. In Eq. (2.160) we introduced \hat{a}_a , the annihilation operator, which removes one electron of the spin-orbital a , and \hat{a}_α^\dagger , the creation operator, which creates an electron in the spin-orbital α . These latter act on Ψ_0 , the HF wavefunction. To recover the correlation between the electrons, the full *wf* in the CI formalism, Ψ_0^{CI} , is constructed as a linear combination of all possible determinants,

$$\Psi_0^{CI} = c_0 \Psi_0 + \sum_{a\alpha} c_a^\alpha \Psi_a^\alpha + \sum_{\substack{a<b \\ \alpha<\beta}} c_{ab}^{\alpha\beta} \Psi_{ab}^{\alpha\beta} + \dots \quad (2.161)$$

The determinants are constructed thanks the occupied and virtual molecular orbitals resulting from an HF calculation. Using the variational principle and the definition of the CI wavefunction, a set of equations can be derived to optimise the different coefficients, without optimizing the molecular orbitals. The problem of this method results from the number of determinants that must be constructed to obtain the CI wavefunction, which depends of the size of the primitive basis used. Methods using truncated CI *wf*, for instance considering

only single and double excited determinants, are employed and give accurate results for the study of the electronic ground-state wavefunction for different systems. But concerning the excited states it turns out that the convergence is usually slow and the choice of the configurations that should be used is not trivial.

Multiconfigurational Self-consistent field Method

The problem of the convergence of the CI method, when only few excitations are considered, comes from the orbitals. As they are not optimised during the process, it turns out that a large number of configuration have to be included. The solution that has been proposed is to optimise, once again thanks to the variational principle, the expansion coefficients and the molecular orbitals to ensure convergence with a reduced expansion. The MCSCF wavefunction can be written as,

$$\Psi_{MCSCF} = \sum_I C_I \Phi_I \quad (2.162)$$

where Φ_I describes a configuration I and C_I is its associated coefficient. The first attempts were done with an optimisation in two steps, with first an optimisation of the coefficients, then an updating of the molecular orbitals, recursively [99]. In the new methods, the optimisation of both the CI coefficients and the molecular orbitals is done simultaneously to improve convergence [100, 101]. The idea is to apply a unitary transformation on the molecular orbitals to minimise the energy of the system. Indeed, If we consider that the CI wavefunction is the exact one, according to the choice of the primitive basis, to obtain the closest MCSCF wavefunction with less vector basis, the basis set is optimised.

The choice of the configuration that should be included in the MCSCF expansion is a key ingredient of the method. In our cases we use a so-called Complete Active Space (CAS), which is defined as a set of occupied and virtual orbitals, for which a full CI expansion is used [102]. Then to obtain the largest part of the correlation energy, after the MCSCF based on the CAS, a Multi-Reference Interaction Configuration (MRCI) considering single and double (SD) excitation is used. For this stage all the determinants are taken into account. The crucial point of this method is how to define the CAS, which is limited to few electrons and orbitals, this point will be detailed in Sec. 3.2.1.

The MCSCF method can be used to compute ground state wavefunction as well as excited states. In order to avoid convergence issues due to root flipping behaviour, it is useful to use state averaged MCSCF methods. In the case of avoiding crossing, two or more electronic states have close energies and during the SCF process the energy may converge to one or the other electronic state. To discard such problem, it is possible to compute more than one states using the same molecular orbital. Then the orbitals are not optimised individually for each solution but the set of orbitals is optimised to lower the energy of a set of electronic states. The average energy of the states is optimised as a weighted sum, where the coefficients are normalised.

Evaluation of the spin-orbit coupling

The spin property of the particle is intrinsically linked to the foundation of the quantum mechanics with its discovery by Stern and Gerlach [103, 104], in their famous experiment, demonstrating its existence. In the case of the above theory of the electronic calculation, the spin of the electron appears as an ad-hoc quantity, which has been introduced because we know that it exists. This intrinsic electronic angular momentum only appears naturally in the Dirac equation [105], which makes use of a full-relativistic description of the electron and has been interpreted as the angular momentum of the particle at rest. The Dirac equation shows also the possible coupling of the spin of the electron with its angular momentum. This effect is known as the spin-orbit coupling (SOC). The Dirac equation has been derived for one electron, and nowadays no many body fully-relativistic equation is established [106]. Then an approximate Hamiltonian is used in the case of a molecular (multi-electron) system. The one used in this work, and probably the most famous, is the so-called Breit-Pauli spin-orbit Hamiltonian, \hat{H}_{SO}^{BP} , which has been derived from the relativistic approximate many body Hamiltonian known as the Dirac-Coulomb-Breit Hamiltonian. One draw-back of this operator is its relativistic nature, and contains coupling terms involving the electronic continuum states and the positronic one (with negative energy continuum), and then the variational principle can not be used anymore. It is the principal reason why the SOC calculation are always limited to the first-order perturbation theory [78] and can applied to the electronic wavefunctions of different order of approximation, and in our case the MRCI level has been chosen. The detailed implementation of this operator in Molpro [107] (used for our work), which can be found in Ref. [108], while an interesting historical and technical discussion about the theory of the SOC can be found in the review of C. Marian [106]. We just stress that a large work is performed

nowadays to avoid the reduction of the relativistic operator, as the development of the Dirac package [109].

2.5 Spectroscopy as an important experimental probe

2.5.1 One photon absorption spectroscopy: Weak field regime

Spectroscopy is historically the experiment that reveals the quantum nature of atoms and molecules, and is still the best way of understanding and probing the quantum effects in systems. A very large expansion of spectroscopy methods appears over the last decades, which gives the possibility to probe systems on a large range of time scales with a high spatial resolution. It is crucial, to continue the progress of our understanding of the matter, to develop models and methods to simulate the experimental observables. In the following, we are discussing three different kinds of spectroscopy and how we manage to compute experimental observables.

The first kind of spectroscopy method that we have to introduce is photoabsorption, which historically was first accessible. To describe the one photoabsorption cross section $\sigma(E)$ in a molecular or atomic system with the time-independent Schrödinger equation the use of the time-dependent perturbation theory up to the first order leads to [110],

$$\sigma_{i \rightarrow f}(E) = \frac{4\pi^2\alpha}{3} E |\langle \psi_f | -\boldsymbol{\mu}_{fi} \cdot \boldsymbol{\epsilon} | \psi_i \rangle|^2 \delta(E - \Delta E_{fi}). \quad (2.163)$$

We introduced $\psi_{i,f}$ for the initial (i) and the final (f) state of the system and $\Delta E_{fi} = E_f - E_i$ is the energy difference between them. The electronic transition dipole matrix element is noted $\boldsymbol{\mu}_{fi}$ and $\boldsymbol{\epsilon}$ is the electric field strength. In addition α stands for the fine-structure constant. Starting from an initial state and being interested to all possible vibrational and electronic transitions, Eq. (2.163) has to be rewritten as a sum over all the transitions,

$$\sigma_{tot}(E) = \frac{4\pi^2\alpha}{3} E \sum_e \sum_\nu |\langle \psi_{\nu,e} | -\boldsymbol{\mu}_{\nu e} \cdot \boldsymbol{\epsilon} | \psi_i \rangle|^2 \delta(E - \Delta E_{\nu e}) \quad (2.164)$$

where the index e runs over all possible electronic states and ν over all vibrational ones. Using the time-independent formalism, the knowledge of the eigenstates of the system is required, but, as discussed before, this is not easily evaluated for molecules. Using the symmetry properties of the Dirac's function, its integral formulation and extending the modulus of the matrix element of the transition [111], Eq. (2.164) can be

expressed as,

$$\sigma_{tot}(E) = \frac{2\pi\alpha}{3} E \sum_e \sum_\nu \int_{-\infty}^{\infty} dt \langle \psi_i | -\boldsymbol{\mu}_{\nu_e i} \cdot \boldsymbol{\epsilon} | \psi_{\nu,e} \rangle \langle \psi_{\nu,e} | -\boldsymbol{\mu}_{\nu_e i} \cdot \boldsymbol{\epsilon} | \psi_i \rangle e^{i(E+E_i-E_{\nu_e})t}. \quad (2.165)$$

The above expression can be further simplified. First, noticing the presence of the completeness relation, and then the propagator on the final electronic states,

$$\sigma_{tot}(E) = \frac{2\pi\alpha}{3} E \int_{-\infty}^{\infty} dt \langle -\boldsymbol{\mu}_{\nu_e i} \cdot \boldsymbol{\epsilon} \psi_i | e^{-iH_e t} | -\boldsymbol{\mu}_{\nu_e i} \cdot \boldsymbol{\epsilon} \psi_i \rangle e^{i(E+E_i)t}. \quad (2.166)$$

Physically it means that the photoabsorption spectrum is related to the time-dependent propagation, under the influence of the Hamiltonian of the electronic *excited* states, of an initial wavefunction $|\psi_0\rangle = |-\boldsymbol{\mu}_{\nu_e i} \cdot \boldsymbol{\epsilon} \psi_i\rangle$. This latter is nothing else than the initial state of the system multiplied by the electronic transition dipole along the laser field polarisation axis. Introducing the autocorrelation function $c(t) = \langle \psi_0 | \psi_0(t) \rangle$ the relation is the Fourier transform from the temporal to the energetically domain of the autocorrelation function,

$$\sigma_{tot}(E) = \frac{2\pi\alpha}{3} E \int_{-\infty}^{+\infty} c(t) e^{i(E_i+E)t} dt. \quad (2.167)$$

This relation between the photoabsorption spectrum and the wavepacket (*wp*) propagation makes very attractive and popular the time dependent formalism, because it does not require the diagonalisation of the Hamiltonian to compute observables [84, 87]. This relation is often not used directly like this but restriction of the integral, used of gate function to avoid Gibbs oscillation and time symmetry are useful and implemented in MCTDH and are discussed for instance in the Ref. [87].

Since the seminal work of Zewail [112], experiments using short laser pulses can excite a coherent superposition of vibrational eigenstates of a molecule, providing a time evolution of the nuclear density. To study and model such a kind of experiments the above method cannot be used anymore and the laser field has to be explicitly taken into account. In the framework of the dipole approximation, which results from the consideration that the molecular characteristic length is negligible compare to the laser wavelength, the

interaction with the field can be described by the following interaction Hamiltonian,

$$H_I(t) = -\mathbf{E}(t) \cdot \boldsymbol{\mu}. \quad (2.168)$$

Here $\mathbf{E}(t)$ is the electric field and $\boldsymbol{\mu}$ the transition dipole moment operator. The solution of the TDSE with the explicit consideration of electric field can be done by discretizing the time variable in such way that for a time interval τ the time-dependent Hamiltonian is assumed to be constant, i.e.

$$H_I(t_i, t_f) \approx \sum_{n=0}^{(t_f-t_i)/\tau} H(t_i + n\tau). \quad (2.169)$$

This expression holds with the help of the linearity of the TDSE according to the time variable. The methods presented to numerically solve the problem can be used if τ is small according to the characteristic time evolution of $H_I(t)$, which in the present case is the frequency of the electric field.

2.5.2 Time resolved photoelectron spectra

We have been as well interested by the photoionisation of the molecule. The total photoelectron spectra can be obtained in a similar way than the photoabsorption one. But to study the ionisation of the molecule taking into account explicitly the laser field, another model has to be used. The following will present the key point of the method, valuable additional information may be found in Refs. [113, 114, 115]. The idea here is to describe a set of p neutral states, $|\psi_p^N\rangle$ which can be ionised toward a set of q ionic states $|\psi_q^I\rangle$, the full wavefunction of the system reads,

$$|\Psi_{tot}\rangle = \sum_p |\psi_p^N\rangle + \sum_q \int_0^\infty dE |\psi_q^I(E)\rangle \quad (2.170)$$

where the integration over the electron energy E takes explicitly into account the electronic continuum associated to each ionic state. These latter are considered as a free-electron continuums, i.e. the electron does not interact with the molecular ion after ionisation. The full Hamiltonian of the system can be written as,

$$\hat{H} = \begin{pmatrix} \hat{H}_p & \tilde{\hat{H}}_l(t) \\ \tilde{\hat{H}}_l(t) & \hat{H}_q \end{pmatrix}, \quad (2.171)$$

where $\hat{H}_{p,q}$ are the Hamiltonians describing the dynamics into the neutral and ionic manifolds, respectively. No assumption has been done concerning these Hamiltonians and can describe coupled dynamics into each manifolds. The Hamiltonian describing the interaction through the laser field is denoted $\tilde{\hat{H}}_l(t)$, where the time dependence arises from the explicit consideration of the laser pulse. The particularity arises from the elements labelled by "·", which means that they are infinite due to the presence of the electronic continuum. Each elements ij of $\tilde{\hat{H}}_q$, diagonal ($i = j$) or off-diagonal ($i \neq j$), reads

$$\tilde{H}_q^{ij} = V_{q_i q_j}(\mathbf{R}) + \int_0^\infty dE |\psi_q^I(E)\rangle E \langle \psi_q^I(E)|. \quad (2.172)$$

Where $V_{q_i q_i}$ denotes the electronic PES of the ionic state q_i and $V_{q_i q_j}$ a possible coupling between the ionic states q_i and q_j . The photoelectron spectrum is then obtained from the population of the different continuum states by integration over the nuclear coordinates when the laser pulse is over at time t_l ,

$$P(E) \propto \sum_q |\langle \Psi_{tot}(t_l) | \psi_q^I(E) \rangle|^2. \quad (2.173)$$

The transition matrix element for the ionisation is considered to be independent of the kinetic energy of the released electron as well as the photon energy of the exciting laser pulse. With these additional approximations, the description of the continuum can make use of the "quasi-continuum" description of Burkey and Cantrell [113, 114], which turns out thanks to the work of Seel and Domcke [115] to be adequately described by a DVR. Moreover, as shown in these studies, the range of the continuum can be truncated after a critical value due to the fact that the matrix element of the transition converges to zero when the energy tends to infinity. The integrals in the above equations are reduced to a sum over N point of a DVR, and following the implementation of G. Worth et al [116], the continuum energy is described as a coordinate of the full wavefunction,

$$\Psi_{tot}(\mathbf{R}, E, t) = \sum_p \psi_p^N(\mathbf{R}, E, t) + \sum_q \psi_q^I(\mathbf{R}, E, t) \quad (2.174)$$

which is suitably propagated by the MCTDH package.

2.5.3 High-order Harmonic Generation

The strong field approximation

From classical electro-dynamics, we know that the emitted field comes from the acceleration $a(t)$ of the electron. The power spectrum is given by the Fourier transform of $a(t)$:

$$a(\Omega) = \int e^{-i\Omega t} \langle \Psi(t) | a | \Psi(t) \rangle dt , \quad (2.175)$$

which, by integration by parts, leads to

$$a(\Omega) \propto \Omega^2 \int e^{-i\Omega t} D(t) dt \quad \text{with} \quad D(t) = \langle \Psi(t) | x | \Psi(t) \rangle \quad (2.176)$$

and $|\Psi(t)\rangle$ is the wavefunction of the electron at time t . Eq. (2.176), shows that the harmonic spectrum emitted by a system can be computed thanks to the dipole moment, $D(t)$. But the evaluation this latter requires the knowledge of the electronic time-dependent wavefunction. Solving the TDSE for a poly-electronic system, such as SO_2 , even in the clamped nuclei model, is far to be manageable. Recently, theoretical investigation have been carried out to describe such kind of systems, but their are still limited to few electrons [117, 118, 119]. In the following we consider the *single active electron* approximation and the interaction with a linearly x-polarised laser field, $\mathbf{E}(t) = E_0 \cos(\omega t) \cdot \mathbf{e}_x$, is described in the dipole approximation. In the length gauge, we can write the Schrödinger equation for one active electron, describes by $|\Psi(t)\rangle$, as:

$$i \frac{\partial}{\partial t} |\Psi(t)\rangle = \left[-\frac{1}{2} \nabla^2 + V(\mathbf{r}) - E_0 \cos(\omega t) x \right] |\Psi(t)\rangle \quad (2.177)$$

where the dipole approximation is used to take into account the interaction with the laser field and we introduced $V(\mathbf{r})$, the Coulomb interaction between the electron and the nucleus. It is possible to solve Eq.(2.177) numerically, but to simplify the problem we used the Strong Field Approximation (SFA)[73],

1. We consider only the contribution of the ground state $|0\rangle$ and continuum states $|\mathbf{v}\rangle$, the other bound states are neglected.
2. The depletion of the ground states is neglected.
3. After tunneling the electron is assumed free in the laser field (the potential $V(\mathbf{r})$ is neglected).

Thanks to these set of approximation it is possible to greatly simplify the TDSE. With the first assumption we can write the time dependent wavefunction as,

$$|\Psi(t)\rangle = e^{iI_p t} \left(b_0(t)|0\rangle + \int d^3\mathbf{v} b(\mathbf{v}, t)|\mathbf{v}\rangle \right) \quad (2.178)$$

with $b(\mathbf{v}, t)$ the amplitude of continuum state $|\mathbf{v}\rangle$ and $|0\rangle$ is the ground state of the system with an ionisation potential I_p and its amplitude $b_0(t)$. According to the second assumption, the ground state amplitude remains unity, i.e. $b_0(t) = 1$. This assumption holds if the ionisation of the system remains weak. The third assumption, which is the more drastic one, approximates the continuum states $|\mathbf{v}\rangle$ with plane waves. Using the ansatz of Eq.(2.178) in the TDSE (Eq. (2.177)), we obtain the Schrödinger equation for the continuum amplitudes $b(\mathbf{v}, t)$, which can be solved exactly [73],

$$b(\mathbf{v}, t) = i \int_0^t dt' E_0 \cos(\omega t') d_x[\mathbf{v} + \mathbf{A}(t) - \mathbf{A}(t')] \exp \left(-i \int_{t'}^t dt'' [(\mathbf{v} + \mathbf{A}(t) - \mathbf{A}(t''))/2 + I_p] \right) \quad (2.179)$$

where we introduce $d_x[\mathbf{v}] = \mathbf{d}[\mathbf{v}] \cdot \mathbf{e}_x = \langle \mathbf{v} | \mathbf{x} | 0 \rangle \cdot \mathbf{e}_x$, the atomic dipole matrix element for the bound-free transition and $\mathbf{A}(t)$ the vector potential of the electric field, $(\mathbf{E}(t) = -\frac{\partial \mathbf{A}(t)}{\partial t})$.

Proceeding with the $b(\mathbf{v}, t)$ coefficients, the dipole moment in Eq. (2.176) can be write:

$$D(t) = \int d^3\mathbf{v} d_x^*(\mathbf{v}) b(\mathbf{v}, t) + c.c. \quad (2.180)$$

and introducing the canonical momentum $\mathbf{p} = \mathbf{v} - \mathbf{A}(t)$, we get the final expression

$$D(t) = i \int_0^t dt' \int d^3\mathbf{p} E \cos(\omega t') d_x[\mathbf{p} + \mathbf{A}(t')] e^{-iS(\mathbf{p}, t, t')} d_x^*[\mathbf{p} + \mathbf{A}(t)] + c.c. \quad (2.181)$$

where

$$S(\mathbf{p}, t, t') = \int_{t'}^t dt'' \left(\frac{(\mathbf{p} + \mathbf{A}(t''))^2}{2} + I_p \right) \quad (2.182)$$

is the semi-classical action. Equation (2.181) has a nice physical interpretation, with from left to right, the product of probability amplitude of three distinct phenomena. The first term describes the probability amplitude for an electron to make the transition to the continuum at time t' with the canonical momentum \mathbf{p} . The second one describes the phase accumulation during the propagation in the continuum through out

the semi-classical action and the third corresponds to the probability amplitude to recombine with the parent ion.

Reinjecting the new expression of the dipole into the spectrum expression (2.176) we obtain

$$a(\Omega) \propto i\Omega^2 \int dt \int_0^t dt' \int d^3\mathbf{p} E \cos(\omega t') d_x[\mathbf{p} + \mathbf{A}(t')] e^{-i\tilde{S}(\mathbf{p}, t, t', \Omega)} d_x^*[\mathbf{p} + \mathbf{A}(t)] + c.c. \quad (2.183)$$

where $\tilde{S}(\mathbf{p}, t, t', \Omega)$ is defined as:

$$\tilde{S}(\mathbf{p}, t, t', \Omega) = S(\mathbf{p}, t, t') - \Omega t \quad (2.184)$$

This model has been widely used to describe HHG in atomic target and this even with the crude approximations that are used. It turns that this formulation leads to an useful interpretation of the results which can be more difficult in the case of the resolution of the time-dependent Schrödinger equation. The different integrals of Eq. (2.183), can be solved using the saddle-point approximation as we will discussed latter. This model has then been extended to the study of the molecular system by M. Lein [74], and successfully applied [120, 121, 122].

Molecular SFA

Using the total wavefunction of the system as a product of a vibrational nuclear function $\chi(\mathbf{R}, t)$ and an electronic wavefunction $\phi_{\mathbf{R}}(\mathbf{r}, t)$,

$$\Psi(\mathbf{r}, \mathbf{R}, t) = \chi(\mathbf{R}, t) \phi_{\mathbf{R}}(\mathbf{r}, t), \quad (2.185)$$

and considering the assumptions of Ref. [73], M. Lein [74] showed that the time dependent dipole moment along an axis \mathbf{n} can be expressed as,

$$D_{\mathbf{n}}(t) = -iN_v \int_0^t dt' \int \frac{d^3\mathbf{p}}{(2\pi)^3} \int_0^\infty d\mathbf{R} \chi_0^*(\mathbf{R}) \mathbf{n} \cdot \mathbf{d}_{rec}^*[\mathbf{p} + \mathbf{A}(t), \mathbf{R}] e^{-iS(t', t, \mathbf{p}, \mathbf{R})} U_R(t - t') d_{ion}[\mathbf{p} + \mathbf{A}(t'), \mathbf{R}, t'] \chi_0(\mathbf{R}) + c.c. \quad (2.186)$$

where N_v take into account the number of equivalent electron, and $U_R(t, t')$ is the evolution operator of the molecular ion for the time duration of the excursion of the electron in the continuum. In the following we consider a molecular system with n electrons in the framework of the SAE. The coordinates of the active electron will be denoted by \mathbf{r} and the coordinates of the $n - 1$ remaining inactive electrons are collected in

$\mathbf{r}' \equiv (\mathbf{r}_2, \mathbf{r}_3, \dots, \mathbf{r}_n)$. The ionisation and recombination dipole matrix elements can be expressed as [120],

$$d_{ion}[\mathbf{p}, \mathbf{R}, t] = \int \frac{d\mathbf{r}d\mathbf{r}'}{(2\pi)^{3/2}} [e^{i\mathbf{p}\cdot\mathbf{r}}\phi_{\mathbf{R}}^+(\mathbf{r}')]^* \mathbf{E}(t) \cdot \mathbf{r} \phi_{\mathbf{R}}(\mathbf{r}, \mathbf{r}'), \quad (2.187)$$

$$\mathbf{d}_{rec}[\mathbf{p}, \mathbf{R}] = \int \frac{d\mathbf{r}d\mathbf{r}'}{(2\pi)^{3/2}} [e^{i\mathbf{p}\cdot\mathbf{r}}\phi_{\mathbf{R}}^+(\mathbf{r}')]^* \mathbf{r} \phi_{\mathbf{R}}(\mathbf{r}, \mathbf{r}'). \quad (2.188)$$

where we introduced the neutral $\phi_{\mathbf{R}}(\mathbf{r}, \mathbf{r}')$ and the ionic $\phi_{\mathbf{R}}^+(\mathbf{r})$ electronic wavefunctions, which parametrically depends of the nuclear coordinates \mathbf{R} . To simplify the expression of the time-dependent dipole according to the integration over the nuclear coordinates it is assumed that the ionisation launches a vibrational *wp* $\chi(\mathbf{R})$ which is uncorrelated with the initial momentum \mathbf{p} of the ionised electron,

$$d_{ion}[\mathbf{p}, \mathbf{R}]_{\chi_0(\mathbf{R})} \approx \bar{d}_{ion}[\mathbf{p}]\chi(\mathbf{R}). \quad (2.189)$$

This approximation removes actually the nuclear dependence of the time-dependent dipole expression and gives the possibility to factorise the nuclear wavefunction,

$$D_{\mathbf{n}}(t) = -iN_v \int_0^t dt' C(t-t') \int \frac{d^3\mathbf{p}}{(2\pi)^3} \mathbf{n} \cdot \mathbf{d}_{rec}^*[\mathbf{p} + \mathbf{A}(t)] e^{-iS(t',t,\mathbf{p})} d_{ion}[\mathbf{p} + \mathbf{A}(t'), t'] + c.c. \quad (2.190)$$

where the autocorrelation function $C(t)$ is introduced and describes then the projection of the propagated ionic *wp* onto the initial one [123]. The autocorrelation function plays the role of a damping function as function of the excursion time of the electron in the continuum. Indeed with an initial normalised *wp* $\chi_0(\mathbf{R})$, if no dynamics occurs in the ionic states then $C(t)$ remains unity, and if dynamics occurs, the autocorrelation function will decay toward its minimum value 0. It is interesting to compare this approximation to the method used in our work to compute the photoelectron spectra, for which we project the vibrational ground state wavefunction onto the different electronic ionic states. The photoelectron spectrum was then computed by using the Fourier transform of the autocorrelation function, which turns to be exactly the same autocorrelation function introduced in Lein's model. The coefficient of the different eigenstates of the ionic *wp* are simply the Franck-Condon (FC) factors. Theoretical and experimental works gave evidence that in the strong field regime the vibrational distribution of the ionic molecule after the ionisation is strongly different to the FC distribution, which point out the strongest weakness of the model. To go further different works took into account the correlation between the ionic *wp* and the electron momentum of the ionised electron

but so far only 1D model have been used.

Another problem appears, this time concerning the suppression of the \mathbf{R} dependence of the transition-dipole matrix element, which obviously should depend of the nuclear coordinates. Actually it has been demonstrated that interferences, related to "double slit" interferences, appear in HHG spectra, and results from the transition-dipole. Such interference are only possible, for a diatomic system, if the projection of internuclear axis onto the polarisation axis of the laser does not cancel, and leads to a high oscillatory behaviour of the transition dipole. Then for a general molecular system such interferences are not present if the polarisation axis and the molecular plan are orthogonal.

As in the atomic case the power spectrum of harmonic emission is obtained by the Fourier transform of the dipole acceleration and reads,

$$a(\Omega) = -iN_v\Omega^2 \int dt \int_0^t dt' C(t-t') \int \frac{d^3\mathbf{p}}{(2\pi)^3} \mathbf{n} \cdot \mathbf{d}_{rec}^*[\mathbf{p} + \mathbf{A}(t)] e^{-i\tilde{S}(t',t,\mathbf{p},\Omega)} d_{ion}[\mathbf{p} + \mathbf{A}(t'), t'] + c.c. \quad (2.191)$$

where the modified semi-classical action \tilde{S} has the same expression than previously.

Saddle-point approximation

In the framework of the SFA approximation the time-dependent dipole can be obtained by solving the numerous integral over the momentum, times, and for molecules \mathbf{R} . While the integral in the definition of the semi-classical action is often analytical, the others need to be evaluated numerically. However according to the expression of \tilde{S} , in Eq. (2.184), its exponential give a highly oscillatory term in the integrand and the numerical integration has to be done with precaution. Actually as pointed out directly by M. Lewenstein [73], the fast oscillations of the integrand as function of \mathbf{p} can be advantageously used to perform the integration with the saddle point approximation (*sdp*). For the molecular case the stationary condition of \tilde{S} according to \mathbf{p} reads,

$$\begin{aligned} \nabla_{\mathbf{p}} \tilde{S}(\mathbf{p}, t, t', \Omega) &= \int_{t'}^t (\mathbf{p} + \mathbf{A}(\tau)) d\tau = 0 \\ \Rightarrow \mathbf{p}_{st}(t, t') &= -\frac{\int_{t'}^t dt'' \mathbf{A}(t'')}{(t-t')} \end{aligned} \quad (2.192)$$

and the power spectrum after the *sdp* integration turns to,

$$a(\Omega) = -iN_v\Omega^2 \int dt \int_0^t \frac{dt'}{(i(t-t') + \epsilon)^{3/2}} C(t-t') \mathbf{n} \cdot \mathbf{d}_{rec}^*[\mathbf{p}_{st} + \mathbf{A}(t)] e^{-i\tilde{S}(t',t,\mathbf{p}_{st},\Omega)} d_{ion}[\mathbf{p}_{st} + \mathbf{A}(t'), t'] + c.c. \quad (2.193)$$

where ϵ is a regularisation parameter to avoid singularities and for convenience we drop the temporal dependence of \mathbf{p}_{st} . This approximation holds if the other quantities of the integrand are smooth functions of \mathbf{p} , which is not the case when the molecular plane and the field polarisation are not orthogonal. In our work we will only discuss the case of the orthogonality relation holds to simplify the resolution of the equation and also because experimental results are available for this case. The use of the *sdp* approximation as then be extended by [124] on the integration over temporal integrals to lead to the so-called quantum orbit model. The stationary conditions according to t' and t reads,

$$\frac{\partial}{\partial t'} \tilde{S}(\mathbf{p}, t, t', \Omega) = \frac{(\mathbf{p} + \mathbf{A}(t'_{st}))^2}{2} + I_p = 0 \quad (2.194)$$

$$\frac{\partial}{\partial t} \tilde{S}(\mathbf{p}, t, t', \Omega) = \frac{(\mathbf{p} + \mathbf{A}(t_{st}))^2}{2} - \Omega + I_p = 0 \Leftrightarrow \Omega = \frac{(\mathbf{p} + \mathbf{A}(t_{st}))^2}{2} + I_p \quad (2.195)$$

The *sdp* equations show the three different steps of the semi-classical model. Equation (2.194), concerns the ionisation step, and indicates that the sum of the kinetic energy of the electron and the ionisation potential must be null. The only possibility to fulfil this condition is to use imaginary time, and assigns it to a trace of the (classically forbidden) tunnel process. Eq. (2.192) deals with the propagation of the electron in the continuum, expressed as:

$$\int_{t'}^t \mathbf{p}(\tau) d\tau = \int_{t'}^t \dot{\mathbf{x}}(\tau) d\tau = \mathbf{x}(t) - \mathbf{x}(t') = 0 \quad (2.196)$$

This means that the electron's dominant path is closed and starts from the nucleus and comes back to it. Finally, Eq. (2.195) is related to the recombination of the electron on to the nucleus. From this equation, which is the energy conservation law, energy of the emitted photon is the sum of the electron's kinetic energy and the ionisation potential. Finally, the expression for the HHG spectrum reads,

$$a(\Omega) \propto -iN_v\Omega^2 \sum_u \left(\left(i \frac{(t_{st} - t'_{st})}{2} \right)^3 \det(\tilde{S}'') \right)^{-\frac{1}{2}} C(t_{st} - t'_{st}) \mathbf{n} \cdot \mathbf{d}_{rec}^*[\mathbf{p}_{st} + \mathbf{A}(t_{st})] \times e^{-i\tilde{S}(t'_{st}, t_{st}, \mathbf{p}_{st}, \Omega)} d_{ion}[\mathbf{p}_{st} + \mathbf{A}(t'_{st}), t'_{st}] + c.c. \quad (2.197)$$

where the summation over u runs over all the stationary solutions. The interpretation of the set of approximations is that only the main electronic path is taken into consideration. Then the only computation needs to determine the stationary times and momentum, then the resolution is fully analytical. Even if the quantum orbit model has weakness, and many of them, it is a useful tool to understand physical mechanism of the HHG, and is still widely studied and used.

Dynamics in neutral states and conical intersection

The influence of the nuclear dynamics, in the HHG spectra, has been exclusively studied theoretically for the dynamics occurring in the molecular cation [13, 74, 120, 121]. The dynamics in the ionic states influence the HHG and it gives the possibility to probe nuclear dynamics with attosecond resolution. These interesting properties have been experimentally extended to nuclear dynamics into the neutral state, but no theoretical consideration is available to describe such process. However it raises considerable interest especially to understand non-adiabatic dynamics [18].

The model described above is not suitable especially because of the approximations that have been used to describe the nuclear dependencies of the different electronic quantities. If we want to follow a dynamics in the neutral states thanks to HHG, then quantities such as the ionisation potential or the transition dipole matrix elements are expected to change. Their evolution during the wp motion will impact the harmonic generation and will be detected in the experiments. It seems clear that to describe these evolutions the nuclear dependencies of the different electronic quantities must be explicitly considered. Another possibility, which have been used, is the calculation at different key geometries of the different electronic quantities, to point out the likely mechanisms. But these methods can leads to substantial difference with the inclusion of the quantum nature of the nuclei [125]. Moreover this description is clearly not suitable in the case of multidimensional wp , with a much more delocalised wp evolution.

To describe such kind of experimental steep for a molecule, we try to keep the SFA approximation and the saddle-point method to ensure fast calculations. In addition it provides a simple pictures for the HHG process. We extend the above model to apply it when wp dynamics in the neutral states is considered. If we want to correctly describe a time-evolution of a nuclear wp and the impact in HHG spectroscopy,

we first need to look at the different time-scales involved in the process. On the time scale of the nuclear dynamics the electrons instantaneously adjusted their motion to the nuclei one. This reasoning gives rise to the well-known concept of PES. The characteristic time evolution of a nuclear wavefunction is hundreds of femtosecond for the vibrational periods, but in the case of a conical intersection the electronic structure of the molecule can change on a femtosecond time scale. The goal of this work is to probe the correlated nuclear/electronic dynamics induced by the nuclear dynamics and once again the concept of PES is well adapted. To go beyond these approximations, the TDSE for the nuclei and the electron should be solved, which is impossible. Keeping a femtosecond time scale for the coupled dynamics, it is fruitful to compare it with the time scale of the HHG process in the SFA approximation [73] within the three steps model [126]. The first step is the *tunnel* ionisation, which occurs *only* at the maximum of the IR-laser field, and its characteristic time is 0.05 laser period if we consider either the long or short trajectory or 0.1 for both of them. In the case of a Ti-saphir laser at 800 nm, this time corresponds to ~ 0.13 fs for the first case and ~ 0.26 fs for the second. On this time scale the nuclei, especially for heavy element such as oxygen and sulfur atoms, the time dependent nuclear *wp* can be assumed fixed, i.e.

$$\chi(\mathbf{R}, t) \approx \chi(\mathbf{R}). \quad (2.198)$$

In order to obtain the nuclear wavefunction at the interesting time t , just before the amplitude maxima of the probe laser pulse, the time-dependent Schrödinger equation is solved, neglecting the interaction between the molecule and the laser field. This scheme gives the possibility to achieve the first step of the three-step model. The second step is the excursion of the electron in the continuum and the propagation of the nuclear wavepacket on the ionic potential energy surfaces, assuming as previously no correlation between the released electron and the remaining ionic *wp*,

$$a(\Omega) \propto -iN_v\Omega^2 \int_0^\infty d\mathbf{R} \sum_u \left(\left(i \frac{(t_{st}(\mathbf{R}) - t'_{st}(\mathbf{R}))}{2} \right)^3 \det(\tilde{S}''_{\mathbf{R}}) \right)^{-\frac{1}{2}} \chi(\mathbf{R}) U_R(t_{st}(\mathbf{R}) - t'_{st}(\mathbf{R})) \chi(\mathbf{R}) \quad (2.199)$$

$$\mathbf{n} \cdot \mathbf{d}_{rec}^*[\mathbf{k}_{st}(\mathbf{R}) + \mathbf{A}(t_{st}(\mathbf{R})), \mathbf{R}] e^{-i\tilde{S}_{\mathbf{R}}} d_{ion}[\mathbf{k}_{st}(\mathbf{R}) + \mathbf{A}(t'_{st}(\mathbf{R})), t'_{st}(\mathbf{R}), \mathbf{R}] + c.c.$$

where we drop the variable of $\tilde{S}_{\mathbf{R}}$ for visibility. If the nuclear dynamics in the ionic states is neglected, the nuclear term, $\chi(\mathbf{R}) U_R(t_{st}(\mathbf{R}) - t'_{st}(\mathbf{R})) \chi(\mathbf{R})$, can be approximated by $|\chi(\mathbf{R})|^2$ and becomes a factor of the

summation over the *sdp* solutions. Thus it describes the averaging of the HHG over the nuclear coordinates. Basically the model is natural and simple it just reestablished the coordinate dependence of the electronic properties, which were neglected so far. Because of the assumption that no dynamics occurs in the molecular ion, the autocorrelation function is transformed to the density probability. Then the model can be view as the SFA calculation which is computed for each molecular geometry and weighted according to the probability density of the nuclear wavefunction. In the case of a *wp* dynamics in a set of coupled electronic states, the vibrational wavefunction is expanded on each of the electronic state (see Eq. (2.10) of Sec. 2.2.1). For the time of ionisation, using the approximation of Eq. (2.198), the full wavefunction reads,

$$\Psi(\mathbf{R}, \mathbf{r}) = \sum_j \chi_j(\mathbf{R}) \phi_j(\mathbf{r}; \mathbf{R}). \quad (2.200)$$

In addition, as the electronic wavefunctions $\phi_j(\mathbf{r}; \mathbf{R})$ are solution of the time-independent electronic Schrödinger equation, we have

$$|\Psi(\mathbf{R})|^2 = \sum_j \langle \chi_j(\mathbf{R}) \phi_j | \sum_i \chi_i(\mathbf{R}) \phi_i \rangle = \sum_j |\chi_j(\mathbf{R})|^2 \quad (2.201)$$

Eq. (2.199) can be rewritten in this case as,

$$a(\Omega) \propto -iN_v \Omega^2 \sum_j \int_0^\infty d\mathbf{R} |\chi_j(\mathbf{R})|^2 \sum_u \left(\left(i \frac{(t_{st}(\mathbf{R}) - t'_{st}(\mathbf{R}))}{2} \right)^3 \det(\tilde{S}''_{\mathbf{R}}) \right)^{-\frac{1}{2}} \quad (2.202)$$

$$\mathbf{n} \cdot \mathbf{d}_{rec}^*[\mathbf{p}_{st}(\mathbf{R}) + \mathbf{A}(t_{st}(\mathbf{R})), \mathbf{R}] e^{-i\tilde{S}_{\mathbf{R}}} d_{ion}[\mathbf{p}_{st}(\mathbf{R}) + \mathbf{A}(t'_{st}(\mathbf{R})), t'_{st}(\mathbf{R}), \mathbf{R}] + c.c.$$

We include an initial wavefunction, which is expanded on different electronic states, then the transition-dipole matrix elements are also to be reconsidered, because the final ionic states can change depending on the neutral excited state. Let's first assume that only the highest occupied molecular orbital (HOMO) can be ionised, and this for each neutral electronic states. Then the transition dipole matrix element for the neutral state j reads,

$$d_{ion}^{jl}[\mathbf{p}, \mathbf{R}, t] = \int \frac{d\mathbf{r}d\mathbf{r}'}{(2\pi)^{3/2}} [e^{i\mathbf{p}\cdot\mathbf{r}} \psi_{\mathbf{R}}^l(\mathbf{r}')]^* \mathbf{E}(t) \cdot \mathbf{r} \phi_{\mathbf{R}}^j(\mathbf{r}, \mathbf{r}'), \quad (2.203)$$

$$\mathbf{d}_{rec}^{jl}[\mathbf{p}, \mathbf{R}] = \int \frac{d\mathbf{r}d\mathbf{r}'}{(2\pi)^{3/2}} [e^{i\mathbf{p}\cdot\mathbf{r}} \psi_{\mathbf{R}}^l(\mathbf{r}')]^* \mathbf{r} \phi_{\mathbf{R}}^j(\mathbf{r}, \mathbf{r}'). \quad (2.204)$$

where $\psi_{\mathbf{R}}^l(\mathbf{r}')$ is the electronic *wf* of the final ionic state l . Including all the relevant states of the molecule

but neglecting the propagation in the ionic states, the emitted harmonic spectrum reads,

$$a(\Omega) \propto -iN_v\Omega^2 \sum_j \sum_t \int_0^\infty d\mathbf{R} |\chi_j(\mathbf{R})|^2 \sum_u \left(\left(i \frac{(t_{st} - t'_{st})}{2} \right)^3 \det(\tilde{S}''_{\mathbf{R}}) \right)^{-\frac{1}{2}} \quad (2.205)$$

$$\mathbf{n} \cdot \mathbf{d}_{rec}^{jl*}[\mathbf{p}_{st} + \mathbf{A}(t_{st}), \mathbf{R}] e^{-i\tilde{S}_{\mathbf{R}}} d_{ion}^{jl}[\mathbf{p}_{st} + \mathbf{A}(t'_{st}), t'_{st} \mathbf{R}] + c.c.$$

where we dropped the \mathbf{R} dependence of the sdp solutions. The first step in the HHG is the tunnel ionisation of the active electron, which in the SFA exhibits an exponential decay as a function of the ionisation potential and then the summation over the ionic states can be limited to the lower one.

Transition dipole matrix element

The method described above requires the evaluation of the different transition dipole matrix elements as a function of the nuclear geometry. First, to simplify the reasoning we use the relation between the ionisation and recombination dipole,

$$d_{ion}^{jl}[\mathbf{p}, \mathbf{R}, t] = \mathbf{E}(t) \cdot \mathbf{d}_{rec}^{jl}[\mathbf{p}, \mathbf{R}], \quad (2.206)$$

i.e. the ionisation dipole is just the projection of the recombination dipole onto the polarisation axis of the laser field. The recombination matrix element can be reexpressed as,

$$\mathbf{d}_{rec}^{jl}[\mathbf{p}, \mathbf{R}] = \int \frac{d\mathbf{r}d\mathbf{r}'}{(2\pi)^{3/2}} [e^{i\mathbf{p}\cdot\mathbf{r}} \psi_{\mathbf{R}}^l(\mathbf{r}')]^* \mathbf{r} \phi_{\mathbf{R}}^j(\mathbf{r}, \mathbf{r}') = \frac{1}{\sqrt{n}} \int \frac{dr}{(2\pi)^{3/2}} e^{-i\mathbf{p}\cdot\mathbf{r}} \psi_{\mathbf{R}}^{Dyson}(\mathbf{r}). \quad (2.207)$$

where n is the number of electrons in neutral state and the Dyson orbital $\psi_{\mathbf{R}}^{Dyson}(\mathbf{r})$, a single electron function, which describes the orbital which was occupied by the ionised electron. This orbital takes into account the relaxation of the electronic wavefunction after the ionisation, as well as the electron correlation, and is defined by [127],

$$\psi_{\mathbf{R}}^{Dyson}(\mathbf{r}) = \sqrt{n} \langle \psi_{\mathbf{R}}^l | \phi_{\mathbf{R}}^j(\mathbf{r}) \rangle_{\mathbf{r}'}. \quad (2.208)$$

Then the recombination dipole can be expressed as the partial derivative over the electron momentum of the Fourier transform of the overlap between the ionic and the neutral electronic functions. Note that the ionised

electron is described by a plane wave and we can rewrite Eq. (2.207) as

$$\mathbf{d}_{rec}^{jl}[\mathbf{p}, \mathbf{R}] = i \frac{\partial}{\partial \mathbf{p}} \int \frac{d\mathbf{r}}{(2\pi)^{3/2}} e^{-i\mathbf{p}\cdot\mathbf{r}} \psi_{\mathbf{R}}^{Dyson}(\mathbf{r}). \quad (2.209)$$

The Dyson orbital can be expressed in the basis of the molecular orbitals of the neutral wavefunction, using the cofactor expansion of the Slater determinant of the neutral wavefunction,

$$\psi_{\mathbf{R}}^{Dyson}(\mathbf{r}) = \sum_m (-1)^{m+1} \varphi_m^{neutral}(\mathbf{r}) \langle \psi_{\mathbf{R}}^l | \hat{a}_m \phi_{\mathbf{R}}^j \rangle_{\mathbf{r}'}. \quad (2.210)$$

where $\varphi_m^{neutral}(\mathbf{r})$ is the molecular orbital of the neutral wavefunction, for which we drop notation for its nuclear geometry dependence, and the index m runs over all the molecular orbitals of the neutral electronic wavefunction. The annihilation operator \hat{a}_m remove the electron of the m^{th} orbital and the sign holds for the cofactor expansion according to the first line of the Slater determinant. Using the linearity of the Fourier transform, and noting that $\langle \psi_{\mathbf{R}}^l | \hat{a}_m \phi_{\mathbf{R}}^j \rangle_{\mathbf{r}'}$ is nothing else than a coefficient, the transition dipole matrix element can be rewritten as,

$$\mathbf{d}_{rec}^{jl}[\mathbf{p}, \mathbf{R}] = i \sum_m (-1)^{m+1} \langle \psi_{\mathbf{R}}^l | \hat{a}_m \phi_{\mathbf{R}}^j \rangle_{\mathbf{r}'} \frac{\partial}{\partial \mathbf{p}} \tilde{\varphi}_m^{neutral}(\mathbf{p}) \quad (2.211)$$

where $\tilde{\varphi}_m^{neutral}(\mathbf{p})$ stands for the Fourier transform of the molecular orbital. As introduced previously the solution of the electronic Schrödinger equation has been obtained using the LCAO approximation, then the molecular orbital can be expressed by a linear combination of primitive basis functions,

$$\varphi_m^{neutral}(\mathbf{r}) = \sum_{\mu} C_{m\mu} \chi_{\mu}(\mathbf{r}; \mathbf{R}) \quad \Rightarrow \quad \tilde{\varphi}_m^{neutral}(\mathbf{p}) = \sum_{\mu} C_{m\mu} \tilde{\chi}_{\mu}(\mathbf{p}; \mathbf{R}). \quad (2.212)$$

The interesting point is that almost all the calculations can be performed using Quantum Chemistry package, and the Fourier transform of the primitive basis functions is analytical. Thus their evaluation does not present any particular difficulty, which is the major advantage of using the SFA approximation. The difficult task actually occurs for the evaluation of the coefficient of the Dyson orbital, and is addressed now.

The evaluation of the set of coefficient needed to define the Dyson orbital depends of the accuracy of the

total electronic wavefunction, which is used for the neutral and ionic states. For instance if we make use of the Hartree-Fock wavefunction and the Koopman's approximation, this evaluation is straightforward and leads to

$$\psi_{\mathbf{R}}^{Dyson}(\mathbf{r}) = \varphi_{HOMO}^{neutral}(\mathbf{r}), \quad (2.213)$$

where the Dyson orbital is equivalent to the HOMO orbital of the molecule. But we discussed that the HF approximation fails in many cases, especially to describe electronically excited states. More sophisticated methods have to be employed, such as for example in the work of A. Krylov [128, 129], where she uses EOM-CCSD equations to compute the Dyson orbitals. Another possibility is to use a single expansion of SD to describe both the neutral and the ionic state using a CI expansion. The problem of using standard method for separate calculation of the neutral and ionic wavefunctions is that we end up with non-orthogonal Slater determinants to describe our system. Here we present how we solve the problem in the case of a CASSCF followed by an MRCI(SD) calculation, which remains quiet a well spread method in Quantum Chemistry. Let us first introduce the notation of the neutral and ionic wavefunctions,

$$|\Phi_{neut.}\rangle = \sum_I A_I \phi_I \quad (2.214)$$

$$|\Psi_{ion}\rangle = \sum_J B_J \psi_J \quad (2.215)$$

where A_I , B_J are the coefficients of the different configurations ϕ_I , ψ_J of the neutral and ionic wavefunction, respectively. After MRCI step, each configuration, either as Configuration state function (CSF) or a Slater determinant, is a special arrangement of the electrons in the molecular orbitals obtained after the MCSCF optimisation. Let us consider the evaluation of the coefficient of the $\phi_I^m(\mathbf{r})$ molecular orbital,

$$\langle \Psi_{ion} | \hat{a}_m \Phi_{neut} \rangle = \sum_J \sum_I A_I B_J^* \langle \psi_J | \hat{a}_m \phi_I \rangle. \quad (2.216)$$

Applying the annihilation operator directly defines the cofactor $\phi_I^{(m)}$, which is a Slater Determinant built with $n - 1$ orbitals. To obtain the general expression let us assume that the electronic wavefunctions are described by CSF, the other case being an exception of this general formulation. Each CSF can be written as a sum of SD, which are constituted by the same set of molecular orbitals with a different organisation of

the spin of the lonely electrons. We obtain,

$$\langle \Psi_{ion} | \hat{a}_m \Phi_{neut.} \rangle = \sum_J \sum_I A_I B_J^* \sum_{i \in CSF_I} \sum_{j \in CSF_J} c_i d_j \langle \psi_{J,j}^{SD} | \phi_{I,i}^{SD(m)} \rangle, \quad (2.217)$$

where c_i (d_j) is the weight of the Slater determinant $\phi_{I,i}^{SD}$ ($\psi_{J,j}^{SD}$) in the CSF of the configuration I (J). Now let's discuss the overlap between the two Slater determinants. In the case of orthogonal molecular orbitals, Slater's rules can be used to compute it, but as we have non-orthogonal molecular orbitals the Lödwin rules must be used. There are an extension of the Slater ones especially for this case. Introducing $\zeta(\mathbf{r})$ as the molecular orbital of the ionic wavefunction, the Lödwin rule reads [130],

$$\langle \psi_{J,j}^{SD} | \phi_{I,i}^{SD(m)} \rangle = \det\{d_{JI}(kl)\}, \quad (2.218)$$

where $d_{JI}(kl)$ is the overlap between the orbital k of the ion and the orbital l of the neutral molecule, i.e.

$$d_{JI}(kl) = \int \zeta_k^*(\mathbf{r}) \varphi_l(\mathbf{r}) d\mathbf{r}. \quad (2.219)$$

Then Eq. (2.218) reduces the calculation of the overlap between two Slater determinants to the determinant of all the overlap integrals of the different set of ionic and neutral orbitals. Using the molecular orbital expansion in the primitive basis functions, the overlap reads,

$$\int \zeta_k^*(\mathbf{r}) \varphi_l(\mathbf{r}) d\mathbf{r} = \sum_{\mu} \sum_{\nu} C_{l\mu}^N C_{k\nu}^I \int \chi_{\mu}(\mathbf{r}; \mathbf{R}) \theta_{\nu}(\mathbf{r}; \mathbf{R}) d\mathbf{r}. \quad (2.220)$$

Where $C_{l\mu}^N$, $C_{k\nu}^I$ are the expansion coefficients of the molecular orbital in the primitive basis functions for the neutral and ionic wavefunction, respectively. It turns out that the above equation can be greatly simplified if we use the same primitive basis for both wavefunction, which is not a constraint because it is more consistent for ab-initio calculation, then

$$\int \zeta_k^*(\mathbf{r}) \varphi_l(\mathbf{r}) d\mathbf{r} = \sum_{\mu} \sum_{\nu} C_{l\mu}^N C_{k\nu}^I S_{\mu\nu}(\mathbf{R}) \quad (2.221)$$

the overlap matrix $S_{\mu\nu}$ appears, and is naturally computed during the electronic calculation.

Collecting all the above results give an "ugly" equation, which becomes our working equation for the transition dipole matrix element in the SFA approximation, but as shown each part of the calculation is straightforward and uses either analytical results or data obtained directly using Quantum Chemistry package. The point with this method is that the multi-electron nature of the molecule is taken into account concerning the correlation between electron and the relaxation after ionisation.

We would like just to mention that the calculation of the Dyson orbital is not specific to the Strong field physics and High order harmonic generation. Its role is as well relevant for the photoelectron study, as discussed by A. Krylov [128, 129], because the Dyson orbital contains all the required information for the electron ionisation.

Chapter 3

Electronic Structure Results

3.1 Introduction

We propose in this section the presentation and the discussion of the different results obtained concerning the application of the different theories introduced previously in order to solve the Schrödinger equation. While, until now the formalism was rather general, the molecular system under interest (SO_2) is now considered. The sequential application of the different methods is presented in the following, with first the results of the adiabatic calculations, followed by the discussion of the diabaticization scheme employed, their comparison and their limits. Then the formalism introduced in order to take into account the spin-orbit couplings between the manifolds of electronic states is presented, and its application is discussed. The end of the methodological application will discuss the diabaticization of the different electronic properties and the calculation of the transition matrix elements in the framework of the strong-field approximation.

3.2 Adiabatic potential energy surfaces

3.2.1 Active space and primitive basis

In this section we will discuss the Potential Energy Surfaces (PES) computed ab-initio using the MRCI level of theory. An important point concerns the need of a consistent set of PES for the different electronic states. The latter are the electronic ground state, the two first singlet excited states, the three lowest triplet excited

states and finally the three first ionic states. The idea is to try to describe these states with the same level of accuracy employing similar techniques. Even if this is not primordial to describe neutral and ionic states on the same footings, it is mandatory for the singlet and triplet excited states, which are in a close energy range, involving different crossing between the states.

To compute different electronic states at the same level of accuracy using the MC-SCF followed by a MRCI calculation, the active space has to be appropriately chosen. The optimization of the latter has to be done to lower the energy of the state (variational principle), keeping in mind that CPU timing must be under control to proceed on the evaluation of thousands of points for different geometries. We choose 18 active electrons in 12 orbitals consisting for the C_{2v} symmetry of: five orbitals of a_1 symmetry with four occupied orbital and one virtual, two of b_1 symmetry with one occupied and one virtual orbitals, four orbitals of b_2 symmetry with three occupied and one virtual orbitals and finally one occupied orbital of a_2 symmetry. In C_s symmetry, the same CAS space is used with nine actives orbital of a' symmetry composed by seven occupied and two virtual orbitals and three actives orbitals of a'' symmetry with two occupied and one virtual. This active space has been already used in [48] and is known as the full-valence active space. The CPU effort to include one additional orbital increased drastically. We used the correlation consistent polarized valence triple zeta (cc-pVTZ) basis set [131] for all our calculations.

3.2.2 Adiabatic electronic ground state 1^1A_1 and singlet excited states 1^1B_1 and 1^1A_2

Performing a geometry optimization in C_{2v} and C_s symmetry, we found equal SO bond lengths of 1.447 Å for the equilibrium geometry of the ground state in the C_{2v} symmetry. The comparison with the optimization in C_s symmetry confirmed the C_{2v} geometry of the GS with a bond length difference (Q_u) found to be smaller than 1.2×10^{-4} Å, which lies within the expected accuracy of the method. The $O\hat{S}O$ valence angle ϕ , is optimized in C_{2v} to 119.05°, 0.02° larger than in C_s . Concerning the absolute energy both optimizations agreed up to the fourth decimal to give -547.9022 Hartree. This absolute energy is only interesting concerning the variational principle, but is not comparable with experiments in which relative energies are observed. In the same way, we performed geometry optimizations for the two lowest singlet excited states in C_{2v} symmetry, while in C_s symmetry, because of the conical intersection, the optimization did not converge. The point of

minimum energy of the 1^1B_1 state is obtained for equal bond length of 1.544 Å and a bending angle ϕ of 118.83°. Concerning the equilibrium geometry of the 1^1A_2 state, a similar bond length is obtained, 1.554 Å but with a much smaller bending angle $\phi = 94.64^\circ$. The absolute energy of both state minimum are -547.7606 and -547.7798 Hartree for the 1^1B_1 and 1^1A_2 state, respectively.

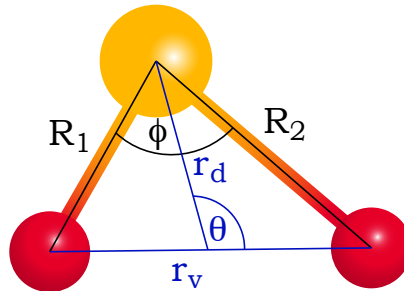


Figure 3.1: Definition of the two sets of coordinates used throughout this work. In black, the two SO bond lengths R_1 and R_2 and the OSO angle ϕ represent the internal coordinates which have been used in the PES calculations. In blue, r_v , r_d , and θ represent the Jacobi coordinates used to formulate the Hamiltonian and perform dynamical calculations.

The potential energy surfaces have been computed along the three degrees of freedom $R_s = (R_1 + R_2)/2$, $Q_u = (R_1 - R_2)/2$ and ϕ , see Fig. 3.1. The following grid parameters have been used, $1.1 \leq R_s \leq 2.15$ Å with a variation ΔR_s of 0.025 Å, $70 \leq \phi \leq 177.5^\circ$ with a step of 2.5° and $0 \leq Q_u \leq 0.3$ with $\Delta Q_u = 0.05$ Å and is extended by symmetry to -0.3 Å. It turns out that the grid is large enough for the electronic GS, but to study the photodynamics involving the excited states, the previous grid has been extended. The angle ϕ has been decreased to 60° , while the R_s and Q_u coordinates have been increased to 2.2 Å and 0.85 Å, respectively.

The electronic configurations are obtained from the coefficient of the CI vector after the MRCI calculation. The two predominant electronic configurations at the equilibrium geometry of the GS are:

$$[\text{core}]^{14} (5a_1)^2(3b_2)^2(6a_1)^2(4b_2)^2(7a_1)^2(2b_1)^2(5b_2)^2(1a_2)^2(8a_1)^2(3b_1)^0(9a_1)^0(6b_2)^0$$

$$[\text{core}]^{14} (5a_1)^2(3b_2)^2(6a_1)^2(4b_2)^2(7a_1)^2(2b_1)^2(5b_2)^2(1a_2)^0(8a_1)^2(3b_1)^2(9a_1)^0(6b_2)^0$$

with a coefficient of ~ 0.94 for the first and ~ -0.15 for the second. While the first configuration represents the arrangement of the electrons in the Hartree-Fock MO of lowest energy, the second configuration depicts

the promotion of both electrons of the $1a_2$ to the $3b_1$ orbital. For larger values of R_s , the mixing between both configurations becomes more important and they are almost on the same footing for $R_s \sim 2.0$ Å. For small angle (lower than 80°) and small R_s , an avoiding crossing with the 2^1A_1 state ($\sim 70^\circ$) changes abruptly the configuration of the ground state to:

$$[\text{core}]^{14} (5a_1)^2(3b_2)^2(6a_1)^2(4b_2)^2(7a_1)^2(2b_1)^2(5b_2)^0(1a_2)^2(8a_1)^2(3b_1)^2(9a_1)^0(6b_2)^0$$

Concerning the excited states, at the minimum of energy, the electronic configurations of the 1^1B_1 state are principally:

$$\begin{aligned} & [\text{core}]^{14} (5a_1)^2(3b_2)^2(6a_1)^2(4b_2)^2(7a_1)^2(2b_1)^2(5b_2)^2(1a_2)^2(8a_1)^1(3b_1)^1(9a_1)^0(6b_2)^0 \\ & [\text{core}]^{14} (5a_1)^2(3b_2)^2(6a_1)^2(4b_2)^2(7a_1)^2(2b_1)^2(5b_2)^1(1a_2)^1(8a_1)^2(3b_1)^2(9a_1)^0(6b_2)^0. \end{aligned}$$

The first configuration, which represents an excitation of one electron from the HOMO ($8a_1$) to the LUMO ($3b_1$), has a preponderant weight ~ 0.88 . The second configuration is relevant with a smaller coefficient -0.19 , standing for a double excitation from $1a_2$ and $5b_2$ to $3b_1$. For the 1^1A_2 state, the dominant configurations are:

$$\begin{aligned} & [\text{core}]^{14} (5a_1)^2(3b_2)^2(6a_1)^2(4b_2)^2(7a_1)^2(2b_1)^2(5b_2)^1(1a_2)^2(8a_1)^2(3b_1)^1(9a_1)^0(6b_2)^0 \\ & [\text{core}]^{14} (5a_1)^2(3b_2)^2(6a_1)^2(4b_2)^2(7a_1)^2(2b_1)^2(5b_2)^2(1a_2)^1(8a_1)^1(3b_1)^2(9a_1)^0(6b_2)^0. \end{aligned}$$

The first configuration, with a weight of ~ 0.88 , results from an excitation of one electron in the $5b_2$ orbital to the $3b_1$ orbital. The second configuration has a lower weight (-0.21) and describes a double excitation from $8a_1$ and $1a_2$ orbitals to the $3b_1$ orbital.

These results can be compared with previous and subsequent works of the literature as well as the CCSD evaluation of A. Komainda from his master thesis (cf. Tab. 3.1). In addition to the published investigation [132], three new studies have been published later and the results are included here. The calculations by Li *et al.* [68] were performed using the CASSCF-MRPT2 and the cc-pVTZ basis, the work of Xie *et al.* [133] used the same method than our with a slightly larger primitive basis (aug-cc-pVTZ) and larger number of states in the state-averaging. Then Mai *et al.* [134] used a smaller CAS (12,9) with a ano-rcc-vdzp primitive basis and Wilkinson *et al.* [71] used a CAS (12,9) with modified aug-cc-pVTZ and MCQDPT2 approach

for dynamical correlation. Our MRCI optimizations give consistent results regarding experimental data and former computations. We notice that the CCSD optimization ($\phi = 118.7^\circ$ and $R_s = 1.436 \text{ \AA}$) gives results for R_s close to those of Li *et al.* which are smaller than our MRCI results. One can notice that only the work of Mai *et al.* gives an error of 1° in the angle estimation, probably due to the small size of the CAS space. For excited states there is no experimental data available. We see that the CASSCF-MRPT2 results of Li *et al.* and our CCSD give a larger value for ϕ in the 1^1B_1 than in the 1^1A_1 state. This is the opposite for all other works at the MRCI level of approximation, which obtained a larger angle ϕ in the 1^1A_1 than in the 1^1B_1 state.

Table 3.1: Geometries of the minima of the 1^1A_1 ground state and the 1^1A_2 and 1^1B_1 excited states of SO_2 in C_{2v} symmetry. The results of the present work are compared with literature data. (R_s in \AA and ϕ in degree).

State	Coord.	MRCI ^a	CCSD ^a	Li ^b	Xie ^c	Mai ^d	Wilkinson ^e	Expt ^f
1^1A_1	R_s	1.448	1.436	1.437	1.454	1.453	1.439	1.432
	ϕ	119.1	118.7	119	119.2	120.5	119.4	119.5
1^1B_1	R_s	1.544	1.515	1.527	1.550	1.549	1.559	-
	ϕ	118.8	120.7	120	118.7	117.8	116.9	-
1^1A_2	R_s	1.554	1.527	1.537	1.558	1.556	1.554	1.53
	ϕ	94.7	93.4	93	93.6	95.3	97	99

^aFrom Ref. [132] ^bFrom Ref. [68] ^cFrom Ref. [133] ^dFrom Ref. [134] ^eFrom Ref. [71] ^fFrom Ref. [42, 41]

It is also important to compare the vertical and adiabatic excitation energies. The first one is obtained as the energy difference between one excited state and the ground state at the equilibrium geometry of the GS. The second one is obtained as the energy difference of the equilibrium geometries of each state. In both cases the energy minimum of the GS is used as reference. The results are reported in Tab. 3.2 and are compared with other available results.

Table 3.2: Computed vertical (vert., i.e., for the ground state equilibrium geometry) and adiabatic (adiab.) excitation energies (in eV) for SO_2 .

State	Exc.	MRCI ^a	CCSD ^a	Li ^b	Xie ^c	Mai ^d	Wilkinson ^e	Expt ^f
1^1B_1	Vert.	4.23	4.39	-	4.19	4.46	-	3.46
	Adia.	3.78	4.03	4.10	3.750	-	3.1	-
1^1A_2	Vert.	4.61	4.84	-	4.61	4.85	-	3.95
	Adia.	3.32	3.62	3.58	3.263	-	3.5	-

^aFrom Ref. [132] ^bFrom Ref. [68] ^cFrom Ref. [133] ^dFrom Ref. [134] ^eFrom Ref. [71] ^fFrom Ref. [41, 135]

Concerning the vertical excitation energy of the 1^1B_1 state, all the results predict a similar energy with

the largest difference, 0.27 eV, between the works of Xie *et al.* and Mai *et al.* Our MRCI and CCSD calculations are consistent with an energy difference of 0.16 eV. The results of Xie *et al.* are slightly lower than our MRCI ones, probably due to the larger primitive grid used. Finally, the ones of Mai *et al.* are 0.23 eV above our MRCI results, probably due to the smaller CAS used. The Adiabatic excitation energies, in relation to the vertical ones, are a useful piece of information to compare the PES used in the different works, because it reveals the topology of the two important points, i.e. the Franck-Condon point and the minimum of the PES. We can see that the energy difference between the vertical and the adiabatic excitations in our MRCI calculations and the one of Xie *et al.* differ from 0.01 eV, which seems to indicate a close topology of the PES with a global shift for the 1^1B_1 state. CCSD and MRCI results are also similar within 0.03 eV. We can note the low adiabatic energy obtained by Wilkinson *et al.* (3.1 eV) and the large one of Li *et al.* (4.10 eV). For the 1^1A_2 state, the differences of vertical excitation energy are in the same range than for the 1^1B_1 state, with an equal result between our MRCI and Xie *et al.* results concerning the vertical excitation and 0.06 eV concerning the adiabatic one. Mai *et al.* results are closer to the CCSD results with 4.85 eV for vertical excitation. Concerning the relative energy between the excited states all the results agreed up to 0.07 eV for the vertical excitation and 0.11 eV for the adiabatic ones.

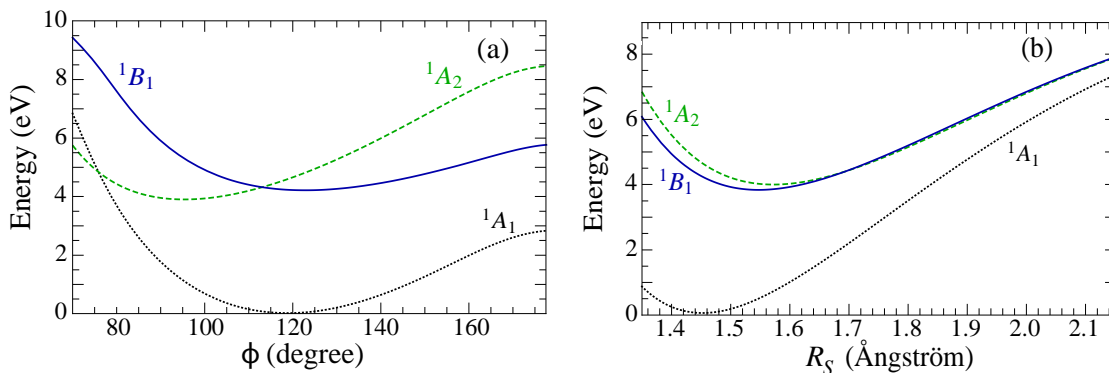


Figure 3.2: Left panel, cut of the PES along the bending angle with $R_s = 1.448 \text{ \AA}$ and $Q_u = 0 \text{ \AA}$, the GS equilibrium geometry. And right panel, similar than previously with variation of R_s for $\phi = 119.8^\circ$. The black line represents the electronic ground state, blue line the 1^1B_1 state and the green line the 1^1A_2 state. Along the bending angle the conical intersection between the 1^1B_1 and 1^1A_2 states appears at 113° . The intersection between 1^1A_1 and 1^1A_2 is not vibronically active, and both states are coupled only rotationally.

We show, in Fig. 3.2, a cut along the bending angle ϕ of the GS and the two lowest excited states in C_{2v} symmetry with R_s fixed at the GS geometry, i.e. 1.448 \AA . In the C_{2v} subspace (i.e. $Q_u = 0$) the two potential energy surfaces of the excited states cross freely each other because they belong to different

irreducible representations of the C_{2v} point group. The intersection in this subspace is not limited to a point but follows a one-dimensional line, later called the seam of conical intersections. The energy minimum of this seam has been estimated using an interpolation of the PES. We found an energy of 3.79 eV and the following geometry: $R_s = 1.55 \text{ \AA}$ and $\phi = 115.7^\circ$. The latter lies 0.44 eV below the vertical excitation to the 1^1B_1 . Xie *et al.* found a similar geometry with $\phi = 115.8^\circ$ and $R_s = 1.55 \text{ \AA}$, while Mai *et al.* obtained an identical bond length but a slightly larger angle $\phi = 117.3^\circ$. Their result results provide a geometry similar to the one obtained for the equilibrium geometry of the 1^1B_1 state, while Xie *et al.* and our work found it 3° smaller. This small difference may play a substantial role in the dynamics. The geometry of the molecule at this point is slightly different to the GS geometry with a smaller angle (115.7°) and longer SO bonds (1.55 \AA). This geometry is consistent with the work of Weis [136], which estimates $R_s = 1.53 \text{ \AA}$ and $\phi = 116.5^\circ$, and also with the one of Katagari *et al.* [48] with an angle of $\phi = 115^\circ$. In their work, Wang *et al.* fixed the angle ϕ at 118° and then obtained the bond length at the crossing point with $R_s = 1.57 \text{ \AA}$. This value is also in good agreement with our results.

For small angle ($\phi < 80^\circ$), one can see (Fig. 3.2) that the 1^1A_1 and 1^2A_2 states cross each other. But they belong to two different irreducible representations in both C_{2v} and C_s symmetries and these states do not interact through the molecular vibration. Nevertheless, the consideration of the molecular rotation would couple these two states, but this is beyond the scope of the present work. The cut of the PES along the R_s coordinate shows that for large values of R_s , the 1^1B_1 and 1^1A_2 states are almost degenerate. One should keep in mind that for angles larger than $\sim 115^\circ$, the 1^1B_1 state has a lower energy than the 1^1A_2 state, while for smaller angle it is the opposite.

In the C_s point group both electronic excited states belong to the same irreducible representation (A'') and the two states repulse each other as shown in Fig. 3.3. For $Q_u = 0$ one can see that the blue and green curves cross each other, but for displacement along the Q_u coordinate, this crossing is avoided. The consequence is that the electronic configuration of the lower and upper adiabatic surfaces in the C_s symmetry changes abruptly. Considering the lower adiabatic state, for small angle the dominant character is similar to the one of the 1^1A_2 state, while for larger angle ($> 115^\circ$) the dominant character is close to the one of the 1^1B_1 state.

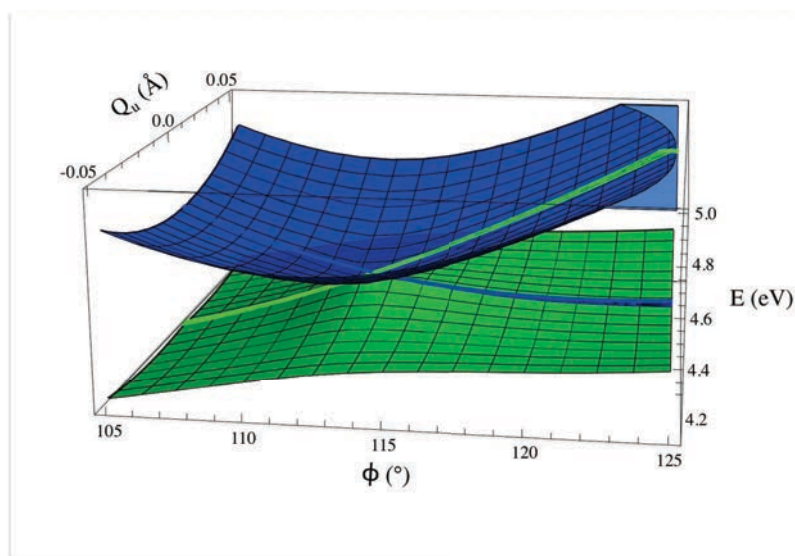


Figure 3.3: Conical intersection between the $1^1A''$ (blue) and $2^1A''$ (green) adiabatic electronic states for $R_s = 1.448$ Å as a function of Q_u and ϕ . In C_{2v} symmetry ($Q_u = 0$) the two states cross freely each other.

3.2.3 Adiabatic triplet excited states 1^3B_1 , 1^3A_2 and 1^3B_2

Three excited triplet states are lying within the same energy range than the singlet ones. Using the same active space and a state-averaging over these states, we computed the three dimensional PES. The same grid parameters have been employed, with the variation of ϕ from 70° to 177.5° , R_s from 1.35 to 2.15 Å, and Q_u between 0 to 0.5 Å and extended by symmetry to -0.5 Å. The energy minimum of the 1^3B_2 state and its geometry have been computed from the interpolated PES and is obtained for a bending angle of 105° and an equal SO bond length of 1.577 Å. In the vicinity of the equilibrium geometry, the electronic configuration of the state is:

$$[\text{core}]^{14} (5a_1)^2(3b_2)^2(6a_1)^2(4b_2)^2(7a_1)^2(2b_1)^2(5b_2)^2(1a_2)^1(8a_1)^2(3b_1)^1(9a_1)^0(6b_2)^0,$$

with a weight of 0.91, approximately. For valence angles larger than 150° , the 1^3A_1 state converging to the $^3\Pi_u$ state at linearity ($\phi = 180^\circ$), crosses the 1^3B_2 state. While in C_{2v} this crossing is allowed by symmetry, in C_s a symmetry-allowed conical intersection takes place between them. This changes abruptly the electronic

configuration of the 1^3B_2 PES to:

$$[\text{core}]^{14} (5a_1)^2(3b_2)^2(6a_1)^2(4b_2)^2(7a_1)^2(2b_1)^2(5b_2)^2(1a_2)^2(8a_1)^1(3b_1)^0(9a_1)^1(6b_2)^0.$$

This intersection occurs at high energies (> 6 eV) and the 1^3B_2 state is approximated to the lowest adiabatic $1^3A'$ state. In other words we neglect the non-adiabatic coupling and the conical intersection (note that this approximation is later supported by the dynamical results).

Table 3.3: Geometries of the minima of the 1^3B_1 , 1^3A_2 and 1^3B_2 electronic states in C_{2v} symmetry. Results of the present work are compared with literature data. (R_s in Å and ϕ in degree)

State	Coord.	MRCI ^a	CCSD ^a	Li ^b	Xie ^c	Mai ^d	Wilkinson ^e	Expt ^f
1^3B_1	R_s	1.517	1.491	1.484	1.517	1.517	1.522	1.493
	ϕ	126.1	125.6	129	125.0	125.7	124.5	126.2
1^3A_2	R_s	1.554	1.528	1.538	1.547	1.556	1.553	-
	ϕ	94.0	93.5	94	92.1	95.0	96.9	-
1^3B_2	R_s	1.576	1.558	1.561	-	1.576	1.572	-
	ϕ	105.4	106.2	106	-	106.6	106.9	-

^aFrom Ref. [132] ^bFrom Ref. [68] ^cFrom Ref. [133] ^dFrom Ref. [134] ^eFrom Ref. [71] ^fFrom Ref. [137]

Concerning the 1^3B_1 and 1^3A_2 states, they have the same electronic configurations than the singlet states of the same symmetry discussed previously (Sec. 3.2.2), but with parallel spin for the single electrons. In agreement with the Hund's rules, their energy are slightly below the energy of the respective singlet states. The equilibrium geometries are $R_s = 1.517$ Å and $\phi = 126^\circ$ for the 1^3B_1 state and $R_s = 1.554$ Å and $\phi = 94^\circ$ for the 1^3A_2 state. While the geometry of the latter is almost identical to the one for the 1^1A_2 state, a larger difference is obtained for the 1^3B_1 state and its homologue. The banding angle is ($\sim 5^\circ$) larger and bond length (~ 0.3 Å) smaller for the triplet state. Note that all the theoretical results are in good agreement, and describe accurately the experimental results for the 1^3B_1 , see Tab. 3.3.

The vertical and adiabatic excitation energies are also reported in Tab. 3.4 using the energy minimum of the GS as reference. Our MRCI and CCSD results and Xie's calculations agree for the state ordering with respect to the vertical energy. The 1^3B_1 state has the lowest energy, followed by the 1^3B_2 state, lying ~ 0.88 eV above. On the top the 1^3A_2 state lies ~ 1 eV above the 1^3B_1 state. A very good agreement is obtained between the MRCI and CCSD results for the 1^3B_1 and 1^3B_2 states. These methods provide slightly different

energies (0.2 eV) for the 1^3A_2 state. Concerning the adiabatic energies, more information are available in the literature and gave the possibility to compare the results of the 1^3B_2 state, not considered in the work of Xie *et al.* Concerning the 1^3B_1 and 1^3A_2 states, their relative energy minimum are slightly different depending on the methods. While in our MRCI results the 1^3A_2 minimum is 0.02 eV above the 1^3B_1 state, Xie *et al.* obtained the opposite with a difference of 0.007 eV between these states. The CCSD calculations provide the same ordering than the one obtained in our MRCI calculations, but with a difference of 0.11 eV. This difference of energy is similar to the one obtained by Li *et al.* Wilkinson *et al.* found an energy difference even larger for these states with 0.2 eV. The work of Mai *et al.* is the only one which obtained the 1^3A_2 state 0.11 eV above the 1^3B_1 state. According to the experimental data available, our results are in close agreement concerning the energy difference and ordering.

Table 3.4: Computed vertical (vert., i.e., for the ground state equilibrium geometry) and adiabatic (adia.) excitation energies (in eV) for the triplet states of SO_2 .

State	Exc.	MRCI ^a	CCSD ^a	Li ^b	Xie ^c	Mai ^d	Wilkinson ^e	Expt ^f
1^3B_1	Vert.	3.34	3.39	-	3.33	-	-	-
	Adia.	3.07	3.14	3.20	3.057	3.41	3.0	3.19
1^3A_2	Vert.	4.30	4.50	-	4.37	-	-	-
	Adia.	3.09	3.25	3.29	3.050	3.32	3.2	3.22
1^3B_2	Vert.	4.18	4.27	-	-	-	-	-
	Adia.	3.22	3.53	3.41	-	3.54	3.5	-

^aFrom Ref. [132] ^bFrom Ref. [68] ^cFrom Ref. [133] ^dFrom Ref. [134] ^eFrom Ref. [71] ^fFrom Ref. [137, 43]

A symmetry-allowed conical intersection takes place between the 1^3B_1 and 1^3A_2 states, Fig. 3.4. Using an interpolation of the PES, we localized in the C_{2v} symmetry the geometry and the energy of the energy minimum of the seam of conical intersections. The equal bond lengths are 1.547 Å and the angle is 109.15°, with a energy of 3.345 eV. Only Mai *et al.* reported in the literature this characteristic point with an equal value of R_s , a slightly larger angle of 111.1° and an energy of 3.59 eV. Differences between the angles and the energies are in the same order than the differences between the different characteristic points of the electronic states.

We present in Fig. 3.4 two different cuts of the adiabatic PES, the first one along the bending angle ϕ for fixed value of R_s and the second along the R_s coordinate for a fixed ϕ , both are in C_{2v} symmetry with $Q_u = 0$. On the left panel, the lowest triplet state change as a function of ϕ , with at small angle ($< 107.5^\circ$)

the 1^3A_2 state has the lower energy while the 1^3B_1 is the lower for larger angles. Concerning the variation along R_s , the 1^3B_2 state is the lowest for values larger than ~ 1.65 Å.

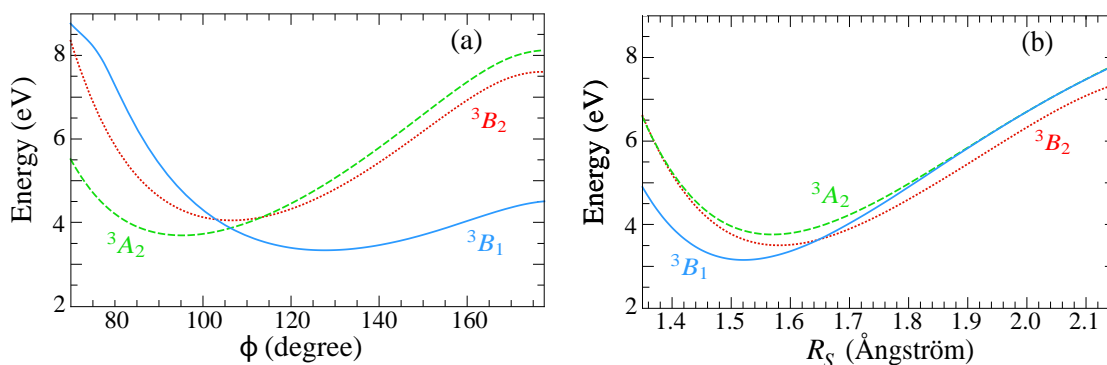


Figure 3.4: Left panel, cut of the PES along the bending angle with $R_s = 1.448$ Å and $Q_u = 0$ Å, the GS equilibrium geometry. And right panel, similar than previously with variation of R_s for $\phi = 119.8^\circ$. The Red line represents the 3B_2 state, blue line the 3B_1 state and the green line the 3A_2 state. Along the bending angle the conical intersection between the 3B_1 and 3A_2 states appears at 105° . The intersection between 3B_2 and the other states is not vibronically active, but the spin-orbit coupling can leads to coupling between them.

We do not show a representation of the conical intersection for the triplet states, because of its similitude with the one of the singlet states. In the previous section we discussed on the electronic GS (Sec. 3.2.2), which is singlet of spin, as well as the operator to describe the interaction with light (Sec. 2.5.1). The latter does not operate on the spin of the electrons, so no transition may occur between the GS and the triplet excited states if we neglect the coupling between the singlet and triplet states. To take into account these interactions, the spin-orbit coupling (SOC) must be introduced as discussed later. At this point, it is interesting to look at the singlet and triplet excited states. In Fig. 3.5, the different electronic states are represented as a function of the bonding angle into the C_{2v} symmetry. The singlet and triplet states of the same symmetry (A_2 or B_1) never cross each other and are almost parallel for all the C_{2v} geometries. There is an intersystem crossing between the 1^3A_2 and 1^1B_1 states nearby by the minimum of the latter, and the same occurs as well between the 1^1A_2 and 1^3B_1 . In the vicinity of this crossing, the 1^3B_2 state cross both singlet states at almost the same energy range. Turning in the C_s symmetry ($Q_u = 0.05$ Å), the crossing pattern changes radically for the adiabatic states. The higher adiabatic singlet state ($2^1A''$) does not cross any triplet state anymore and this holds for all the geometries computed. The lowest triplet adiabatic state ($1^3A''$) crosses the lowest singlet adiabatic state ($1^1A''$) for small angle, large Q_u and R_s . But both $2^3A''$ and $1^3A'$ states still cross the lowest adiabatic singlet state.

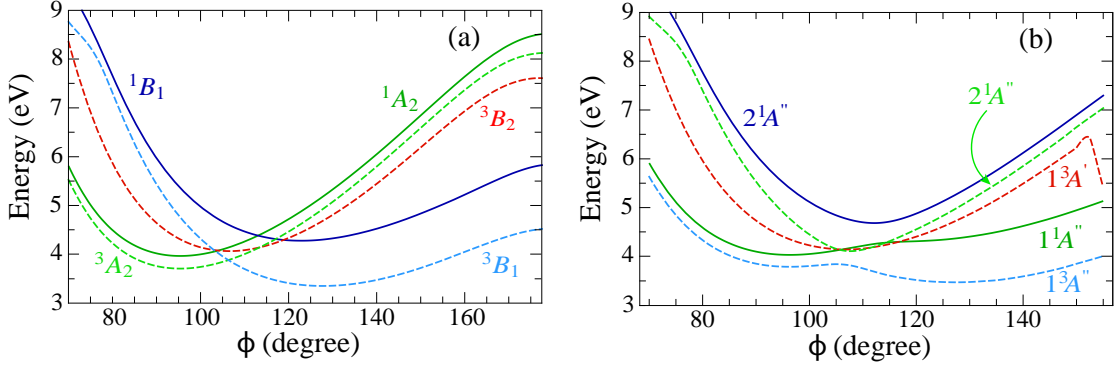


Figure 3.5: Representation of the PES along the bonding angle for $R_s = 1.448$ and $Q_u = 0$ (left panel) and $Q_u = 0.05$ (right panel). The same colour code as previously is used dashed lines depict the triplet states. One can notice the numerous intersystem crossings between the sets of states, and the triplet and singlet of the same symmetry are essentially parallel to each other without crossing.

3.2.4 Adiabatic ionic doublet states 1^2A_1 , 1^2B_2 and 1^2A_2

The three lowest ionic doublet states 1^2A_1 , 1^2B_2 and 1^2A_2 have also been computed during this study, because they are required to compute photoelectron spectra as well as for the calculation of the HHG spectra. The same level of accuracy and the same active space than for neutral states have been used. In order to correctly describes the nuclear dynamics the value of the R_s coordinate has been decreased to 1.25 \AA . The other parameters of the grid are the same than for the electronic triplet excited states. At the GS equilibrium geometry, the three lowest ionic states of the molecular cation SO_2^+ have the following dominant electronic configurations:

$$\begin{aligned}
 1^2A_1 &: [\text{core}]^{14} (5a_1)^2(3b_2)^2(6a_1)^2(4b_2)^2(7a_1)^2(2b_1)^2(5b_2)^2(1a_2)^2(8a_1)^1 \\
 1^2B_2 &: [\text{core}]^{14} (5a_1)^2(3b_2)^2(6a_1)^2(4b_2)^2(7a_1)^2(2b_1)^2(5b_2)^1(1a_2)^2(8a_1)^2 \\
 1^2A_2 &: [\text{core}]^{14} (5a_1)^2(3b_2)^2(6a_1)^2(4b_2)^2(7a_1)^2(2b_1)^2(5b_2)^2(1a_2)^1(8a_1)^2.
 \end{aligned}$$

The ionic ground state for the equilibrium geometry of SO_2 , namely 1^2A_1 , is obtained from an ionisation of the electron in the $8a_1$ orbital, while the two first doublet excited states result from ionisation of the $5b_2$ and $1a_2$ orbitals for the 1^2B_2 and 1^2A_2 state, respectively. While only optimization of the different characteristic points of the ionic states has been previously discussed in the literature, no full 3-D PES has ever been computed before the present work. We have compiled in Table I our data compared to the earlier theoretical ones.

Table 3.5: Equilibrium geometries of the ionic states of SO_2 , namely 1^2A_1 , 1^2B_2 and 1^2A_2 in C_{2v} symmetry. Results of the present work are compared with literature data. (R_s in Å and ϕ in degree)

State	Coord.	MRCI ^a	CCSD ^a	Zhang ^b	Chang ^c	Li ^d	Wilkinson ^e
1^2A_1	R_s	1.449	1.430	1.444	-	1.439	1.446
	ϕ	131	130.7	132.6	-	132	128.3
1^2B_2	R_s	1.497	1.472	-	1.494	1.491	1.486
	ϕ	99.7	99.5	-	99.2	99.9	100.9
1^2A_2	R_s	1.511	1.488	-	1.51	1.504	1.501
	ϕ	108.7	108.5	-	108.5	109.3	109.7

^aFrom Ref. [138] ^bFrom Ref. [139] ^cFrom Ref. [140] ^dFrom Ref. [141] ^eFrom Ref. [71]

Note that we did not optimise the stationary points of the PES but extracted them from the interpolation performed after the computation of the 3D PES. In general, there is a very good agreement between all values (few pm in bond length or degrees in $O\hat{S}O$ angle), indicating that the various methods employed, e.g. MRCI (our work), CASPT2 (Li *et al.* [141]), CCSD(T) with either 6-311+G (2d,p) primitive basis set (Zhang *et al.* [139]) or aug-cc-pVTZ primitive basis (Chang *et al.* [140]) and CASSCF with MCQDPT2 from Wilkinson *et al.* [71] are all consistent.

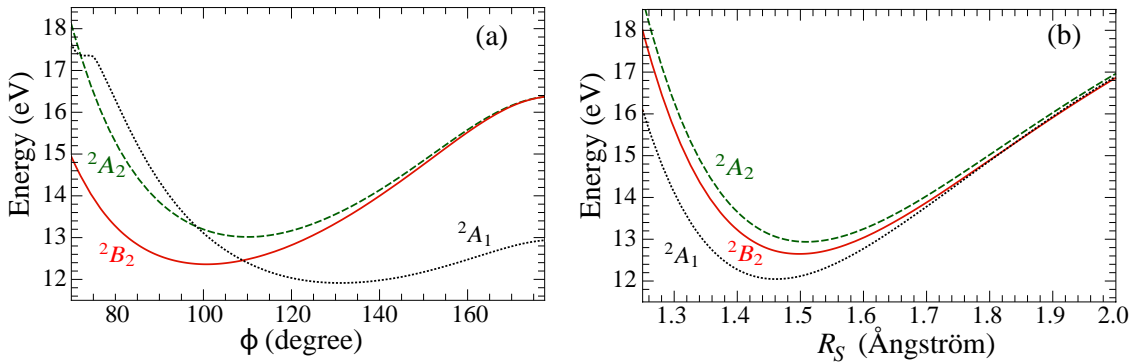


Figure 3.6: One-dimensional cut of the ionic PES in C_{2v} symmetry. Panel (a), representation of the electronic states as a function of the symmetric stretching (R_s). In dotted black, the ionic ground state 1^2A_1 , in full red the 1^2B_2 state and in dashed green the 1^2A_2 state. Panel (b) the same colour code is used to represent the PES as a function of the bending angle ϕ .

The vertical and adiabatic ionisation energies of the different states have been reported in Tab. 3.6 in addition to the experimental work of Wang *et al.* [143]. Our results are slightly lower (~ 0.2 eV) than Palmer's ones [142] for the two first excited states and ~ 0.15 eV for the ionic GS. these differences are similar with the work of Zhang *et al.* with 0.22 eV for the GS and 1^2A_2 state and 0.27 eV for the 1^2B_2 state. Our results are fully consistent with a global shift of ~ 0.2 eV which can results from the CAS space

Table 3.6: Computed vertical (vert., i.e., for the ground state equilibrium geometry) and adiabatic (adiab.) excitation energies (in eV) for the ionic states of SO₂.

State	Exc.	MRCI ^a	CCSD ^a	Zhang ^b	Palmer ^c	Wilkinson ^d	Expt ^e
1 ² A ₁	Vert.	12.06	12.14	12.28	12.21	12.2	12.35
	Adia.	11.9	-	-	12.03	-	-
1 ² B ₂	Vert.	12.78	12.46	13.05	12.97	12.7	12.99
	Adia.	12.23	-	-	12.48	-	-
1 ² A ₂	Vert.	13.14	13.07	13.36	13.33	13.3	13.34
	Adia.	12.80	-	-	13.03	-	-

^aFrom Ref. [138] ^bFrom Ref. [139] ^cFrom Ref. [142] ^dFrom Ref. [71] ^eFrom Ref. [143]

chosen to be identical than the one of neutral states, and not especially optimized for the ionic states. For calculation of the ionic states, Wilkinson *et al.* used a different CAS (11,10) than for the neutral states by adding a new active virtual orbital. While they obtained close results than Li *et al.* and Palmer for the ionic ground state and 1²A₂ excited state, it seems that they obtained an "over stabilization" of the 1²B₂ state, with a vertical energy lying 0.5 eV higher than the ionic GS. This is in contradiction with experimental and other theoretical results, but somehow consistent with the CCSD results, for which we obtained an energy difference of 0.32 eV between the 1²A₁ and 1²B₂ states. Only Palmer reported the adiabatic energies of the ionic states, which are in close agreement with ours concerning the relative energy of the three different states and the difference between adiabatic and vertical energy for the two excited one. It turns out that our results are the closest to the experimental data for the relative energy of the different ionic states, with a global shift of ~ 0.3 eV. The global shift is encouraging, because we can expect that the topology of the different PES is correct.

In C_{2v} symmetry (i.e. Q_u = 0), the minimum of the 1²A₁ (1²B₂) state is obtained for a bond length R_s = 1.449 Å (1.497 Å) and an angle $\phi = 131^\circ(99.7^\circ)$. The difference of the equilibrium angle of $\sim 30^\circ$ between both surfaces is rather large. For the 1²A₂ state, we get R_s = 1.511 Å and an angle $\phi = 108.7^\circ$. We have plotted in Fig. 3.6 a cut of the PES for these three states along the bond length R_s (a) or the bending angle ϕ (b). The question of the Conical intersection between the two lowest ionic states has never been raised. This latter, taking place between 1²A₁ and 1²B₂ is visible for $\phi \approx 110^\circ$ in Fig. 3.6 (b). For these two states, we present in Fig. 3.7 the 2-D PES as a function of the angle ϕ and the asymmetric stretching coordinate Q_u for R_s = 1.49 Å. The bottom PES, in C_s symmetry, presents a characteristic double-well

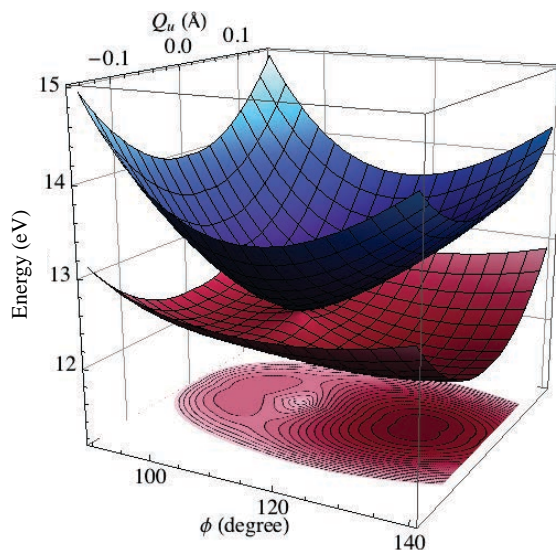


Figure 3.7: Representation of the conical intersection between the two lowest adiabatic ionic states, namely, $1^2A'$ in red and $2^2A'$ in blue, as a function of the asymmetric stretching (Q_u) and the bending angle (ϕ). A contour plot of the $1^2A'$ state is represented on the bottom.

shape. We localized the energy minimum of the seam of conical intersections at 12.36 eV for $R_s = 1.489 \text{ \AA}$ and $\phi = 110^\circ$. Its energy lies above the vertical and adiabatic energies of the ionic ground state 1^2A_1 but is energetically below the vertical energy of the 1^2B_2 state.

3.3 Diabatization of the adiabatic states coupled through conical intersection

3.3.1 Diabatization of the 1^1B_1 and 1^1A_2 adiabatic states

Because of the singularity of the non-adiabatic coupling in the adiabatic basis, it is compulsory to transform this latter into a "quasi-diabatic" basis in order to consider the nuclear dynamics. For the case of the singlet states, we propose two different approaches of diabaticization (see Sec. 2.2.4). The numerical determination of the coupling constant λ from the PES follows two different ways. It has been shown that both ways remove the singular part of the non-adiabatic coupling but do not handle the non-singular part in the same manner [24]. But, as the singular part should govern the dynamics, both methods should give similar results. The first method implies the computation of λ along the seam of CI. An interpolation of the PES has been used

to localise this seam, and λ was computed from Eq. (3.1) (see Sec. 2.2.4 Eq. (2.66)).

$$\lambda_{seam} = \frac{1}{2} \frac{\partial(E_c^1 - E_c^2)}{\partial Q_u} \Big|_{R_s^{seam}, \phi^{seam}} \quad (3.1)$$

This evaluation of λ_{seam} is cumbersome because the seam of conical intersections must be determined and for system with more than 3 *dofs*, the determination of the hyper-plane of intersection becomes a hardly manageable task. But the attractive point is that the approximation of the model is well defined. A more systematic approach to compute the coupling term, $\lambda_{C_{2v}}$, is to project onto the high-symmetry sub-space the differentiation of the two PES difference along Q_u , as presented in Eq. (3.2) (see Sec. 2.2.4 Eq. (2.70)).

$$\lambda_{C_{2v}} = \left[\frac{1}{2} \frac{\partial^2 \Delta}{\partial Q_u^2} \right]_{R_s^{seam}, \phi^{seam}}^{1/2}. \quad (3.2)$$

The results of both methods are presented in Fig. 3.8. Note that λ_{seam} is a function of the seam coordinates only, which, in our case is similar to a function of R_s , while $\lambda_{C_{2v}}$ is a function of the two symmetric coordinates, i.e. R_s and ϕ . As expected both methods give exactly the same values of λ along the seam of conical intersection. We can note that the largest values of $\lambda_{C_{2v}}$ are not obtained along the seam of CI, but rather for $100^\circ < \phi < 110^\circ$ and $1.55 < R_s < 1.7 \text{ \AA}$ with a maximum value at 4.71 eV/\AA for $R_s = 1.63 \text{ \AA}$ and $\phi = 102.5^\circ$. The maximum of $\lambda_{seam} = 4.572 \text{ eV/\AA}$ is slightly smaller than the case of $\lambda_{C_{2v}}$ and is obtained for $R_s = 1.65 \text{ \AA}$. The Franck-Condon (FC) point is near the seam of CI and both methods give different coupling values, $\lambda_{C_{2v}} = 3.7 \text{ eV/\AA}$ and $\lambda_{seam} = 4.19 \text{ eV/\AA}$. Then concerning the minimum energy of conical intersection, which is at lower energy than the FC point, both methods give 4.46 eV/\AA close to the maximum. In the work of Müller *et al.* [70], a single average value of λ has been used to construct diabatic states. This value (3.29 eV/\AA) is smaller than ours with both methods used and this difference ($\sim 30\%$) will change slightly the time evolution of the wavepacket.

An important point of Fig. 3.8 is that $\lambda_{C_{2v}}$ is null for small values of R_s and either $\phi < 90^\circ$ or $\phi > 125^\circ$. Actually, these regions of uncoupled geometries have been artificially set to zero, because the coupling turns from a real value function to an imaginary one. It can easily be understood from Eq. (3.2) that it occurs at geometries for which the difference between both PES is larger in the C_{2v} sub-space than in the C_s one. Physically this means that for these geometries, there is no repulsion between the PES anymore. This feature is a direct consequence of the method, which removes only the singular part of the derivative coupling, leading,

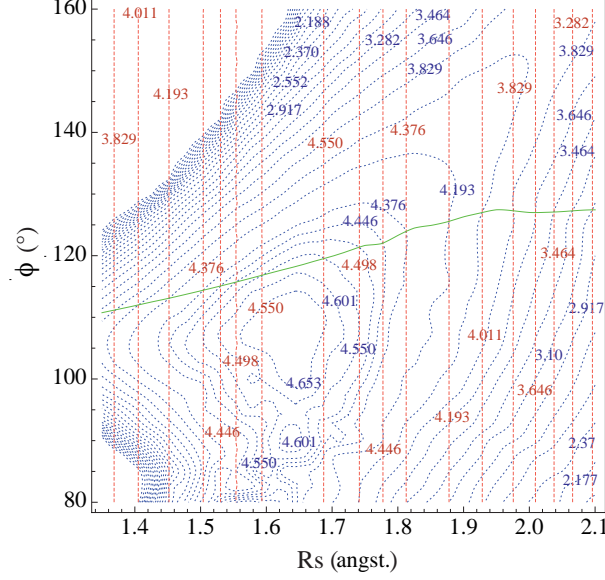


Figure 3.8: Representation of the evaluated λ according to the two methods detailed in the text. In dashed blue are isolines of the values of $\lambda_{C_{2v}}$ (eV/Å), and in dashed red the same for λ_{seam} . Both result coincide along the seam of conical intersection represented by the full green line.

as stated in Sec. 2.2.4, to the linear form of W_{12} in Eq. (2.63). We assume that interactions between states can be neglected in such cases (i.e. $\lambda = 0$), which implies that diabatic states recover adiabatic ones. This approximation affects the treatment of the non-singular derivative couplings only, which are not the goal of the concept of regularized diabatic states. The good agreement of the two diabaticization variants, emerging below, shows that the non-singular derivative couplings are indeed of minor importance also from a more practical point of view (see also Ref. [24] for related findings).

In this framework, the diabatic Hamiltonian for our system can be established as

$$\mathbf{H}_{dia} = (T_N + \Sigma)\mathbf{1} + \frac{\Delta(R_s, \phi, Q_u)}{\sqrt{\Delta_0^2(R_s, \phi) + \lambda^2 Q_u^2}} \begin{pmatrix} \Delta_0(R_s, \phi) & \lambda Q_u \\ \lambda Q_u & -\Delta_0(R_s, \phi) \end{pmatrix}. \quad (3.3)$$

Collecting the diagonal potential terms, it defines the diabatic potential energy surfaces which reads,

$$W_{dia}^{11,22} = \Sigma \pm \frac{\Delta(R_s, \phi, Q_u) \cdot \Delta_0(R_s, \phi)}{\sqrt{\Delta_0^2(R_s, \phi) + \lambda^2 Q_u^2}}. \quad (3.4)$$

The results of the diabatic PES are presented in Fig. 3.9 for either $\lambda = \lambda_{C_{2v}}$ or $\lambda = \lambda_{seam}$. By construction

both methods give diabatic states identical to the adiabatic one in C_{2v} symmetry, but are different in the C_s one. For a small value of asymmetric coordinate ($Q_u = 0.05 \text{ \AA}$), the difference between both methods are hardly noticeable for the entire range of bending angle, except that the diabatic states obtained from $\lambda_{C_{2v}}$ exhibit a faster convergence to the adiabatic states far from the conical intersection, where the diabatic ${}^1B_1(\lambda_{C_{2v}})$ state (full blue) join the ${}^1A''$ state (black line) for $\phi \sim 127^\circ$, while the ${}^1B_1(\lambda_{seam})$ (dashed blue) stay above the latter.

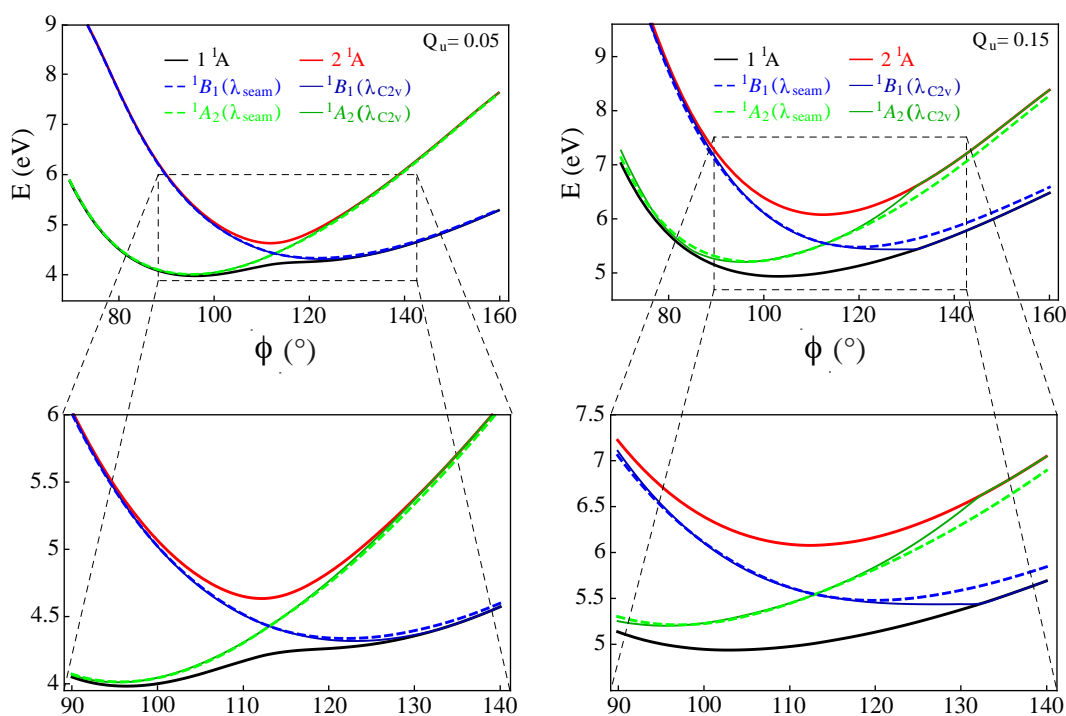


Figure 3.9: Representation of the adiabatic and diabatic surfaces for the two methods. The two left panels are a cut for fixed $R_s = 1.448 \text{ \AA}$ and $Q_u = 0.05 \text{ \AA}$ and the two right panels for $Q_u = 0.15 \text{ \AA}$. Note that the bottom panels are zoom in of the upper ones. The lower (upper) adiabatic state is represented in black (red), while the diabatic 1B_1 state is in blue, and the diabatic 1A_2 state is in green. The dashed line is for diabatization from λ_{seam} and the full line for $\lambda_{C_{2v}}$. For the smaller value of Q_u both methods give similar results while for larger value the diabatic states from $\lambda_{C_{2v}}$ recover to fast the adiabatic states, introducing a discontinuity in the PES.

For a larger value of the asymmetric stretching ($Q_u = 0.15 \text{ \AA}$), the difference between both methods becomes more important. In the case of $\lambda_{C_{2v}}$, for which we enforced $\lambda_{C_{2v}} = 0$ for large angles, it leads to an unphysical behaviour of the ${}^1B_1(\lambda_{C_{2v}})$ and ${}^1A_2(\lambda_{C_{2v}})$ states. The convergence of these diabatic states to the adiabatic ones is abrupt and a discontinuity appears in the diabatic states. For the second method, both diabatic states obtained from λ_{seam} are smooth and with a much slower convergence to the adiabatic states

with a smoother behavior. As along the seam of conical intersection both methods give identical results for λ , the position of the intersection between the diabatic states is unchanged from a method to another, as well as the shape of the diabatic potential in its vicinity. The two methods have the same properties because both take care of the singular part of the derivative coupling and away from the conical intersection the diabatic states recover the adiabatic ones because the coupling is weak and the adiabatic picture is valid. This feature has already been discussed by the authors of Ref. [24], pointed out the interpolating behaviour of the method between a good diabatic basis, i.e. the C_{2v} subspace, and the the adiabatic basis away from the intersection, when the non-adiabatic coupling becomes weak. The problem with the method involving $\lambda_{C_{2v}}$ is rather general, we found the same behaviour concerning the diabaticization of the doublet and triplet states, while the other method gives always smooth diabatic PES.

The non-adiabatic coupling terms (off-diagonal elements of the diabatic potential matrix), is defined by (see Sec. 2.2.4 Eq. (2.69)):

$$W_{12} = \frac{\Delta(R_s, \phi, Q_u) \cdot \lambda Q_u}{\sqrt{\Delta_0^2(R_s, \phi) + \lambda^2 Q_u^2}}. \quad (3.5)$$

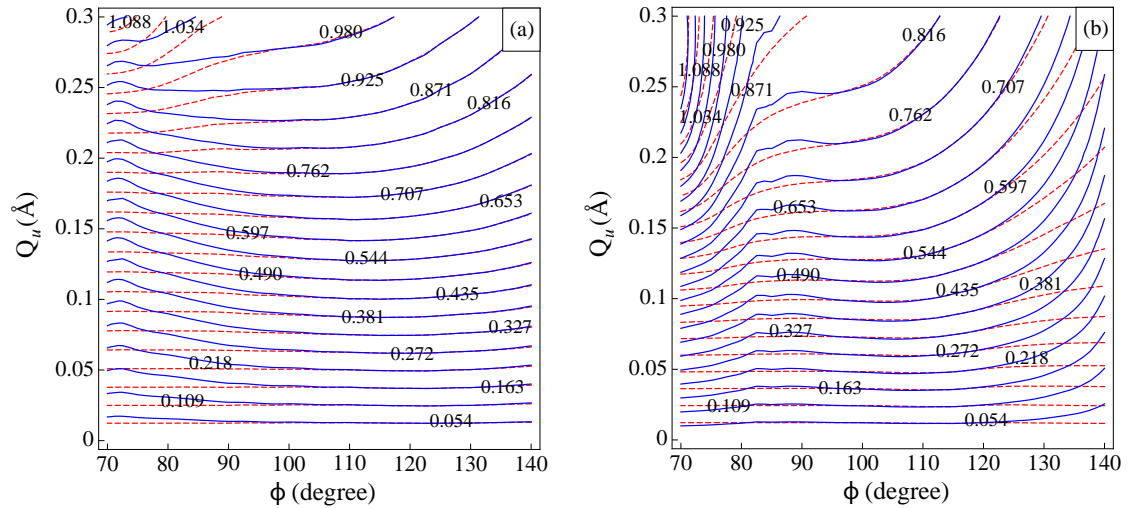


Figure 3.10: Potential coupling term W_{12} for both methods are presented in this figure for two values of $R_s = 1.55$ Å (left) and $R_s = 1.8$ Å (right). The blue lines are results from $\lambda_{C_{2v}}$ and dashed red are results from λ_{seam} , both give in Hartree. We see that for small R_s the coupling $W_{12}^{C_{2v}}$ is falling to zero for angle larger than 140° , accordingly to the zero value of $\lambda_{C_{2v}}$. Otherwise both methods give similar results.

A representation of it is shown in Fig. 3.10, where each panel depicts W_{12} for both methods ($W_{12}^{C_{2v}}$ in

blue and W_{12}^{seam} in dashed red) at two different values of the symmetric coordinates, namely $R_s = 1.55 \text{ \AA}$ and $R_s = 1.8 \text{ \AA}$. This choice is motivated to avoid the complex values of $\lambda_{C_{2v}}$, which obviously leads to vanishing couplings. In the first case, we remark an overall good agreement between both methods, especially for angles in the vicinity of the conical intersections. For angles larger than 135° , $W_{12}^{C_{2v}}$ drops to zero while W_{12}^{seam} is smoother and for large Q_u and small angles $W_{12}^{C_{2v}}$ increases faster. Concerning larger values of R_s , the overall agreement between both methods is better, principally for large bending angles, and for smaller ones. It is the opposite than for $R_s = 1.55 \text{ \AA}$, with W_{12}^{seam} increasing faster with larger values of Q_u . Of course both behaviours are consistent with the values of λ of Fig. 3.8.

3.3.2 Diabatization of the $1^3B_1/1^3A_2$ and $1^2A_1/1^2B_2$ adiabatic states

The conical intersections between either the triplet or doublet states are also symmetry-allowed and the diabatization scheme is thus identical to the case of the singlet states. As pointed out in the previous section, it turns out that both methods are not equally convenient. So, we decide to continue only with the determination of λ along the seam of conical intersections, because as it will be presented later (Sec. 4.2.1), both methods lead to almost identical results for the wavepacket dynamics.

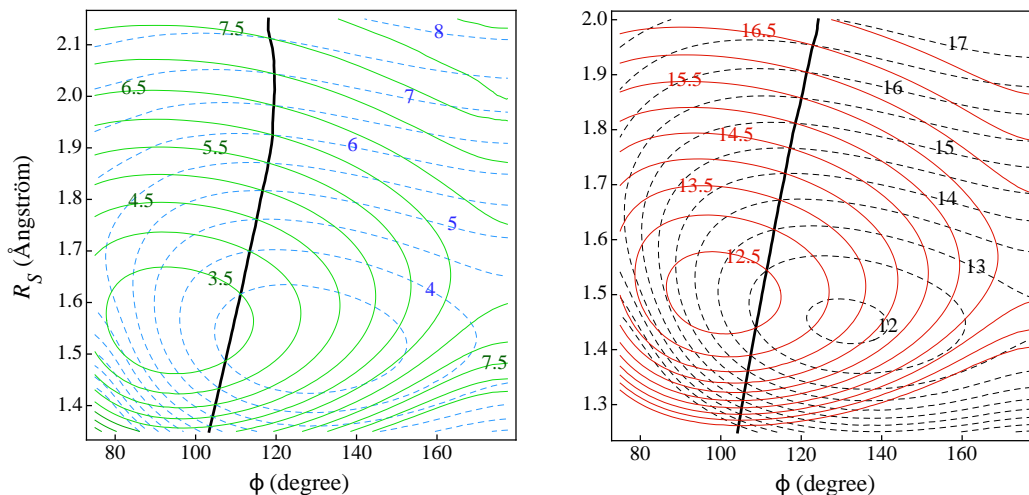


Figure 3.11: Localization of the seam of conical intersection (black line) between the ${}^3B_1/{}^3A_2$ (left panel) and ${}^2A_1/{}^2B_2$ states (right panel). In addition the two PES are represented in the C_{2v} symmetry as lines of iso-energy with a step of 0.5 eV. For the triplet states the green and dashed blue line represent the 3B_1 and 3A_2 states, respectively. Concerning the ionic states, the red line is for the 2A_1 state and the dashed blue for 2B_2 state.

3.3. DIABATIZATION OF THE ADIABATIC STATES COUPLED THROUGH CONICAL INTERSECTION 89

The seam of conical intersections (see Fig. 3.11) has been evaluated thanks to the interpolation of the PES on the ab-initio grid. Its topology is similar than the one of the singlet states, and can be defined as a function of the R_s coordinate. For both set of state, its variation with respect to the bonding angle is similar, with $\phi \sim 100^\circ$ for small values of R_s and smoothly increases to $\sim 120^\circ$ while R_s becomes larger. For the ionic states the seam is almost a linear function of the symmetric coordinates, while seam of CI of the triplet states is curved for $R_s > 1.9 \text{ \AA}$ and the value of ϕ starts to decrease to smaller values. One can notice that in both cases the seam of conical intersections is located at smaller angles than in the case of the singlet states (see Sec. 3.3.1). An important feature can be stressed from Fig. 3.11, noticing that the seam of conical intersections are in both cases located near the minimum of the coupled states, which presage that its impact on the wavepacket dynamics.

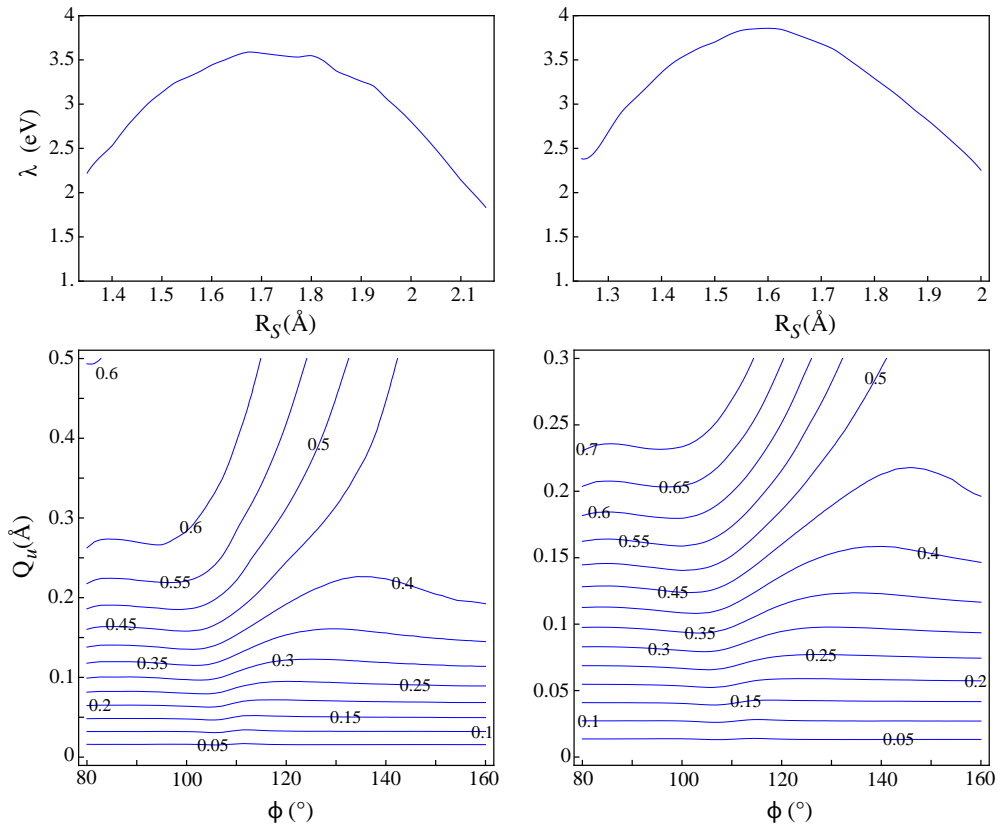


Figure 3.12: We report the value of λ (upper panel) in the case of the triplet states (left) and the ionic states (right). In the lower panel the potential coupling between the diabatic states is given for the triplet (left) and ionic states (right), at fixed value of $R_s = 1.448 \text{ \AA}$.

The coupling constant λ has been evaluated for the ionic and the triplet states and the results are reported on Fig. 3.12. For both set of states the values of λ are smaller than in the case of the singlet states, with roughly ~ 0.5 eV/Å for the ionic states and ~ 1.0 eV/Å for the triplet states. These results will directly affect the coupling between the states, and we expect a stronger role of the conical intersection in the dynamics of the singlet states than for the ionic states and then for the triplet states. Of course the time-dependent evolution of the wavepacket can overcome this statement. On the bottom of the Fig. 3.12 are shown the different coupling terms (W_{12}) for the triplet (left) and ionic (right) states. The coupling is slightly smaller in the case of the triplet states.

3.3.3 Grid for quantum dynamics

The different PES that we will consider in the wavepacket dynamics have been computed on a three dimensional grid as a function of adapted internal coordinates. As introduced in the theoretical part of this manuscript (see Sec. 2.3.1), the dynamics needs also a grid to describe the nuclear wavefunction and a DVR as been used. The PES have to be evaluated at each point of the DVR and the coordinate system has been changed from the internal coordinates system $\{ \phi, R_s, Q_u \}$ to a set of Jacobi coordinates $\{ r_v, r_d, \theta \}$. This consideration arises naturally after the diabaticization of the PES because for the coupled states the adiabatic PES are not smooth functions of the nuclear coordinates and present as well a double minima, which leads to difficulties to accurately interpolate or fit them. On the contrary, the diabatic states are smooth, thus this procedure is more convenient and a better accuracy is usually achieved. To transform and evaluate the PES on the DVR points, two possibilities have been adopted. First we fit the 3D PES with a function to obtain an analytical form in the first set of coordinates and the second option is to use an interpolation of the PES to transform them, which is related to a polynomial fit. The first possibility has been used at the first stage of this work to study the *w**p* dynamics on the singlet states [132]. Let's see the advantage of the method and the issue.

The good point with a fitting procedure is that one can choose physical and smooth functions of the nuclear coordinates and expect that, if required, an extrapolation of the ab-initio grid will be accurate enough. The R_s and Q_u coordinates are combined to give the two SO bonds $R_1 = R_s + Q_u$ and $R_2 = R_s - Q_u$ and a

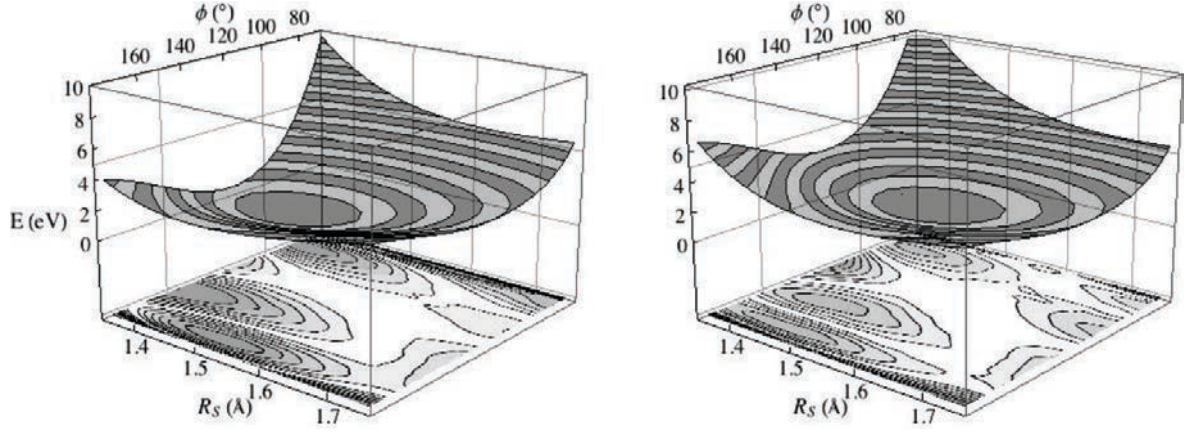


Figure 3.13: Three dimensional plot of PES of the ground state 1^1A_1 from polynomial fitting for $Q_u = 0$ (left panel) and $Q_u = 0.15 \text{ \AA}$ (right panel). The contour plot on the bottom represents the error in eV between the interpolation and the fit. The white shading is for error below 0.01 eV and the error increases by 0.01 eV for each darker zones.

Morse potential is used to describe them:

$$V_{1,2}(R_{1,2}) = \beta^{-1}(1 - \exp(-\beta(R_{1,2}/R_{1,2}^0 - 1))) \quad (3.6)$$

where β and R_i^0 are parameters controlling the width and the bottom of the Morse potential, respectively.

For the bending angle ϕ , a third order polynomial expansion has been used:

$$V_3(\phi) = A_1(\phi - \phi^0) + A_2(\phi - \phi^0)^2 + A_3(\phi - \phi^0)^3 \quad (3.7)$$

where the coefficient A_i and the reference angle ϕ^0 are also parameters, note that we use ϕ in radian for the fit. As the above functions are only dependent of one coordinate, we use a polynomial expansion of them, up to the fourth order:

$$V(R_1, R_2, \phi) = \sum_{a,b,c}^{a+b+c \leq 4} C_{a,b,c} V_1(R_1)^a V_2(R_2)^b V_3(\phi)^c. \quad (3.8)$$

The fit has been carried out with Mathematica software [144] using the least-square method and as it is a non-linear problem, only locally optimized fitting parameters can be obtained. The off diagonal coupling term has also to be fitted and a polynomial function of the internal coordinates is used:

$$W_{12}^{fit} = \sum_{a=0}^{12} \sum_{b=0}^{12} \sum_{c=0}^4 C_{abc} \phi^a R_s^b Q_u^c. \quad (3.9)$$

This polynomial fitting function gives very accurate fit of the off-diagonal potential but no extrapolation can be done. As we showed in the previous section, far away from the seam of conical intersections the diabatic states converge to the adiabatic ones due to the lack of interaction. Then outside our ab-initio grid, the fitted potential W_{12}^{fit} is set to zero. This is required because the polynomial fit often diverges outside the fitted region and would give anomalous strong couplings in region for which it is almost negligible. The fit of the electronic ground state PES is presented in Fig. 3.13 as a function of the symmetric coordinate for two different values of Q_u set to 0 and 0.15 Å. As a contour plot, we also represent the difference (in eV) between the interpolated and the fitted PES. The geometries nearby the equilibrium geometry are the most important part of this state for us, because it is only used to obtain its lowest vibrational nuclear wavefunction.

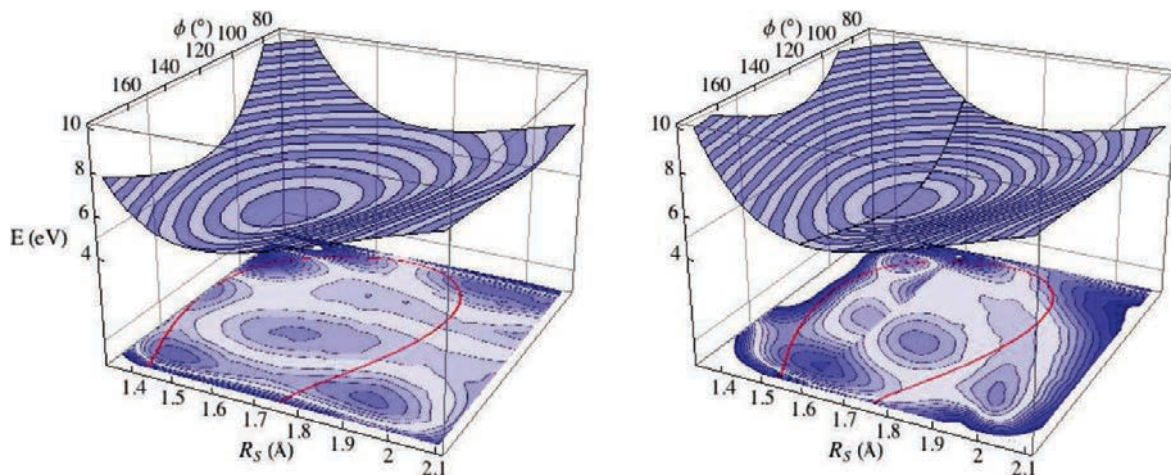


Figure 3.14: Three-dimensional plot of PES of the 1^1B_1 excited state from polynomial fitting for $Q_u = 0$ (left panel) and $Q_u = 0.15$ Å (right panel). The contour plot on the bottom represents the error in eV between the interpolation and the fit. The lightest blue shading is for error below 0.01 eV and the error increases by 0.01 eV for each darker blue zones. The red contour line is an iso-line for energy at 6 eV, which is slightly higher than the Franck-Condon energy and the upper boundary of the photo absorption spectrum under interest (< 5.5 eV). The error does not exceed 0.05 eV, except for large angle ϕ but remains below 0.1 eV. The black line on the PES indicates the junction between the two fits (see text) for small and large R_s .

For this region, an accuracy below 0.01 eV is obtained for the fitted PES and this for the total range of Q_u . In general, the largest part of the PES remains below an error of 0.05 eV. The accuracy becomes worst for the grid boundary of ϕ where the maximum of error is 0.1 eV, but this part of the PES is not used in the dynamics. The fit of the excited potential is not that straightforward because we expect a dynamic of the wavepacket, which will explore a larger set of geometry than in the case of the GS. Then the accuracy

should be, as far as possible, kept high for a larger region. According to the experimental spectrum resulting from an excitation to these states, it results that energy below 5.5 eV are involved in the dynamics and the accuracy will be focused on this region of the PES. The fit of the full PES does not fulfilled our requirements, especially along the R_s coordinate and we decide to split the PES in two parts for $R_s < 1.6 \text{ \AA}$ and $R_s > 1.575 \text{ \AA}$. The overlap between the two regions is done on purpose to avoid an abrupt connection between them.

The results of the fitted 1B_1 PES are reported in Fig 3.14 for $Q_u = 0$ (left panel) and $Q_u = 0.15 \text{ \AA}$ (right). On the same figure, the red contour line indicates energies below 6.0 eV of the ab-initio potential, which may be involved in the dynamics. For this region the fit in the C_{2v} geometry as an error below 0.05 eV, except at the grid edges of the ϕ coordinate, which is satisfactory. As mentioned, for the C_s geometries such accuracy has been obtained thanks to two different fitting functions, for which, the connection is indicated by a black line on the PES. In this way a similar convergence is obtained for the region below 6.0 eV. Note that the energy at the junction between the two functions does not exceed 0.04 eV and usually stays below 0.02 eV, which is reasonable.

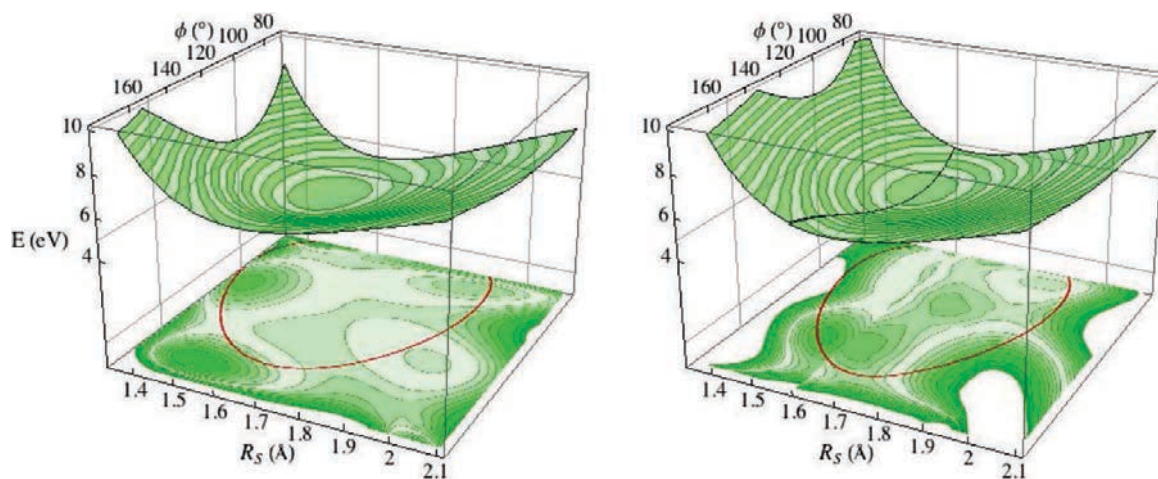


Figure 3.15: Three-dimensional plot of PES of the 1A_2 excited state from polynomial fitting for $Q_u = 0$ (left panel) and $Q_u = 0.15 \text{ \AA}$ (right panel). See legend Fig. 3.14

The same results are presented also for the 1A_2 state in Fig. 3.15. The general accuracy is similar to the one obtained for the 1B_1 state, but we can notice that for energies higher than 6.0 eV, either for small or

large values of R_s the error exceeds 0.1 eV. The branching between the two fitted parts of the PES exhibits an energy difference below 0.02 eV. An important point to notice is that the fit of the 1A_2 state describes correctly the PES nearby its energy minimum but also the PES in the vicinity of the 1B_1 minimum. The same holds for the fit of the 1B_1 PES. As both states are coupled through the coupling W_{12} , an incorrect description would have lead to erroneous adiabatic surfaces.

Let's discuss now the case of the diabatic states obtained with $\lambda_{C_{2v}}$, for which we already pointed out the problem of the imaginary values of λ and the discontinuity in the PES. This feature is clearly problematic and particularly to fit the PES, because the accuracy of the fitting function is determined thanks to the relative energy difference between the ab-initio points and the analytical function. Then, in this case, an inherent error comes from the "cusp" of the diabatic states that makes the convergence not possible. Furthermore an intrinsic error (~ 0.2 eV) is introduced in a non-controllable way because smooth analytical functions are used. The following strategy has been used to obtain the most accurate fitting function. First we noticed that irregularities in the PES arise principally at high energies (~ 5.5 eV) and the lower energy part of the PES is mandatory, so the ab-initio point at energy higher than 5.75 eV have been discarded to enforce convergence of the smooth part of the PES. Moreover only values of $R_s < 1.925$ Å and $\phi < 165^\circ$ have been used. These restrictions of the grid have been obtained thanks to the results of wp dynamics with the other diabatization scheme (see Sec. 4.2.1). Finally the diabatic states are transformed back into the adiabatic basis to check the accuracy as rigorous as possible.

We present the results for both fitted diabatic states in Fig. 3.16. We can see that the fitting procedure chosen manages to obtain a global accuracy below ~ 0.1 eV, with a maximum error of 0.2 eV in the higher energy regions of the PES represented by the red line. This holds for various values of Q_u but the global accuracy decreases when Q_u increases. These results are reasonable according to the PES to be fitted. The fitting process avoids the irregularity of the diabatization scheme providing smooth diabatic PES. From the fitted diabatic PES we transform them back to the adiabatic basis, and we found that the error does not exceed 0.2 eV in the energy region under interest. Nevertheless this difference of accuracy with the other diabatization scheme is not negligible and can lead to different results in the dynamic.

The difference of accuracy between the two diabatization scheme is not negligible and clearly the deter-

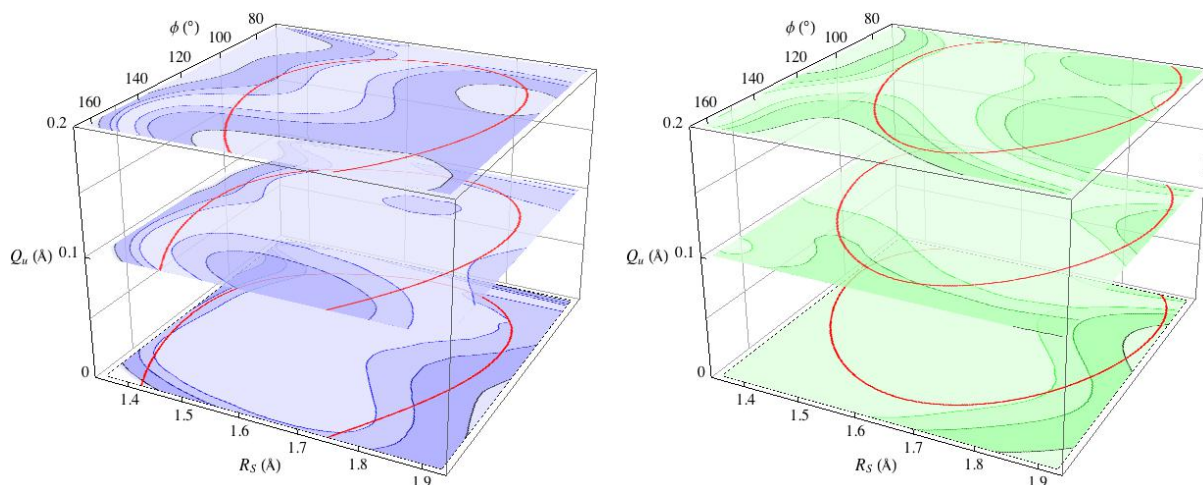


Figure 3.16: Contour line of the error of the fitted PES ($|W_{ab-initio} - W_{fitted}|$) for the 1^1B_1 (blue) 1^1A_2 (green) states for diabaticization performed with $\lambda_{C_{2v}}$ as a function of ϕ and R_s for Q_u fixed at 0, 0.1 and 0.2 Å. The error increased with darker zone, 0.05 (light), 0.1 (intermediate) and < 0.15 eV (dark).

mination of λ along the seam of conical intersection is a better choice in our case, providing convenient PES to be fitted. Actually, the fitting process always introduces an error in comparison to the bare ab-initio data, but we expect a correct extrapolation of the PES in comparison to an interpolation procedure. It turns out that the extrapolation is not good as well (as discussed later) and introduces a non-negligible error in the dynamics of the *w.p.* Then we decided to compute large ab-initio grid and to use the interpolation of the PES to change the coordinate system and evaluate the PES on the DVR grid. In the case of a three-dimensional system the time to compute extra data or obtain a correct fit is similar but the result are clearly superior with the former.

3.4 Spin-orbit Coupling and Transition dipole moment

3.4.1 Spin-orbit Coupling

In the theoretical part (Sec. 2.4.2), we already introduced the way of computing the SOC with the Molpro package [107] by the use of the perturbation theory and the Breit-Pauli operator. In our study, the SOC between the three singlet and the three triplet states have been considered, as they are in close vicinity. Previous study rarely considered the geometry dependency of the SOC and/or considered an average potential of the non-degenerate components of the triplet states. As the goal is to study the photodynamics of the

molecule and to be as accurate as possible, we computed the SOC elements for ~ 2000 different geometries.

The full potential matrix of our system reads then,

$$\mathbf{V}_{\text{tot}}^{\text{soc}} = \begin{pmatrix} V_{1A_1} & 0 & 0 & C_1 & 0 & -C_1 & R_1 & R_2 & C_2 & C_3 & R_1 & R_2 \\ 0 & V_{1B_1} & 0 & R_3 & C_4 & R_3 & -C_5 & C_6 & 0 & 0 & C_5 & -C_6 \\ 0 & 0 & V_{1A_2} & R_4 & C_7 & R_4 & -C_8 & -C_9 & 0 & 0 & C_8 & C_9 \\ -C_1 & R_3 & R_4 & V_{3B_2^+} & 0 & 0 & -C_{10} & -C_{11} & R_5 & -R_6 & 0 & 0 \\ 0 & -C_4 & -C_7 & 0 & V_{3B_2^0} & 0 & -R_5 & R_6 & 0 & 0 & R_5 & -R_6 \\ C_1 & R_3 & R_4 & 0 & 0 & V_{3B_2^-} & 0 & 0 & -R_5 & R_6 & C_{10} & C_{11} \\ R_1 & C_5 & C_8 & C_{10} & -R_5 & 0 & V_{3B_1^+} & 0 & 0 & -C_{12} & 0 & 0 \\ R_2 & -C_6 & C_9 & C_{11} & R_6 & 0 & 0 & V_{3A_2^+} & C_{12} & 0 & 0 & 0 \\ -C_2 & 0 & 0 & R_5 & 0 & -R_5 & 0 & -C_{12} & V_{3B_1^0} & 0 & 0 & -C_{12} \\ -C_3 & 0 & 0 & -R_6 & 0 & R_6 & C_{12} & 0 & 0 & V_{3A_2^0} & C_{12} & 0 \\ R_1 & -C_5 & -C_8 & 0 & R_5 & -C_{10} & 0 & 0 & 0 & -C_{12} & V_{3B_1^-} & 0 \\ R_2 & C_6 & -C_9 & 0 & -R_6 & -C_{11} & 0 & 0 & C_{12} & 0 & 0 & V_{3A_2^-} \end{pmatrix} \quad (3.10)$$

with each off-diagonal elements being the SOC matrix element coupling two states and the diagonal elements are the adiabatic PES presented previously (see Sec. 3.2.2 and 3.2.3). The SOC elements can be either real or imaginary and are labelled by R_i and C_i , respectively. The label also indicates which SOC element are identical between different states and in this case the relative sign is indicated. To be general, the discussion will consider the C_s symmetry (C_{2v} being a particular case of it), but to keep the discussion as clear as possible the electronic states are labelled in the C_{2v} symmetry. Due to the introduction of the SOC, the degeneracy of the different spin components ($m_S = 0, \pm 1$) is lifted and they have to be considered separately, resulting of 12 coupled states. Using the symmetry adapted spin basis functions, which results from the linear and anti-linear combinations of the spin basis function with $m_S = \pm 1$,

$$|S, M_S\rangle_+ = \frac{1}{\sqrt{2}}(|S, M_S\rangle + |S, -M_S\rangle) \quad (3.11)$$

$$|S, M_S\rangle_- = \frac{1}{\sqrt{2}}(|S, M_S\rangle - |S, -M_S\rangle), \quad (3.12)$$

it is possible to rewrite the potential matrix in a block diagonal form with one block of A' symmetry,

$$\mathbf{V}_{A'}^{\text{soc}} = \begin{pmatrix} V_{1A_1} & \sqrt{2}C_1 & \sqrt{2}R_1 & \sqrt{2}R_2 & C_2 & C_3 \\ -\sqrt{2}C_1 & V_{3B_2^-} & -C_{10} & -C_{11} & \sqrt{2}R_5 & \sqrt{2}R_6 \\ \sqrt{2}R_1 & C_{10} & V_{3B_1^+} & 0 & 0 & \sqrt{2}C_{12} \\ \sqrt{2}R_2 & C_{11} & 0 & V_{3A_2^+} & -\sqrt{2}C_{12} & 0 \\ -C_2 & \sqrt{2}R_5 & 0 & \sqrt{2}C_{12} & V_{3B_1^0} & 0 \\ -C_3 & \sqrt{2}R_6 & -\sqrt{2}C_{12} & 0 & 0 & V_{3A_2^0} \end{pmatrix} \quad (3.13)$$

which contains the electronic ground state, the triplet 1^3B_1 and 1^3A_2 with two different spin components (0 and +) as well as the triplet 1^3B_2 state with spin component (-). The other states, i.e. $\{1^1B_1, 1^1A_2, 1^3B_2(+), 1^3B_2(0), 1^3B_1(-), 1^3A_2(-)\}$ belong to the A'' symmetry block,

$$\mathbf{V}_{A''}^{\text{soc}} = \begin{pmatrix} V_{1B_1} & 0 & \sqrt{2}R_3 & -C_4 & \sqrt{2}C_5 & \sqrt{2}C_6 \\ 0 & V_{1A_2} & \sqrt{2}R_4 & -C_7 & \sqrt{2}C_8 & \sqrt{2}C_9 \\ \sqrt{2}R_3 & \sqrt{2}R_4 & V_{3B_2^+} & 0 & C_{10} & C_{11} \\ C_4 & C_7 & 0 & V_{3B_2^0} & \sqrt{2}R_5 & \sqrt{2}R_6 \\ -\sqrt{2}C_5 & -\sqrt{2}C_8 & -C_{10} & \sqrt{2}R_5 & V_{3B_1^-} & 0 \\ -\sqrt{2}C_6 & -\sqrt{2}C_9 & -C_{11} & \sqrt{2}R_6 & 0 & V_{3A_2^-} \end{pmatrix}. \quad (3.14)$$

The usual next step is to diagonalise the full potential energy matrix to obtain the new electronic states, which are mixed between singlet and triplet states. Here the diagonalization is not performed for two reasons. On the one hand, it facilitates the interpretation of the results by keeping unmixed states of different spin. On the other hand, it also facilitates the diabaticization of the states. Because of the different conical intersections taking place in the manifold of states, we need to transform the full potential matrix into the diabatic electronic basis. Making use of Eq. (2.50) from Sec. 2.2.5, we can build the adiabatic-to-diabatic transformation matrix \mathbf{U} for each manifold of states. Starting with the symmetry A' , let's call \mathbf{U}_{T_r} the transformation matrix which diabaticizes the triplet 3A_2 and 3B_1 states obtained in the previous section.

Then the full transformation matrix, which diabatizes the A' manifold can be written as

$$\mathbf{U}_{A'} = \begin{pmatrix} \mathbf{1}_2 & \mathbf{0} & \mathbf{0} \\ \mathbf{0} & \mathbf{U}_{\text{Tr}} & \mathbf{0} \\ \mathbf{0} & \mathbf{0} & \mathbf{U}_{\text{Tr}} \end{pmatrix}, \quad (3.15)$$

using the notation introduced in Sec. 2.2.5 and $\mathbf{1}_2$ the two-by-two identity matrix. The adiabatic states V_{1A_1} and $V_{3B_2^-}$ are not coupled vibronically with any other states, and we collect them with their SOC into $\mathbf{P}_{\text{no CI}}$,

$$\mathbf{P}_{\text{no CI}} = \begin{pmatrix} V_{1A_1} & \sqrt{2}C_1 \\ -\sqrt{2}C_1 & V_{3B_2^-} \end{pmatrix}. \quad (3.16)$$

The remaining states are coupled through the symmetry-allowed conical intersection with respect to their spin components and they are collected into \mathbf{V}_{Tr}^+ and \mathbf{V}_{Tr}^0 ,

$$\mathbf{V}_{\text{Tr}}^{+,0} = \begin{pmatrix} V_{3B_1^{+,0}} & 0 \\ 0 & V_{3A_2^{+,0}} \end{pmatrix}. \quad (3.17)$$

The SOC between the different block are then denoted by $\mathbf{I}_{\text{P/T}^{+,0}}$ between the blocks $\mathbf{P}_{\text{no CI}}$ and $\mathbf{V}_{\text{Tr}}^{+,0}$, $\mathbf{I}_{\text{T}^+/T^0}$ between \mathbf{V}_{Tr}^+ and \mathbf{V}_{Tr}^0 . The A' block, Eq. (3.13), reads now:

$$\mathbf{V}_{A'}^{\text{soc}} = \begin{pmatrix} \mathbf{P}_{\text{no CI}} & \mathbf{I}_{\text{P/T}^+} & \mathbf{I}_{\text{P/T}^0} \\ \mathbf{I}_{\text{T}^+/P} & \mathbf{V}_{\text{Tr}}^+ & \mathbf{I}_{\text{T}^+/T^0} \\ \mathbf{I}_{\text{T}^0/P} & \mathbf{I}_{\text{T}^0/T^+} & \mathbf{V}_{\text{Tr}}^0 \end{pmatrix}. \quad (3.18)$$

The potential matrix is then transformed into the diabatic basis as,

$$\mathbf{U}_{A'} \cdot \mathbf{V}_{A'}^{\text{soc}} \cdot \mathbf{U}_{A'}^\dagger = \begin{pmatrix} \mathbf{P}_{\text{no CI}} & \mathbf{I}_{\text{P/T}^+} \cdot \mathbf{U}_{\text{Tr}} & \mathbf{I}_{\text{P/T}^0} \cdot \mathbf{U}_{\text{Tr}} \\ \mathbf{U}_{\text{Tr}}^\dagger \cdot \mathbf{I}_{\text{T}^+/P} & \mathbf{U}_{\text{Tr}}^\dagger \cdot \mathbf{V}_{\text{Tr}}^+ \cdot \mathbf{U}_{\text{Tr}} & \mathbf{U}_{\text{Tr}}^\dagger \cdot \mathbf{I}_{\text{T}^+/T^0} \cdot \mathbf{U}_{\text{Tr}} \\ \mathbf{U}_{\text{Tr}}^\dagger \cdot \mathbf{I}_{\text{T}^0/P} & \mathbf{U}_{\text{Tr}}^\dagger \cdot \mathbf{I}_{\text{T}^0/T^+} \cdot \mathbf{U}_{\text{Tr}} & \mathbf{U}_{\text{Tr}}^\dagger \cdot \mathbf{V}_{\text{Tr}}^0 \cdot \mathbf{U}_{\text{Tr}} \end{pmatrix}. \quad (3.19)$$

A similar scheme can be used to diabatize the block of A'' symmetry if we consider the full transformation matrix defined by

$$\mathbf{U}_{A''} = \begin{pmatrix} \mathbf{U}_{\text{Si}} & \mathbf{0} & \mathbf{0} \\ \mathbf{0} & \mathbf{1}_2 & \mathbf{0} \\ \mathbf{0} & \mathbf{0} & \mathbf{U}_{\text{Tr}} \end{pmatrix}, \quad (3.20)$$

where we introduced the transformation matrix of the singlet coupled states 1A_2 and 1B_1 as \mathbf{U}_{Si} . After the diabatization of the potential matrix, the potential part of the Hamiltonian can be built on the DVR grid using an interpolation to define it at the different DVR points. One of the issues is that the sign of the electronic wavefunction of each state is arbitrarily defined and can change from one geometry to another. An example of this issue is presented in Fig. 3.17, where the surface represents the interpolation of the absolute value of the spin-orbit coupling and the red and green points are the ab-initio data with positive and negative values, respectively.

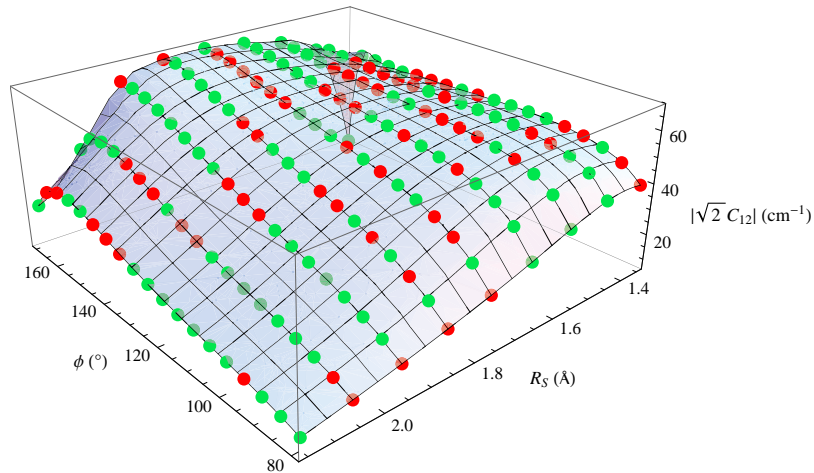


Figure 3.17: Modulus of the SOC between the ${}^3B_1^+$ and ${}^3A_2^0$ states as a function of R_s and ϕ for fixed value of $Q_u = 0.05 \text{ \AA}$. The surface presents a smooth evolution as a function of the coordinates and the dots represent the ab-initio data points. The sign of the SOC changes arbitrarily from one geometry to another, alternating between positive (red) and negative (green) values.

The variation of the sign between to different geometries does not affect the eigenvalues of the system, but the ab-initio data must be interpolated to evaluate the PES at the DVR points used for the dynamics. The fact that the sign changes is only a problem because we do not have ab-initio data at each point of the DVR used for the forth-coming propagation. Note that if the mixed singlet/triplet states are used (i.e. the

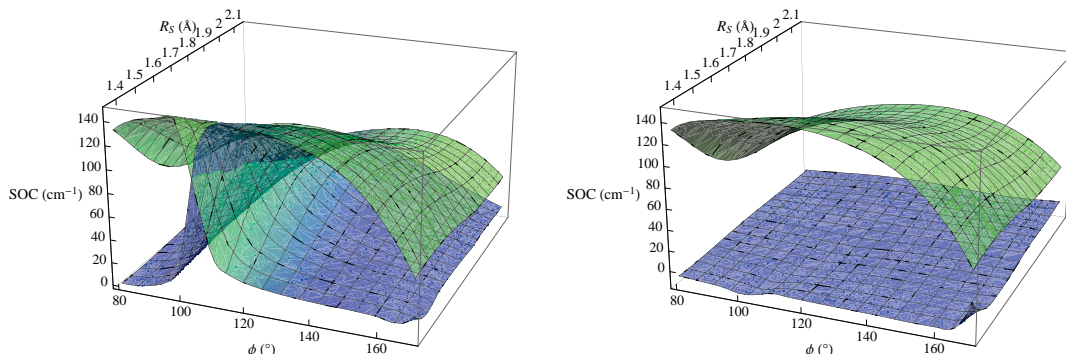


Figure 3.18: Spin-orbit coupling with respect to the bending angle and symmetric stretching coordinates for $Q_u = 0.05$ Å. Left panel is the adiabatic SOC between the electronic ground state and the coupled $1^3B_1(0)/1^3A_2(0)$ triplet states. Right panel is the result of the diabatization for the SOC between the $1^1A_1/1^3B_1(0)$ states (green) and $1^1A_1/1^3A_2(0)$ states (blue).

potential matrix is diagonalized) the problem would have not appeared and then is inherent to the method used here. The sign flipping can arise between two geometries for any of the electronic wavefunction, but as the SOC is computed using the perturbation theory, the sign of each spin component of one triplet state is the same, reducing the possibility distributed over six states. The result of changing the sign of one electronic wavefunction in the potential matrix is simply obtained by multiplying on the left and right the potential matrix by a diagonal matrix with elements equal to one except for the desired state for which it is -1 . Considering all the possible permutation over all the number of states leads to

$$\sum_{i=0}^{n-1} \binom{n}{i} \quad (3.21)$$

where n is the number of states. In our specific case, it gives 72 different transformations that must be applied at the different geometry. Starting from one geometry as a reference to have the relative sign of the different SOC elements, the transformations are applied to minimise the variation of the sum of the SOC elements. It ensures that the larger SOC elements do not experience anymore sign flipping. Concerning the smaller SOC elements (less than 10 cm^{-1}), the method is not optimal but the error in the interpolation and evaluation over the DVR grids will be small. Then to avoid to store the transformed potential over the ~ 2000 geometries the diabatization step is performed directly for each geometry after optimization of it sign. It is useless to present all the 18 SOC elements and the result of the diabatization, so we propose to

study one specific case of each symmetry block, i.e. A' and A'' .

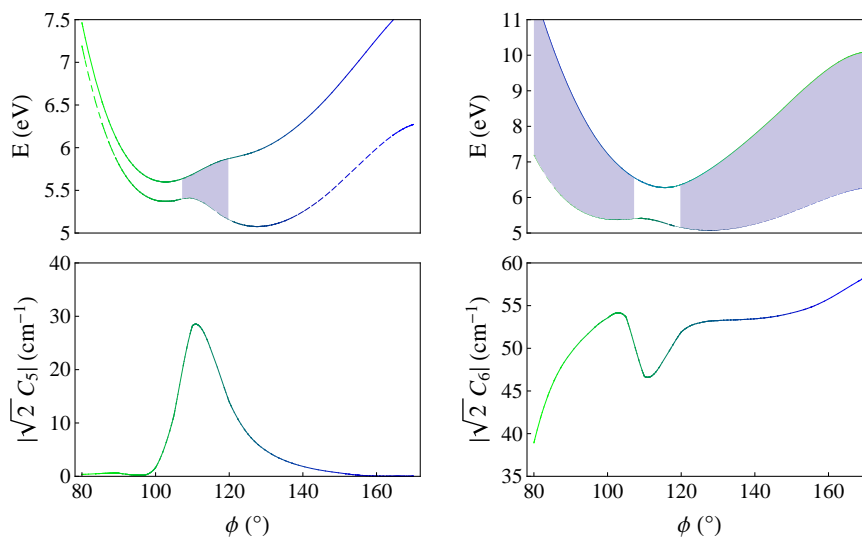


Figure 3.19: Adiabatic SOC between adiabatic states when a conical intersection occurs in the triplet and singlet manifold. The left column presents results for $1^1 A''$ (full) and $1^3 A''$ (dashed) states, on top the two lowest adiabatic states are presented with the colour code changing from green (A_2 character) to blue (B_1 character) along the bending angle ϕ the dashed area indicate when both states have different characters, which occurs in-between the two CI. For these geometry the SOC is expected to be non-vanishing as presented on the bottom. The right column is similar for $2^1 A''$ (full) and $1^3 A''$ (dashed) states. Note that $R_s = 1.448 \text{ \AA}$ is fixed at GS equilibrium geometry and $Q_u = 0.05 \text{ \AA}$.

First let's remind that all the conical intersections are symmetry allowed. Then in the C_{2v} subspace no diabatization is required because the PES cross each other and the electronic character remains for all nuclear geometries of this subspace and then only the C_s subspace has to be carefully studied. First let consider the case where the SOC matrix elements are determined between two states with a conical intersection ($1^3 B_1(0)/1^3 A_2(0)$) and a third one ($1^1 A_1$). With respect to the increasing or decreasing bond angle the electronic character of the adiabatic states changes and the influence on the SOC appears as displayed in Fig. 3.18. For values of ϕ for which the adiabatic states are associated to a A_2 symmetry, the SOC is rather small, as shown in blue, and an opposite behaviour is obtained for the B_1 symmetry in green. Applying the adiabatic-to-diabatic transformation, the electronic character is preserved, providing a smooth and large SOC between the GS and the diabatic $1^3 B_1(0)$ state (green in Fig. 3.18, left panel). A vanishing coupling is obtained for the diabatic $1^3 A_2(0)$ state (blue), as expected from symmetry consideration.

We also present a more complicated case when the SOC are evaluated between singlet and triplet states coupled through a conical intersection. The results are presented in Fig. 3.19 for two different SOC elements. The behaviour of the SOC according to the bending angle shows a particularly interesting dependency. In one case the SOC is almost null for all the geometries, except for few angles between 105° and 115° . In the second case, the opposite appears with large values of the SOC except for the angles discussed before, for which smaller values are obtained. These variations of the SOC are simply explained by looking at the different CI between the singlet and triplet states. The CI between the singlet states occurs at 115° , while the one between the triplet states takes place at 105° . It results that when we consider the lowest singlet and triplet adiabatic states (first case), for small angles ϕ , the SOC is computed between states of the "same" symmetry A_2 and is weak (forbidden in C_{2v} subspace). After the CI between the singlet states, the SOC is evaluated between states of A_2/B_1 symmetry and is large. Then, after the CI between the triplet states the SOC is once again computed between states of "same" symmetry (B_1) and becomes weak again (see Fig. 3.19). The opposite scheme appears for the SOC between the lowest adiabatic singlet (triplet) and higher adiabatic triplet (singlet) states (second case). Applying the diabaticization scheme introduced above,

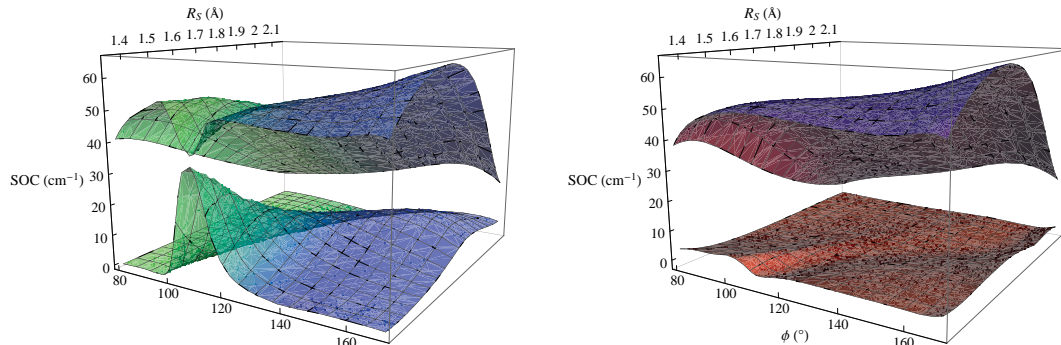


Figure 3.20: Spin-orbit coupling with respect to the bending angle and symmetric stretching coordinates for $Q_u = 0.05$ Å. Left panel is the adiabatic SOC introduced in Fig. 3.19. Right panel is the result of the diabaticization for the SOC between the ${}^1A_2/{}^3B_1^-$ states (purple) and ${}^1B_1/{}^3B_1^-$ states (red).

we obtained the SOC matrix elements between the diabatic states, which preserve the electronic character from one side of the conical intersection to the other. Then a smooth dependency according to the bending angle is obtained, as presented in Fig. 3.20. The SOC between the singlet and triplet states of the same symmetry (B_1) depicted by the red surface is weak, while the SOC between the singlet and triplet states of different symmetries (1A_2 and ${}^3B_1^-$) is smooth and large. In the same figure, the SOC in the adiabatic basis

is showed and for the higher surface the green part corresponds to the SOC between 1B_1 and ${}^3A_2^-$, while the blue part of the SOC, after the CI corresponds to the one between 1A_2 and ${}^3B_1^-$.

3.4.2 Transition Dipole Moment

The transition dipole moment (TDM) is needed to describe the interaction between the electrons of the molecule and an electric field, which leads to the electronic excitation of the molecule. The latter has been computed using Molpro [107] at MRCI level of theory on the same grid than the SOC, because to be accurate the nuclear coordinates dependency of this latter has also to be considered. The TDM associated with all possible transitions between the manifold of states have been computed according to the different polarisation of the electric field in the Cartesian coordinates system used to describe the molecular coordinates. The presence of the different conical intersections between electronic excited states leads to an abrupt evolution of the TDM depending of the nature of the adiabatic states. Thus it is required to transform it into the diabatic basis. This transformation is straightforward and is handled in the same way than the diabatization of SOC.

Table 3.7: Summary of the non-vanishing element of the dipole operator between the different electronic states.

state	${}^1A_1/1^1A'$	${}^1B_1/1^1A''$	${}^1A_2/2^1A''$	${}^3B_1/1^3A''$	${}^3A_2/2^3A''$	${}^3B_2/1^3A'$
${}^1A_1/1^1A'$	z/y,z	x/x	-/x	-/-	-/-	-/-
${}^1B_1/1^1A''$	x/x	z/y,z	y/y,z	-/-	-/-	-/-
${}^1A_2/2^1A''$	-/x	y/y,z	z/y,z	-/-	-/-	-/-
${}^3B_1/1^3A''$	-/-	-/-	-/-	z/y,z	y/y,z	0/x
${}^3A_2/2^3A''$	-/-	-/-	-/-	y/y,z	z/y,z	x/x
${}^3B_2/1^3A'$	-/-	-/-	-/-	0/x	x/x	z/y,z

The transition between states of different spin multiplicities are forbidden when the SOC are not taken into account but it relaxes when there are included in the Hamiltonian. In our approach the electronic GS stays purely singlet but the full wavefunction, i.e. the electronic times vibrational wavefunctions (or vibronic) will also being partially of triplet character. This will appear by a small fraction of the vibrational wavefunction partially delocalized on the triplet states and then the full wavefunction of the vibrational lowest level reads,

$$\Psi_0(\mathbf{R}, \mathbf{r}) = \sum_{\mathbf{s} \in \mathbf{A}'} \mathbf{a}_{\mathbf{s}} \chi^{\mathbf{s}}(\mathbf{R}) \phi^{\mathbf{s}}(\mathbf{r}; \mathbf{R}). \quad (3.22)$$

This formulation of the vibrational ground state will be discussed in more details in the next part of this manuscript, but due to this formulation different excitations from the perturbed GS to the triplet states can take place. We reported in Tab. 3.7 the different transitions allowed by symmetry (C_{2v} and C_s) according to the different polarisation of the electric field.

An interesting point appears, as the GS total wavefunction lies into A' symmetry, the polarisation of the electric field in the molecular plan leads to transition in the manifold of A' states either with y - or z -direction. Concerning the x -polarized exciting light, it will lead to excitation from the A' manifold to the A'' manifold of states. To study these different transitions, the TDM have been computed and as previously diabatized when a conical intersection appears between two states.

3.4.3 Recombination matrix element in the SFA approximation

Using the Molpro package [107], we used the configuration interaction vector of the different electronic states in order to reconstruct the electronic wavefunctions. Thus the Dyson orbitals for the relevant ionisation channels are constructed, and subsequently the SFA recombination matrix elements. These latter are required to study the HHG process in SO_2 . The diabatization of the recombination matrix elements does not present any particular difficulty. We first present the results obtained for the electronic GS, 1^1A_1 , which can ionise to the coupled 1^2A_1 and 1^2B_2 states. The geometry dependency of the transition matrix element, in the adiabatic basis, presents an abrupt variation for $\phi \sim 100^\circ$, where the seam of conical intersections between the $1^2A_1/1^2B_2$ states is located. The diabatization of the electronic states leads to a smooth variation of transition matrix element with respect to the molecular geometry. We obtained almost vanishing recombination matrix elements between the GS and the 1^1B_2 state.

The ionization of the singlet excited states, 1^1B_1 and 1^1A_2 , to the lowest ionic states 1^2A_1 and 1^2B_2 is slightly more complicated, because the two initial and final states are vibronically coupled. Thus it required the evaluation of the Dyson orbitals and the recombination matrix elements for all the possible channels. The results in the adiabatic basis are displayed in Fig. 3.22. A strong variation of the recombination matrix elements is obtained for $100 < \phi < 120^\circ$. These variations take place between the seam of CI between the ionic states and the one between the singlet states. This behaviour is the same than the one obtained for the SOC elements of Fig. 3.20, discussed previously (see Sec. 3.4.1). The results in the diabatic basis for

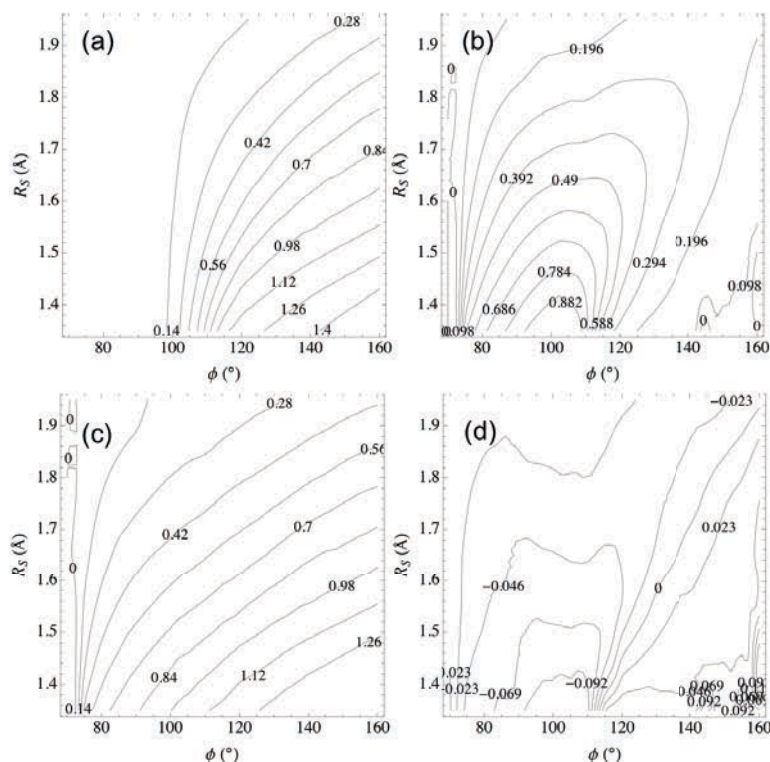


Figure 3.21: Transition matrix element (in a.u.) displayed as a function of the R_s and ϕ coordinates for $Q_u = 0.05$ Å and an electron momentum $p = 0.9$ a.u. (a) Results for the calculation in the adiabatic electronic basis between the 1^1A_1 and $1^2A'$ state. (b) Adiabatic matrix element for ionisation of the 1^1A_1 and $2^2A'$. (c-d) Results after the diabaticization of the conical intersection between the ionic states. (c) Transition from the 1^1A_1 state to the 1^2A_1 ionic state. (d) Transition from the 1^1A_1 state to the 1^2B_2 ionic state.

the ionisation of the 1^1B_1 state to the ionic 1^2A_1 state and for the ionisation the 1^1A_2 state toward the ionic 1^2B_2 state are presented in Fig. 3.23. The remaining transition matrix elements are close to zero after the diabaticization procedure. This two transition matrix elements are very similar concerning their variation with respect to the molecular geometry and also concerning their values. It emanates because for the two ionisation channels the same electron is ionized, i.e. the one from the $3b_1$ orbital. The ionisation of the different triplet states has also to be considered. The triplet states of spatial symmetry B_1 and A_2 can be ionised following the same channels than the ones of the singlet states. The electron of the $3b_1$ orbital is ionized and because of their similarity with the singlet states, we decided to use the results from the singlet states ionisation to describe their recombination matrix elements. Concerning the 1^3B_2 state the lowest ionisation energy is obtained from removing the electron of the $3b_1$ orbital, leading to the 1^2A_2 ionic state. The matrix elements for this channel has been evaluated and it exhibit a similar behaviour in comparison to

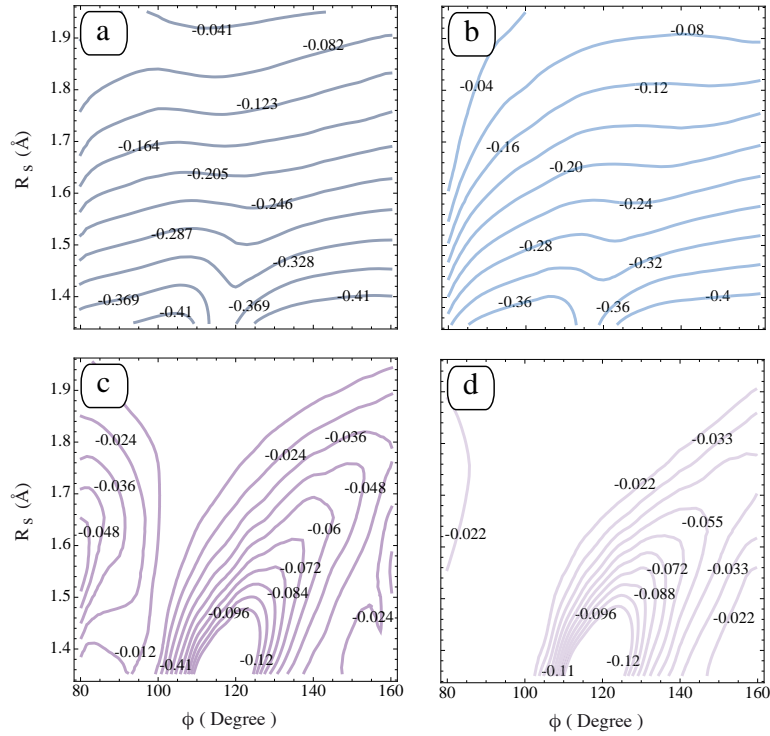


Figure 3.22: Transition matrix element (in a.u.) displayed as a function of the R_s and ϕ coordinates for $Q_u = 0.05$ Å and an electron momentum $p = 0.9$ a.u. (a) between the $1^1A''$ state and $1^2A'$ state, (b) between the $2^1A''$ state and $2^2A'$ state, (c) between the $2^1A''$ state and $1^2A'$ state and (d) between the $1^1A''$ state and $2^2A'$ state.

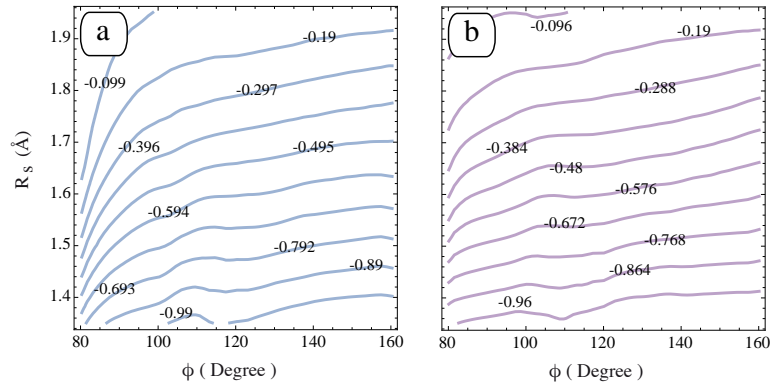


Figure 3.23: Diabatic transition matrix element (in a.u.) displayed as a function of the R_s and ϕ coordinates for $Q_u = 0.05$ Å and an electron momentum $p = 0.9$ a.u. (a) For the ionisation of the 1^1B_1 state to the 1^2A_1 . (b) For the ionisation of the 1^1A_2 state toward the 1^2B_2 state.

the ones obtained for the singlet states but with slightly larger values.

Chapter 4

Weak field spectroscopy: Photoabsorption and photoelectron spectra

4.1 Introduction

Different methods of spectroscopy can be applied to a system to learn about its properties. The following results have been obtained using the theoretical work introduced in Sec. 2 and the results presented in the Sec. 3. We propose the following organisation of the discussion, starting with the dynamics in the singlet excited states and the resulting photoabsorption spectra. Then we introduce the role of the triplet states in this simple system and we discuss the role of the SOC and the "forbidden band" of the experimental spectrum.

4.2 Photoabsorption: the Clements band

4.2.1 Time dependent wavepacket propagation

The photoabsorption spectrum of the sulfur dioxide molecule has been already widely studied experimentally. In the UV regime (3-8 eV) the spectrum can be classified in three distinct parts, with first the so-called "forbidden band" (3.1-3.6 eV) which has been experimentally associated with a transition from the electronic ground state to the lowest triplet state (3B_1). Then the first allowed band, in the energy region of 3.5-5.5 eV, has been studied by Clements and results from a transition to the 1B_1 state, strongly perturbed by the presence of the 1A_2 state. At higher energies, the second allowed band occurs at 5.5-7.5 eV and has been assigned to a transition to the 1B_2 state.

In this part we consider only the first allowed band, which presents an interesting vibrational progression with a well separated vibronic absorption in the low energy range called the "Clements bands" and usually labelled by Latin letters. In the higher energy range a pseudo-continuum of absorption is observed. Using the 3D diabatic states introduced in Sec. 3.3.1, the TDSE can be numerically solved using as initial wavefunction the vibrational GS, on which the transition dipole operator is applied. This is similar to an experiment with a laser pulse of an infinitesimal time duration. Thus results to an infinite frequency spectrum, giving the full absorption spectrum in one calculation. The full wavefunction is expanded on the two electronic singlet states ($1^1B_1/1^1A_2$) and reads,

$$\Psi(t) = \phi_1\chi_1(t) + \phi_2\chi_2(t). \quad (4.1)$$

and evolves under the action of the excited states Hamiltonian, including the diabatic potential of the excited states. \hat{T}_N is the nuclear kinetic energy operator, expressed in Jacobi coordinates Fig. 3.1 as,

$$\hat{T}_N = -\frac{1}{2\mu r_d} \frac{\partial^2}{\partial r_d^2} r_d - \frac{1}{2Mr_v} \frac{\partial^2}{\partial r_v^2} r_v - \frac{1}{2I_\theta \sin \theta} \frac{\partial}{\partial \theta} \sin \theta \frac{\partial}{\partial \theta} \quad (4.2)$$

where the following notations have been introduced:

$$M = \frac{1}{2}m_O \quad (4.3)$$

$$\mu = \frac{2m_S m_O}{m_S + 2m_O} \quad (4.4)$$

$$I_\theta = \left[\frac{1}{Mr_v^2} + \frac{1}{\mu r_d^2} \right]^{-1} \quad (4.5)$$

with m_O and m_S the masses of the oxygen and of the sulphur atom respectively and I_θ the three-body moment of inertia.

As only the transition to the 1B_1 state is symmetry allowed, the initial excited wavepacket lies exclusively on the diabatic 1B_1 state, as depicted by the diabatic electronic population of Fig. 4.1.

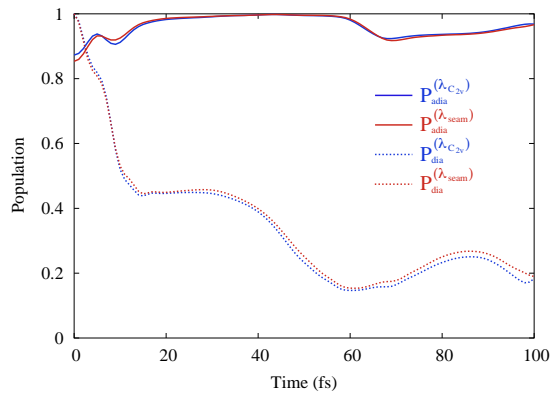


Figure 4.1: Time-dependent diabatic and adiabatic populations of SO_2 . The full lines represent the adiabatic population and the dashed lines depict the diabatic population. The blue lines show the results for $\lambda = \lambda_{C_{2v}}$, determined in the total C_{2v} subspace and the red lines indicate populations for $\lambda = \lambda_{seam}$, evaluated along the seam of CI.

In the theoretical Section 2., we used the system of atomic units, but this system is not specially adapted to discuss the evolution of SO_2 . Principally, the atomic unit of time, $\hat{\tau} \sim 24.18884 \text{ as}$, is not adapted to follow the nuclear dynamics, taking place on the femtosecond time scale. In the following we use the conversion $1 \text{ fs} = 41.3414 \hat{\tau}$. The time-dependent evolution of the wavepacket gives us piece of information on the time evolution of the density probability as a function of the nuclear geometry. While the initial wavepacket is well localised, its time evolution produces a fast delocalisation and after tens of femtosecond it usually

span the energetically allowed part of the PES, render tedious its analysis. In the following we focus on its propagation on the coupled electronic states during the first 65 fs. We report in Figs. 4.2 and 4.3 the reduced density (integrated over θ for Fig. 4.2 and over r_d for Fig. 4.3) of the w_p , superimposed on the contour plot of the corresponding adiabatic potential energy surfaces, i.e. the lower adiabatic surface for the left column and the upper adiabatic state for the right column on both figures. We kept the third coordinate, on which the integration has been performed, at the equilibrium geometry of the GS: $\theta = 90^\circ$ and $r_d = 0.743 \text{ \AA}$. The seam of conical intersections is indicated by the blue dashed line, the FC point by a green circle and the minimum of conical intersection by an open red circle. From the w_p propagation we compute the diabatic and adiabatic populations which are represented in Fig. 4.1. An important quantity is the auto-correlation function, from which we can extract the absorption spectrum. These quantities are presented in Figs. 4.4 and 4.5, respectively.

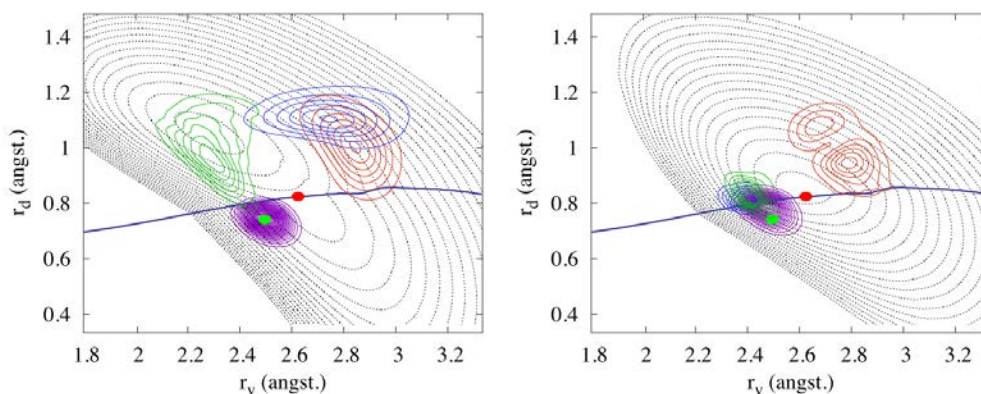


Figure 4.2: Time-dependent reduced adiabatic densities $|\Psi(r_v, r_d)|^2$ integrated over θ and drawn separately for the lower (left) and upper (right) states. The densities are plotted for different times, 0 fs (purple), 20 fs (red), 40 fs (blue) and 65 fs (green). The densities are superimposed on iso-energy contour of the adiabatic PES (black dotted line) in C_{2v} symmetry. The green closed circle indicates the Franck-Condon point and the open red circle the minimum energy CI. The thick blue line indicates the CI seams. For clarity the upper adiabatic density at 20 and 40 fs have been multiply by 10 to be visible.

At time $t = 0$ fs the initial wavepacket is entirely located on the 1^1B_1 diabatic state; this transition is the only dipole-allowed (no transition to the 1^1A_2 state). Then 100% of the population is on this state as seen in Fig. 4.1, however the w_p is already partially localised on the seam of conical intersections, as shown on Fig. 4.2 for $t = 0$, and when projected onto the adiabatic electronic states, 85% of the population belongs to the Lower Adiabatic State (LAS), see Fig. 4.1. Then the w_p starts to move under the action of the excited-state

Hamiltonian away from the Franck-Codon (FC) area, responsible of the fast decay of the autocorrelation function, Fig. 4.4, which reaches 0 during the first 10 fs. During the first 15 fs of the propagation a large amount of population ($\sim 55\%$) is transferred from the 1^1B_1 state to the 1^1A_2 diabatic state. This fast and efficient transfer results from the double minimum shape in the $\{\theta, r_v\}$ coordinates (see Fig. 4.3, left panel) of the LAS where the wp exhibits strong non-adiabatic couplings.

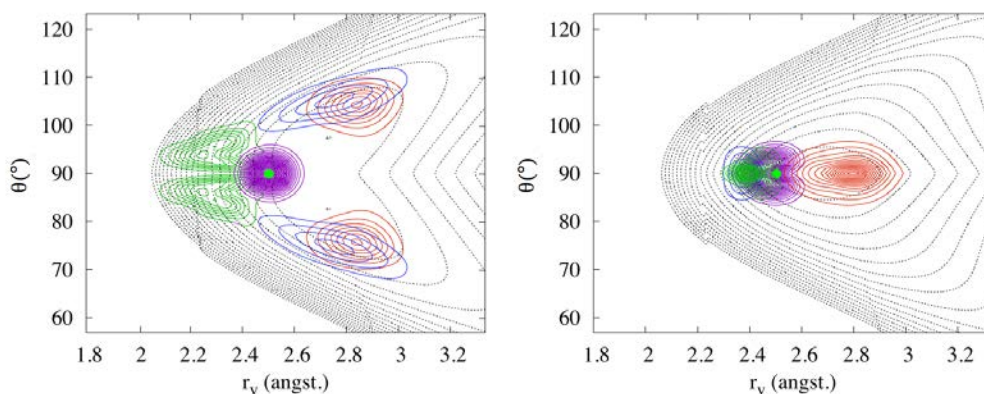


Figure 4.3: Same as Fig. 4.2, for the reduced density $|\Psi(r_v, \theta)|^2$.

The wp splits in two and starts to explore both, minima, exciting thereby the asymmetric stretching mode in Fig. 4.3 (red contour lines). The wp belongs then exclusively in the C_s symmetry, along the seam of conical intersections where the electronic states are close in energy and the non-adiabatic-coupling is strong. At ~ 28 fs the wp reaches its turning point along θ and turns backwards to smaller value of $|\theta - 90^\circ|$, i.e. small values of Q_u (blue contour lines). The two other modes of the molecule are also excited with an important increase of r_v at 20 and 40 fs (red and blue). In the same time, relative increases of the r_d coordinate is observed, see Fig. 4.2. During this nuclear motion, the adiabatic population becomes close to unity (99.8%) on the LAS, while after its fast population transfer, the diabatic population exhibits a plateau from 15 to 35 fs. The radically different behaviours of the adiabatic and diabatic populations can be clarified if we look at the adiabatic-to-diabatic mixing angle. We computed it for a sample of coordinates explored during these times and we found values close to $\pi/4$. For this value the diabatic wavefunctions are an equal mixture of adiabatic states; the same mixing occurs for the densities.

At 40 fs the part of the wp evolving on the Upper Adiabatic State (UAS) is coming back to the FC area, as shown in blue line on Fig. 4.2. In the autocorrelation function this manifests itself by a small revival at

$T_{UAS} = 40$ fs. This revival is small because the population on the UAS is low and also the component on the LAS is moving towards the minimum of the LAS, far from the FC area, see the w_p at the same time of Fig. 4.3 and does not participate in $C(t)$.

A large transfer of diabatic population (30%) occurs again from 40 to 60 fs from the 1^1B_1 state to the 1^1A_2 state: then the population on the 1^1B_1 state is 15%, while the adiabatic population does not change significantly. During these times the w_p is exploring decreasing values of $|\theta - 90^\circ|$ (i.e. decreased of Q_u), after reaching the turning point along this coordinate and then turns back to C_{2v} symmetry, as seen when comparing this two timing (blue and green) in Fig. 4.3. This is accompanied by a decrease of the bond angle. For motion on the LAS this amounts to a population transfer from the 1^1B_1 to the 1^1A_2 state.

At 65 fs the part of the w_p located on the LAS is coming back to the seam of CI near the FC area (green lines in Figs. 4.2-4.3). A part of the w_p on the LAS is transferred to the UAS, as it appears on the left panel. Thereby 8% of the population is transferred between the states as shown in Fig. 4.1. The smaller recurrence at $t \sim 65$ fs comes from a return of the w_p on the LAS along $R_1 + R_2 \sim r_v + r_d$. However, the difference $r_v - r_d$ ($\sim \phi$) clearly deviates from the value at $t = 0$, i. e. the bond angle ϕ is smaller. Then the w_p starts to broaden and the interpretation becomes difficult. We can stress that we obtain another small revival at around 80 fs ($2 T_{UAS}$) and one around 130 fs ($2 T_{LAS}$). Another important revival is observed at 150 fs.

The absorption spectra are computed as the Fourier transform of the autocorrelation function. Since we start with real initial wavefunctions, we compute $C(2t) = \langle \Psi^*(t) | \Psi(t) \rangle$, from the wavefunction at time t [145, 146]. The spectra from the propagation on the coupled diabatic states are given in Fig. 4.5 and compared with the experiment from Ref. [60]. The red (black) line represents the theoretical (experimental) spectrum. The theoretical spectrum has been shifted by 1960 cm^{-1} (0.243 eV) in order to match the first oscillations of the experimental spectrum, with the correction of the Zero-point energy (ZPE). Our calculation reproduces quantitatively the low-energy part of the spectrum, with an accurate matching of the spacing of the absorption peaks and a satisfactory agreement concerning the relative intensities. A recent theoretical study of [69], was able to give a rough agreement with the experimental spectrum. The difference with the experiment was explained by the neglect of the anharmonicity of the potential. In our study we consider the full potential, which seems crucial and this is a very important point of the method used in this work. Also the high-energy part of the spectrum is qualitatively well reproduced: there is no total matching, but still a good overall agreement with the experiment.

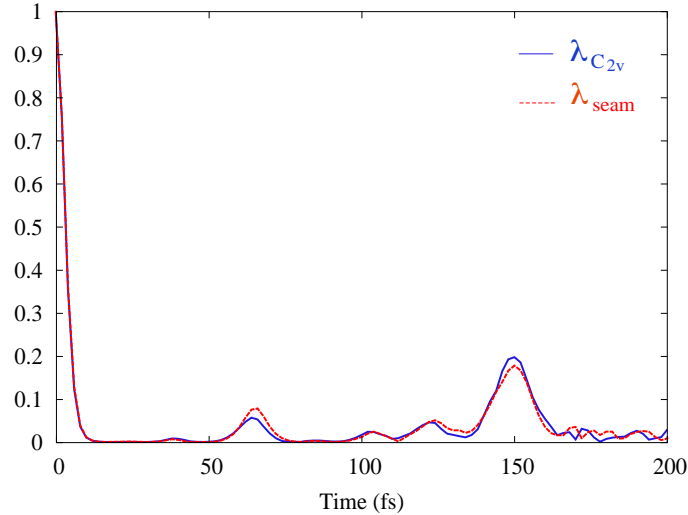


Figure 4.4: Result for the autocorrelation function $\langle \Psi(t=0) | \Psi(t) \rangle$ between 0 and 200 fs. The propagation has been extended to 200 fs in order to obtain a better resolution. The full blue line is for $\lambda = \lambda_{C_{2v}}$ and the red dashed line for $\lambda = \lambda_{seam}$.

We emphasised that we performed our study concerning the diabaticization following two different ways. The bottom panel of Fig. 4.5 compares the simulated spectra with the two methods. In blue we show the result by determining λ in the C_{2v} subspace and in red the one by determining λ along the seam of CI. We shifted both to match the oscillations of the experimental spectrum (1960 cm^{-1} for the red and 1890 cm^{-1} for the blue spectrum). Both methods match perfectly in the low-energy part with each other as well as with experiment. For the high-energy part the spectral structures are very similar with a shift of 70 cm^{-1} . It was shown in Ref. [24] that the method using the computation of λ in the total C_{2v} space contains also a non-singular part of the derivative coupling and may explain the shift obtained between the two methods.

The pronounced - and seemingly quite regular - peak progression at lower energies in Fig. 4.5 raises the question of the underlying vibrational motion involved, which would be better dubbed as vibronic in view of the coupled electronic and vibrational degrees of freedom. From our results we first note that the energy spacing ΔE is $\sim 220 \text{ cm}^{-1}$ corresponds to a time $T = 2\pi\hbar/\Delta E \sim 152 \text{ fs}$, i.e. the time when we see the most prominent recurrence in $C(t)$ in Fig. 4.4. This happens, as seen in Fig. 4.6, when the wp approached again the FC zone, but somewhat closer and from another side than at $t \sim 65 \text{ fs}$. Here, larger values of ϕ (around $\phi \approx 120\text{-}140^\circ$) are explored, where the LAS corresponds to the 1^1B_1 -state. In this sense, the revival

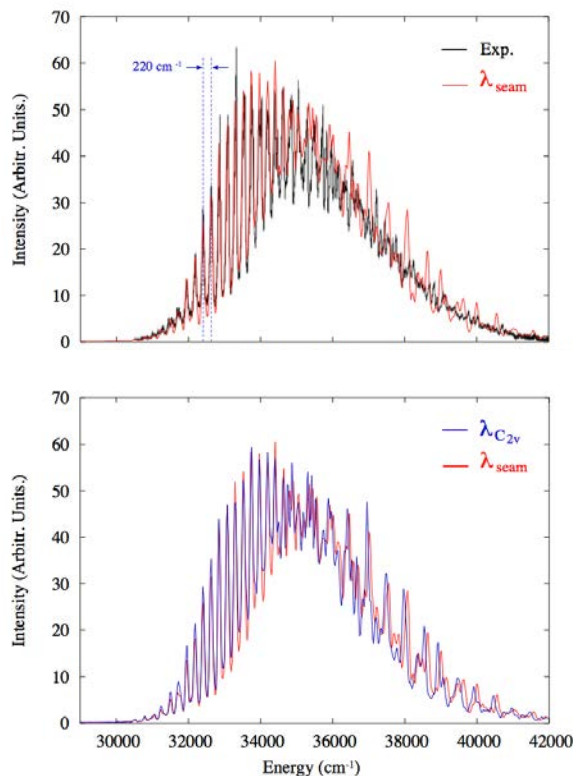


Figure 4.5: Comparison of the theoretical and experimental absorption spectra of SO_2 . (Top) Experimental [60] (black line) and theoretical spectrum with λ_{seam} (red). (Bottom) Spectrum computed with λ_{seam} (red) and with $\lambda_{C_{2v}}$ (blue). Theoretical spectra are obtained from the Fourier transform of the autocorrelation function with a damping time equal to 300 fs. The same extended propagation time is used as in Fig.4.4. The theoretical spectra are shifted to match with the first oscillation of the experimental one (1960 cm^{-1} for the red and 1890 cm^{-1} for the blue with ZPE correction).

time 150 fs could be related to the oscillation period of the bending mode. However, one should keep in mind that the w_p does not evolve on the uncoupled 1^1B_1 -state, but on both states, 1^1B_1 and 1^1A_2 , with the 1^1A_2 state dominating (see Fig. 4.1). This is further confirmed when computing the absorption spectra (Fig. 4.7) from the uncoupled surfaces, which displays a vibrational spacing of $\sim 220 \text{ cm}^{-1}$ for the hypothetical 1^1A_2 state spectrum but not for the (dipole-allowed) 1^1B_1 state. Moreover, the uncoupled 1^1B_1 spectrum shows a similar envelop than the coupled one Fig. 4.5, but a drastically different vibrational features. The comparable envelop is consistent with the fact that the 1^1B_1 state is the dipole-allowed transition. The uncoupled spectrum is probably due to a succession of the symmetric stretching mode for the high intensity features which present a spacing of $\sim 760 \text{ cm}^{-1}$. The systematic pics of low intensity arising $\sim 380 \text{ cm}^{-1}$

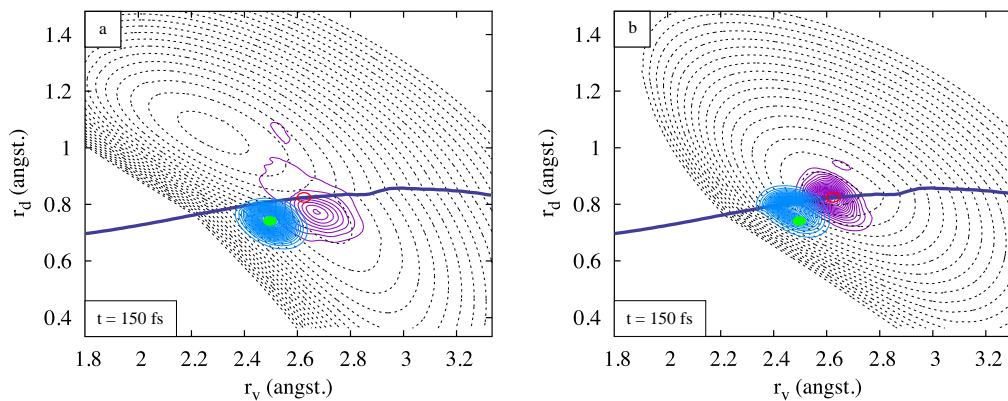


Figure 4.6: As Fig. 4.2 at time $t = 150$ fs when a strong revival appears in $C(t)$. In light blue, the initial wavepacket ($t = 0$ fs) is shown.

after the ones of high intensity results from a transition to the first excitation level of the bending mode, subsequent to the excitation of the symmetric stretching. This assignment is consistent with the equilibrium geometries of the GS and the 1^1B_1 state (Tab. 3.1), which exhibit similar values of ϕ but different ones for the R_s coordinate. As only the first bending mode is excited in the 1^1B_1 state, its energy spacing is higher than the one observed in the Clements bands. But when we compare with the hypothetical uncoupled spectrum of the 1^1A_2 state, a higher density of states is excited, probably lead by the bending mode. This is due to the large difference of $\phi \sim 25^\circ$ between the equilibrium angle of the GS and the 1^1A_2 state. The energetic spacing is smaller (~ 200 cm^{-1}) and more consistent with the one observed in the total spectrum. The Clements bands seem then to arise from the coupling of the few vibrational levels of the 1^1B_1 state with the high density of vibrational level of the 1^1A_2 state and a quantitative study is presented in the next section.

Both theoretical spectra exhibit in the high-energy range a regular absorption pattern, which is not observed experimentally. According to the energetic spacing of these peaks, its results from the revival in the autocorrelation function at $t \sim 65$ fs, when the wavepacket is along the double minimum of the PES. The w_p is moving on part of the PES which has been extrapolated from the analytical fit performed, but gave a potential energy higher than the subsequent ab-initio calculation of this part of the PES. Using the large ab-initio grid and an interpolation of the PES, these features do not appear anymore in the spectrum, see for instance Fig. 4.22 a. The agreement is better but the result remains qualitative for this energy range.

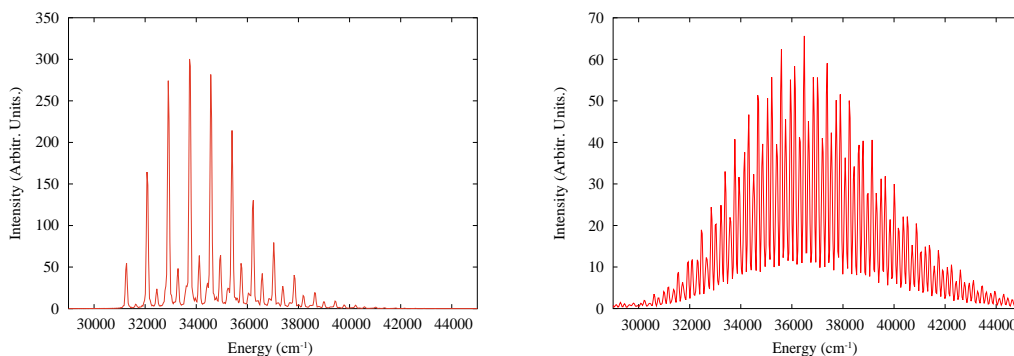


Figure 4.7: Theoretical absorption spectra from propagation on uncoupled diabatic surfaces. (Left panel) Spectrum from propagation on the diabatic 1^1B_1 state. (Right panel) Spectrum from propagation on the diabatic 1^1A_2 state. Spectra are obtained from the Fourier transform of the autocorrelation function with a damping time equal to 300 fs.

Concerning earlier experimental work, low-energy vibrational progressions in this band system have been assigned to the bending mode [135]. Also, it has been known for a long time that the geometrical parameters underlying the rotational structure correspond more to the A_2 than to the B_1 state [147]. Our present findings are consistent with these results but also extend them to higher energies. This holds for the regular "bending mode" progression in Fig. 4.5 as well as for the nuclear motion proceeding more on the A_2 than on the B_1 state, see Fig. 4.1 (thus dominating the rotational constants). In this sense we have achieved, for the first time, an unified and ab-initio based interpretation of the key features underlying both the vibrational and rotational structures of the complex absorption spectrum of SO_2 . This makes the photoabsorption spectrum fascinating, because the excitation occurs from the GS to the 1^1B_1 state but the forbidden transition is the observed one! As the ab-initio spectrum describes quantitatively this energy range, we can go toward a deeper understanding by analysing the different eigenstates of the system. This step can be performed either by direct diagonalisation of the Hamiltonian or making use of the spectral quantisation method.

Latter Xie *et al.* proposed a similar study [133], with slightly larger primitive basis for the ab-initio calculations and using the diabatization scheme implemented in Molpro [107]. Their results concerning the photoabsorption spectrum is similar to our results without any significant improvement.

4.2.2 Quantum attribution of the lowest part of the photoabsorption spectrum

The assignment of the spectrum is obtained by the determination of the nodal planes along the different vibrational modes of the molecule. In the case of SO_2 three vibrational modes are involved (n_1, n_2, n_3) , with

n_1 the symmetric stretching mode (symmetric elongation of both bond lengths), n_2 the bending mode (variation of $\hat{O}\hat{S}\hat{O}$ angle) and n_3 the asymmetric stretching mode. Even so we consider the lowest vibronic states

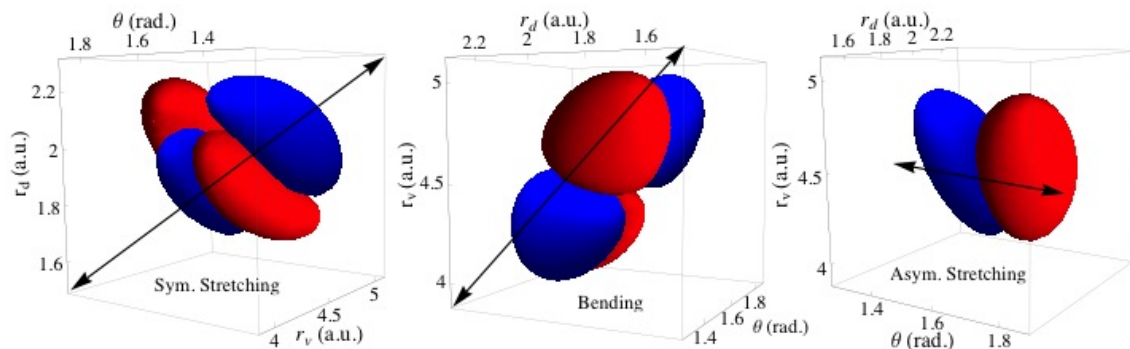


Figure 4.8: Representation of an isosurface ($\Psi_{A_2}=0.002$) of vibrational wavefunction of the electronic 1^1A_2 state as a function of r_v, r_d and θ with its positive (red) and negative (blue) sign. From right to left are presented the third (E_3), fifth (E_5) and tenth (E_{10}) eigenfunctions, to respect the usual assignment order. E_3 corresponds to one nodal plane in the asymmetric stretching mode, E_5 exhibits in addition to the previous nodal plane a new one along the bending mode (increases of r_v and decreases of r_d). E_{10} exhibits the first nodal plane for the symmetric stretching mode (simultaneous increasing of r_v and r_d).

of the excited molecule, the photoabsorption spectrum presents numerous features, which make tedious the attribution. Thus we limited our study to the first 175 eigenvalues and we consider only the eigenstates with a non-negligible intensity ($> 10^{-7}$). As the computations were performed using the Jacobi coordinates, let us first link them to the internal coordinates to facilitate the discussion. The symmetric stretching mode, described by the R_s internal coordinate, matches to a simultaneous increase of both r_v and r_d coordinates (Fig. 4.8, left panel). The bending mode, described by ϕ , corresponds to a simultaneous increase of r_v and decrease of r_d (middle panel). Finally, the asymmetric stretching mode describes by Q_u matches directly the angle θ in the Jacobi coordinates, as presented in Fig. 4.8 (right panel). It is preferable, as presented in Fig. 4.8, to study the vibrational wavefunctions using iso-surfaces directly represented with respect to the three coordinates. This choice avoided the issue of the partial integration over one degree of freedom, which washed out partially the nodal plane of the eigenstates.

The intensity of the different excited vibrational states is directly linked to the Franck-Condon factors as only non-vanishing overlap between the vibrational GS (without any node) and the vibrational excited states will play a role in the spectrum. In our case, the electronic state plays also a preponderant role, because

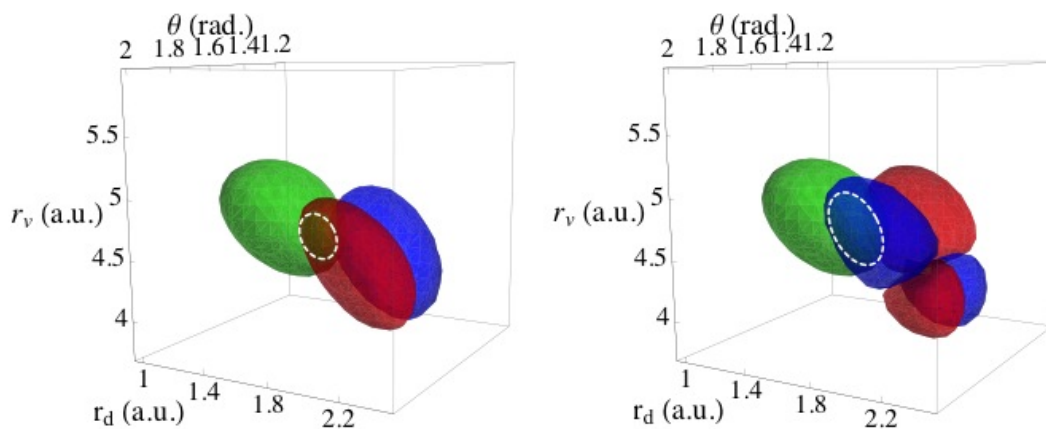


Figure 4.9: Overlap between the lowest vibrational state (0,0,0) of the electronic ground state (green) and the two first one (E_1 and E_2) lying on the 1^1B_1 electronic state (red and blue), which is a dipole-allowed transition. The isosurface of the wavefunctions is $\Psi_{GS} = \Psi_{B_1} = 0.0001$. The white dashed circles indicate the overlap zone between the two vibrational functions.

only the transition to the 1^1B_1 electronic state is dipole allowed. Then only eigenstates with density on the electronic 1^1B_1 state and an even number of nodal planes according to θ lead to a spectral intensity. To illustrate this symmetry property, the GS vibrational and the two first vibrational excited wavefunctions are presented in Fig.4.9. As represented by the dashed white circle, the overlap between the GS wavefunction (green) and the lobe of sign (either red or blue) of the excited wf is cancelled out by the equal contribution of the second lobes of the opposite sign.

Symmetry properties also enter into account concerning the wf , which belongs to the 1^1A_2 electronic states. As a direct transition from the GS is dipole-forbidden, the vibrational wf of this state must be coupled to the one of the 1^1B_1 electronic state through the non-adiabatic coupling. As it takes place only during the excitation of the asymmetric stretch of the molecule, only odd quantum number of this mode is present in the vibrational wf of the 1^1A_2 state. It is verified from the attribution presented in Tab. 4.1. These symmetry considerations show that the optically active transition results from eigenstates for which the total vibrational wf is a combination of a symmetric wf on the 1^1B_1 state and an asymmetric wf one on the 1^1A_2 state with respect to the asymmetric stretching mode.

We mentioned already the peculiarity of the spectrum which exhibits features assigned to the forbidden electronic state. This statement holds when the vibrational eigenfunction are studied, particularly for the low

energy part, where more than 70% of the total wavefunction lies on the 1^1A_2 electronic state. We decided to label the different transitions according to this part of the wavefunction. The first 80 eigenfunctions present a simple pattern in the nodal structures that allows a direct assignment. It give primordial pieces of information according the energy of the bending ($\sim 270 \text{ cm}^{-1}$), the symmetric stretching ($\sim 760 \text{ cm}^{-1}$) and the asymmetric stretching mode ($\sim 1150 \text{ cm}^{-1}$).

From the assignment and the shape of the vibrational eigenstates, it is possible to understand the intensity evolution of the different series of quantum number. For instance, we observed that the intensity of a transition depends on the population on the 1^1B_1 state, because this transition is dipole-allowed. This dependence is, for instance, observed for series $(0, n_2, 1)$. When the number of node for the bending mode (n_2) increases, the intensity of the transition increased because the population of the 1^1B_1 state increases, see Tab. 4.1. But for $n_2 \geq 4$ the population of the 1^1B_1 state increases but not the intensity. The wf on the 1^1B_1 state is displayed for this series in Fig. 4.10. One can clearly see that with increasing values of n_2 the wavefunction is localised closer to the GS one and the FC overlap becomes larger. While for $n_2 < 4$ the lobe becomes more and more predominant in the FC area, for larger values of n_2 lobes with an opposite sign start to reduce the FC factor. Note that there is no nodal plan along the asymmetric stretching mode, but we notice a weak probability of the wf in the C_{2v} symmetry, i.e. $\theta = \pi/2$. It is due to the shape of the PES, which presents a local maximum in C_{2v} . Similar explanations can be provide as well for the other series, also according to n_1 and n_3 . The study of the eigenfunctions has been performed until 4.05 eV, energies of the low energetic Clements bands (A-D). The results of the preponderant series are presented in Fig. 4.11, with in full black line the spectrum obtained from the Fourier transform of the autocorrelation function (cf. part wf dynamics) superimposed in dashed dark blue the intensities of the eigenvalues resulting from the diagonalisation of the Hamiltonian. The band A is constituted principally from transitions to $(2, 2, 3)$ and $(4, 1, 1)$. The band B is assigned almost exclusively to a transition to the $(4, 2, 1)$ level. Concerning the band C, again two transitions, $(5, 0, 1)$ and $(4, 3, 1)$, are equally represented, while the D band results from absorption to $(4, 4, 1)$ level. It turns out that only one series appears recurrently in the description of the Clements bands $(4, n_2, 1)$, with a variation of the bending mode n_2 . According to this statement the absorption to $(4, 0, 1)$, below the Clements band A, is the first element of the pattern. For all the series identified in these first bands, the bending mode plays the most dominant role and gives this energy difference of 220 cm^{-1} . Concerning higher energies, the assignment has not been established, but the repartition of the eigenvalues shows that the complexity increases involving

Table 4.1: Attribution of the low energy part of the photo absorption spectrum (3.56 – 4.05 eV) according to the vibrational structure of 1^1A_2 state. Each entry is labelled by its energetical order in the full-spectrum of the Hamiltonian, and the intensity (overlap with vibrational GS) and the electronic probability are reported.

Eigen.	En. (eV)	Intensity	$1A_2/1B_1$	(n_1, n_2, n_3)	Eigen.	En. (eV)	Intensity	$1A_2/1B_1$	(n_1, n_2, n_3)
3	3.564958	$2.52 \cdot 10^{-7}$	0.88/0.12	(0,0,1)	96	3.929194	$2.86 \cdot 10^{-6}$	0.73/0.27	(0,10,1)
5	3.598468	$2.04 \cdot 10^{-6}$	0.84/0.16	(0,1,1)	97	3.929803	$1.64 \cdot 10^{-4}$	0.76/0.24	(2,1,3)
8	3.632683	$5.88 \cdot 10^{-6}$	0.82/0.18	(0,2,1)	99	3.931641	$3.10 \cdot 10^{-3}$	0.75/0.25	(4,0,1)
10	3.656871	$5.72 \cdot 10^{-6}$	0.84/0.16	(1,0,1)	102	3.938554	$2.36 \cdot 10^{-4}$	0.73/0.27	(1,4,3)
12	3.667956	$7.75 \cdot 10^{-6}$	0.80/0.20	(0,3,1)	103	3.940095	$2.07 \cdot 10^{-3}$	0.71/0.29	(3,3,1)
15	3.690758	$2.87 \cdot 10^{-5}$	0.82/0.18	(1,1,1)	104	3.943425	$5.94 \cdot 10^{-5}$	0.71/0.29	(1,8,1)
17	3.703499	$1.32 \cdot 10^{-5}$	0.84/0.16	(0,0,3)	108	3.948526	$2.24 \cdot 10^{-4}$	0.82/0.18	(1,0,5)
18	3.704196	$1.05 \cdot 10^{-7}$	0.81/0.19	(0,4,1)	111	3.955914	$2.54 \cdot 10^{-4}$	0.74/0.26	(0,3,5)
22	3.725570	$6.94 \cdot 10^{-5}$	0.80/0.20	(1,2,1)	112	3.956340	$3.61 \cdot 10^{-6}$	0.71/0.29	(2,6,1)
24	3.738501	$2.47 \cdot 10^{-5}$	0.83/0.17	(0,1,3)	114	3.957773	$9.36 \cdot 10^{-5}$	0.72/0.28	(0,7,3)
25	3.740672	$1.76 \cdot 10^{-8}$	0.78/0.22	(0,5,1)	116	3.961821	$3.64 \cdot 10^{-3}$	0.69/0.31	(4,1,1)
28	3.750606	$5.95 \cdot 10^{-5}$	0.81/0.19	(2,0,1)	117	3.963284	$3.52 \cdot 10^{-3}$	0.75/0.25	(2,2,3)
30	3.761022	$8.07 \cdot 10^{-5}$	0.78/0.22	(1,3,1)	120	3.967614	$1.52 \cdot 10^{-7}$	0.72/0.28	(0,11,1)
34	3.773866	$3.23 \cdot 10^{-5}$	0.80/0.20	(0,2,3)	123	3.972480	$5.17 \cdot 10^{-4}$	0.68/0.32	(3,4,1)
35	3.777726	$2.53 \cdot 10^{-7}$	0.76/0.24	(0,6,1)	125	3.974702	$2.78 \cdot 10^{-4}$	0.73/0.27	(1,5,3)
37	3.784264	$2.69 \cdot 10^{-4}$	0.78/0.22	(2,1,1)	127	3.980318	$1.11 \cdot 10^{-4}$	0.70/0.30	(1,9,1)
40	3.796921	$5.18 \cdot 10^{-5}$	0.77/0.23	(1,4,1)	129	3.981481	$6.63 \cdot 10^{-4}$	0.79/0.21	(1,1,5)
42	3.802236	$2.52 \cdot 10^{-7}$	0.83/0.17	(1,0,3)	134	3.990196	$6.58 \cdot 10^{-3}$	0.69/0.31	(4,2,1)
45	3.809746	$2.46 \cdot 10^{-5}$	0.79/0.21	(0,3,3)	135	3.991155	$1.07 \cdot 10^{-3}$	0.67/0.33	(2,7,1)
47	3.815158	$4.76 \cdot 10^{-8}$	0.75/0.25	(0,7,1)	136	3.992558	$6.87 \cdot 10^{-5}$	0.75/0.25	(0,4,5)
49	3.818261	$5.73 \cdot 10^{-4}$	0.76/0.24	(2,2,1)	137	3.993211	$1.22 \cdot 10^{-3}$	0.72/0.28	(3,0,3)
52	3.833031	$5.34 \cdot 10^{-5}$	0.76/0.24	(1,5,1)	139	3.995662	$5.23 \cdot 10^{-4}$	0.78/0.22	(0,0,7)
53	3.834103	$9.11 \cdot 10^{-5}$	0.81/0.19	(1,1,3)	141	3.997698	$8.60 \cdot 10^{-4}$	0.75/0.25	(2,3,3)
56	3.841549	$3.01 \cdot 10^{-4}$	0.78/0.22	(3,0,1)	145	4.006069	$7.79 \cdot 10^{-6}$	0.68/0.32	(3,5,1)
58	3.846100	$5.17 \cdot 10^{-6}$	0.77/0.23	(0,4,3)	146	4.006206	$5.45 \cdot 10^{-6}$	0.70/0.30	?
59	3.847545	$2.00 \cdot 10^{-4}$	0.83/0.17	(0,0,5)	149	4.010092	$1.90 \cdot 10^{-4}$	0.70/0.30	(1,6,3)
61	3.852629	$3.86 \cdot 10^{-4}$	0.74/0.26	(2,3,1)	153	4.015568	$2.22 \cdot 10^{-3}$	0.75/0.25	(1,2,5)
62	3.853055	$2.06 \cdot 10^{-4}$	0.74/0.26	(0,8,1)	154	4.017403	$1.28 \cdot 10^{-6}$	0.68/0.32	(1,10,1)
66	3.868219	$1.56 \cdot 10^{-4}$	0.79/0.21	(1,2,3)	155	4.017864	$5.90 \cdot 10^{-3}$	0.68/0.32	(5,0,1)
67	3.869783	$5.80 \cdot 10^{-6}$	0.74/0.26	(1,6,1)	158	4.020738	$6.03 \cdot 10^{-3}$	0.71/0.26	(4,3,1)
69	3.874532	$1.47 \cdot 10^{-3}$	0.75/0.25	(3,1,1)	160	4.025305	$2.54 \cdot 10^{-6}$	0.70/0.30	(3,1,3)
73	3.882800	$1.43 \cdot 10^{-7}$	0.76/0.24	(0,5,3)	161	4.025453	$5.66 \cdot 10^{-6}$	0.64/0.36	(2,8,1)
74	3.883607	$2.93 \cdot 10^{-4}$	0.81/0.19	(0,1,5)	164	4.029071	$1.61 \cdot 10^{-7}$	0.73/0.27	(0,5,5)
76	3.887461	$3.50 \cdot 10^{-4}$	0.72/0.28	(2,4,1)	165	4.030261	$6.22 \cdot 10^{-4}$	0.71/0.29	(2,4,3)
78	3.890961	$2.43 \cdot 10^{-6}$	0.73/0.27	(0,9,1)	166	4.032745	$9.20 \cdot 10^{-5}$	0.73/0.27	(0,9,3)
81	3.899081	$6.33 \cdot 10^{-4}$	0.80/0.20	(2,0,3)	167	4.033398	$5.45 \cdot 10^{-8}$	0.77/0.23	(0,1,7)?
83	3.903397	$1.25 \cdot 10^{-5}$	0.77/0.23	(1,3,3)	171	4.040167	$1.04 \cdot 10^{-4}$	0.67/0.33	(3,6,1)
84	3.906429	$1.90 \cdot 10^{-4}$	0.72/0.28	(1,7,1)	174	4.044692	$2.10 \cdot 10^{-3}$	0.69/0.31	(1,11,1)?
85	3.907239	$2.59 \cdot 10^{-3}$	0.72/0.28	(3,2,1)	175	4.044904	$1.04 \cdot 10^{-2}$	0.70/0.30	(4,4,1)
90	3.919710	$1.74 \cdot 10^{-4}$	0.77/0.23	(0,2,5)	176	4.045618	$7.64 \cdot 10^{-4}$	0.69/0.31	(1,7,3)
91	3.919784	$6.84 \cdot 10^{-5}$	0.75/0.25	(0,6,3)	177	4.047467	$8.26 \cdot 10^{-4}$	0.74/0.26	(1,3,5)
93	3.922294	$1.50 \cdot 10^{-4}$	0.70/0.30	(2,5,1)					

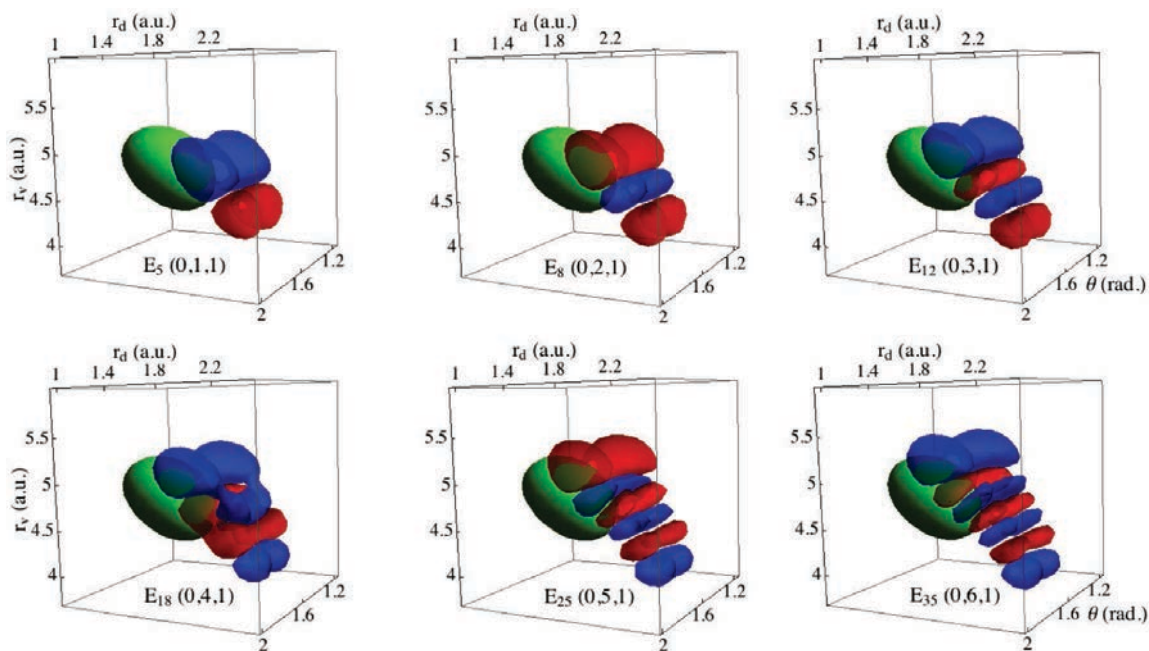


Figure 4.10: Evolution of the overlap between ground state wf (green) and the 1^1B_1 vibrational wf (red and blue) for the series $(0,n,1)$ with $n = 0$ to 6. The GS wf is represented for an iso-density of 0.0001 and the excited one for 0.0006 to highlight the overlap. The overlap for $0 \leq n \leq 3$ increases thanks to the increased density of the excited state in the FC area, but for larger n the total overlap decreases because of the sign variation of the excited vibrational state in the FC zone.

more transitions for all the bands. The band E seems to result from one predominant transition as well as for the F band with for both of them an intensity ~ 3.5 higher than the other. The G band is the most complex one, with five transitions of similar weight, while the bands H-J turn again describe by one predominant transition.

4.3 Including the triplet states

The Clements bands are well described by the consideration of the singlet states only, as we discussed previously. Nevertheless many experimental studies pointed out evidences of the role of the low-lying triplet states in this energy range. The "forbidden-band" of the photoabsorption spectrum ($\sim 3.1 - 3.7$ eV) has been attributed to triplet excited electronic states [37] thanks to the Zeeman effect observed in the presence of strong magnetic field. Later, this state has been identified as the 1^3B_1 electronic state [38]. The theoretical work of Hillier and Saunders [39], using SCF calculations, predicted not one but three triplet states in the

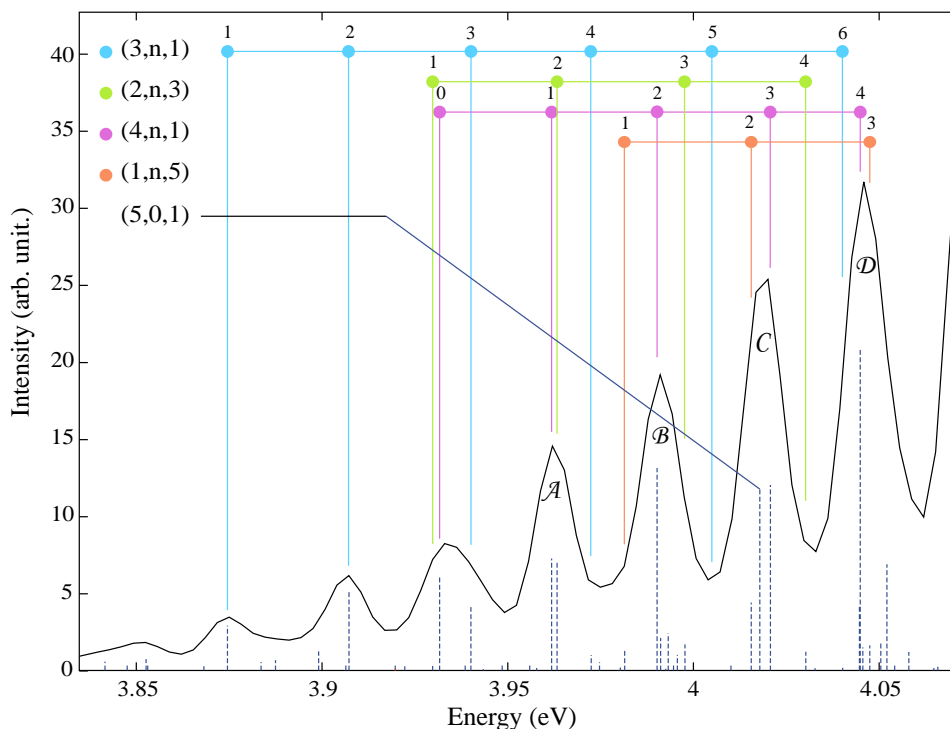


Figure 4.11: Contribution in the Clements bands of the different series, which have been identified in this study. The stick spectrum in dashed line represent the overlap between the GS wavefunction and the eigenfunction obtained from Lanczos diagonalisation. The full-line spectrum in black line results from the Fourier transform of the autocorrelation function, and the Clements band in this energy range have been labelled ($A - D$). Only the predominant eigenstates are highlight, for the weaker contributions c.f. Tab. 4.1. Interestingly the Clements bands A and C arise for almost two equivalent excitations, but the B and D exhibit only one transition. This behaviour has been observed also for the two next bands $E - F$ but their attributions have not been completed at this stage.

energy range of the "forbidden band", namely 1^3B_2 , 1^3B_1 and 1^3A_2 from lower to higher energy, respectively. Attempts to a direct observation of the two "new" triplet states failed [43], but they have been observed by indirect coupling with the 1^3B_1 state; vibronic in the case of the 1^3A_2 state and rotational concerning the 1^3B_2 state [148]. The question of the role of these states and of the intersystem crossing yields remain open and we propose to consider them in the following. To conduct this study we take advantage of the block diagonal form of the Hamiltonian (see Sec. 3.4.1) to reduce the number of electronic states required. The excited singlet 1^1B_1 state belongs to the A'' manifold and is the only allowed transition in the region of interest. Therefore this manifold of state is considered in the dynamics of the w_p . The different SOC matrix elements playing a role between the states of the A'' manifolds have been already discussed. For clarity of the following discussion, we mention again that the A'' manifold is composed of the following

electronic states, $\{1^1B_1, 1^1A_2, 1^3B_2(+), 1^3B_2(0), 1^3B_1(-), 1^3A_2(-)\}$. It results a complex system with the presence of two *symmetry-allowed* conical intersections between the electronic states of symmetry B_1 and A_2 for either singlet or triplet spin. This complexity is increased by numerous intersystem crossings between the singlet and triplet states of the different symmetry. The situation is summarised in Fig. 4.12, where these different intersections have been labelled either "CI" or "ISC" for conical intersection and intersystem crossing, respectively. As already mentioned, both 1^3B_2 states cross the two singlet electronic states nearby their energy minimum, while the remaining triplet states present only one crossing at similar energies.

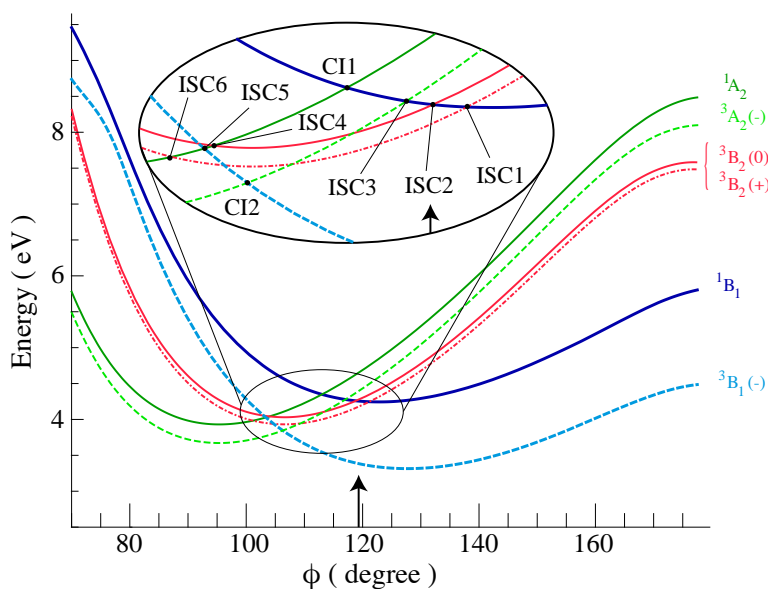


Figure 4.12: One-dimensional cut through the PES of the A'' states, along the bending angle ϕ . The two singlet states, 1^1B_1 (1^1A_2), are represented in thick dark blue (thin green) line, respectively. In the same way, the triplet 1^3B_1 (1^3A_2) states are represented in thick dashed light blue (thin dashed light green) line. The triplet 1^3B_2 state has two different spin components, (0) or (+), both represented in full and dotted-dashed red, respectively, with an artificial shift to separate them. In the inset we magnify the central region where ICS and CI occur.

To solve the time dependent Schrödinger equation, the same method as before is used and the initial state is obtained by the projection of the vibrational GS through the transition dipole operator. Note that in our case the SOC is totally included in the diabatic potential matrix of the Hamiltonian and the dipole operator that must be used is the one obtained in the electronic basis of *pure* spin states and *not* the one computed after the diagonalisation of the electronic Hamiltonian. Then the initial wf is strictly the same than the one in the case of the singlet states only.

We report, in Fig. 4.13, the time-dependent electronic populations of the full wavefunction integrated over the different electronic states for 1 picosecond. The population into the triplet states occurs only after few femtoseconds but become important after hundreds of femtoseconds, with at the end of the calculation $\sim 30\%$ of the total population being into triplet electronic states. Interestingly, the time dependent profile of the singlet states population presents the same oscillatory behaviour as when we did not consider the triplet states. Except for the 100 first femtoseconds, the population of all the triplet states increase monotonically with the time. The population of the ${}^3B_2(0)$ state is predominant with 17% and this for all the time of the propagation. The population in the ${}^1{}^3B_2(+)$ is also relevant with 8%. The coupled ${}^3B_1(-)$ and ${}^3A_2(-)$ states end up with less than 10% of the total population with an oscillation due to the conical intersection.

As schematised on Fig. 4.12, the system is complex and to understand its time evolution and the underlying

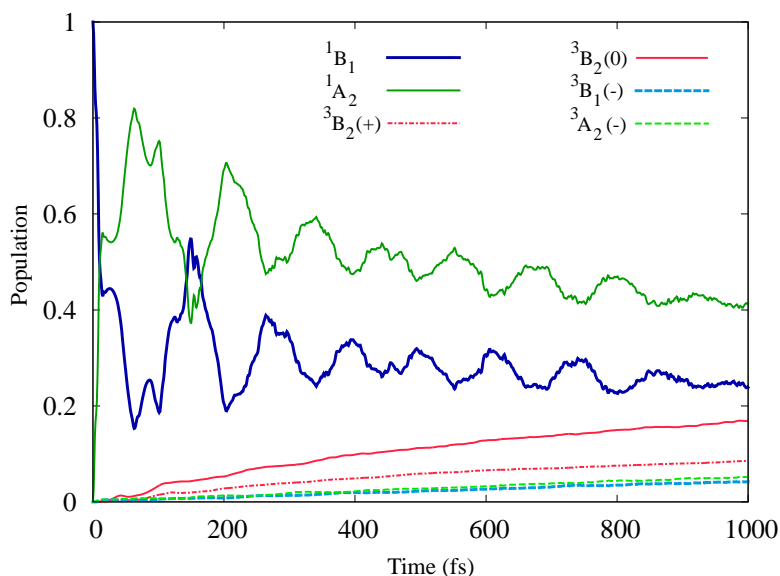


Figure 4.13: Populations on the different electronic states as a function of time. The same colour code as in Fig. 4.12 is used. In thick dark blue and thin dark green lines are the population in the electronic singlet 1B_1 and 1A_2 , respectively. The major part of the population into the triplet manifolds belongs to the ${}^1{}^3B_2(0)$, in full red and ${}^1{}^3B_2(+)$, in dotted-dashed red. The remaining density is shared between the ${}^1{}^3B_1(-)$, in thick dashed light blue and ${}^1{}^3A_2(-)$ in thin dashed light green.

mechanisms for the singlet-triplet conversion, we focus on the first hundreds of femtosecond of the propagation, a time for which the w_p does not spread much over the singlet state surfaces but remains localised. In the following, we will refer to the different crossings or CIs that are labelled in Fig. 4.12, and adopt a divide

and conquer way, by simplifying the full system to understand the different mechanisms.

4.3.1 Intersystem crossing to the $1^3B_1(-)$ and $1^3A_2(-)$ states

We start with the case of the $1^1B_1(-)$ and $1^3A_2(-)$ electronic states (the spin component $(-)$ is drop at this point because there is no confusion), which are coupled through a conical intersection. Because of this coupling both states have to be studied simultaneously. We displayed in Fig. 4.14 (left panel) the population of these states as well as their sum for the first 200 fs. The latter is a relevant quantity because the conical intersection (CI2) between these two states allows the wp to move from one state to another and could hide the dynamics of the SOC-triggered transfer. We have also added the autocorrelation function $C(t) = |\langle \Psi(0) | \Psi(t) \rangle|$, with $\Psi(t)$, being the full wavefunction of the system. We clearly see three steps during the internal conversion, the first one takes place between 0 and 16 fs, the second between 55 and 65 fs and the third one for times between 150 and 165 fs. Systematically, these transfers are accompanied by a revival in the autocorrelation function. Following the wp dynamics in not trivial for many states and 3 degrees of freedom and in order to get insight we start by studying the different transfer in different model Hamiltonians. First we discard the role of the SOC among the manifold of triplet states, keeping active only direct transfer from singlet to triplet states. The result for the population in the 1^1B_1 and 1^3A_2 states is presented on Fig. 4.14 (middle panel) by the orange line. The population is almost identical to the one obtained from the total Hamiltonian. Thus it establishes that the indirect couplings are not relevant during the propagation of the first 200 fs. In the same spirit the triplet states of B_2 symmetry are artificially removed from the Hamiltonian and again (dotted-dashed blue line) the lack of difference in the time evolution shows that they do not play a significant role for the intersystem crossing to the 1^1B_1 and 1^3A_2 states. It means that the system is actually well described over this period of time as a four-state problem, which greatly decreases the number of possible channels to populate the states.

Switching on and off, successively or simultaneously, the remaining four couplings between the states, gives a simple way to identify the mechanism, as presented Fig. 4.14 (left panel). The simulation that includes the SOC between the two singlet states and the 1^3A_2 (dotted brown) shows two of the three steps observed in the population transfer. The missing step is obtained when the simulation includes the SOC between the singlet and the 1^3B_1 state (dotted green). In addition simulations with the coupling with only one singlet state

have been performed, with either the coupling $1^1B_1/1^3A_2$ or $1^1A_2/1^3B_1$ (solid lines). The comparison with the previous results shows that the SOC between the singlet and triplet states of the same spatial symmetry do not play a significant role. Indeed, in the C_{2v} symmetry, only the SOC between the $1^1B_1/1^3A_2$ and $1^1A_2/1^3B_1$ states are not vanishing. The coupling between the $1^1B_1/1^3B_1$ and $1^1A_2/1^3A_2$ states are null in C_{2v} and remain very weak even in the C_s symmetry, with values below $10 - 15 \text{ cm}^{-1}$ for all the geometries. From these simulations the three-step transfer, similar to the ones of the full system are observable when the sum of the different channels is considered (blue line). In addition the wp motion in the singlet states of the full Hamiltonian give the physical interpretation as a function of the ISC and CI in the system (Fig. 4.15).

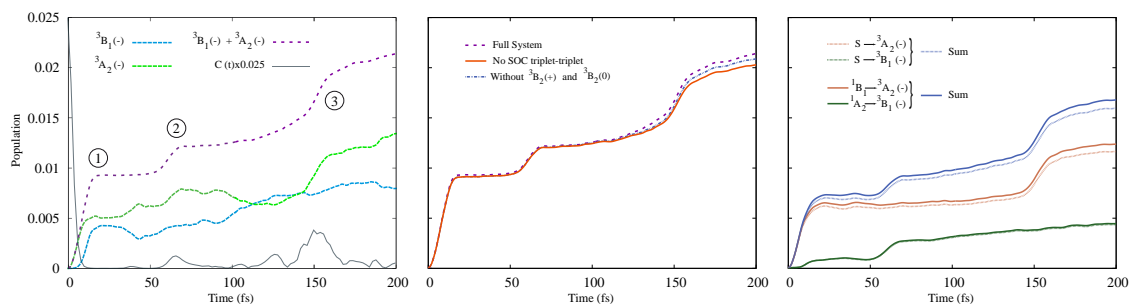


Figure 4.14: (left panel) Populations on the $1^3B_1(-)$ (dashed green) and $1^3A_2(-)$ (dashed blue) electronic states as a function of time for the first 200 fs. In addition the sum of the population of these two states is presented in dashed purple as well as the autocorrelation function in grey full line. The three steps of the transfer are labelled for the discussion. (middle) Comparison of the population's sum in the triplet $1^3B_1(-)$ and $1^3A_2(-)$ states for different model Hamiltonian. The population in orange line results from considering all electronic states and switching off the SOC between all the triplet states, while in dashed-dotted grey the triplet states of spatial B_2 symmetry are not considered. In dashed purple the result of the full calculation is added for comparison. (right panel) Results from state-by-state coupling, with in green line for including only the $1^1A_2/1^3B_1(-)$ coupling, while in dotted green the couplings between both singlet states and the $1^3B_1(-)$ are considered. In orange line (dotted) similar results from the consideration of the coupling between 1^1B_1 (singlet states) and $1^3A_2(-)$ states. Then the blue line (dotted) is the sum of the obtained population of the two previous simulations.

The first step is attributed to the principal contribution of a $1^1B_1 \rightarrow 1^3A_2$ transfer, when the nuclear wp , launched on the 1^1B_1 state, is in the direct vicinity of the intersection with the 1^3A_2 state (ISC3) and follows this intersection over the first ~ 15 fs of the dynamics. A small contribution of a $1^1A_2 \rightarrow 1^3B_1$ transfer takes place after ~ 10 fs with a rather short duration ~ 5 fs. The weakness of the transfer is not due to the low population of the 1^1A_2 state, already 50% of the total wp transferred through (IC1), but results from the fast motion of the wp in vicinity of ISC5, and the asymmetric elongation (see Fig. 4.17 where the same wp is plotted in different coordinates). This shifts the seam of ISC5 (see Fig. 4.15) making the transfer less

efficient. Then the non-adiabatic coupling between 1^3A_2 and 1^3B_1 (CI2) will transfer in a few fs (~ 7 fs) the population from the former to the latter, but the sum of populations remains constant until $t \sim 55$ fs. During this time, the majority of the singlet population is transferred to $1A_2$ through CI1. According to the results of Fig. 4.14, the second step can be attributed to the $1^1A_2 \rightarrow 1^3B_1$ interaction, when the w_p comes back near the Frank-Condon (FC) area, but with a smaller angle (110°), which is located in the vicinity of ISC5 (Fig.4.15).

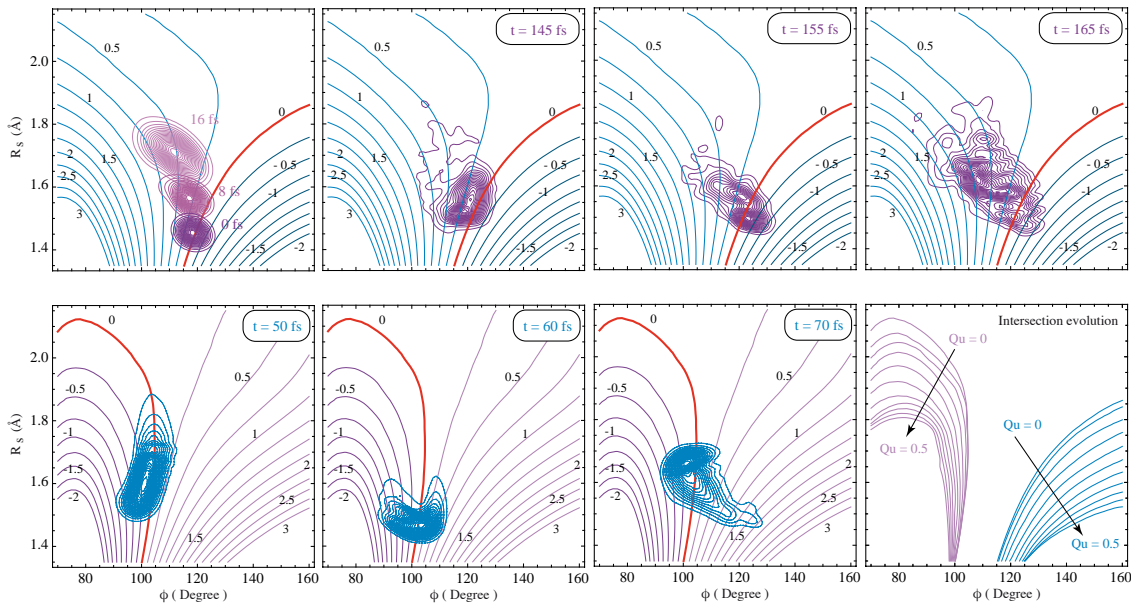


Figure 4.15: (top row) Snapshot of the reduced density (purple line) as a function of R_s and ϕ of the 1^1B_1 electronic state for different characteristic times of the intersystem conversion. This time evolution is superimposed with the energy difference ($W_{1B_1} - W_{3A_2}$) of the diabatic 1^1B_1 and 1^3A_2 states, in blue for $Q_u = 0$ Å. The red line indicate the intersystem crossing.(bottom row) The first three panels present the reduced density (blue line) of the 1^1A_2 electronic state in the same coordinates than previously at times indicated in the inset. The superimposed contour purple plot shows the energy difference ($W_{1A_2} - W_{3B_1}$) of the diabatic 1^1A_2 and 1^3B_1 states. The last panel shows the evolution as a function of Q_u of the intersystem crossing seam between the $1^1B_1/1^3A_2$ in blue and $1^1A_2/1^3B_1$ in purple with a variation of $\Delta Q_u = 0.05$ Å.

This dynamics of the w_p is confirmed by the revival in $C(t)$ at $t \sim 65$ fs. This transfer turns to be efficient because ISC5 occurs at a turning point of the w_p , where it spends tens of fs in its vicinity. After this time, the population of the considered triplet states is not as constant as before but weakly increases. This phenomenon seems to result from the partial delocalisation of the w_p allowing transfer such as in the first step for $1^1A_2 \rightarrow 1^3B_1$. More interestingly, the third step takes place during the 16 fs following the next revival in $C(t)$ at $t \sim 150$ fs, when the w_p returns to a geometry very close to the initial one, allowing the same transfer

as step 1. Here again the turning point of the w_p makes the transfer efficient. We did not identify any other relevant mechanisms for the intersystem crossing and we believe that the different channels presented above are active for longer time of propagation but the delocalisation of the w_p smooth the step-like transfer. The dynamics of the singlet/triplet transfer is highly sensitive to the localisation of the ISC. In the case of ISC 3 and 5, the energy difference between $1^1A_2/1^3B_1$ and $1^1B_1/1^3A_2$ present a sharp profile, as displayed in the contour line of Fig. 4.15, and due to the weakness of the SOC elements the transfers take place only at localised geometries on the PES.

4.3.2 Intersystem crossing to the $1^3B_2(+)$ state

We follow the same reasoning to understand the population transfer to the $^3B_2(+)$ state, which presents a similar but slightly smoothed step-like time evolution shown in Fig. 4.16. Similar reduced Hamiltonians have been used to target the possible mechanisms and gave us the possibility to work with the consideration of the singlet states and the $^3B_2(+)$ state only without loss of generality (Fig. 4.16 left panel). In the first ~ 50 fs two clean steps are obtained in the population of the triplet state for the reduced (right panel) and full (left panel) Hamiltonian. But unlike the previous states a decay of the population occurs at ~ 43 and ~ 120 fs for a duration of ~ 10 fs. Considering the first transfer, which occurs between 0 and ~ 10 fs, it can be assigned to a $1^1B_1 \rightarrow 1^3B_2(+)$ transfer, exclusively. It takes place thanks to the location of the Franck-Codon zone nearby by ISC1, as confirmed by the w_p in Fig. 4.17. The transfer is weak because the SOC values between 1^1B_1 and $1^3B_2(+)$ are small for $90^\circ < \phi < 120^\circ$, see Fig. 4.17. This transfer does not play any significant role before ~ 150 fs, when the w_p is back to the FC zone as discussed previously, with again a weak efficiency.

Interestingly, the result of the simulation where only the SOC between the 1^1A_2 and the $1^3B_2(+)$ states is considered, displayed by the green line of Fig. 4.16 (left), is similar to the one obtained by the full Hamiltonian. This shows the preponderant role of the $1^1A_2 \rightarrow 1^3B_2(+)$ transfer. This transfer occurs first at ~ 8 fs (see inset Fig. 4.16), time for which the w_p starts to move along the Q_u coordinate and thus explores the C_s symmetry. Doing so the w_p is leaving geometries for which the SOC and the non-adiabatic coupling are nulls. A sequential transfer from the 1^1B_1 state to the 1^1A_2 state (IC1) occurs and is directly followed by the $1^1A_2 \rightarrow 1^3B_2(+)$ transfer. It will take place again with a stronger yield between $\sim 25 - 40$ fs, when the w_p in the 1^1A_2 state reveals the turning point along the Q_u coordinate. The w_p is during this time, in the vicinity of ISC6 where the SOC elements are large, see Fig. 4.17. Only 20 fs later a second similar transfer

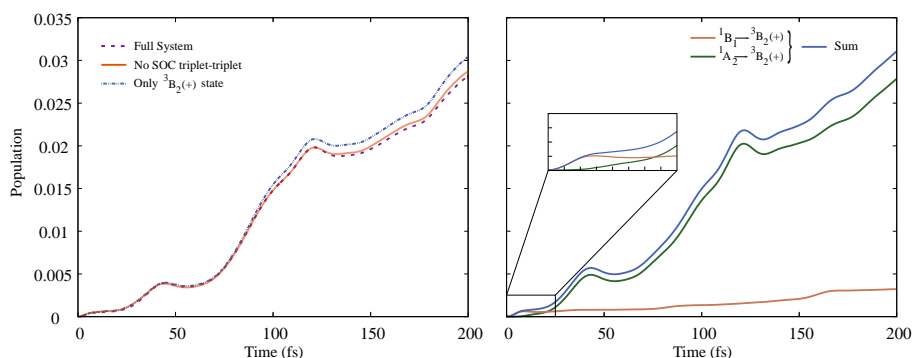


Figure 4.16: (left panel) Population of the electronic $1^3B_2(+)$ state for the first 200 fs, considering the full Hamiltonian (dashed purple), without the SOC between the triplet states manifold (orange full line) and with only the $1^3B_2(+)$ state and the two singlet ones in dotted-dashed blue line. (right panel) Results of the state-by-state simulations considering only the SOC between the 1^1B_1 and $1^3B_2(+)$ states in red or only the $1^1A_2/1^3B_2(+)$ coupling in green. The blue line is the sum of the two previous simulations. The inset presents a zoom for the first 25 fs of the calculations.

occurs, but three times more efficient. During the short interval of time between the two transfers, the wp turns back to C_{2v} symmetry (small value of Q_u) and overlaps the FC area with small values of $\phi \sim 90^\circ$, see Fig. 4.17. For these geometries the SOC is weaker and this can explain the break observed in the transfer and allows a backward transfer $1^1A_2 \leftarrow 1^3B_2(+)$ (decay of $1^3B_2(+)$ population). In the mean time population of the 1^1A_2 state increased through non-adiabatic coupling nearby IC1, reaching its highest value ($\sim 80\%$). The wp in the 1^1A_2 state experiments again an asymmetric elongation render possible a new transfer, highly efficient thanks to the large population of 1^1A_2 and the direct vicinity of ISC6. This mechanism is then taking place again along the time propagation while the wp spreads over the PES.

4.3.3 Intersystem crossing to the $1^3B_2(0)$ state

Both triplet states B_2 share the same PES and thus also the different intersystem crossings with either the singlet or triplet states. Then any difference of the time dependent population should arrived from the different SOC values with the manifold of states. The population of the $1^3B_2(0)$ state, in the different simulations performed and displayed in Fig. 4.18, presents a similar evolution in comparison to the one of the $1^3B_2(+)$ but with a stronger yield ($\sim \times 2$). From the state-by-state analysis (Fig. 4.18, left panel), we observed also the predominant role of the $1^1A_2 \rightarrow 1^3B_2(0)$ transfer but in this case the $1^1B_1 \rightarrow 1^3B_2(0)$ transition is somehow larger, especially for the first 50 fs of the propagation where both channels provide similar transfer yields.

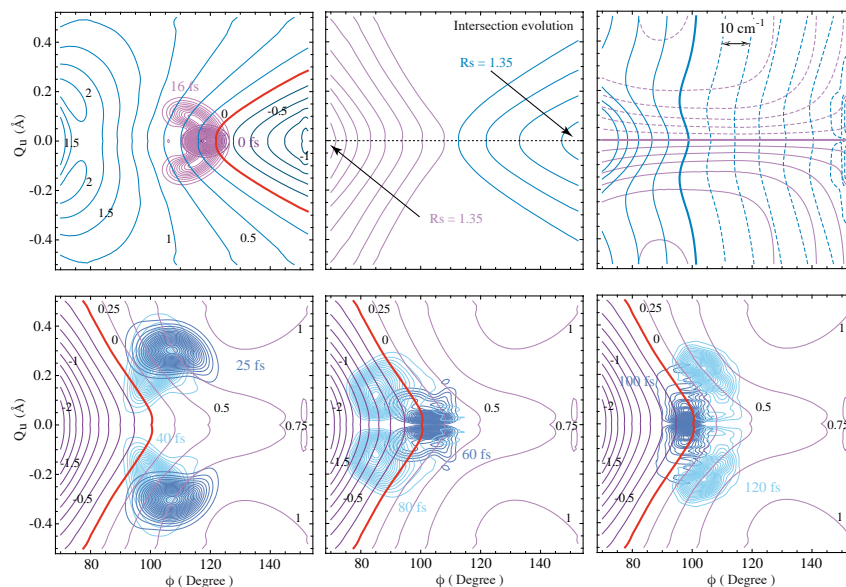


Figure 4.17: (top row) Snapshot of the reduced density (purple line) as a function of Q_u and ϕ of the 1^1B_1 electronic state at $t = 0$ fs (dark purple) and $t = 16$ fs (light purple). Superimposed is the energy difference ($W_{1B_1} - W_{3B_2}$) of the diabatic 1^1B_1 and 1^3B_2 states, in blue for $R_s = 1.45$ Å. The red line indicates the intersystem crossing. The middle panel shows the intersystem crossing seam evolution as a function of R_s for the $1^1B_1/1^3B_2$ in blue and $1^1A_2/1^3B_2$ in purple with a variation of $\Delta R_s = 0.1$ Å. The left panel presents the SOC element between the $1^1B_1/1^3B_2$ in blue with the thick line being 0 cm^{-1} , the full line $SOC > 0$ and in dashed line $SOC < 0$. The same holds for the purple lines of the SOC between $1^1A_2/1^3B_2$. In both cases the step is 10 cm^{-1} . (bottom row) The first three panels present the reduced density (blue line) of the 1^1A_2 electronic state. The superimposed contour purple plot shows the energy difference ($W_{1A_2} - W_{3B_2}$) of the diabatic 1^1A_2 and 1^3B_2 states.

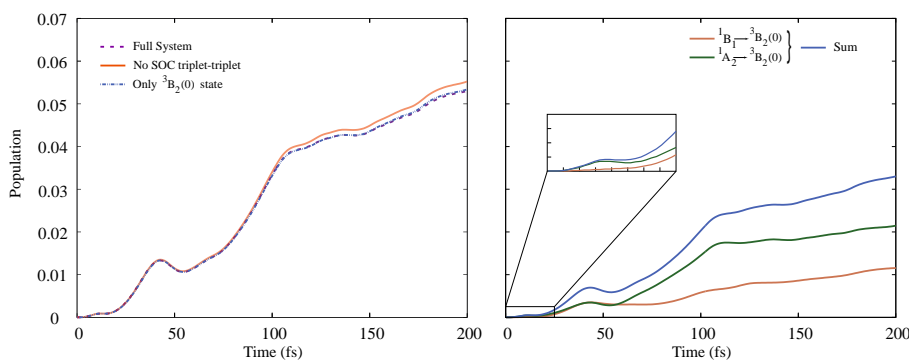


Figure 4.18: (left panel) Population of the electronic $1^3B_2(0)$ state for the first 200 fs, considering the full Hamiltonian (dashed purple), without the SOC between the triplet states manifold (orange full line) and with only the $1^3B_2(0)$ state and the two singlet ones in dotted-dashed blue line. (right panel) Results of the state-by-state simulations considering only the SOC between the 1^1B_1 and $1^3B_2(0)$ states in red or only the $1^1A_2/1^3B_2(0)$ coupling in green. The blue line is the sum of the two previous simulations. The inset presents a zoom for the first 25 fs of the calculations.

A weak $1^1A_2 \rightarrow 1^3B_2(0)$ transfer is observed few fs after the excitation. The wp starting on the 1^1B_1 state, the transfer can take place only subsequently to the non-adiabatic transition to the 1^1A_2 state (IC1). The interesting point here is to understand the difference with the case of the $1^3B_2(+)$ state. For the first few femtoseconds of the dynamics, we noticed (see inset Fig. 4.18) that the population of the $1^3B_2(0)$ state occurs with a small delay and results from $1^1A_2 \rightarrow 1^3B_2(0)$ transfer. In the FC area the wp lies nearby both intersection lines between the 1^3B_2 and either 1^1B_1 and 1^1A_2 states. In opposite of the previous case, now the SOC between 1^1B_1 and $1^3B_2(0)$ is null in the C_{2v} symmetry but not the one between 1^1A_2 and $1^3B_2(0)$, and right after the non-adiabatic coupling induced by IC1 the population ($\sim 20\%$) can transfer through ISC2. Then with the extension of the wp along the Q_u coordinate the transfer from 1^1B_1 becomes possible. Concerning the second steps of the transfer, we clearly see another difference with previously with a similar importance of the from both singlet states. While $1^1A_2 \rightarrow 1^3B_2(0)$ remains similar to previously a transfer of similar amplitude occurs from 1^1B_1 . This can be interpreted thanks to the SOC evolution, which becomes large for displacement along Q_u , while the wp remains in the vicinity of ISC2. For longer time, the transfer from 1^1A_2 are the same than previously with a slightly higher efficiency because of the SOC non-vanished in C_{2v} , while the transfer from the 1^1B_1 state results from the variation of the SOC along the nuclear geometry which make it likely in this case. The mechanisms proposed and the explanations of the transfer to the $1^3B_2(0)$ are consistent concerning the simplified model, but as presented the SOC values differ from the ones of the $1^3B_2(+)$ but hardly explain the large difference of population between these two states (factor of ~ 1.9) in the total system.

4.3.4 Quantum Interferences

Our simplified Hamiltonians and the wp evolution in the singlet states gave us the possibility to quantitatively describes the different mechanisms involved in the intersystem crossing of SO_2 . But it raised also an interesting question. For each reduced Hamiltonians, describing either the coupled $1^3A_2(-)/1^3B_1(-)$, the $1^3B_2(0)$ or the $1^3B_2(+)$ states, a large difference in the total yields of the intersystem conversion is observed in comparison to the state-by-state simulations. It is also true when we consider the full Hamiltonian of the system. The most spectacular example is difference of a factor ~ 1.7 observed in the populations of the $1^3B_2(0)$ state. A factor of ~ 1.3 is also noticed in the case of 1^3A_2 and 1^3B_1 states. Concerning the $1^3B_2(+)$ state the difference is smaller and presents an opposite behaviour than the two previous ones with a global

decreased of the population.

In the following, the reduced Hamiltonians (see Sec. 4.3.1-3) are considered. Each of them includes the two singlet states and the relevant triplet states, namely $1^3B_2(0)$, $1^3B_2(+)$ or both $1^3A_2(-)/1^3B_1(-)$ states. In the case of the two triplet 1^3B_2 states, the population in these latter can come from the 1^1A_2 or the 1^1B_1 states, leading to two different pathways. In the case of the $1^3A_2(-)/1^3B_1(-)$ states, the population in these coupled states can results from four different paths. Indeed the wp in each singlet state can end up in each triplet states. But the couplings between the singlet and triplet states with the same spatial symmetry are too weak to be observed and then its reduced to two relevant pathways. Physically speaking, in the state-by-state simulations we artificially removed the pathways one after the other, while both are active at the same time in the reduced Hamiltonian. It is strongly reminiscent to well known Young interference experiment and makes thing about quantum interferences because the sum of the population obtained from the incoherent paths leads to a large difference with the coherent sum. To ensure that constructive interferences are indeed observed, we arbitrary change the sign of one of the SOC element. Doing so we obtained destructive interferences leading to a yield 10 times smaller for the final population in the $1^3B_2(0)$ state, see Fig. 4.19. This trick provides us as well an indication on how interference occurs as well as when, we can notice that during the first step of population transfer at ~ 45 fs, the incoherent simulations gave the same population transfer to the triplet state.

The case of $1^3B_2(+)$ presents the only example of destructive interferences, which modulate the yields in function of the time. For the time considered here, the interferences are either constructive or destructive for one triplet state but no flipping is observed. Continuing this simulation for longer time scales could be instructive to track such kind of behaviour. What we can state from this results is also the interferences seems involved principally when the transfer occurs between both singlet states on the same time, and are preponderant when the transfer have comparable weights, as seen at ~ 45 fs for the $1^3B_2(0)$ state. These interesting phenomena deserve clearly a deeper investigation, to be correctly understood because of its predominant role in the intersystem crossing yield.

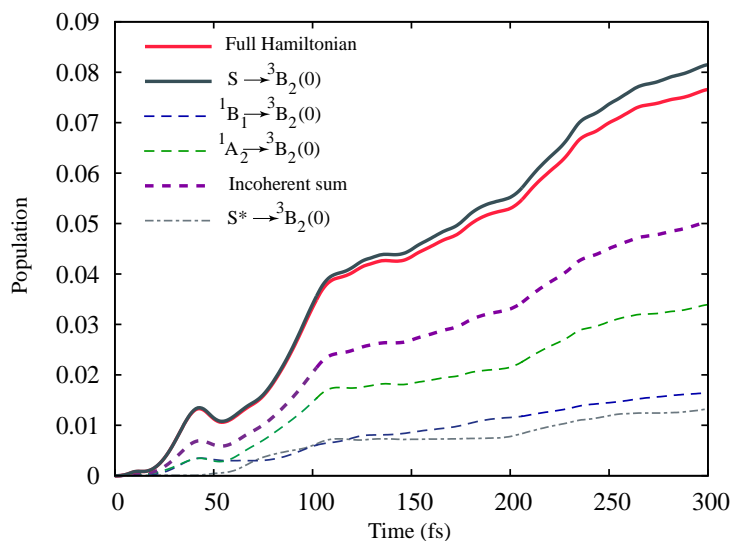


Figure 4.19: In full thick red is represented the result from the full Hamiltonian in addition the full thick grey line is the population when only the coupling between the singlet ($1^1A_2/1^1B_1$) states and $1^3B_2(0)$ is considered. In thin dashed blue (thin dashed green), we represent the population when only SOC between 1^1B_1 (1^1A_2) and $1^3B_2(0)$ is used. The incoherent sum of these former populations is represented in thick dashed purple. The destructive interference (dotted-dashed thin grey) is obtained by changing arbitrarily the sign of the coupling between 1^1B_1 and $1^3B_2(0)$ states.

4.3.5 The "Forbidden band"

Experimentally, the existence of the 3B_1 and 3A_2 states is evidenced via the observation of the forbidden band (3.1 – 3.7 eV). But there is no direct observation of the 3B_2 state, which, according to our simulations seems inducing a predominant intersystem crossing. The simulation including the full Hamiltonian can be used to compute the photoabsorption spectrum of the A" manifold, using the Fourier transform of the autocorrelation. In comparison to the one obtained when only the singlet excited states were considered, no signature of the triplet states is obtained, see Fig. 4.22 a. Using the Lanczos diagonalisation, the forbidden band is obtained and surprisingly it is not comparable to the experimental one (red line in Fig. 4.22 d), concerning its intensity and also its vibrational progression (see Fig. 4.22 b). As the forbidden band has been assigned to the 3B_1 state, we computed the spectrum of an hypothetical excitation to this state, launching directly the initial w_p on the PES and discarding the SOC. It confirms that the vibrational progression of our ab-initio PES is in good agreement with the experiment (not shown). In addition, it supports that the forbidden band arises from the 3B_1 state, but it does not appears from the wavepacket propagation in the

A'' manifold.

In the full Hamiltonian, we neglected so far the SOC between the A' states (1^1A_1 , $1^3B_2(-)$, $1^3B_1(+)$, $1^3A_2(+)$, $1^3B_1(0)$, $1^3A_2(0)$). Due to the SOC between the electronic GS and the excited triplet states, the total nuclear wavefunction of the initial state can not anymore be assumed as purely singlet but reads,

$$\Psi_0(\mathbf{R}, \mathbf{r}) = \sum_{s \in \mathbf{A}'} \mathbf{a}_s \chi^s(\mathbf{R}) \phi^s(\mathbf{r}; \mathbf{R}). \quad (4.6)$$

where the index s runs over all the states of the A' block. The electronic and nuclear coordinates are collected, as before, in \mathbf{r} and \mathbf{R} , respectively. The coefficients a_s are the amplitudes, $\chi^s(\mathbf{R})$ the vibrational wavefunctions on the electronic state s , and $\phi^s(\mathbf{r}; \mathbf{R})$ the corresponding electronic wavefunctions. This new vibrational state will be referred to as the *perturbed* vibrational GS to distinguish it from an *unperturbed* GS resulting from the 1^1A_1 state alone. The perturbed vibrational GS wavefunction is then obtained using the Lanczos diagonalisation of the full Hamiltonian of the A' states that is, including all the SOC elements. Despite the large energetic gap (~ 3 eV) between the 1^1A_1 and the manifolds of triplet states, a small but non negligible contribution from the triplet states is found, with the principal contributions coming from the triplet states $1^3B_1(0)$ with a coefficient of $\sim 2.6 \cdot 10^{-5}$ and the $1^3A_2(+)$ state with $\sim 2 \cdot 10^{-6}$. The other triplet states are involved with coefficients smaller than 10^{-8} and the weakest weight is obtained for the $1^3B_2(-)$. These different contributions can be understood by looking at the different SOC elements between the electronic GS and the triplet states for geometry of the minimum energy of this state. The SOC with the $1^3B_1(0)$ is the strongest with a value $\sim 145 \text{ cm}^{-1}$, then the one with the $1^3A_2(+)$ $\sim 50 \text{ cm}^{-1}$. The perturbation mainly occurs from direct coupling with the GS and the excited states. The coupling with the $1^3B_2(-)$ state is particularly small ($\sim 0.5 \text{ cm}^{-1}$), explaining its weak contribution to the perturbed GS. While the two remaining triplet states present vanishing SOC with the GS in the C_{2v} symmetry, their non-zero contribution can be explained by the conical intersections $1^3A_2(0)/1^3B_1(0)$ and $1^3A_2(+)/1^3B_1(+)$ with states with a strong SOC with the GS. Then we computed the photoexcitation process when we consider the full Hamiltonian (including twelve states see Fig. 4.20).

An important fact arises from dealing with the perturbed GS, is the appearance of new transitions that

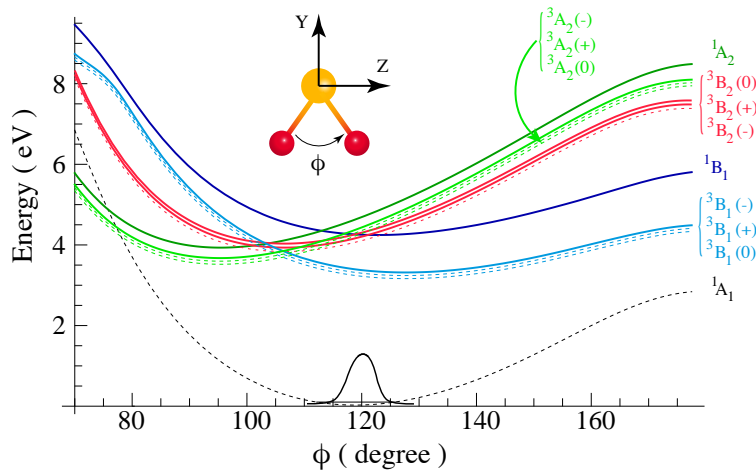


Figure 4.20: Cut of the potential energy surfaces of SO_2 along the bending angle ϕ for the 12 electronic states considered. Those belonging to the A' or A'' block of the Hamiltonian are represented as dashed and solid lines, respectively. The electronic GS of SO_2 is in black. The 1^3B_1 (1^1B_1) states are in light (dark) blue, while the light (dark) green lines represent the 1^3A_2 (1^1A_2) states and the magenta lines are the 3B_2 states. Splitting between the different spin components is artificial, and given for a better graphical representation. In the cartoon the molecule and the Cartesian reference system used along this work are displayed. The molecule lies in the $\{y, z\}$ plane, the x axis being perpendicular to the figure.

can take place not only between the A' and A'' states but also between the A' states depending in the light polarisations that interact with SO_2 . If we assume the unperturbed GS of the molecule, the only allowed transition, will be between the $1A_1$ state and the $1B_1$ state, implying a x -polarised light. Then, due to the non-adiabatic coupling and the SOC between the different excited states involved, the wavepacket would spread over the A'' states, as it was considered in the previous section. In Fig. 4.21a, we present the mechanisms of excitation consistent with this scheme. This is *usually* the only excitation considered in the absorption process, thus no polarisation issue has ever been addressed.

However, if we consider the perturbed GS more transitions may take place depending on the polarisation of the exciting radiation, see Figs. 4.21b and 4.21c. Let $\hat{\mu}$, be the total dipole moment operator and $\hat{\mu}_x$, $\hat{\mu}_y$, $\hat{\mu}_z$ its Cartesian components. From symmetry considerations $\hat{\mu}_x$ induces transitions between states of the A' and A'' blocks, while $\hat{\mu}_y$, $\hat{\mu}_z$ provide transitions between states within the same symmetry block (see Tab. 3.7). Before the excitation, the initial wavefunction, *perturbed* or *unperturbed*, belongs to the A' block, and

thus the $\hat{\mu}_y, \hat{\mu}_z$ operators provide excitations within the A' block only. The transition matrix can be written as:

$$\langle \Psi_f | \hat{\mu} | \Psi_0 \rangle = \sum_u \langle \chi^u | \left[\sum_{s \in A''} \langle \phi^s | \hat{\mu}_x | \Psi_0 \rangle + \sum_{s \in A'} \langle \phi^s | \hat{\mu}_y | \Psi_0 \rangle + \sum_{s \in A'} \langle \phi^s | \hat{\mu}_z | \Psi_0 \rangle \right]. \quad (4.7)$$

Here, the initial wavefunction Ψ_0 is projected, through the dipole moment operator, onto a final state Ψ_f . The index u runs over all the vibrational states of the excited electronic states, the vibrational state of Ψ_0 being already included in its definition. Due to the specific form of Ψ_0 , the transition dipole moments as well as the dipole moments are involved in the excitation. More precisely, y-polarised excitation is dominated by the dipole moment (expectation value) promoting the triplet contribution of the perturbed GS to the corresponding triplet excited states, while z-polarised excitation is mostly governed by the transition dipole moment between different electronic states. Therefore interferences between the different mechanisms are hardly noticeable. Additionally, one should keep in mind that, as (i) we work in a diabatic basis and (ii) the SOC matrix elements are off-diagonal couplings, transitions between pure states of different spin multiplicities are *forbidden*.

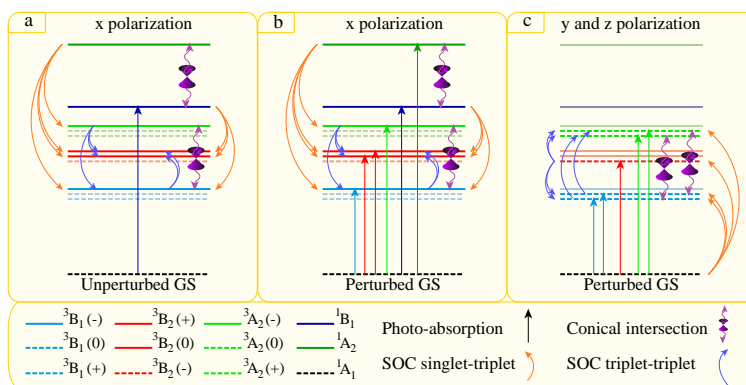


Figure 4.21: Different mechanisms and couplings for the photoexcitation of SO₂. We use the same colour code as in Fig. 4.20. (a) Excitation from the unperturbed electronic GS of SO₂. A direct photoabsorption (straight arrow) can take place from the GS to the 1^1B_1 state with x-polarised light. The vibrational excited states are coupled through a conical intersection between the 1^1B_1 and 1^1A_2 states and SOC (blue and orange bent arrows) between all the different states of the A'' block. Additionally, a conical intersection occurs between the states 1^3B_1 and 1^3A_2 . (b) The GS is perturbed by the SOC in the A' block. More direct transitions could take place considering x-polarised light, where the same coupling occurs as in (a). (c) Direct transitions from the perturbed GS to the states of the A' block with y-or z-polarised light. A direct excitation to the triplet A' states takes place. Then, different couplings occur such as two conical intersections between the same spin components of the 1^3B_1 and 1^3A_2 states.

We shall consider now, from a formal perspective, the two possible coupling schemes among the electronic

states and their influence in the photoabsorption processes, in particular in relation to the "forbidden band". The most straightforward picture results from the consideration of the excitation of the *unperturbed* GS to the A" manifolds where spin-orbit coupling induce an intersystem crossing between excited singlet and triplet states. Then, after a certain time after the excitation process, the wavepacket would start spreading over the remaining coupled states. But an additional mechanism would arise if the SOC also induced a mixing of the singlet electronic ground state and the triplet states leading to the *perturbed* GS, notwithstanding the energetic gap between them. The *unperturbed* GS is responsible for the time-dependent population transfer between excited singlet and triplet states in the molecule seems more plausible at first glance, as addressed previously. This allowed transition dominates the excitation of the molecule in the 3.5-5.5 eV energy range and enables for the intersystem crossing to take place but does not account for the photoabsorption spectrum. For x-polarised light, the spectrum (Fig. 4.22b) exhibits features in the low energy region ($E < 3.5$ eV), which are two orders of magnitude smaller than the experimental ones, and show a totally different vibrational progression. This strong discrepancy refutes this idea. If, on the other hand, we consider the excitation of the *perturbed* GS by using y- or z-polarised radiation (Fig. 4.21c), we obtain the characteristic part of the triplet spectrum (Figs. 4.22c,d) with an excellent agreement with experiment [61], both regarding the spectral intensity distribution as well as and the absolute intensity for the y-polarised excitation. This result demonstrates that the perturbation occurring on the GS vibrational wavefunction due to the SOC in the A' manifold of states is mandatory to interpret the experimental spectrum.

To clarify further the role of the SOC in the different manifolds of states (A' or A"), we have performed simulations where we either include the SOC in the excited states with the unperturbed GS wavefunction (Fig. 4.21a) or neglect the SOC in the excited states keeping the perturbed wavefunction for the GS, the results are presented in Fig. 4.23. In the first case, only a transition along the x-polarisation can take place as the y and z excitations are forbidden by symmetry. The resulting spectrum Fig. 4.23a is identical to the one in Fig. 4.22b, when the perturbed GS is considered. It shows that the perturbed GS plays no significant role in the dynamics in the A" manifolds as we implicitly assumed in Sec. 4.3.1-4. In the second case, when the SOC is not included in the A" manifolds, the y- and z-polarised spectra, Figs. 4.23c and b, respectively, no significant modifications are obtained, while the x-polarised spectrum presents no features anymore below 3.55 eV. Therefore, we conclude that the triplet spectrum of SO₂ is attributed *exclusively* to

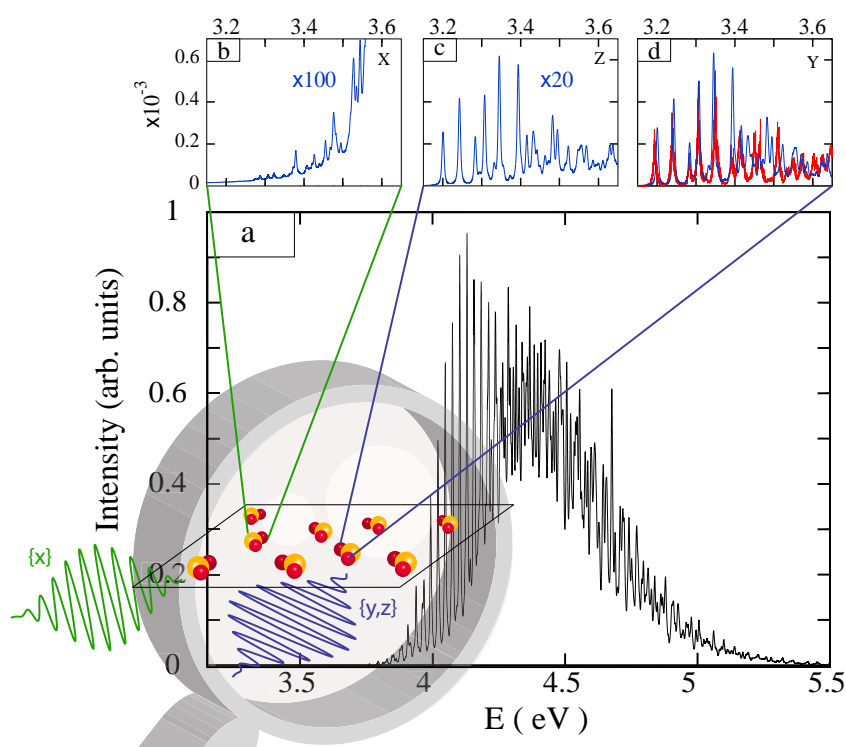


Figure 4.22: Theoretical photoabsorption spectra obtained from the Fourier transform of the autocorrelation function from a wavepacket propagation for 1 ps (except for x-polarisation for which we used diagonalisation due to the weakness of the spectrum in comparison to the singlet one (a)). A damping function of 300 fs is used to reproduce the experimental linewidth. (a) Full spectrum in the range 3.15 – 5.5 eV, with the Clements bands resulting from the singlet states ($E > 3.7$ eV). Frames b-d present the spectra of the triplet states (three orders of magnitude lower in intensity) after alignment of the molecules and for x-, y- and z-polarised light, respectively. The theoretical spectrum (blue line) of d is superimposed with the experimental spectrum (red line) of Hermans *et al.* [61], showing very good agreement.

the perturbed GS wavefunction, resulting from the SOC within the A' state manifold. To the best of our knowledge, the proposed mechanism has never been suggested before in this context and provides a new way to depict the photoexcitation of SO_2 . It is reminiscent of what is reported in the spectroscopy of certain transition metal complexes [149], for which a strong SOC induces a large mixing for both ground and excited states and permits the observation of bands otherwise forbidden. In contrast, in SO_2 , the GS mixing is the *only* relevant aspect present in the triplet absorption spectrum. It should be mentioned that, in the context of the radiative lifetime of formaldehyde, P. Phillips and E. Davidson pointed out in their ab-initio study [150] a similar mixing scheme between distant electronic states (energetic gap 1 eV). The study was limited to the computation of the transition dipole moment, and the effect on the vibronic states of the molecule

was not included. However this makes us believe that this effect is not limited to the sulfur dioxide but is a rather general one.

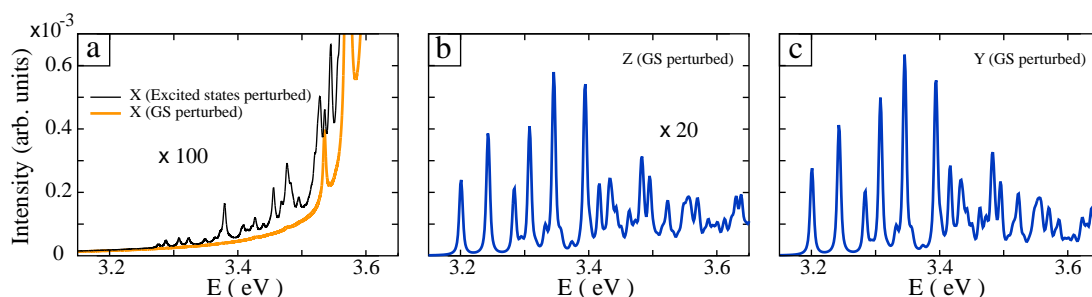


Figure 4.23: To ensure that the SOC between the GS and the A' triplet states is the only responsible mechanism of the observation of the "forbidden-band", three test have been performed. (a) For the x-polarised excitation the SOC have been only considered either in the A'' manifold with an unperturbed GS (thin black line), or only in the A' manifold (perturbed GS) and neglected for the states of A'' symmetry (thick orange line). In both cases the intensity is far to low and the vibronic structures do not match the experiment. (b) Photoabsorption spectrum for z-polarised excitation when the SOC in the A'' manifold is neglected. If the SOC in the A' states is not considered no transition can occur with this polarisation. The spectrum is similar to the one obtained with the full Hamiltonian for features and intensity. (c) Same as previously for the case of a y-polarised excitation. The experimental spectrum is obtained with only the consideration of the SOC in the A' manifold, and demonstrates that these coupling are compulsory to explain the experiments.

These results also give the possibility to understand the mysterious role of the 1^3B_2 states, which dominates the intersystem crossing, but it is no observed experimentally. First we established its role in the A'' manifold for its spin component (0) and (+) states for which there is no coupling with the GS. Secondly, for this manifold no signature of the triplet states has been found in our simulations, with a very low intensity in the energy range of the forbidden band and masked by the singlet spectrum for higher energies. In the A' manifold, the $1^2B_2(-)$ state does not play a role because of its extremely low weight (10^{-11}) in the perturbed GS. As we shown that the experimental spectrum results *exclusively* from the perturbed GS and excitations in the A' manifold, it is not surprising anymore that information concerning the 1^3B_2 state has not been directly obtained experimentally.

The interesting point that should be stressed is that the excitation to the A'' and the A' manifolds present an antagonistic dependence on the polarisation of light. Thus provides us with an experimental way to disentangle their contribution. To this end, the SO₂ molecules should be oriented prior to excitation with linearly polarised UV light. This orientation could be achieved for instance through impulsive laser excitation

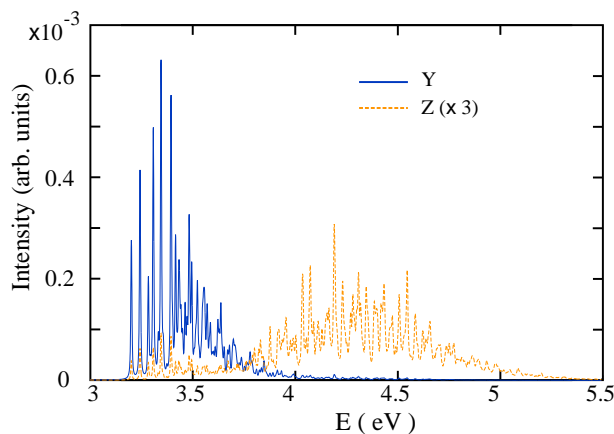


Figure 4.24: Theoretical photoabsorption spectra (same as Fig. 4.22b,c) depicted from 3 to 5.5 eV that is, in the energy range of the Clements bands. In the full blue line the spectrum is shown resulting from a y-polarised excitation and in the dashed orange line as resulting from z-polarised excitation. For better visibility, the z-polarised spectrum has been multiplied by a factor 3

[151, 152] as it has been already successfully demonstrated precisely for SO_2 [153, 154]. We show, in Fig. 4.24, the signal from the y-polarisation, which is strongly damped at energies higher than 4 eV. But for the z-polarised excitation, the spectrum exhibits a stronger absorption for energies between 3.7 and 5 eV. This new part of the spectrum, never observed or predicted before, results mainly from the excitation from the $1^3B_1(0)$ component of the GS wavefunction to the excited $1^3A_2(0)$ state via the transition dipole moment operator along the z-axis. Of course an experimental perfect alignment in order to avoid any excitation into the A'' states does not seem realistic, but the antagonistic effect of the polarisation on the A' and A'' sub-systems, makes it possible to elucidate the different mechanisms and obtain the corresponding spectra. The experimental probe/test of role played by the perturbed GS relies on the fact that the triplet part of the spectrum shows up at lower energies than the singlet signal. For an anisotropic distribution of the molecules in the sample, incident polarised light will modulate the relative intensity between the singlet and triplet part of the spectrum. We emphasise that our reasoning is not limited to SO_2 , but is relevant to many other systems where a symmetry element is present, allowing one to distinguish experimentally the SOC effects involving the ground state (here A' symmetry) from the SOC within the excited-state manifold (here A''

symmetry). Thus, it may apply to any triatomic molecule and also to larger systems where, for a given dynamic process, a plane of symmetry (or similar) plays a role [150, 155, 156, 157, 158].

4.3.6 General discussion about the intersystem crossing

Our work concerning the role of the triplet states in SO₂ raised two fundamental points for the description of such complex systems. The first one is obviously the role of quantum interferences, which strongly governed the efficiency of the intersystem crossover. They result from the consideration of the geometry dependency of the SOC matrix elements as well as the consideration of the different spin components of the triplet states, which have been explicitly included. Looking at the previous works concerning the spin-orbit coupling, the latter is often computed for selected molecular geometries and assumed to be constant, see for instance Ref. [157]. Such approximation has been used recently for the specific case of the SO₂ molecule [133], but we demonstrate that we need to go beyond this approximation to achieve quantitative results. It may be possible that the yields of intersystem crossing can be either under or over estimated by a important factor when such approximations are used and it shows the benefits of our method. An other advantage of this method is the straightforward possibility to handle many conical intersections in the system. Moreover the method can be easily extended to study larger systems, keeping in mind that the limiting factor is the computation of the SOC elements. In addition the physical interpretation of the results is simplified thanks to the used of the spin-pure and diabatic electronic states, providing in our case a new interpretation of mechanisms involved in the photoabsorption spectra of the triplet states. We actually do not believe that this effect is a peculiarity of the sulfur dioxide molecule but should be rather general as far as two or more pathways conducts to the same final states. In the literature, the role of the triplet states is often not considered in the same way that we did. Indeed in the majority of the study, the different SOC between the considered states are computed (with or without geometry dependency), as well as the transition dipole moment including the SOC. But the initial w_p is obtained by applying the different transition operators and the propagation is performed on one electronic state considering an "averaged" electronic states for the different spin components. We clearly established in this study that this approximation could be actually dangerous because it is not possible to know the quality of such statement when different states are involved. Such kind of approximation should give results closer to the incoherent sum of populations, missing in such way a large contribution of the triplet states or overestimated it.

During the elaboration of this work, two studies have been performed concerning the role of the triplet states in the sulfur dioxide molecule. The first published one considered a simpler model than our and obtain a correct agreement with the experimental "forbidden band". Moreover a quite large intersystem crossing to an "adiabatic" triplet state, without any distinction of spin components, has been pointed out. The second work, published recently, used surface hopping techniques to investigate the intersystem crossing and provides results in agreement with our work, with a slight difference concerning the yields. This difference can results from the different methods used, because the semi-classical description of the system cannot take into account the interference effects that we observed. The PES can also be involved in the discrepancy, because the intersystem conversion is strongly dependent of the localisation of the seam of intersection between the singlet and triplet states, as discussed in Sec. 4.3.1-3. In our case, we obtained the photoabsorption spectrum of the triplet states which give us the possibility to adjust, with a global energy shift, the energy of these states. The coupled $1^3B_1/1^3A_2$ states must be shifted by the same amount, but the 1^3B_2 state could be shift in a different way. As no experimental results are available for this state, we shifted it with the same energy than the other triplet states to be consistent. So caution as to be taken when considering the different yields, because the interference may change when the energy change but as they are present for all the states, their primordial role remains believed.

The photoabsorption spectrum of Ref. [133] puzzled us because with our elaborated model we do not obtained similar results. It turns out, after a set of simulation, that it occurs only from an unphysical SOC introduced in the model of the "adiabatic" triplet state and the constant SOC. Then two wrong couplings are implicitly introduced between the triplet states of same spatial symmetry. But these couplings are extremely weak for C_s symmetry and null for the C_{2v} sub-space. Without these strong ($\sim 60 \text{ cm}^{-1}$) but unphysical couplings, the photoabsorption spectrum is not obtained anymore. Actually, the spectrum of Ref. [133] results *exclusively* from the coupling between the $1^1B_1/1^3B_1$ states.

4.4 Photoelectron spectra

In a large variety of pump-probe scheme used to follow the molecular dynamics experimentally, the ionic states of the molecule are involved either as a final states, for instance in time-resolved photoelectron spectroscopy, or as an intermediate state in the case of High Harmonic spectroscopy. In order to theoretically describes such kind of experiments, the evaluation of accurate cationic states for the molecule is primordial.

The photoelectron spectrum of the molecule, in the 12-18 eV energy range, presents three distinct bands which have been experimentally investigated by Wang *et al.* in 1987 [143] and later by Holland *et al.* [159]. The first two bands (12-15 eV) are close in energy and have been assigned to three different electronic states, \tilde{X} for the first and two (\tilde{A} and \tilde{B}) for the second band, respectively. The third band (including the \tilde{C} , \tilde{D} and \tilde{E} states), 2.5 eV higher in energy, has already been widely studied [160, 161, 162, 163] and will not be discussed here.

Based on the theoretical work available at that time [39, 164], the different electronic states \tilde{X} , \tilde{A} and \tilde{B} have been identified as 1^2A_1 , 1^2A_2 , and 1^2B_2 , respectively. This designation was valid until the work of Li *et al.* [141], in which they computed, at the CASPT2 level, the three lowest ionic states of SO₂ and the corresponding ionisation potentials. They pointed out that the ordering of the electronic states of the second band should be in fact 1^2B_2 and 1^2A_2 . This new assignment has been confirmed then by many other ab-initio works [142, 162, 140]. Note that, while a cut along the bending mode of the molecule in C_{2v} symmetry was computed in [141], revealing the presence of a symmetry-allowed conical intersection (CI) between the 1^2A_1 and the 1^2B_2 states, it was not addressed in that work nor in any other subsequent ones.

Photoelectron spectra of SO₂ were already computed in two theoretical works where they addressed different bands. In the first one, Zhang *et al.* [139] studied the first band (\tilde{X}) of the spectrum using an iterative Franck-Condon analysis from optimised geometry calculations. In spite of not handling the CI in the system, they obtained a very good agreement between their results and the experimental ones [159]. The second work, carried out by Chang *et al.* [140], addressed the issue of the \tilde{B} state of the spectrum. It has been obtained from the calculation of the Franck-Condon factors in a harmonic approximation, including only the C_{2v} symmetry. As the state 1^2A_2 , which gives rise to this band, is not coupled with the lower ones, their results are also in good agreement with the experimental ones [143, 159]. Note that no work addressed

the role of the \tilde{A} state in the spectrum before ours.

In the same manner than the case of photoabsorption, the photoelectron spectra can be computed using the Fourier transform of the autocorrelation function Eq. (2.166) in Sec. 2.5.1. The only difference resides in the transition matrix elements for the transition. In the case of the photoelectron spectra, the transition matrix elements of the ionisation should be considered. These latter depend on the final electronic states as well as the photo energy of the exciting radiation and the geometry of the molecule. These quantities can be accurately computed thanks to the use of the Dyson orbital [128, 129]. Such kind of study is relevant when the role of the photon energy and/or the molecular orientation according to the light polarisation are considered. In our case we want to compare our results with experiments carried out without alignment and with a large photon energy in comparison to the ionisation potential of the system. Thus we prefer to use a set of approximations. First, as we work in a diabatic electronic basis, we assume a smooth variation of the photoionisation cross section with the molecular geometry. Then we consider that no resonance or autoionising state is involved. With this two statements, we can approximate the photoionisation cross section as a constant, here takes to unity. The selection rules for the ionisation are different from the case of bond-state excitations, because no transition is forbidden by symmetry, then the ground state ionises to any of the three ionic states.

To obtain the first band \tilde{X} , we start the propagation of the initial wavepacket on the 1^2A_1 state. Due to its coupling with the 1^2B_2 state through the CI, the propagation includes both states. The time dependent diabatic (dashed green) and adiabatic (red line) populations are reported in Fig. 4.25a. Despite the presence of the conical intersection, the wavepacket stays almost exclusively on the 1^2A_1 state, leading to a very small difference between the adiabatic and diabatic populations over 300 fs.

This behaviour can be understood when we look at the vertical ionisation energies (IP) (see Tab. 3.6). The vertical IP from the GS to the 1^2A_1 state is ~ 0.3 eV lower than the minimum energy of conical intersection lying at 12.36 eV. Then only a small amount of the wavepacket can reach the upper diabatic state 1^2B_2 . The autocorrelation function $C(t)$, see Fig. 4.26(a), presents a strong revival with a period of ~ 86 fs, which is responsible for the energy spacing in the spectrum of the \tilde{X} band presented in Fig. 4.27(a). The progression of low energy frequencies in the spectrum results from the successive excitation of the bending mode of the molecule. It is consistent with the equilibrium geometry of the two states reported in Tab. 3.1 and Tab. 3.5. The bond length of the GS and the 1^2A_1 state are identical with $R_s = 1.448$ Å, but the bending angle ϕ is

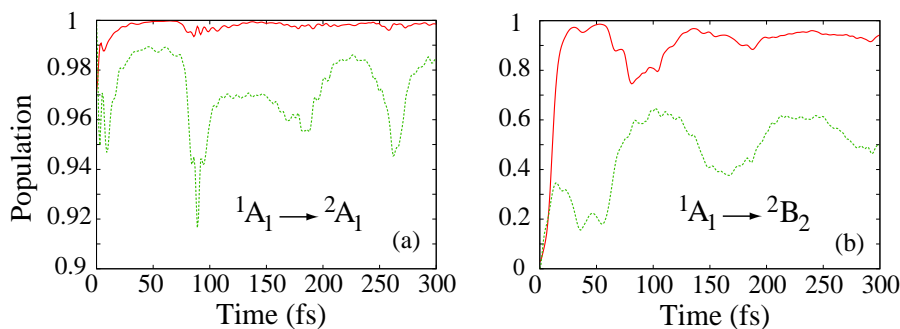


Figure 4.25: (a) Representation of the lower adiabatic (red) and 1^2A_1 diabatic (dashed green) populations as a function of the time. The wavepacket starts on the 1^2A_1 state and only a small fraction reaches the 1^2B_2 state. (b) Lower adiabatic (red) and same diabatic (dashed green) population with the initial wavepacket launched on the 1^2B_2 state.

slightly different ($\sim 10^\circ$) between these states. Thus, few levels of the bending mode are populated. The comparison with the experimental results [143, 159] and the theoretical work of Ref. [139] is very good. For the first six peaks of the spectrum, we found a constant energetic gap of $\sim 403 \text{ cm}^{-1}$ between two successive excitations, identical to the experimental one ($404 \pm 1 \text{ cm}^{-1}$). Our results of the time-dependent population show a strong adiabatic behaviour of the *wp*, and confirm the adiabatic approximation used in Ref. [139].

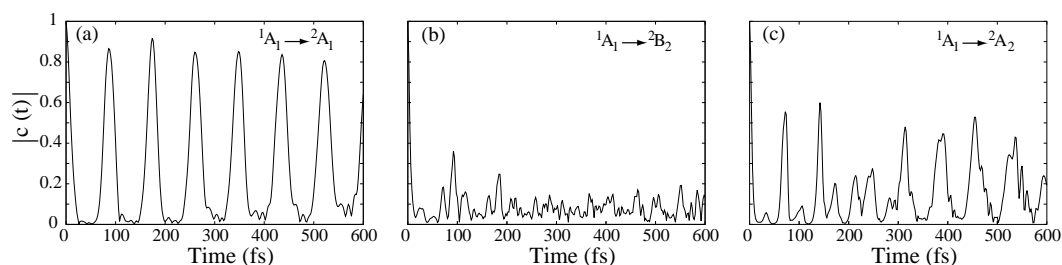


Figure 4.26: Representation of the autocorrelation function as a function of the time. (a) Resulting from the propagation starting on the 1^2A_1 state, (b) starting on the 1^2B_2 state, and (c) starting on the 1^2A_2 state.

We performed a similar calculation for the \tilde{B} band. It originates from the photoionisation of the GS to the 1^2A_2 state, which does not interact with the other ones. This gives us the possibility to propagate the initial wavepacket only on this state. The spectrum, see Fig. 4.27(c), is again in excellent agreement with previous theoretical work [140] and the available experimental data [143, 159]. The energy spacing of $\sim 460 \text{ cm}^{-1}$ between the first intense peaks comes from the periodic revival at 72 fs seen in the autocorrelation function in Fig. 4.26(c). The second peak progression, with a lower intensity, is also well reproduced with an energetic

spacing of $\sim 500 \text{ cm}^{-1}$. This part of the spectrum has been already studied in Ref. [140] and results from the excitation of the bending mode of two different series of the symmetric stretching mode. This assignment is consistent with the equilibrium geometry of the 1^1A_1 and 1^2A_2 PES (see Tabs. 3.1 and 3.5). The difference between the bending angles is $\sim 11^\circ$ and the difference between the bond length is $\sim 0.06 \text{ \AA}$.

We now turn to the last band (\tilde{A}) of the spectrum taking place between the \tilde{X} and \tilde{B} bands. This part of the photoelectron spectrum has never been discussed before. It emanates from the ionisation to the 1^2B_2 state, once again coupled to 1^2A_1 state. The time-dependent population, see Fig. 4.25(b), presents a radically different profile than the one obtained for the \tilde{X} state. The wavepacket is launched on the 1^2B_2 state, $\sim 0.42 \text{ eV}$ higher in energy than the energy minimum of conical intersections. The wp starts on the Upper Adiabatic State (UAS) almost exclusively ($\sim 97\%$), because the seam of CI is not in the direct vicinity of the FC area. A fast and efficient transfer of the adiabatic population (red line) is observed between the UAS and the Lower Adiabatic State (LAS). During the first 10 fs, 50% of the total wp is carried over the LAS and the population of the latter reaches 95% after $\sim 25 \text{ fs}$. After this fast transfer, the wavepacket remains principally located on the LAS until the end of our propagation. This second part of the dynamics is reminiscent to the one obtained in Sec. 4.2.1 for the dynamics in the singlet excited states.

The diabatic population in the 1^2A_1 state (dashed green line) presents a totally different variation. For the first 60 fs, its population first increases to reach $\sim 35\%$ until 20 fs and then decreases below 20% until 60 fs. This behaviour was not observed in the case of the singlet states dynamics. The adiabatic PES of the two lowest ionic states are similar to the ones of the singlet states (see Fig. 4.3 and 4.3). The UAS exhibits a minimum for geometries of C_{2v} symmetry with respect to the Q_u coordinate, while the LAS has a double minima. When the wp reaches the seam of CI, it is most likely in the UAS with a predominant C_{2v} symmetry, for which the non-adiabatic coupling is nil. Thus only a small transfer occurs to the 1^2A_1 , because of the small spatial extension of the wp along the asymmetric coordinate. For the first fs of the dynamics, the wp shows that the R_s coordinate is increased. Then it starts to explore small bending angle towards the minimum energy of the 1^2B_2 state ($\phi \sim 100^\circ$). For small angles the PES surface of the 1^2A_1 state is higher in energy than the 1^2B_2 state (see Fig. 3.6) and the diabatic wp quickly turns back to the FC zone (small revival in the autocorrelation function Fig. 4.26(b)). On its way back, it reaches the seam of CI and, as it

belongs exclusively in the C_s symmetry, a transfer to the 1^2B_2 state occurs efficiently. Then both diabatic wp explore the respective minimum of their PES. At $t = 60$ fs, the wp on the 1^2B_2 state turns back to the seam of CI in the direction of the FC area, its larger extension in Q_u provides a large non-adiabatic coupling and subsequently an efficient transfer. The decay in the adiabatic population indicates that a part of the wp goes back to the initial state and a large revival in the autocorrelation function appears. This dynamics shows up again between 100-200 fs, but the wp remains now principally in the LAS state. The wp on this state is split in two parts, each of them localised near one of the minimum along ϕ . This explains the damping in the autocorrelation function and the time-dependent evolution of the population in the different states.

Interestingly, one should note that the spectrum of the \tilde{A} state (Fig. 4.27(b)) presents some features in the same energy range than the spectrum of \tilde{X} ($12.1 < E < 12.4$ eV) with a shift of one quantum of oscillation in the asymmetric stretching mode ($\omega \approx 1200$ cm^{-1}). Furthermore, the fact that the small peaks around 12.4-12.5eV are also present in the experimental results indicates that: (i) it is not an experimental artefact; (ii) the primordial role of the CI in this system. More specifically, through the mixing of the 2A_1 and 2B_2 electronic states, vibrational levels of the 2A_1 state with B_2 vibronic symmetry, i.e. with an odd number of quanta of the coupling mode (asymmetric stretching), become excited in the 2A_1 band. This amounts to the "shifted progression" in question and constitutes the intensity borrowing effect well known in spectroscopy [23] but never addressed so far for SO_2 .

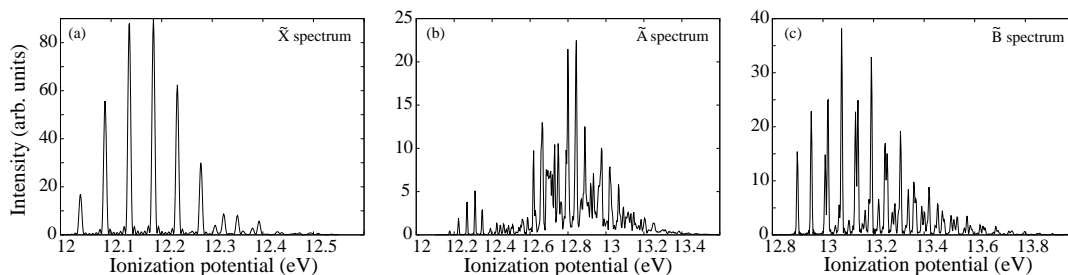


Figure 4.27: Theoretical photoelectron spectra for the different ionic states. On the left panel, the photoelectron spectrum for wp initially launched on the 1^2A_1 state. In the middle, spectrum from an initial wavepacket on the 1^2B_2 state and on the right panel, spectrum for the uncoupled 1^2A_2 state.

The total photoelectron spectrum can be obtained by summing incoherently the contributions from the different states, as represented in Fig. 4.28(a), in comparison with the experimental one [159] 4.28(b). The agreement is excellent for the reproduction of the features of the full energy range. The relative intensities of

the two bands are different and this difference results from the arbitrary assumption of a constant photoionisation cross-section $\tau_f = 1$ for all the states. In the experiment of Holland *et al.* [159], the photoelectron spectrum has been recorded using He II excitation (photon energy of 40.81 eV). The comparison with this experiment gives us the possibility to extract relative values of the partial photoionisation cross-section τ_f for the final ionic state f . Assuming that $\tau_{A_1} = 1$ we find that $\tau_{B_2} \approx \sqrt{1.88}$ and $\tau_{A_2} \approx \sqrt{2}$. On the other hand the ratio between the first and the second band is closer to the one obtained experimentally in [143], where the He I excitation (photon energy of 21.23 eV) has been used. The difference of the relative intensities between the \tilde{X} , \tilde{A} and \tilde{B} bands in the two experiments [159, 143], results from the different energies of photon used. Indeed, the partial photoionisation cross sections depend on the photon energy. This dependency can be extracted for the different energies, as shown above, and the results are shown in Fig. 4.28(c). This quantitative agreement with the experiment is asserting both the quality of our PES and our wavepacket propagation.

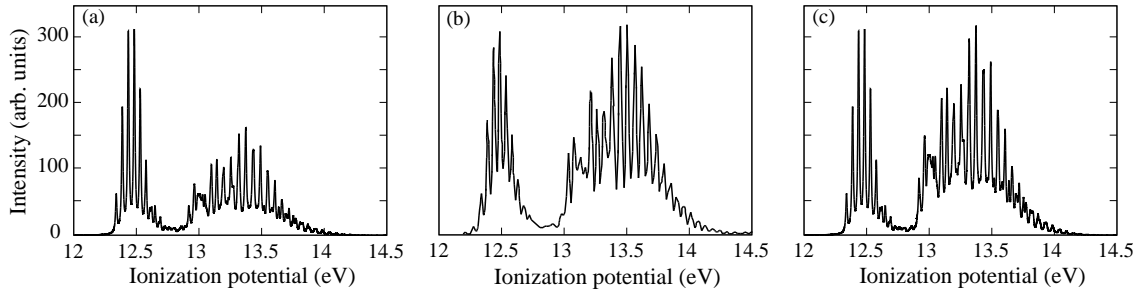


Figure 4.28: Comparison of the theoretical spectrum (a) with the experiment (b) and the adjusted theoretical one (c) according to the partial photoionisation cross section (see text). Very good agreement is achieved between the spectra, except a small shift between the \tilde{X} and \tilde{A} bands ~ 0.1 eV. A global shift of ~ 0.3 eV has been applied to the theoretical spectra.

Chapter 5

Strong field spectroscopy: Following time-dependent dynamics

5.1 Introduction

The different results that we mentioned so far have been obtained by solving the time-dependent Schrödinger equation, introducing in our interpretation of the results the time-dependent evolution of the system. But the experimental results, i.e. the observable of the system, were time-independent and can be described by solving the time-independent Schrödinger equation (see Sec. 4.2.2). The time dependency was introduced as a mathematical tool to simplify the resolution of the equation and to avoid the diagonalisation of the Hamiltonian which describes the system, far too large to be totally solved. This formalism describes an experiment in which the initial wp results from light excitation of a laser field of an infinitesimal time duration, which obviously is not available experimentally, but experimentally it is possible to observe similar dynamics.

5.2 multiphoton ionisation: Following wavepacket dynamics

Time-resolved spectroscopy is nowadays a fundamental method to understand the dynamics that occurs during a physical or chemical process. Since the seminal studies of Zewail [165], in which the femtosecond time

scale was obtained, this method has been widely applied to "follow" chemical reaction or vibration/rotation in molecular systems. The corner stone of the time-resolved spectroscopy is the pump-probe scheme, in which the system is initially excited by a pump to initiate the dynamics in the system and is then probed by a second field, the probe. By varying the delay between the pump and the probe, snapshots of the induced dynamics can be followed. To study vibrational dynamics or bond breaking in a molecular system, the Time-Resolved PhotoElectron Spectroscopy (TRPES) is convenient and well spread technique. The pump is a laser pulse, which excites the molecule and populates different vibrational levels of the electronically excited states. In order to obtain a coherent superposition of vibronic states and thus initiates a dynamics, a short pulse duration is required. Then a second laser is used as a probe and ionises the system after a delay τ . The photoelectrons, ionised by the probe are then collected and the dynamics of the neutral molecule can be followed. A review on the subject has been published a few years ago [166].

Coming back to SO_2 , such experiments have been recently performed by I. Wilkinson *et al.* [71]. In this case the molecule was first excited by the pump to obtain a coherent superposition of the vibrational states involved in the Clements bands. To this end a laser pulse with a duration of 100 fs and three different pump energies have been used: ~ 4.03 eV to excite the C-D bands, ~ 4.12 eV to excite the F-G bands and ~ 4.28 eV to excite the NN'-O system, see Fig. 5.1 from Ref. [71]. Then after some delay τ a probe was used to ionise the system and the photoelectron rate is recorded as a function of τ . To understand the oscillatory behaviour of the photoelectron rate with respect to the time-delay obtained in the experiment [71], see Fig. 5.2, different mechanisms can be evoked. But according to the time period of the photoelectron rate evolution, it seems likely that the *wp* dynamics in the Clements band is observed. To clarify the role of the different steps of the process and determine the most important contributions we carried out a theoretical study of this experiment.

The key points of the experiment have been enumerated in the original article [71] and can be summarised as follow, (i) first the molecule in its vibrational ground state is excited to the first singlet excited states with the pump pulse, (ii) then it freely evolved in the manifolds of states during the pump-probe delay to finally (iii) get ionised by the probe and the photoelectrons are collected. The problem resides in the knowledge of the excitation path, which conducts to the photoelectron emission. In view of the intensities and energies of the pump (10^{12} W/cm², $\omega_p \in [4.03, 4.12, 4.28]$ eV) and probe (4×10^{12} W/cm², $\omega_s = 3.09$ (3.12) eV)

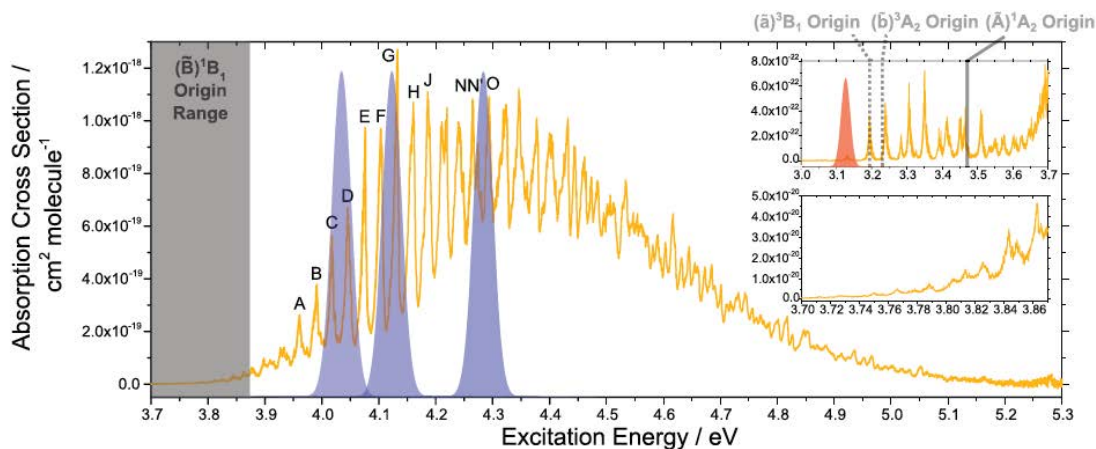


Figure 5.1: Room temperature, gas phase absorption spectrum of SO_2 recorded by Vandaele *et al.* [60] showing the profile of the Clements bands. The (blue) spectral profiles of the femtosecond excitation laser pulses used in this study are overlaid at the relevant excitation energies, the (red) probe pulse spectrum is shown in the upper right inset. The principal discrete absorption bands have been labelled accordingly to the notation used by Clements [28]. Figure from the publication of I. Wilkinson *et al.* [71].

pulses used, multiphoton absorption has to be considered in order to understand the experimental results. The absorption of only one photon of the pump and the probe leaves the system ~ 5 eV below the ionisation threshold. Therefore the ionisation must involve a multiphoton absorption processes, either from the pump or the probe. The energy range of the emitted photoelectrons extend from 0.35 to 4.15 eV. Four principal bands (Fig. 5.2) can be identified and are coming from different photo-absorption processes. All these different paths have been detailed in Ref. [71] and only the first band (0.40-0.75 eV), which exhibits the most interesting time-dependent behaviour, is considered here.

5.2.1 The dynamics of the singlet states in the Clements bands

The total theoretical description of the experiment is beyond what is possible to manage nowadays, with the principal limitation being the evaluation of the ~ 20 electronic states which may play a role. Then the goal of the work proposed here, is to design a model with the principal ingredients needed to interpret the results of the experimental work. The first band of the photoelectron spectra shows a periodic oscillation, consistent with the one of the wp propagation in the Clements bands (see Sec. 4.2.1). Thus, the experiment seems to be sensitive to the wp evolution in the singlet excited states. If we consider only the ionisation potential, inferred as the differences of the neutral and ionic states, this oscillatory behaviour is not obvious because

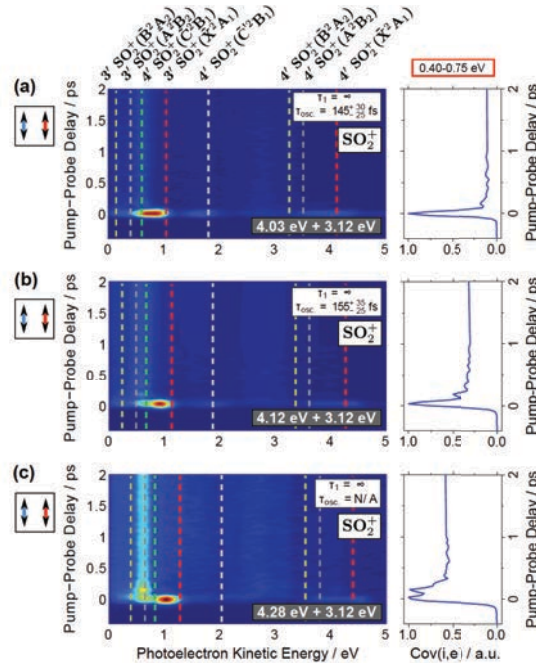


Figure 5.2: TRPES spectra following excitation between 4.03 and 4.28 eV (pump intensity of $\sim 10^{12}$ W.cm $^{-2}$) and multiphoton ionisation at 3.12 eV. The traces on the right-hand side of the spectra show the kinetic energy integrated (0.40-0.75 eV) temporal profiles of the principle photoelectron band. (Figure from the publication of I. Wilkinson *et al.* [71]).

the absorption of one photon from the pump and three from the probe leads to the ionisation of the system for almost any geometry. Therefore, when the wp evolves between the different states no modification of the time-dependent ionisation probability is expected. However if a resonant Rydberg state is invoked, as it has been suggested by Wilkinson *et al.* [71], it can resonantly enhanced one of the ionisation channel. It is the case of the Rydberg state \tilde{G} with a vertical energy of 9.768 eV [167], which is resonant with respect to the absorption of 2 photons of the probe, then a third photon can ionise the system. A two-photon transition is only possible for initial and final states, which belong to the same irreducible representation. Initially, the \tilde{G} state has been assigned by Suto *et al.* [168] to a transition from the $8a_1$ to the $4s$ orbital, providing then A_1 symmetry for \tilde{G} . Later, Xue *et al.* [167] have shown that the transition is in fact from the $8a_1$ orbital to $4p$, thanks to a two-photon experiments. This new assignment of \tilde{G} gives three different possibilities for its symmetry, namely A_1 , B_1 or B_2 depending on the component of the p orbital, p_z , p_x or p_y , respectively. Nonetheless they attributed A_1 symmetry to \tilde{G} following the incorrect assignment of [168]. According to experiment performed in Ref. [167], it seems more likely that they observed the p_x orbital, leading to a B_1

symmetry, which is consistent with the work of Palmer *et al.* [142]. Moreover, according to [142] there is only one state of B_1 symmetry in this energy range. Then, to avoid the computation of a three-dimensional PES for this Rydberg state, we assume that it is equal to the ionic state to which it is converging, i.e. 1^2A_1 , with a global shift in energy. This leads to the introduction of a "gate" in the sense that only one of the singlet excited state, namely 1^1B_1 can be excited toward \tilde{G} and then efficiently ionised compared the 1^1A_2 state.

Then comes the role of the final electronic state of the molecular cation. According to the energy of the released electron (~ 0.6 eV) and the process envisaged for our model, the molecular energy cannot exceed ~ 13.05 eV, for the highest energy pump used. Using our previous results concerning the photoelectron spectra (see Sec.4.4), we showed that the ionisation to the 1^2A_2 state is possible for energy equal or higher than ~ 13.2 eV. Moreover the process include the excitation to the \tilde{G} state, which converge to the GS cation, and as discussed in [71], vibrational overlap with the latter will be preponderant. Then it seems reasonable to consider only the first two ionic states.

All the physical ideas for the experimental interpretation are included in the above model, which includes the electronic GS, the two first singlet excited states, the approximate \tilde{G} state and the two first ionic states. The system still remains fairly large, principally when we keep in mind that the laser field has to be included explicitly in the simulations. We limit our study for values of $\tau > 110$ fs to avoid a temporal overlap between the pump and the probe. Thus the three steps can be simulated separately. The first step is performed on the three lowest singlet electronic states (1^1A_1 , 1^1B_1 and 1^1A_2) with the corresponding Hamiltonian expressed as:

$$\hat{\mathbf{H}}_{\text{pump}}(t) = T_N(\mathbf{Q})\mathbf{1}_3 + \begin{pmatrix} W_{GS} & \mu_{GS1} \cdot \mathcal{E}_p(t) & \mu_{GS2} \cdot \mathcal{E}_p(t) \\ \mu_{GS1} \cdot \mathcal{E}_p(t) & W_{1B_1} & W_{12} \\ \mu_{GS2} \cdot \mathcal{E}_p(t) & W_{12} & W_{1A_2} \end{pmatrix}, \quad (5.1)$$

where $\mathcal{E}_p(t)$ is the pump pulse and $\mathbf{1}_3$ the 3×3 unit matrix. As the excitation can only take place along one polarisation direction, we drop the vectorial representation of the electric field and describe it with a sin-squared envelope:

$$\mathcal{E}_p(t) = \mathcal{E}_{0p} \cos(\omega_p t) \sin^2(\pi t/T_p) \quad \text{for } 0 \leq t \leq T_p \quad (5.2)$$

with ω_p the laser frequency, \mathcal{E}_{0p} its amplitude and T_p the total pulse duration. We choose the same values as in the experiments carried out, namely $\omega_p \in [4.03, 4.12, 4.28]$ eV, $T_p = 100$ fs and the pump intensity $\mathcal{I}_{0p} = 10^{12}$ W/cm². The transition dipole moments μ_{GS1} and μ_{GS2} are expressed as

$$\mu_{GSi}(\mathbf{Q}) = \langle \phi_i^e(\mathbf{Q}) | \mu_e | \phi_{GS}^e(\mathbf{Q}) \rangle, \quad (5.3)$$

collecting the nuclear coordinates in $\mathbf{Q} = \{\phi, R_s, Q_u\}$. We introduced μ_e , the electronic part of the dipole operator and ϕ^e , the electronic wavefunction. Both quantities have been computed at the MRCI level all over the 3D PES. The terms W_{1B_1} , W_{1A_2} and W_{12} are the diagonal and the off-diagonal elements of the potential matrix \mathbf{W}_{reg} of Sec. 3.3.1, while W_{GS} is the PES of the GS 1^1A_1 . In C_{2v} symmetry, the transition from the GS to the 1^1A_2 state is dipole-forbidden ($\mu_{GS2} = 0$) but in C_s symmetry this rule is relaxed and the transition becomes possible with a weak transition dipole moment. We included this transition dipole in our simulations, but neglecting it does not change the results.

For time $t > T_p$, the GS wavefunction is removed from the Hamiltonian because it is uncoupled when the pump laser field is off and the propagation is performed only with the singlet excited states. Physically this second step evolution ends up when the probe excites the system, but it is more efficient to propagate this second step for all the range of time, and store the *wf* as an initial condition for the probe excitation. In the third step, we performed the propagation with a 5-state Hamiltonian built from the singlet excited states (1^1B_1 and 1^1A_2), the two lowest ionic states (1^2A_1 and 1^2B_2) and the intermediate Rydberg state \tilde{G} . Therefore, the full wavefunction has five components and can be written as [115, 116]:

$$|\Psi(t)\rangle = |\phi_{1B_1}(t)\rangle + |\phi_{1A_2}(t)\rangle + |\phi_{Ryd}(t)\rangle + \sum_{i=1,2} \int_0^\infty dE |I_i(E, t)\rangle, \quad (5.4)$$

where the index $i = 1, 2$ corresponds to the ionic electronic state 1^2A_1 , 1^2B_2 , respectively. The Hamiltonian

reads :

$$\hat{\mathbf{H}}_{\text{probe}}(t) = T_N \mathbf{1}_{2N+3} + \begin{pmatrix} W_{1B_1} & W_{12} & \alpha_R \cdot \mathcal{E}_s^2(t) & \bar{0} & \bar{0} \\ W_{12} & W_{1A_2} & 0 & \bar{0} & \bar{0} \\ \alpha_R \cdot \mathcal{E}_s^2(t) & 0 & W_{Ryd} & \bar{\mu}_{R1} \cdot \mathcal{E}_s(t) & \bar{\mu}_{R2} \cdot \mathcal{E}_s(t) \\ \bar{0} & \bar{0} & \bar{\mu}_{R1} \cdot \mathcal{E}_s(t) & \bar{\mathcal{W}}_1 & \bar{\mathcal{W}}_{12}^{ion} \\ \bar{0} & \bar{0} & \bar{\mu}_{R2} \cdot \mathcal{E}_s(t) & \bar{\mathcal{W}}_{12}^{ion} & \bar{\mathcal{W}}_2 \end{pmatrix}. \quad (5.5)$$

The electric field for the probe pulse $\mathcal{E}_s(t)$ is again given by Eq. (5.2), with the following parameters $\omega_s = 3.09$ (3.12) eV, $T_s = 120$ fs and the probe intensity $\mathcal{I}_{0s} = 4 \times 10^{12}$ W/cm² to match the experimental conditions of Ref. [71]. We introduced the coupling constant α_R , which describes the two-photon absorption from the 1B_1 state to the Rydberg state. This is the only possible transition from the valence excited states as the transition from the 1A_2 state is forbidden by symmetry. The description of the electron continuum has been introduced in Sec. 2.5.2. In addition the Hamiltonian, Eq. (5.5), involves 2 other transition matrix elements, μ_{R1} , and μ_{R2} which couple the Rydberg state \tilde{G} to the two ionic states, 1^2A_1 and 1^2B_2 . Computing α_R , μ_{R1} , and μ_{R2} is a rather difficult and tedious task because it requires the determination of the electronic wavefunction associated to \tilde{G} , which we chose not to perform. We opted for empirical determination of these values, with $\alpha_R = 11$ a.u., $\mu_{R1} = 0.25$ a.u. and $\mu_{R2} = 0.05$ a.u. These choices were motivated by (i) the physical meaning of the couplings, (ii) reproducing the experimental results of [71] and (iii) independence, apart from a scaling factor, of the spectrum and time-dependent populations when dividing these coupling constants or the probe intensity by two. For example, the choice of $\mu_{R1} \gg \mu_{R2}$ arises from the fact that μ_{R1} describes the transition $\tilde{G} \rightarrow 1^2A_1$, which corresponds to a direct ionisation of the Rydberg orbital leaving the ionic core unchanged. On the other hand, μ_{R2} describes the transition $\tilde{G} \rightarrow 1^2B_2$, which involves a two electrons process with the ionisation of the Rydberg orbital and the excitation of the ionic core, making it less likely than the previous one. The signal in the experiment present a period of ~ 140 fs, then a step of 25 fs for the delay between the pump and the probe was chosen.

The results of the time-resolved photoelectron spectra are reported in Fig. 5.3. For the lowest pump photon energy, the w_p evolves periodically between the 1B_1 and 1A_2 states, which is well reproduced in the time-dependent photoelectron signal presented in Fig. 5.3 (a) with a period of ~ 150 fs. The integration of the photoelectron spectrum, in the energy range 0.40 to 0.75 eV, reveals that these oscillations are slowly

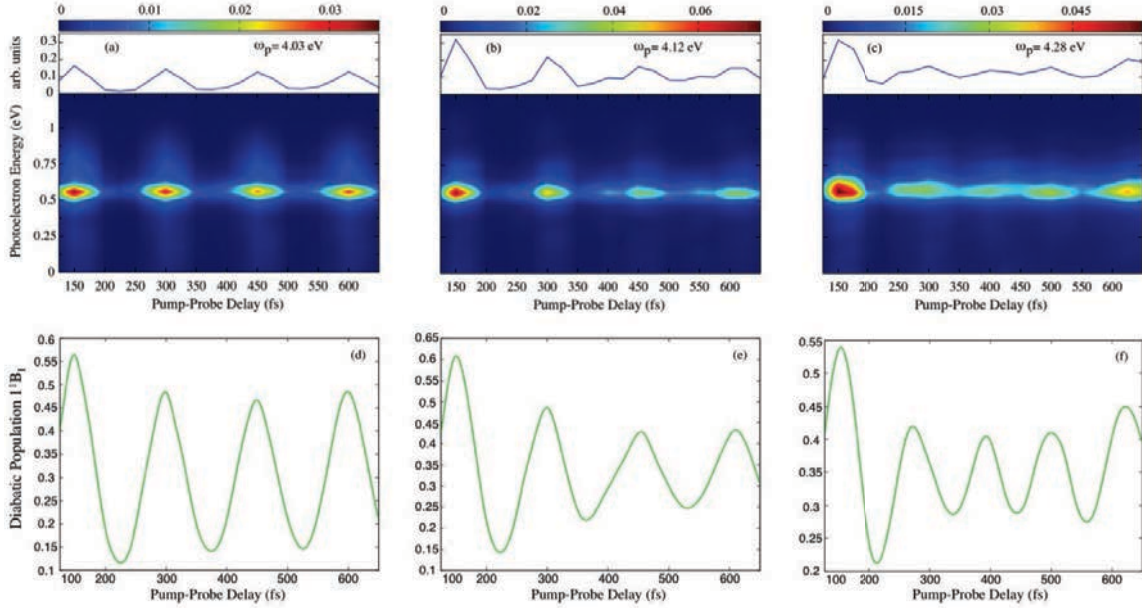


Figure 5.3: (a-c) Photoelectron kinetic energy as a function of the pump-probe delay for different pump frequencies displayed in the upper panels. The colour map indicates the yield of emitted electron. In the upper panels, we plot the kinetic energy integrated temporal profiles of the principal oscillatory band, i.e. $E_{kin} \in [0.4 - 0.75]$. (d-f) Population on the diabatic 1^1B_1 electronic state as a function of the pump-probe delay.

damped. Interestingly, the yield of emitted photoelectrons is close to zero between two maxima. These characteristics are a signature of a well localised wp , providing a strong ionisation when it is localised on the 1^1B_1 state and almost no emission for the time spent on the 1^1A_2 state. In addition, the slow spreading of the wp over the excited states slightly damped the rate of photoelectron during the propagation. For the pump at $\omega_p = 4.12$ eV of Fig. 5.3 (b), the same oscillatory behaviour is observed with a stronger damping in the signal. It results from the excitation by the pump of a higher density of vibrational states. The resulting wp spreads faster on the excited states. For the highest pump energy ($\omega_p = 4.28$ eV), Fig. 5.3 (c), only the first peak in the photoelectron yield is observed for the pump-probe delay $\tau = 150$ fs, then followed by a strong damping. Moreover more than two Clements bands are excited, changing the periodicity in the 1^1B_1 population evolution.

It is interesting to note that, despite the noticeable energy difference of the pump frequency (0.25 eV), the energy of the photoelectron peak remains the same, near 0.55 eV. This behaviour is also observed in the experimental work of I. Wilkinson *et al.* [71] and arises from the two-photon resonance with the Rydberg

state. Due to the similarity of the electronic structure of the \tilde{G} state and the ionic ground state 2A_1 , the PES of both states exhibits similar topographies. While this statement is assumed in our model, the experimental work of Ref. [167] confirms a similar vibrational progressions. Hence, large Franck-Condon factors are obtained when the ionisation leaves the ionic core in the same vibrational states than the ones populated in the Rydberg state. Thus, the additional energy of the pump photon ends up as vibrational excitation of the resulting ion rather than as photoelectron kinetic energy.

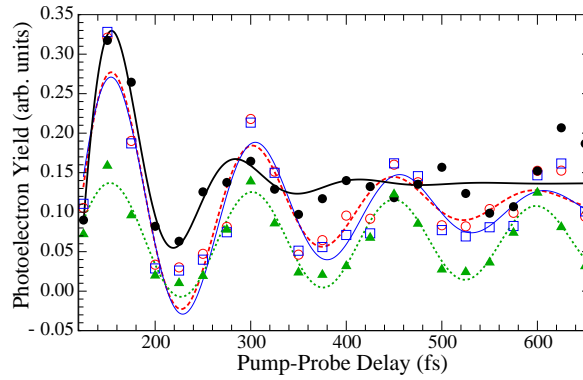


Figure 5.4: Fit of the integrated time-dependent photoelectron yield over the energy range 0.40 – 0.70 eV making use of Eq. (5.6). The solid black line (black dots), the dashed red line (red open circles), and the dotted green line (triangle) represent the fit (data) obtained for $\omega_p = 4.28, 4.12, 4.03$ eV, respectively, in addition to $\omega_s = 3.12$ eV. The thin blue (blue squares) is used to represent the results using $\omega_p = 4.12$ eV and $\omega_s = 3.09$ eV.

In order to determine the period of oscillation ($T = 2\pi/\omega$) and the damping time (τ_d) of the photoelectron spectrum, we fit the yields obtained after integration using an oscillating function with an exponential damping,

$$S(t) = a + e^{-t/\tau_d}(b + c \cos(\Omega t + \phi)). \quad (5.6)$$

The results of the fit are presented in Fig. 5.4 for the different pump frequencies in addition to a different probe energy (3.09 eV) for the 4.12 eV pump. One should note, in the latter case, a shift in the energy of the photoelectron energy ~ -0.06 eV, which is exactly the difference of energy provided during the excitation to the \tilde{G} state, confirming its essential role in the ionisation process. Periods and "lifetimes" extracted from the fits are collected in Tab. 5.1. For all cases, we obtain similar period of oscillation of the signal (~ 149 fs), which is the characteristic time of the Clements bands. The slightly lower value for $\omega_p = 4.28$ eV (~ 130 fs) is probably due to the numerous vibrational states excited by the pump, but its value is not specially accurate because of the very large damping, as seen in Fig. 5.4.

Very different damping times are obtained when changing the pump energy, ranging from rather long ~ 850 fs for $\omega_p = 4.03$ eV to very short ~ 70 fs, obtained for a pump at $\omega_p = 4.28$ eV. For $\omega_p = 4.12$ eV we obtain a signal time constant of ~ 190 fs for both probe energies. This damping time is a direct signature of the spreading of the wavepacket onto the singlet excited states PES.

Table 5.1: Fit parameters. The energies of the pump and probe are indicated in eV.

Pump Probe	Ω	Period (fs)	τ_d (fs)	ϕ	a	b	c
4.12 3.12	0.0426	147.6	173.5	-0.398	0.115	-0.0594	0.457
4.12 3.09	0.0416	151.1	215.1	-0.213	0.107	-0.0310	0.367
4.03 3.12	0.0423	148.6	847.5	-0.203	0.066	-0.0052	0.091
4.28 3.12	0.0484	129.7	70.7	-1.475	0.136	-0.0497	1.836

The excellent agreement obtained when comparing our spectra with those of the experiments [71], demonstrates that our model includes all important physical features of the mechanism. It clearly demonstrates the important role of the two-photon resonance with the \tilde{G} state of symmetry B_1 . Furthermore, we showed the possibility to map directly onto the photoelectron yield the wavepacket dynamics on the lowest excited states (1^1B_1 and 1^1A_2), via a "pump-probe" scheme. This provides us information on both the periodic motion of the wp and its spreading over the time.

5.2.2 Intersystem crossing and experimental evidence of 1^3B_2

Over the first 600 fs of the pump-probe scheme, we showed that the vibrational spreading of the wp on the coupled singlet states is responsible for the damping of the photoelectron signal as a function of the time. In the experimental results, the damping is observed over a large time (picosecond time scale) and the question of the mechanism has to be investigated. In order to know if the vibration is the only mechanism involved, we extend the time delay between the pump and the probe until 1.5 ps, using exactly the same method than for shorter times. The results are presented in Fig. 5.5 and interestingly the damping of the photoelectron yields do not continue and revivals are even observed. These features can be explained by the fact that the pump laser populated few eigenstates of the coupled singlet states and without anymore interaction the wavepacket dynamics remains the same.

It gives us a strong evidence that other mechanisms are responsible for the damping for time larger than 500 fs. We have shown that the triplet states are relevant in SO_2 (see Sec. 4.3) and they should be included

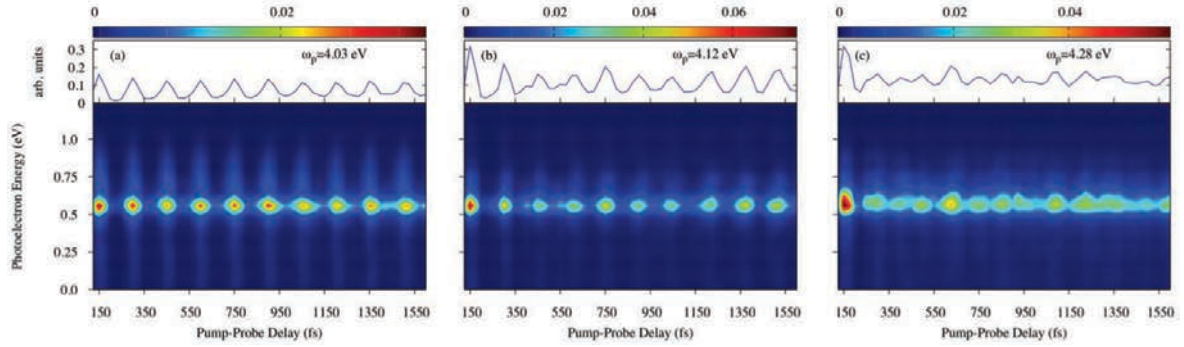


Figure 5.5: Same as Fig. 5.3 for an extension of the pump-probe delay until 1.5 ps.

into our model to describe this "long" time dynamics. We decided to include only the A" block of the full Hamiltonian. It is the one that leads the intersystem crossing of the molecule and we neglect the mixing of the GS wavefunction. The Hamiltonian, which describes the full system with the triplet states, includes 10 electronic states. It can be simplified, as previously, as a 7-state problem for the probe, reading

$$\hat{\mathbf{H}}_{\text{pump}}(t) = T_N(\mathbf{Q})\mathbf{1}_7 + \begin{pmatrix} W_{GS} & \mu_{GS1} \cdot \mathcal{E}_p(t) & \mu_{GS2} \cdot \mathcal{E}_p(t) & 0 & 0 & 0 & 0 \\ \mu_{GS1} \cdot \mathcal{E}_p(t) & W_{1B_1} & W_{12}^s & S_1 & S_2 & S_3 & S_4 \\ \mu_{GS2} \cdot \mathcal{E}_p(t) & W_{12}^s & W_{1A_2} & S_5 & S_6 & S_7 & S_8 \\ 0 & S_1^* & S_5^* & V_{3B_2^+} & S_9 & S_{10} & 0 \\ 0 & S_2^* & S_6^* & S_9^* & V_{3B_2^0} & S_{11} & S_{12} \\ 0 & S_3^* & S_7^* & S_{10}^* & S_{11}^* & W_{3B_1^-} & W_{12}^T \\ 0 & S_4^* & S_8^* & S_{12}^* & 0 & W_{12}^T & W_{3A_2^-} \end{pmatrix}. \quad (5.7)$$

Not taking into account the coupling between the GS and the remaining states of the A' block considerably reduces the complexity of the system, discarding five electronic states as well as the different transition which would take place for a x-polarised excitation. We introduced the non-adiabatic coupling W_{12}^T between the diabatic $W_{3B_1^-}$ and the $W_{3A_2^-}$ states. In addition the different spin-orbit couplings in the diabatic basis (obtained from Sec. 3.4.1) have been labelled S_i . To be accurate, the interaction with the probe should include all the possible the ionisation channels from the 6 neutral electronic states. But to simplify our

simulations, we make the following assumptions: (i) we do not consider the direct 3-photon ionisation but only resonant ionisation, (ii) only the \tilde{G} Rydberg state is taken into account. The former approximation is similar to the one we previously used and we showed that it reproduces the main feature of the TRPES. The second one is more drastic because it has been experimentally shown that a triplet Rydberg state of B_1 symmetry occurs at similar energy range than the singlet \tilde{G} state. This approximation does not result from the fact that including a new intermediate state would be numerically too demanding but because new unknown quantities for the 2-photon absorption and the one photon ionisation matrix elements should be guest. Then depending of their values the role of this mechanism can drastically change and we prefer to assume that it does not play a direct role in the photoelectron rate. With these assumptions, the following Hamiltonian can describe the interaction with the probe,

$$\hat{\mathbf{H}}_{\text{probe}}(t) = T_N \mathbf{1}_{2N+7} + \begin{pmatrix} W_{1B_1} & W_{12}^s & S_1 & S_2 & S_3 & S_4 & \alpha_R \cdot \mathcal{E}_s^2(t) & \bar{0} & \bar{0} \\ W_{12}^s & W_{1A_2} & S_5 & S_6 & S_7 & S_8 & 0 & \bar{0} & \bar{0} \\ S_1^* & S_5^* & V_{3B_2^+} & S_9 & S_{10} & 0 & 0 & \bar{0} & \bar{0} \\ S_2^* & S_6^* & S_9^* & V_{3B_2^0} & S_{11} & S_{12} & 0 & \bar{0} & \bar{0} \\ S_3^* & S_7^* & S_{10}^* & S_{11}^* & W_{3B_1^-} & W_{12}^T & 0 & \bar{0} & \bar{0} \\ S_4^* & S_8^* & S_{12}^* & 0 & W_{12}^T & W_{3A_2^-} & 0 & \bar{0} & \bar{0} \\ \alpha_R \cdot \mathcal{E}_s^2(t) & 0 & 0 & 0 & 0 & 0 & W_{Ryd} & \bar{\mu}_{R1} \cdot \mathcal{E}_s(t) & \bar{\mu}_{R2} \cdot \mathcal{E}_s(t) \\ \bar{0} & \bar{0} & \bar{0} & \bar{0} & \bar{0} & \bar{0} & \bar{\mu}_{R1} \cdot \mathcal{E}_s(t) & \bar{\mathcal{W}}_1 & \bar{\mathcal{W}}_{12}^{ion} \\ \bar{0} & \bar{0} & \bar{0} & \bar{0} & \bar{0} & \bar{0} & \bar{\mu}_{R2} \cdot \mathcal{E}_s(t) & \bar{\mathcal{W}}_{12}^{ion} & \bar{\mathcal{W}}_2 \end{pmatrix}. \quad (5.8)$$

The physical process, described here, is an ionisation occurring exclusively from the singlet 1B_1 state, as previously, but now the dynamics in the neutral states take also into account the intersystem crossing with the triplet manifold. The resulting photoelectron spectra are presented in Figs. 5.6, with $\omega_{pump} = 4.03$ and 4.12 eV for pump-probe delays until 1.5 ps. Compared to the previous results a damping is obtained after 500 fs, which is directly due to the intersystem crossing. Still two issues remain when we want to compare our results with the experiments. First the yield of the emitted photoelectron decreases as a function of the time. It obviously results from our model in which the population of the singlet states is transferred to the triplet states but these latter cannot be ionised. This suggests their role also in the photoelectron signal via

ionisation and *not only* in the dynamics of the neutral molecule. The second difference is the variation of the signal when varying the polarisation between the pump and the probe. This point was not discussed in our previous model because the relevant transition occurs only via the two-photon absorption of the probe and then is independent of the polarisation.

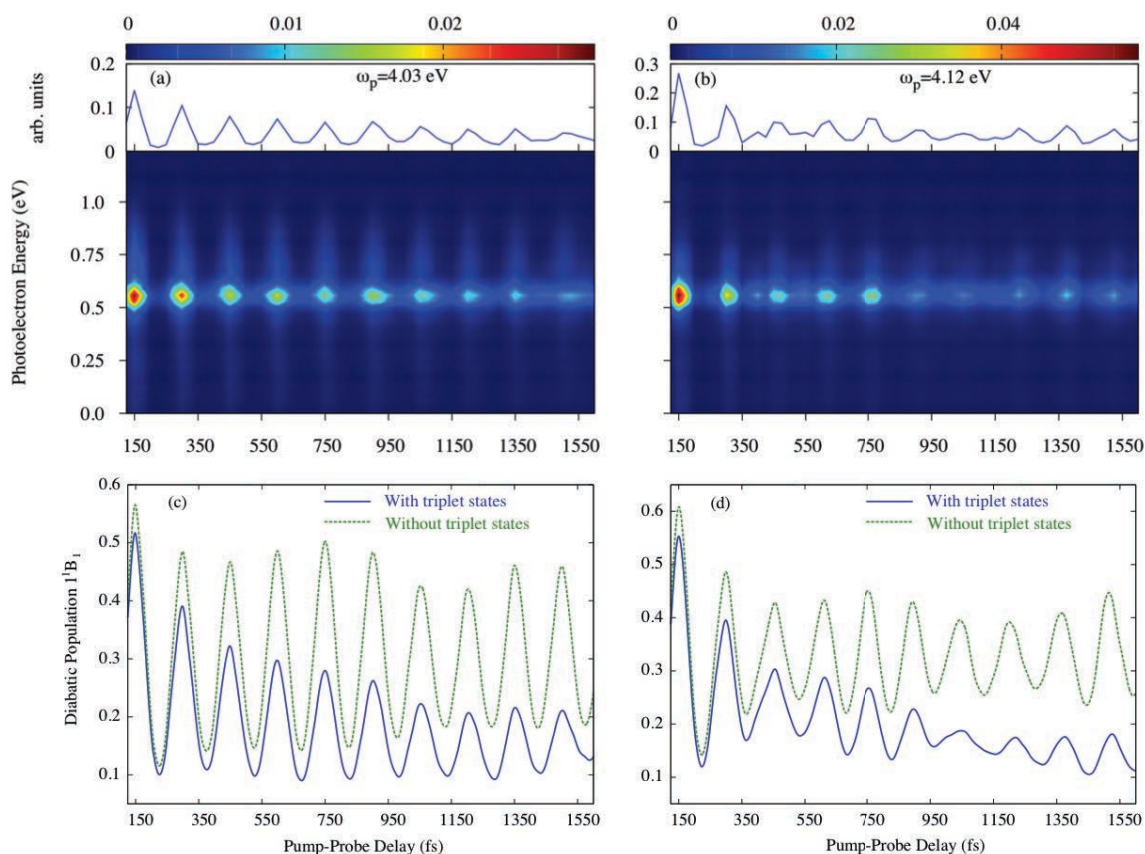


Figure 5.6: (a-b) Photoelectron yields as a function of the pump-probe delay for pump energy of 4.03 eV (a) and 4.12 eV (b), when the dynamics in the neutral states includes the SOC and the all the A'' triplet states. In comparison with the previous results we see a damping of the photoelectron yields for both pump energies when the signal is integrated (solid blue line). (c-d) Population in the diabatic 1^1B_1 electronic state as a function of the pump-probe delay when the triplet states are included (solid blue line) or not (dashed green line). The population when the triplet states are included is systematically lower and the difference increases for longer time delay to end up with a factor ~ 2.5 in both cases.

Even though our simulations do not fully reproduce the experiments, which could disappoint, we can extract information in favour of the experimental interpretation of the role of the 1^3B_2 state. The population of the different electronic states, depending of the pump energies are displayed in Figs. 5.7. The role of the

ionisation of the 1^3B_1 state, according to its low population cannot explain the constant photoelectron rate observed experimentally after 500 fs and its polarisation dependency. Only the ionisation of the 1^3B_2 state can explain the latter with a one photon absorption toward the \tilde{d} , a triplet state of A_1 symmetry, followed by ionisation via three-photon absorption of the probe to the $(\tilde{C})^2B_1^+$ state. The population of the 1^3B_2 states exhibits a similar behaviour than the experimental photoelectron yields, increasing over the first 500 fs and then remaining barely constant. Thus the oscillations are observed when the 1^1B_1 population is higher than the 1^3B_2 ones, and after 500 fs they are masked by the ionisation of the preponderant population of the 1^3B_2 states, which do not present oscillations anymore. Moreover it is consistent with the characteristic time constant of 400 – 700 fs extracted from the experimental data [71] for the different pump energies. The good agreement between the experiments and our simulations, clearly established the preponderant role of the 1^3B_2 state in the photophysics of SO_2 .

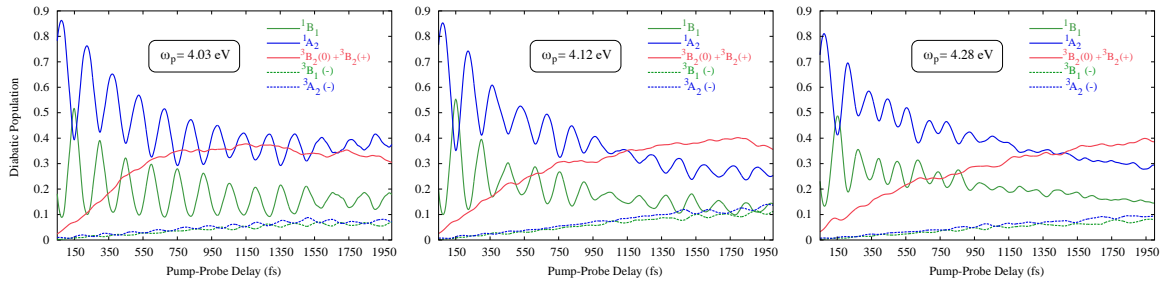


Figure 5.7: Population of the different diabatic states as a function of the pump-probe delay for the three pump energies of the experiment of I. Wilkinson [71]. For the three cases the population in the 1^3B_2 states (sum over (0) and (+) components) presents a fast increasing over the first 500 fs to reach $\sim 40\%$ of the total population (red line). This time scale is in agreement with the experimental one. The role of the $1^3B_1(-)$ state (dashed green) is less important with a population below 10% for all the time.

5.3 Strong field spectroscopy: towards attosecond resolution using HHG

In the previous section we discussed the possibility to follow the nuclear vibration of SO_2 via the TRPES experimental setup. The limitation of the methods is directly linked to the time duration of the probe, which is on the time scale of 100 fs and the complex interpretation of the experimental results. The high-order harmonic generation recently paves the way to the attosecond (as) time scale, taking into account that from

one harmonic to another, the excursion time of the electron in the continuum varies by ~ 100 as. Then, if a time dependent process occurs during the harmonic generation, the different harmonic orders would give information in the *as* time scale. This possibility raised considerable interest to probe electronic and nuclear processes. The electronic dynamics have been successfully observed, for example in the case of the Auger decay [5]. Concerning the molecular dynamics, the work of Baker *et al.* [13] shows that the nuclear dynamics in the H_2^+ cation can be probed via the HHG spectra. This work has been extended by many other theoretical and experimental evidences for a large variety of systems. This experiment used the fact that after the ionisation, the nuclear *wp* is launched on the ionic states and starts to evolve under the action of the ionic Hamiltonian. When the electron is driven back to the molecular cation it recombines with the latter and the efficiency of the recombination will be a direct probe of the overlap between the ionic *wp* and the neutral one. One important point of all the experiments described is that *only* processes which occur during the time of the HHG can be probed. Usually, an IR laser with a period of ~ 2.6 fs is used, which means that the dynamics is probed during a time, which is short compare to chemical reactions. To relate this method to a classical pump-probe scheme, we can use the three-step model [126, 169] to described the HHG process. The first step is the tunnel ionisation of the electron and plays the role of the pump, then the propagation of the electron in the continuum plays the role of the delay line. Finally, the recombination step probes the system and it is why the HHG is often refer to as a self probing scheme. Keeping in mind this possibility of *as* resolution, different experiments have been performed to probe nuclear vibration in molecules as well as dissociation mechanisms. Such kind of experiments has been used to study the vibration of the N_2O_4 molecule [15]. First, a dynamic is initiated by the excitation of one vibrational degree of freedom of the molecule thanks to a short laser pulse. Then the HHG takes place with the irradiation of the system with a strong IR pulse. The rate of the emitted harmonics differ according to the path which is involved in the ionisation step. A weak signal is observed when the HOMO-1 is likely ionised while a strong one occurs from ionisation of the HOMO. More complex systems have been then under consideration, with the possibility of probing dynamics which occurs in the vicinity of a conical intersection, as presented in Ref. [18]. Here again the first step of the experiment is the excitation of the molecule (pump), then the probe is performed by the HHG and the harmonics are detected. For these kind of experiments no previous theoretical model tried to take into account the nuclear *wp* dynamics and our model is applied in the case of SO_2 , for which experimental results have been obtained recently [170].

5.3.1 SO₂ in the vibrational ground state: "Classical" vs "Quantum" description of the molecule for HHG

The High order Harmonic Generation in atoms and molecules has been subject to numerous reviews [171, 172], which deal with the theoretical and experimental side. In this section we consider the Sulfur dioxide molecule in its vibrational ground state. An overview of the important characteristics of the HHG process are depicted for this specific case but here we tried to keep the discussion focus on the novelty of our work. The publications mentioned previously can provide an larger overview of this young research field. We propose in addition to discuss a well spread approximation in the context of the molecular HHG, which consists of the description of the nuclei as a classical system. To solve the electronic part of the problem the *single active electron* (SAE) approximation is used and the TDSE can be solved either numerically or using the Strong Field Approximation (SFA) [73]. In addition, the SFA equation can be solved numerically as well or using the saddle point approximation (*sdp*) to deal with one or all the integrals of Eq. (2.191) of Sec. 2.5.3. These approaches are a direct extension of the atomic case, where the quantum nature of the nuclear is negligible. Here, we want to discuss the quantum nature of the nuclei and the electronic problem is solved with the SFA and the full *sdp* approximation for the integrals. We do not discuss in this manuscript but just stressed that the different approximations mentioned give reasonable results when compared with the TDSE or even the experiments, see for instance [173, 174].

In the classical description of the molecule, the equilibrium geometry of the GS to describe the system. Then the Dyson orbitals (see Sec. 2.5.3) are used to compute the matrix elements describing the ionisation and the recombination of the electron. It is important to note that in this approach, the molecular electronic wavefunction at the MRCI level of theory is used to compute the different matrix elements. The results are presented in Fig. 5.8 for the case of an ionisation to the 1^2A_1 and 1^2A_2 ionic states. In a Hartree-Fock representation, these transitions correspond to an ionisation from the HOMO and the HOMO-2 molecular orbitals, respectively. The ionisation to the 1^1B_2 state is equal to zero in the case of a x-polarised laser field. We first consider the ionisation of the HOMO, which is the most likely case because the tunnel ionisation rate decays exponentially with respect to the ionisation potential. The resulting HHG spectrum is presented in Fig. 5.9 and presents two different parts. The first one, with a constant emission rate for low harmonic orders,

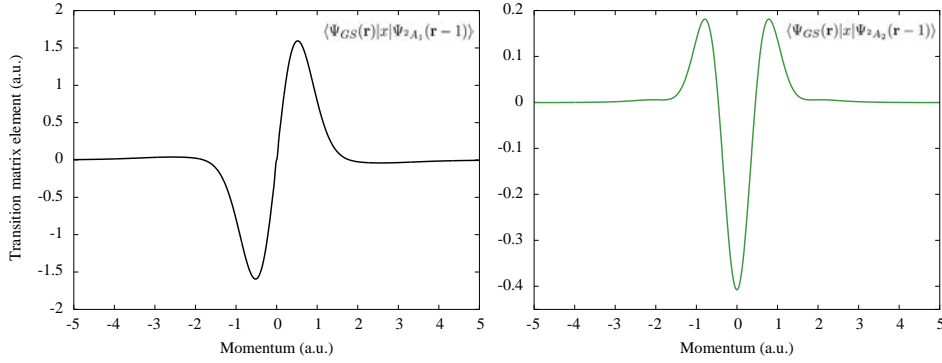


Figure 5.8: (left) Imaginary part of the transition matrix element, as a function of the electron momentum, for the ionisation from the GS (1^1A_1) to the 1^2A_1 state, the real part being zero. (right) Same as before but for the transition to the 1^2A_2 state. In this case the matrix element is only real valued.

is called the "plateau" and the second part, which presents an exponential decay, is the so-called "cut-off". The position of the cut-off can be estimated as $3.17U_p + I_p$ [73], with U_p the ponderomotive energy,

$$U_p = \frac{E_0^2}{4\omega^2}, \quad (5.9)$$

where E_0 is the electric field amplitude and ω its pulsation. Its position depends only on the characteristic of the molecular system (I_p) and the ones of the laser (ω , E_0). Using the saddle-point approximation to solve Eq. (2.191), it introduces naturally in the model the notion of ionisation time t_i and recombination time t_r . In the simple's man (or three-steps model) of Corkum [126] and Kulander *et al.* [169], these times correspond to the time when the electron is released in the continuum and when the electron recombines with the molecular ion, respectively. When the maximal amplitude of the electric field is reached, a burst of electron is released in the continuum depicted by the green squares in Fig. 5.9 and are accelerated by the electric field far from the ionic core. Then the field direction changes and the electrons are driven back to the ion and can recombine with it at different times t_r (green open circles) and a photon is emitted. The energy of the latter is the sum of the kinetic energy acquired by the electron in the continuum and the ionisation potential I_p . From Fig. 5.9, one can see that the harmonics in the cut-off result from one event, i.e. one set of $\{t_i, t_r\}$ (light green). But the harmonics in the plateau result from two different sets of solution for the ionisation and recombination time, describing two different trajectories of the electron. These trajectories are classified according to the time spent by the electron in the continuum. For one harmonic of the plateau, one

trajectory is ionised at a time t_i (intermediate green square) when the field amplitude is maximal and recombine at time t_r after one half-period of the electric field (intermediate green circle). The second trajectory is ionised slightly later (dark green square), when the amplitude of the field already decayed and recombines systematically before 3/4 of the laser period (dark green circle). The first trajectory spent systematically more time ($t_r - t_i$) in the continuum than the second one and thus is called the *long trajectory*, while the second one is the *short trajectory*. The full process appears each half laser cycle (blue colour code) and this periodicity of the process and the symmetry of the system will construct the final shape of the total spectrum with the emission of only odd harmonics of the exciting laser frequency. The saddle-point approximation

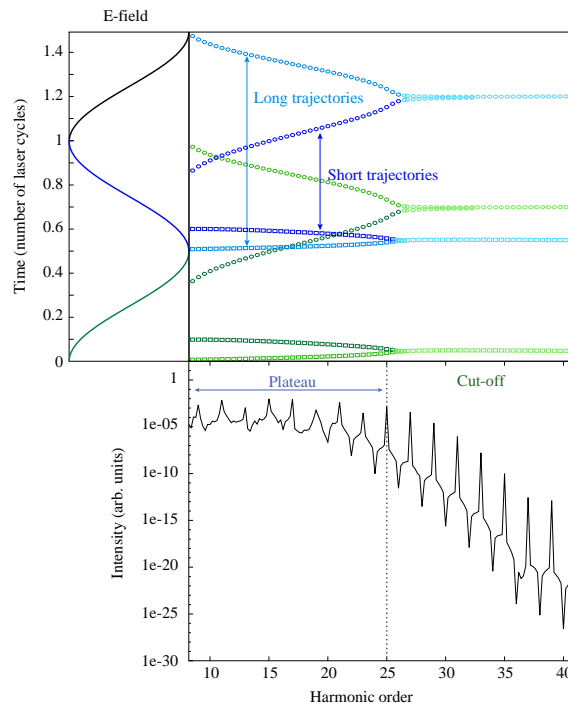


Figure 5.9: The HHG spectrum of the electronic GS of SO_2 is presented, with the indication of the two main characteristics, the "plateau" and the "cut-off". On top, the different trajectories participating to the emission of one harmonic are represented by their emission (open squares) and recombination (open circles) timing, for one and half optical cycle of the laser (left). For each maximum of the laser field, two distinct trajectories emit a photon of the same energy, and are classified as "long" and the "short" trajectory with respect to the electron's excursion time in the continuum.

gives the possibility to compute the emission yields for any frequency because it enters in the set of equation as a parameter. But only the odd harmonics are observed experimentally or theoretically with a "long" (few cycles) laser pulses and from now only the odd harmonics are computed and discussed.

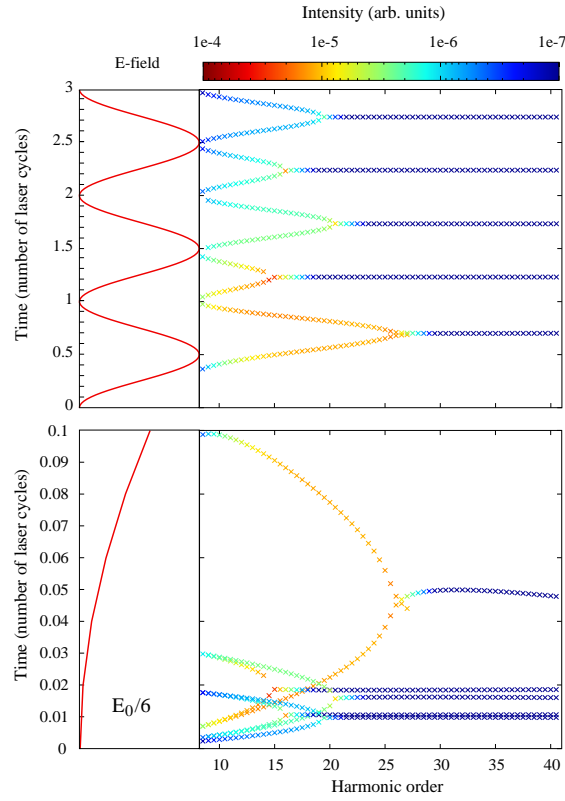


Figure 5.10: After the ionisation, the electron is driving back and forth in the continuum by the laser field and can recombine with the ionic core at different times. When the electron spends more than one optical cycle of the laser in the continuum, the recombination with the core is called "multiple-return" and they are displayed in the top inset. The colour map indicated the intensity of the emitted photons. The bottom displayed the different instant of ionisation for these multiple-returns.

When the electron is in the continuum and is driven back to the parent ion, it is also possible that no recombination happens and the electron continues its evolution in the continuum. In the case of the short trajectories the electron comes back to the ion only once but for the long trajectories the electron visits the ion regularly. At each of these times a recombination can occur and a photon can be emitted. This situation is presented in Fig. 5.10, where only one half-cycle of the laser is used to ionise the system (bottom) but the recombination times are computed over three laser cycles. The colour associated to a set of $\{t_i, t_r\}$ indicates the intensity of the emitted harmonic. We clearly see that the first recombination (first laser cycle) is predominant in the spectrum, the other returns being at least one order of magnitude less efficient.

Looking closer at the ionisation times, it appears that for all the multiple-returns the electron is ionised nearby the maximum amplitude of the laser field. Their emission times are on the same time scale than the emission of the long trajectory of the first recombination. Moreover, these so-called "multiple-returns" do not participate to the higher harmonics of the spectrum, with the cut-off starting systematically before the 20th harmonic. We neglect the multiple-returns in the following, because they weakly participate to the final harmonic spectrum. In addition, for the case of SO_2 their participation in the spectrum decreases when the nuclear dynamics is included. Indeed, this dynamic weights each trajectory with the autocorrelation function (see Eq. (2.191) of Sec. 2.5.3). This function has been depicted in Fig. 4.26 (see Sec. 4.4) for the different ionic states and shows a strong decay for the first 10 fs. Thus trajectories for which the electron spends a long time in the continuum are strongly damped.

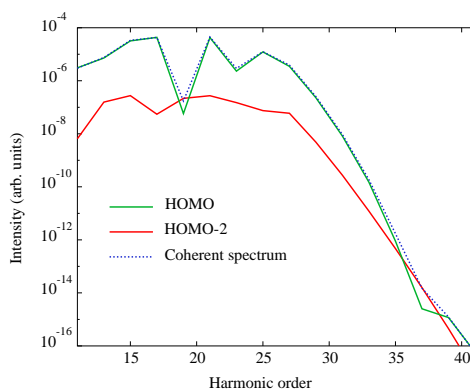


Figure 5.11: High-order harmonic spectra for the ionisation of the electronic GS of SO_2 toward the 1^2A_1 state (HOMO) displayed in solid green line. The spectrum resulting from ionisation to the 1^2A_2 state (HOMO-2) is displayed in solid red line, the coherent sum of the two spectra is presented in dotted blue line.

Not only one channel exists for the ionisation of the molecule. Even if the ionisation of the HOMO is most likely, ionisation can occur for each molecular orbitals during the HHG process. We already mentioned that the transition matrix element to the 1^2B_2 state with a x-polarised laser is zero, but the ionisation to the 1^2A_2 state can play a role with a non-vanishing transition probability, see Fig. 5.8. The incoherent spectra resulting from each of the ionisation channels are presented in Fig. 5.11, as well as their coherent sum. It results that the spectrum is almost not affected by the process involving the 1^2A_2 state and will be not considered anymore. Note that the role of the different molecular orbitals can be strongly affected by the laser polarisation and such study for the special case of SO_2 should be interesting.

Let us now consider our model for the HHG process. Here, the key point is the explicit consideration of the nuclear wavefunction. In the case of the vibrational GS of the molecule, the maximum of probability is obtained for the geometry used to describe the "classical" molecule. Thus, in the case of the classical description, the harmonic spectrum is computed using the mean value of the nuclear wf . For the quantum description (see Eq. (2.202)), the harmonic spectrum is computed for each geometry includes in the DVR and the total spectrum is the coherent sum of all emissions, weighted by the nuclear wf . The lowest vibrational state of the electronic GS is shaped as a Gaussian function and both models give similar results, as presented in Fig. 5.12. The results may seem quiet disappointing because our model required the evaluation of more than 10^5 spectra to finally recover the result of the classical description. It is not surprising that the quantum description agreed that well with the classical one, because nuclear wf exhibits a well defined maximum at the equilibrium geometry. Thus the coherent sum is leaded by the emission of the equilibrium geometry or similar to it. But if the nuclear wf exhibits different maxima or is delocalised, the two descriptions will lead to different results. It is the case, for instance, when a nuclear dynamic is induced prior to the HHG process.

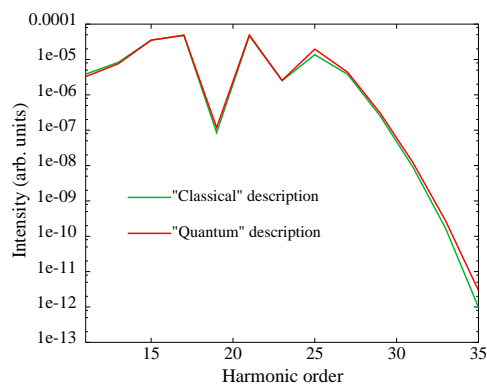


Figure 5.12: High-order harmonic spectra for "classical" description of the nuclei in green and for the "quantum" description in red. In this case only the ionisation to the 1^2A_1 state is considered.

5.3.2 Tracking vibrational dynamics: the case of the electronic ground state

The goal of using HHG spectroscopy, in a chemical point a view, is to be able to follow a chemical reaction thanks to the sensitivity of the HHG with respect to the electronic wavefunction. First, we decided to con-

sider the electronic ground state with a vibrational excited wavefunction. This situation can be obtained experimentally, for instance, by using a non-resonant Raman excitation, because SO_2 has a permanent dipole. No such experiment has been yet performed for this molecule and to simplify the simulation we excited the molecule by simply shifting the ground state PES by 0.6 a.u. along the r_v coordinate. An interesting point of this approach is also the creation of a localised wavepacket with a large amplitude nuclear motion, which seems adequate for our purpose.

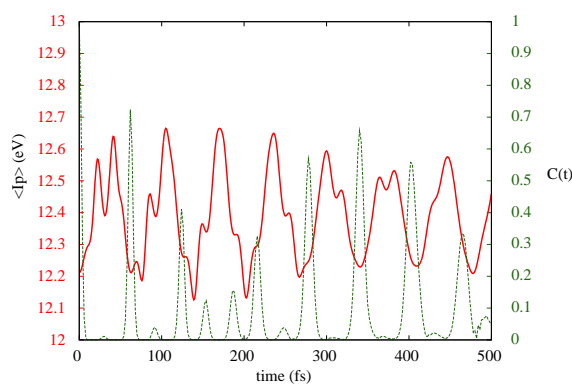


Figure 5.13: The mean value of the ionisation potential (red) and the autocorrelation function (dashed green) are displayed for the time duration of the w_p dynamics.

The two important quantities that are the mean value of the potential ionisation (I_p) and the autocorrelation function are reported in Fig. 5.13. The FC area, where the w_p starts its dynamics, exhibits low I_p values. The mean value of the I_p changes over the dynamics, oscillating between ~ 12.2 and ~ 12.6 eV with a pseudo periodicity ~ 65 fs (see Fig. 5.13). A similar periodicity is obtained concerning the autocorrelation function. Basically the dynamics can be seen as a wavepacket motion with a periodicity ~ 65 fs, which evolves on the PES and presents an I_p variation between the two turning points.

The emission rates of harmonic 11 to 17 are depicted in Fig. 5.14 as a function of the time, for the short (a) and long (b) trajectories. For all the harmonics and for both trajectories the time evolution of the emission rate presents a similar profile. The emission rate exhibits maxima with a periodicity of ~ 65 fs, which is the same than the one obtained in the w_p dynamic. These maxima occur when the mean value of I_p exhibits a minimum, thus the harmonics are highly sensitive to the variation of the I_p . This is not surprising because of the exponential dependency of the ionisation probability with respect to I_p . In addition to the maxima

discussed above, maxima of lower intensity are also observed with a periodicity of ~ 65 fs, but shifted by half a period (~ 32 fs) in comparison to the previous ones. In comparison to the evolution of the mean value of I_p , they appear when the I_p is maximum. The ratio between the different maxima series slightly changes between the long and short trajectories, with a larger difference in the case of the short one. Until 300 fs the rate of the harmonics provides the possibility to follow the variation of the mean value of I_p during the w_p propagation. But for longer time, the w_p spreads over the PES the rate evolution does not follow the one of the I_p . For instance, at $t = 341$ fs a local minimum in the harmonic rate occurs at the minimum value of I_p (see Figs. 5.13 and 5.14). Analysing the wavepacket dynamics over the first 250 fs reveals that the

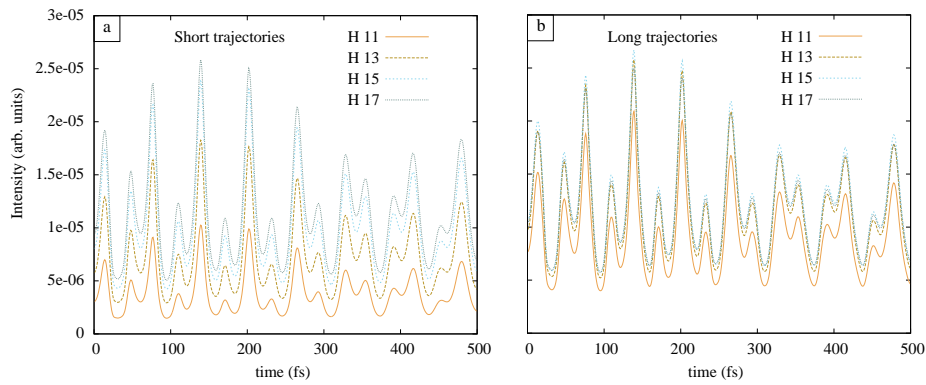


Figure 5.14: Time evolution of the yields of the harmonic 11-17 during the propagation of the w_p on the electronic GS, (a) for the short and (b) long trajectories.

time scale probed by the HHG rates is actually the two turning points. But the maxima of lower intensity appearing for value of I_p close to the maxima are counterintuitive. To clarify this, additional simulations have been carried out to disentangle the role of the two important quantities, the I_p and the transition dipole variations. To study the role of the I_p , we arbitrarily fixed the transition dipole to unity for all geometries and momentum. In the same way, we fixed the value of I_p at 12.5 eV to understand the role of the transition dipole. The results obtained for the 13th harmonic are presented in Fig. 5.15 for the long (a) and short (b) trajectories. The results for the other harmonics are similar. When the dipole transition is fixed, the harmonic yields present roughly an oscillation period ~ 65 fs, and its time variation is an *exact* mapping of the time evolution of the mean value of I_p . For the simulation with a constant I_p , the time evolution of the harmonic rate exhibits a periodicity of ~ 65 fs for the high intensity maxima and the same periodicity for the low intensity maxima, shifted by ~ 32 fs. This result is similar to the full calculation, but the ration between

the high and low maxima is smaller, particularly for the short trajectories. These simulations show that the full calculation exhibits an evolution, which can be seen as the evolution of the transition dipole modulated by the evolution of the ionisation potential. Then, when the I_p is minimum and the transition dipole is at a maximum we get an intense signal. But when the I_p is at the maximum as well as transition dipole the low intensity maxima is observed in the full calculation. The comparison of the full calculation and the simulation with a constant I_p shows that the modulation resulting from the I_p is more important for the short trajectory than for the long one. It is due to the different ionisation timing of these two trajectories. The ionisation of the long trajectory takes place at the maximum of the laser field amplitude, while the ionisation of the short one arises when the field amplitude has already decayed (see Fig. 5.10). As the tunnel ionisation depends exponentially of the ratio: $(-I_p/|E(t)|)$, the short trajectory rate is more sensitive than the long one.

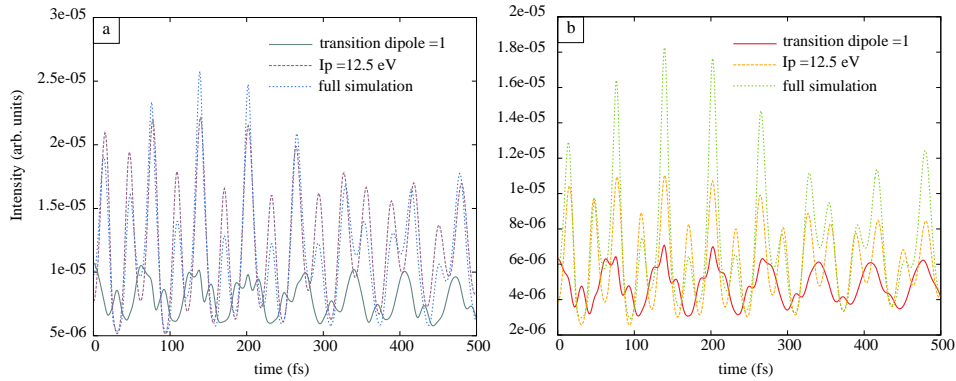


Figure 5.15: (a) To elucidate the role of the ionisation potential and the transition matrix element in the simulation, the I_p has been fixed to 12.5 eV (dashed purple) and the transition matrix dipole to 1 (solid green line) in two different simulations. The results are compared with the full simulation (dashed blue) for the long trajectory of the 13th harmonic. (b) Similar simulations have been performed concerning the short trajectory.

We show here that the HHG spectroscopy is sensitive to the I_p and the transition dipole variations but not in a straightforward way. Nonetheless, when the wavepacket exhibits a "localised" dynamics, our model seems to propose an alternative approach to theoretically describe the time dependent HHG signal. Indeed, it is then possible to consider the time evolution of the mean values of the I_p and the transition dipole to compute the time-evolution of the emission rate. We only discussed the short and long trajectories separately, but we can also coherently sum the emission of the two trajectories. Doing so the time evolution of the rate changes dramatically with the interplay of destructive and constructive interferences. These interferences

cancel out the high intensity maxima observed before. Nonetheless, the signal (not shown) presents the characteristic periodicity of ~ 65 fs, but the low intensity maxima, discussed before, are now the more intense. Thus, separation of the different trajectory greatly simplified the interpretation of the spectra.

The model can be extended in order to take into account the dynamics occurring in the ionic states. It has been shown that HHG spectroscopy is particularly sensitive to the nuclear motion during the time spent by the electron in the continuum. One famous example of this phenomena is the different yields obtained by considering the H_2 and D_2 molecules, which leads to a sub-femtosecond resolution of the nuclear dynamics in the ionic states. In the case of SO_2 , the atoms are much heavier and this effect would be negligible on a time scale of few femtosecond. But as we consider a *wp* dynamic in the electronic GS, different parts of the ionic PES are probed. Because the two lowest ionic states are coupled through a conical intersection (see Sec. 3.3.2) a fast dynamics is expected to occur. Because our initial state is time-dependent, we adopted the following strategy. For each time step (1 fs) of the dynamics in the electronic GS the wavepacket is launched on the diabatic ionic 1^2A_1 state, without any correlation with the outgoing electron. Then the wavepacket is propagated on the coupled ionic states for 3 fs, with a time step of 0.1 fs. This limit has been chosen because all the electrons are coming back to the molecular ion over the first optical cycle of the laser, i.e. 2.6 fs. Then each trajectory is weighted by the overlap between the GS vibrational wavepacket and the ionic one after the excursions time τ , i.e.

$$\Psi_{GS}^*(t, \mathbf{R})\Psi_{Ion}(\tau, \mathbf{R}). \quad (5.10)$$

Considering only the first 200 fs of the dynamic, for every time-step of the propagation in the GS, the *wp* is used as an initial condition for subsequent dynamics in the coupled ionic states. Then the autocorrelation function is computed during the dynamic in the ionic states and is depicted in Fig. 5.16. Even for short time dynamics (3 fs), a large population transfer between the 1^2A_1 and 1^2B_2 state can take place. But the HHG is sensitive to the autocorrelation function. The autocorrelation can decays for two reasons: (i) the *wp* is transferred from the 1^2A_1 state to the 1^2B_2 state or (ii) *wp* stays in the 1^2A_1 state but moves far from the FC area. The first case give a direct information concerning the non-adiabatic dynamics of the *wp* and the second one informs us on the gradient of the PES. Comparing the population transfer between the ionic states and the autocorrelation function (see Fig. 5.16), we can see that a mapping between large population transfer

and a fast decay of the autocorrelation function is not obvious at all. It means that a simple evidence of the non-adiabatic dynamics is not enclosed in the autocorrelation function. But if we compare the dynamics with or without taking into account the non-adiabatic coupling (see Fig. 5.16), the evolution of the autocorrelation function is drastically different. This established that the HHG spectroscopy provides a piece of information of the non-adiabatic dynamics, but requires a comparison with a theoretical description of the system. Thus accurate simulations of the HHG process and experiments can provide enough information to reconstruct the molecular dynamic in such complex situations. Moreover, the HHG provides direct information on the shape of the ionic potential energy surfaces.

We showed that the HHG probes the two different dynamics, (i) the dynamics occurring in the GS thanks to the time-dependent evolution of the emission rate and (ii) for one given time, it probes the dynamics in the ionic states by considering the different harmonic orders. Including explicitly the wavepacket dynamics in both cases shows that the different yields relate the two-dimensional map of the autocorrelation function presented in Fig. 5.16 if we compare it with the case without dynamics in the ionic states. Looking at the emission rate from one harmonic to another at one time t of the dynamic in the GS. For the short trajectories, the emission rate decreases with respect to the increasing harmonic order, because the excursion time τ of the electron in the continuum increases. The opposite effect is obtained when we consider the long trajectories, because the excursion time τ of the electron in the continuum decreases when the harmonic order increases. Experimentally, to observe these effects different isotopes of the molecule must be considered. But in the case of a molecule such as SO_2 the isotopic substitution we lead to a small effect in comparison to molecule with lighter atoms.

To investigate the role of the explicit consideration of the wp dynamics in the ionic states, we compare our results with the one obtained from Eq. (2.197) (see Sec. 2.5.3). In the second case the nuclear dynamics in the ionic states is described by the autocorrelation function. Such a comparison is presented in Fig. 5.17 for the 13th (c) and 19th (a) harmonics. The results are slightly different but time-evolution of the rates are similar for the two harmonics and either the short or long trajectories. We already mentioned that the separation between short and long trajectories seems to be the best choice to obtain the simplest interpretation of the harmonic rate with respect to the nuclear dynamics. But interestingly, when the dynamics in the ionic states

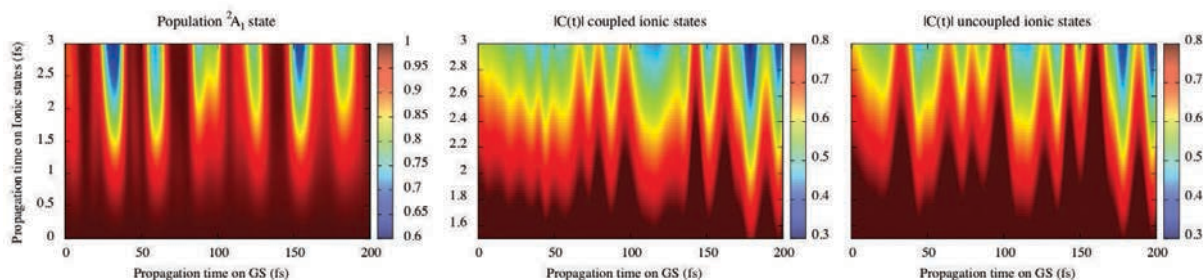


Figure 5.16: (left) Time evolution of the diabatic ionic 1^2A_1 state population over the first 3 fs after ionisation (vertical axis) for the first 200 fs of the dynamics in the electronic ground state 1^1A_1 (horizontal axis). Even for short time dynamics in the coupled ionic states large ($\sim 40\%$) population transfer occurs through the non-adiabatic coupling. (middle) Same as before for the absolute value of the autocorrelation function between ionised wavepacket at time $t = 0$ and the propagated one at time t . A strong variation is obtained for the different propagation times in the GS, but no direct match is found with the population transfer. (right) Absolute value of the autocorrelation function of an hypothetical uncoupled diabatic 1^2A_1 ionic state. The evolution of the autocorrelation function is clearly affected by the presence of the non-adiabatic coupling between the 1^2A_1 and 1^2B_2 state, providing a trace of the conical intersection.

in taken into account with the explicit wp dynamics or with the autocorrelation function, the interferences pattern between the trajectories is strongly different. The case of the 13th and 19th harmonics is the most remarkable, as seen in Fig. 5.17 (b)-(d). These results point out that the HHG is not only sensitive to the displacement of the wp during the dynamics in the ionic states, but also to the evolution of the phase of the nuclear wp during this dynamics.

5.3.3 Probing singlet excited state dynamics

Our previous results showed that the HHG is sensitive to the wp dynamic and the possibility to extract information about the latter. It is possible because transition matrix elements and the ionisation potential depends on nuclear geometry. The method seems ideal to probe chemical dynamics, in which the electronic wavefunction will change over the time and provide information. The dynamics into the excited state manifold presents the principal ingredient of a chemical reaction, with the electronic rearrangement induced by the non-adiabatic coupling and the large amplitude nuclear motion.

Experimentally, the study of the excited state dynamics is particularly difficult, because the pump usually excites only a small fraction of the system. The harmonic emission will principally emanate the molecule in the electronic GS and can mask the emission of the population in the excited states and thus their time-

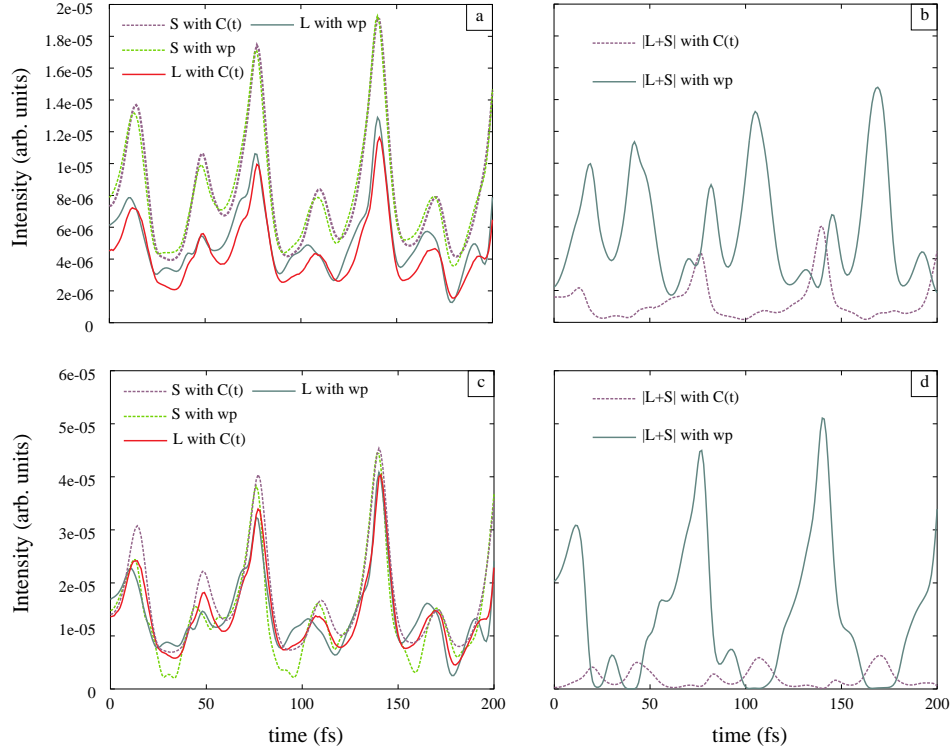


Figure 5.17: (a)-(b) Comparison the time-dependent intensity of the 19th harmonic, when we consider the wp dynamics in the ionic states and when the latter is approximated by the autocorrelation function. (a) The short and long trajectories are presented in both cases. (b) The coherent sum of the short and long trajectories is displayed. (c)-(d) Similar than previously for the 13th harmonic. Note that in this case, the intensity of panel (c) has been multiplied by a factor 6.

evolution. In order to avoid this disagreement, H-J. Wöner *et al.* [17] introduced a judicious experimental setup. A sinusoidal grating of excited molecules is formed in the medium thanks to two crossing laser pulses. Then a probe pulse is used to generate the harmonics, with a delay τ . In the far field the zero order diffracted signal can be approximated as,

$$I_{m=0}(\Omega, t) = |c_g d_g(\Omega) + \sum_i c_i(t) d_i(\Omega)|^2 \quad (5.11)$$

where i runs over the manifold of excited states. The zero-order diffracted signal ($m = 0$) is the coherent sum of the emission of the different states weighted by their respective population. But the first-order diffracted

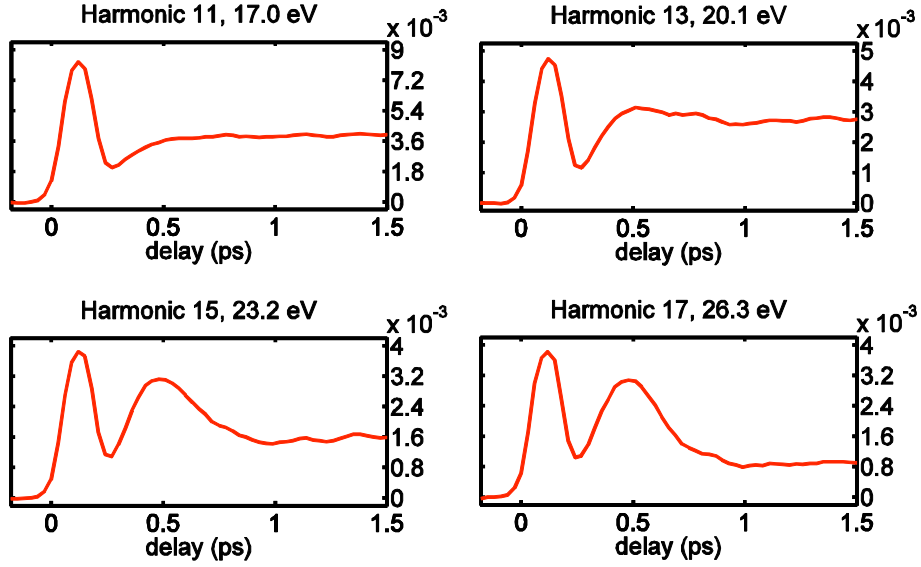


Figure 5.18: Experimental result of the time evolution of the diffracted signal 5.12 with respect to the pump-probe delay for the harmonic 11 to 17. The pump excitation first excites the system in the Clements band, and the excitation is probe by an IR pulse at 800 nm with an intensity of 10^{14} W.cm $^{-2}$. From [170].

signal ($m = \pm 1$),

$$I_{m=\pm 1}(\Omega, t) = \left| \sum_i c_i(t) (d_i(\Omega) - d_g(\Omega)) \right|^2, \quad (5.12)$$

is the interference between the excited and non-excited dipoles, but weighted by the population of the excited states only. It provides a stronger contrast than the zero-order signal.

A pump-probe scheme similar to the one used for the TRPES (see Sec. 5.2) is used. First a pump at 304 nm (4.08 eV) excites the system followed by the HHG probe induced by an IR pulse at 800 nm with an intensity of 10^{14} W.cm $^{-2}$. Considering explicitly the pump, we compute the time-dependent diabatic populations of the excited states, see Fig. 5.19. The results are similar to the one presented in the case of the TRPES experiment (see Sec. 5.2.2). Note that we did not renormalise the population of the excited states because the part of the wavepacket in the GS plays also a role here, see Eq. (5.11). The system is more complicated than the one considered previously (Sec. 5.3.2), principally because of the numerous ionisation channels. To simplify the simulations we neglect the dynamics taking place in the ionics state. The experimental results, displayed in Fig. 5.18, do not exhibit any feature, which could be associated with the dynamics in the singlet states, as previously probed with the use of the TRPES. A feature appears in the signal for a time-delay

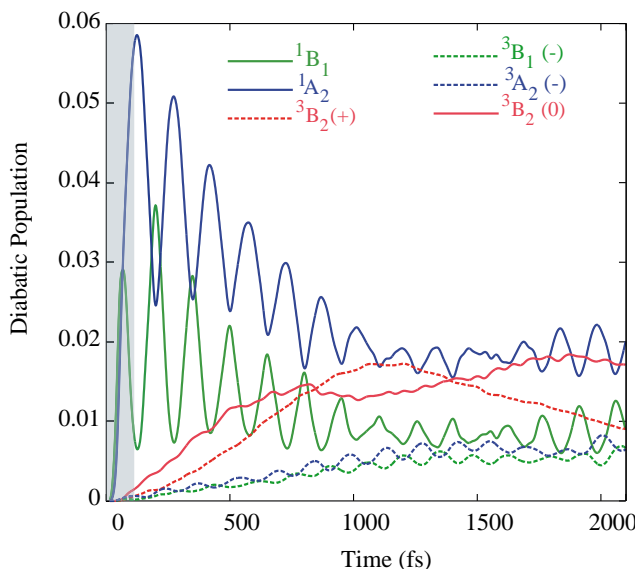


Figure 5.19: Time evolution of the diabatic population of the different electronic states considered with an excitation by a laser pulse of a time duration of 100 fs, energy of 304 nm (4.08 eV) and an intensity of 10^{12} W.cm $^{-2}$ turning on in the grey zone of the plot. In solid blue (green) line is displayed the population of the 1^1A_2 (1^1B_1) state. In the same way the dashed blue (green) depicts the population of the $1^3A_2(-)$ ($1^3B_1(-)$) state. The population of the $1^3B_2(0)$ ($1^3B_2(+)$) state is represented by the solid (dashed) red line. In our model of the HHG, the pump-probe delay and the propagation time are the same.

around 400 fs but this time scale is not observed in the dynamics of the singlet excited states in the Clements bands. In order to describe the experiment, a set of model has been used. First we consider the simple case of a constant transition matrix element for all the transitions and the time-dependent mean value of I_p for each electronic state. This choice is supported by the similar transition dipole matrix elements obtained in Sec. 3.4.3 as well as the previous results obtained concerning the GS dynamics (see Sec. 5.3.2). The calculation of the time-dependent w_p is similar to the one performed for TRPES: during the first 100 fs the system is excited by the pump and then evolves freely in the excited states. Concerning the probe we consider only one-generation cycle, which provides a pump-probe delay identical to the propagation time. The initial time ($t = 0$) is defined as the beginning of the pump pulse. The results of the simulations are displayed in Fig. 5.20 for the 15th and 17th harmonics.

For the two harmonics and either the short or the long trajectory an oscillation of the emission rate with respect to the pump-probe delay is observed. The signal presents strange minima of the emission rate with

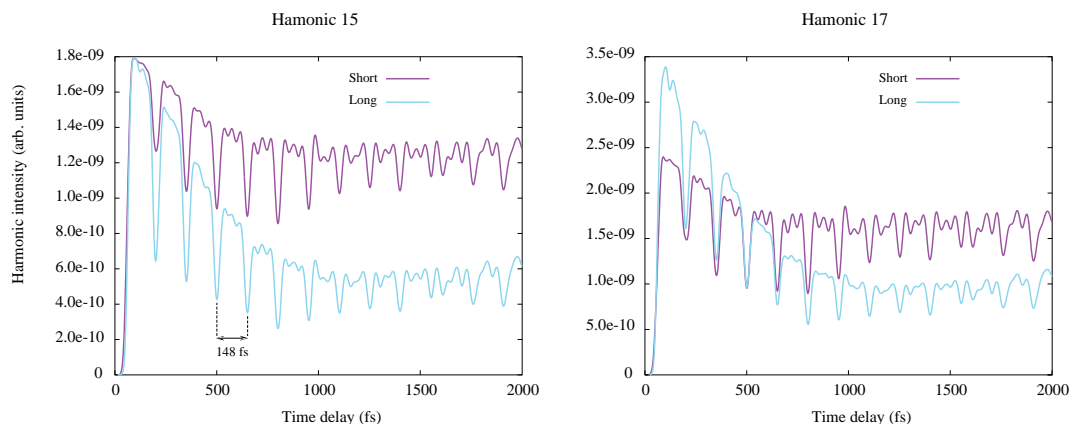


Figure 5.20: Simple model of a constant transition matrix element and a time-dependent variation of the mean value of I_p for each electronic state involved. This simple model was suggested from the results obtained in the case of the GS. The different harmonic, here the 15th (left) and 17th (right) exhibit minima over the time propagation with a period of ~ 148 fs, which is the one obtained for the population dynamics between the two 1^1B_1 and 1^1A_2 states. This sensitivity of the harmonic yields is unfortunately not the one observed experimentally.

periodicity of ~ 148 fs. This periodicity is similar to the one obtained for the oscillation of the population between the 1^1B_1 and 1^1A_2 singlet states in the Clements bands. Thus this simple description of the system suggests the possibility to probe the wp dynamics, but it is in total disagreement with the experimental results. As our simple model can not correctly describe the system, it seems mandatory to take into account explicitly the wp dynamics. These simulations have been performed using the energy difference between the neutral and ionic states to define the ionisation potential at each molecular geometry. In the following we will call this description *model 1*. The results of the simulation are depicted in Fig. 5.21 for the 11th harmonic until the 19th harmonic. For time delays smaller than 1 ps, the long trajectories present, once again, an oscillation of the emission rate characteristic of the wp dynamics in the Clements bands. For larger time delays, the 11th and 19th harmonics do not exhibit features related to the singlet dynamics but rather a faster oscillation with a lower amplitude. Looking at the diabatic population of the excited states (Fig. 5.19), we can see that at ~ 1 ps the population in the 1^3B_2 electronic states becomes higher than the one in singlet states. Thus different behaviour observed before and after 1 ps can result from the emission of the 1^3B_2 states. For the other harmonics, a similar but less pronounced effect is observed. Concerning the short trajectories, maxima in the emission rates are observed for the 11th and 13th harmonics with a period of ~ 148 fs. Minima are observed for the 17th harmonic with a similar period. Model 1 predicts, for the 15th and 19th harmonics, a more complicated time-evolution of the emission rate, from which signature of the wp

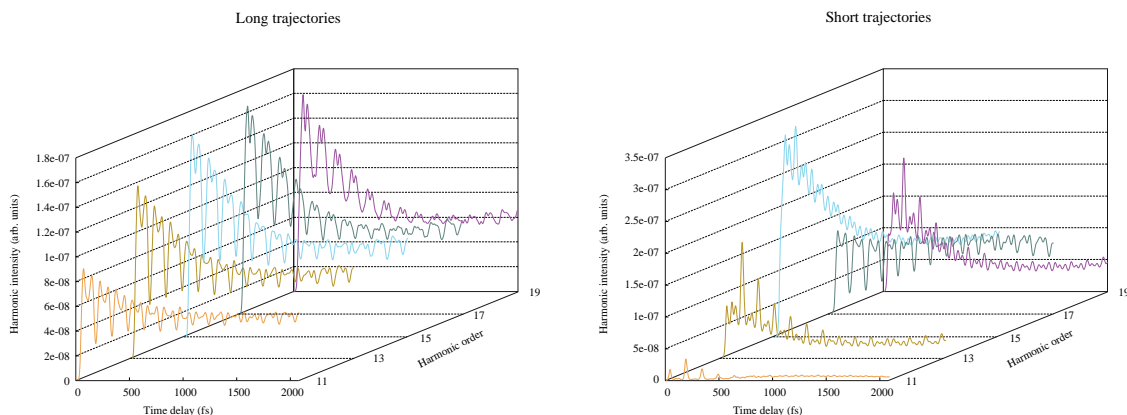


Figure 5.21: First order diffracted signal Eq. (5.12) for the harmonic 11 to 19 for wavepacket propagation of 2.1 ps. In the case of long trajectory (left) a strong suppression of the harmonic yields is periodically obtained. This period is a clear signature of the wavepacket dynamics (~ 148 fs). In the case of short trajectory (right) this signature is obtained by maxima in the case of the 11th and 13th harmonics and minima for the 17th. The harmonic 15th and 19th exhibits a more complex evolution, with no direct relation with the dynamics of the system.

is almost absent. The results for these two harmonics are reminiscent to the experimental observations. The model 1, which explicitly take into account the dynamics of the nuclear wp induced by the pump provides results in better agreement with the experiment, but are still not convincing.

One of the assumption of model 1 concerns the ionisation potential, which is defined as the energy difference between the neutral and ionic states. Physically this definition describes the I_p as the *electronic* ionisation potential. But in the case of a molecular system, the ionisation potential should be evaluated between vibronic levels and is thus different from purely electronic one. Even if this vibronic definition of the I_p the adequate one for a molecule, including this definition in a wavepacket approach is not a trivial task. Moreover, considering a time-independent approach would require the diagonalisation of the nuclear Hamiltonian of the full system, which is far too difficult for large systems. In order to simplify the implementation of a model, which considers the vibronic ionisation, we investigate the physical processes taking place in the system. In the experiment, the pump excites few vibronic states with a spectral width of ~ 30 meV. Within the time-independent picture, these states are eigenstates of the coupled singlet and triplet PES. Moreover, the ionisation of the singlet states will launched a wp onto the two ionic states 1^2A_1 and 1^2B_2 , which also share a set of eigenfunctions because of the conical intersection. First, we assume that the energy difference (~ 30 meV) between the vibronic states populated by the pump is negligible. In other words, we assume

that the wp in the neutral states is described by a single vibronic state with an energy equal to 4.08 eV. Then, we suppose that the ionisation of the singlet vibronic states leads to vibronic state of the coupled ionic PES with the same (or similar) energy. A lower bound of the vibronic I_p can thus be determined from the higher adiabatic excitation energy of the two ionic states, i.e. the one of 1^2B_2 . With these approximations we can roughly estimate the lower value of the vibronic I_p as $I_p = 8.25$ eV (see Tab. 3.6 of Sec. 3.2.4). As the tunnel-ionisation rate exponentially decreases as a function of I_p , we can expect that higher I_p will not contribute to the process. The same approximation holds for the $1^3B_1(-)$ and $1^3A_2(-)$ states, which are ionised to the same ionic states and the same value of I_p is thus assumed. The case of the 1^3B_2 states is slightly different because they ionised to the 1^2A_2 state, which is uncoupled and at higher energies. Following the above reasoning, a constant $I_p = 9.25$ eV is assumed for the 1^3B_2 states. The results obtained with this qualitative model of the vibronic I_p , called *model 2* in the following, are displayed in Fig. 5.22.

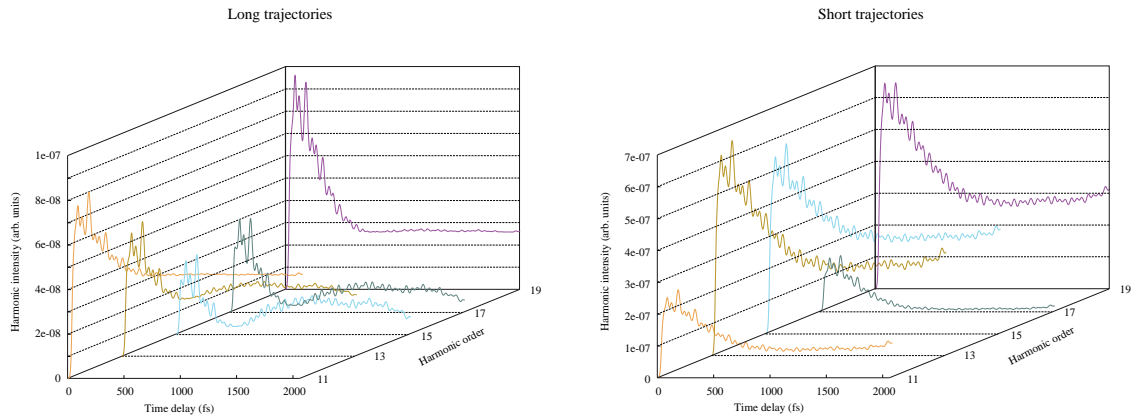


Figure 5.22: First order diffracted signal Eq. (5.12) for the harmonic 11 to 19 for wavepacket propagation of 2.1 ps. In the case of long (left) and short (right) trajectories the vibronic definition of I_p (see text) leads to complex time modulation of the harmonic yields with respect to the time. No clear signature of the underlying wavepacket dynamics is observed. Note that the yields increased for the long trajectories of harmonic 15 (light blue) and 17 (dark green), which is reminiscent to the experimental observations.

In this case, the time-evolution of the emission rate does not exhibit a periodicity similar to the one of the dynamics in the singlet states. The important point is that it is true for the rate of all the harmonics as well as for the short and long trajectories and irrespectively to the time delay between the pump and the probe. In this sense the agreement with the experimental results is good. Interestingly, for the 13th, 15th and 17th harmonics the emission rate of the long trajectories increases for a time delays larger than 500

fs. This behaviour is similar to the one observed experimentally (Fig. 5.18), but somehow smoother and at longer time delays.

To understand why the different definitions of the I_p in the model 1 and 2 considerably affect the results, we performed a state-by-state analysis of the HHG emission. In the following, we will only discuss the results obtained for the long trajectory of the 15th harmonic, because its emission rate is similar to the experimental one for the model 2. To clarify why with the model 1 the dynamics in the singlet states is observed and not in the model 2 we compute the emission rate of the 1^1A_2 and 1^1B_1 , displayed in Fig. 5.23, and the coherent sum of the emission. The two models give very similar results. The variation of the time-dependent emission rate matches the evolution of the population of the electronic states. For each electronic state, the maximum of the emission is obtained when the population in the state is maximum. But the difference occurs when the coherent emission of the two states is considered. Model 1 exhibits constructive interferences for each maximum of the 1^1A_2 emission rate and destructive interferences for each maximum of the 1^1B_1 one. Thus, this interference pattern strongly enhanced the contrast of the dynamics in the singlet states. But model 2 presents a constructive interference pattern for all the pump-probe delays, which leads to a high oscillation of the total rate and the dynamics of the wp in the singlet states is not observed anymore. These results show an interesting point concerning the role of the different definitions of the ionisation potential. The definition of I_p does not influence the time-evolution of the total emission rate because of the exponential decay for the tunnel ionisation, but rather strongly affects the relative phase of the emitted harmonics by the different electronic states.

The fact that different I_p induced a different phase is already known, but we did not suspect that the time-evolution of total emission rate is actually drastically affected by it. Thus to obtain a quantitative description of the HHG in time-dependent molecular systems, we have to define correctly the ionisation potential during the dynamics, which is a real challenge because the vibronic eigenstates are often unknown in these systems. Moreover, in many case the comparison of the different HHG channels for a single geometries, as performed for instance in instance in [15], without considering the vibrational energy can lead to an inaccurate description. Unfortunately, because of a lack of time, we did not manage such kind of study, which seems not adequate on such large system but would be interesting for smaller ones.

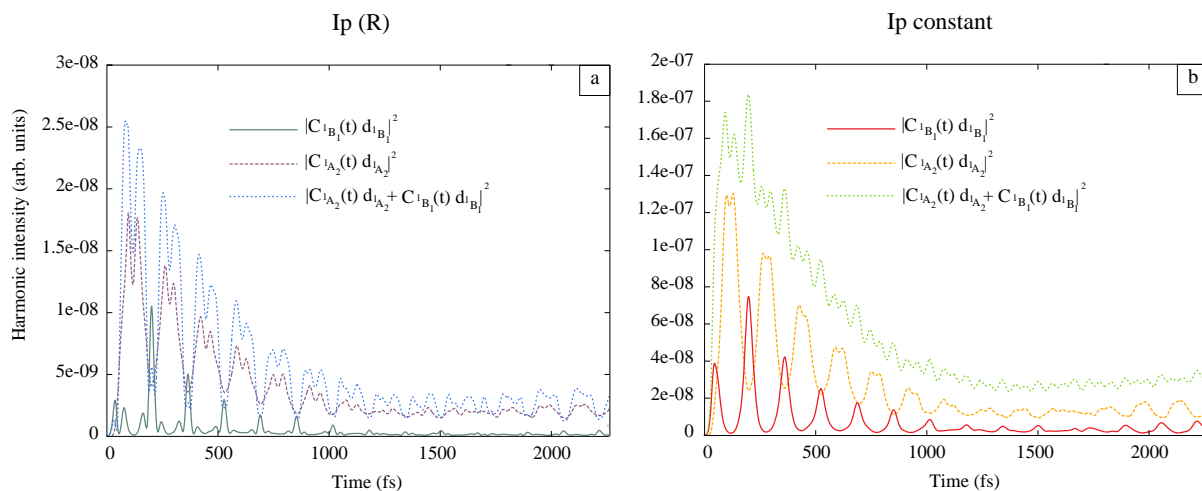


Figure 5.23: Comparison between the two different definition of I_p for the harmonic emission of the singlet electronic states, (a) when the I_p is defined for the electronic wavefunction and depend of the molecular geometry. In solid green (dashed purple) line the emission from the 1^1B_1 (1^1A_2) state. In dotted blue, their coherent sum, which shows coherent interferences for the emission maxima of the 1^1A_2 state and destructive interferences for the maxima of 1^1B_1 . (b) Consideration of a vibronic $I_p = 8.25$ eV, the solid red (dashed orange) line displayed the emission yields of the 1^1B_1 (1^1A_2) state. In this case their coherent sum presents only constructive interferences, which hides the dynamics modulation of the emission yields.

The role of the evolution of the transition matrix elements with respect to the molecular geometry has also been investigated. In order to see its impact we simulate, using model 1 and 2, the harmonic emission using constant transition matrix elements for the two singlet states and equal to unity. We did not observe any influence for the 1^1A_2 state, except a global modification of the emission rate. Concerning the 1^1B_1 state, see Fig. 5.24, an important modification of the time-evolution of the emission rate is obtained. When the constant or geometry dependent I_p is used, the time evolution of the emission rate remains similar. But if the transition dipole is constant, the emission rate exhibits new maxima. According to the results obtained for the GS dynamics (see Sec. 5.3.2), we see that the variation of the transition dipole with respect to the molecular geometry strongly modulate the time evolution of the emission rate. It allows the harmonic emission for only restricted sub-space of molecular geometry for the 1^1B_1 state. Of course the modulation from the population still dominates the total time dependent profile.

Nonetheless, with our approximation of the vibronic I_p in model 2, based on an intuition more than formal demonstration at this point, we can disentangle the role of the different triplet states in the harmonic

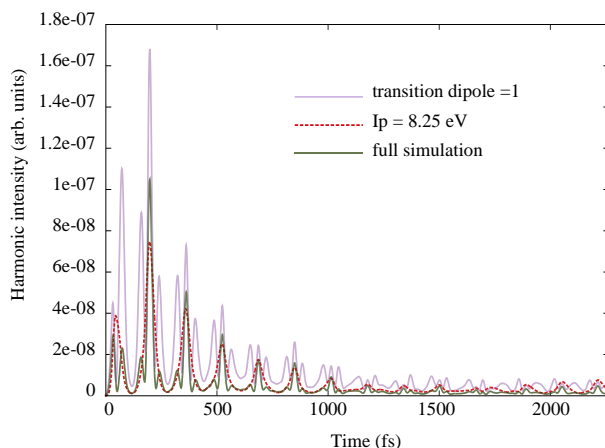


Figure 5.24: Emission yields of the 15th harmonic of the electronic 1^1B_1 state, in the case of a constant transition dipole (purple), a constant value of I_p defined as the vibronic I_p (dashed red) and for the full simulation (green), i.e. with the geometry dependent definition of I_p . The different results obtained between the first and the two last cases show the important role of the geometry variation of the transition matrix elements.

signal. We continue the investigation of the long trajectory of the 15th harmonic for which the emission rate increases when the population in the triplet states becomes important. The first order diffracted signal of the full simulation (model 2) is displayed with coherent signal from the singlet states in Fig. 5.25 a. Two main differences appear the first one for time delays smaller than 500 fs and the second for longer ones. First, for time delays below 500 fs, the emission rate of the full simulation is lower and decreases faster when the triplet states are included, but the features of the time evolution remain the same. For the first tens of femtosecond, almost no difference is observed between the two results, it indicates that destructive interferences arise from the emission of the triplet states. Secondly, after 500 fs, a global minimum of the emission is reached in the full simulation and then increases again. This behaviour is not observed when the triplet states are not included, the emission rate is smaller and remains almost constant for these times. To clarify the role of the different triplet states, simulations including only the triplet states (see Fig. 5.25 b) have been performed. The results show a dominant emission of the 1^3B_2 states for time delays larger than 500 fs. The emission from the $1^3B_1(-)$ and $1^3A_2(-)$ states is much weaker. But this latter interferes destructively with the emission of the 1^3B_2 states, as observed in the total signal. With these simulations the signal of the full simulation can be interpreted as follows: the first 200 fs are lead by the emission of the singlet states because the population in the triplet states remains low (see Fig. 5.19). Between 200 and 500 fs the population in the 1^3B_2 states increases and the emission of these latter interferes destructively with the one of the singlet states. It results

a fast decay in the total emission rate with a global minimum around 550 fs. Then the population in the 1^3B_2 states is higher than the one in the singlet state and leads the evolution of the total signal, which increases between 600 fs and 1 ps.

The role of each triplet B_2 state is displayed in Fig. 5.25 c and shows constructive interferences between their respective emission, because the two states share the same I_p and the same transition matrix elements. The predominance of the emission from the triplet B_2 states is due to the slightly larger transition dipole matrix element, which compensates the larger I_p . The total emission rate does not increase in model 1 and to elucidate why, the emission from the 1^3B_2 states is reported in Fig. 5.25 d. The emission from each state presents more oscillations with respect to the time delay but their emission remains constructive. So the constant value of I_p , assumed in model 2, is not responsible for their phase relation. But the difference between the vibronic (model 2) and the "electronic" (model 1) I_p is large enough to reduce the emission rate by a factor ~ 10 . Even if destructive interferences between the singlet states and 1^3B_2 states are also present, in model 1 the emission of the latter is too weak to be clearly observed in the full signal.

From our different simulations, it seems safe to assign the time evolution of the experimental signal, observed for time delays larger than 400 fs, to the contribution of both 1^3B_2 states. Moreover the vibronic energy of the nuclear wavepacket plays a primordial role to understand the experimental results. Nevertheless, the intersystem crossing in the experiment seems not correctly reproduced in our simulation. These differences could come from our simplified introduction of the vibronic I_p , which could change the interferences and the different emission yields. But actually also physical processes can be involved. We saw in the case of the TRPES that weaker laser intensity was already leads to multiphoton absorption, for either the pump or the probe [71]. Such process could as well occur here, even with a 800 nm laser is used. Moreover, M. Lein *et al.* [175], recently established that the intersystem conversion can be controlled using strong laser field. Thus, this process could occur as well. It lies on the Stark shift effect, which induces a shift of the different PES and as we discussed before (see Sec. 4.3.1-4) the topology of the crossing seam between the singlet and triplet states plays primordial role.

To conclude the comparison with the experimental work, we also stress that we did not include explicitly

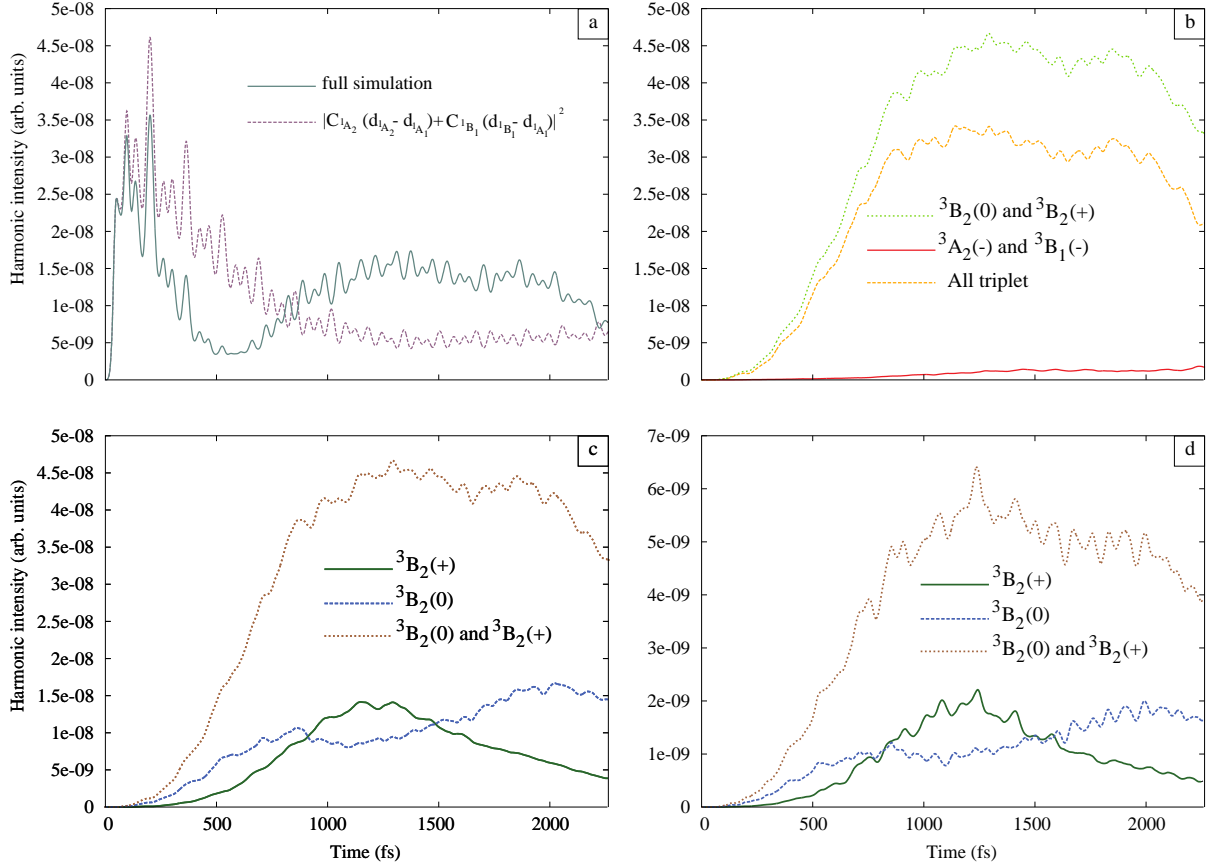


Figure 5.25: First order diffracted signal Eq. (5.12) for the 15th harmonic and comparison of the partial emission of the different states for the vibronic definition of Ip. (a) The full simulation (green), the emission of all the electronic states is considered with signal resulting from the consideration of the singlet states (1^1A_2 and 1^1B_1) only (dashed purple). (b) Partial emission from the $3^3B_2(0)$ and $3^3B_2(+)$ in dotted green, and for the $3^3A_2(-)$ and $3^3B_1(-)$ in solid red line. The coherent sum of these signals is displayed in dashed orange and destructively interfere. (c) Partial signal from the consideration of the $3^3B_2(+)$ ($3^3B_2(+)$) in solid green (dashed blue) line, and their coherent sum in dotted brown. (d) Same as (c) but for the geometry dependent Ip, which leads to weaker emission yields.

the probe pulse, but only consider the harmonic generation from one laser cycle. Experimentally the duration of the probe pulse is 120 fs and the dynamics will be averaged over its duration. To finish with the possible mechanisms responsible for the discrepancy with the experiment, the role of the dynamics in the ionic states as been discard in our simulations and can affect the results (see Sec.).

One advantage of the model, which is not presented here, is the possibility to study the different processes thanks to the wavepacket dynamics. For instance the Stark shift effect [176] and the multiphoton excitation

5.3. *STRONG FIELD SPECTROSCOPY: TOWARDS ATTOSECOND RESOLUTION USING HHG* 187

have been already formulated in the case of nuclear dynamics and the resulting dynamics can be easily used in our model.

Chapter 6

Conclusions and Perspectives

It is time now to conclude this manuscript and make a last point on the work carried out over these past three years. It started with the discussion on unexpected experimental results on the SO₂ molecule when new time-dependent spectroscopic methods are employed, namely TRPES and HHG. The open questions were numerous to understand what was going on, the role of the different known electronic states, the different kinds of couplings present, namely non-adiabatic and spin-orbit and their respective time scales.

With this goal in mind, we first tried to describe accurately the molecular system. First we considered the electronic ground state and the two lowest singlet excited states. The latter are interacting through strong non-adiabatic couplings, leading to a complex photoabsorption spectrum. Our results were particularly accurate, especially for the Clements band energies, and provided the first comprehensive theoretical description of the photoabsorption spectrum. In addition to the validation of our model, we went a step further and assigned the low energy part of the spectrum analysing the different final states of the transition. Our conclusions, in agreement with experiment, are unusual by strong non-adiabatic effects, which lead to the absorption to a "dark" state (1^1A_2) thanks to the coupling with the bright one (1^1B_1).

While these first results were encouraging, the heart of the problem was still unsolved, concerning the role of the different triplet states. In order to describe accurately the intersystem crossing, we extended the quasi-diabatization method in order to include the geometry dependence of the spin-orbit coupling elements.

Our three states model turns into a complex 12 coupled-states system, cleverly reduced into two subsystems. A careful analysis of the different couplings gave us insight into the different mechanisms leading to the inter-system crossing. The two main points, which have been pointed out, are the preponderant role of the 1^3B_2 state, confirmed experimentally by I. Wilkinson [71], and the possibility of quantum interferences during the process. While the first point is specific to SO_2 , the second is general, and shows how these interferences lead the yield of the different populations, making their consideration mandatory to a quantitative description of the experiments.

The second subsystem, which couples the electronic ground state with the triplet excited states, reveals a new mechanism for the "forbidden band". It turned out that this band results exclusively from the SOC in the A' manifold containing the GS, irrespectively of the energetic gap between them. The comparison with the experiment is excellent and validates the model and shows a different polarisation dependence than the singlet states absorption. It provides also a possibility to perform new experiments in order to verify the mechanisms, and excite selectively the triplet states.

While the photophysics of the molecule appears to be more complicated and richer than expected, we turned back to our initial questions concerning the TRPES and HHG spectroscopies. Both methods use ionisation of the system in order to probe the dynamics in the neutral states. Concerning the former, the final state of the system, is the ionised molecule and the released electron, while the latter used ionisation as an intermediate state to produce high harmonics, which are then detected. In order to deal with such an experimental schemes the three lowest ionic states have been considered. Previous experiments assigned the two first photoelectron bands to the three lowest ionic states, and the theoretical description of the lowest one was already performed as well as the higher energetic part of the second one. But no attempts were made concerning the energy range of the 1^2B_2 ionic state. We stressed that there is a symmetry-allowed conical intersection between the two lowest ionic states, responsible for the complexity of the photoelectron spectrum. Our simulations provide a full and accurate description of the photoelectron spectra.

Our different models for the electronic states seem accurate enough to start simulations of the TRPES. Thanks to the interpretations of the observations of the experimental team, we built a simplified model of

the mechanisms involving first an excitation of the singlet states only with the pump, and the dynamics was probed by three-photon ionisation with a two-photon resonance via a Rydberg state. This model provides the characteristic oscillating behaviour of the photoelectron yields according to the pump-probe delay, demonstrating the sensitivity of the method to the coupled dynamics between the 1^1A_2 and 1^1B_1 electronic states. This sensitivity is obtained because the "gating" performed by the Rydberg states. To go beyond this simple model the triplet manifold has later been introduced in the simulation, providing, within our set of approximations, a second decay time constant. Then the analysis of the role of the 1^3B_2 state has been obtained thanks to the study of the time-dependent electronic population according to the energy of the pump pulse. The experiments of Wilkinson are the first experimental evidence for the role of the 1^3B_2 state and are strongly supported by our simulations.

The question of the HHG experiments was somewhat more involved due to the recent and fast evolution of the field. We tackled this issue from a totally different point of view than developed until now. The largest part of the theoretical work in this field primarily focused on the electronic dynamics during the process, which is obviously mandatory. Thanks to a simple quasi-analytical model for the description of the electronic dynamics known to provide qualitative results, we focused on the "quantum nature" of the nuclear motion, and more particularly on its time dependence. Using our model, we first confirm that for time-independent experiments, the model developed by M. Lein *et al.* is more than satisfactory, with no significant variation of the results due to the approximations used. The situation is very different in the case of coherent vibrational wavepackets, for which we show that the time-dependent profile of the emitted harmonics strongly depends on the variation on the transition matrix elements and on the ionisation potential. Moreover the consideration of the dynamics in the ionic states during the excursion of the released electron presents the first evidence of the sensitivity of HHG spectroscopy to the phase accumulated by the nuclear wavepacket.

While numerous investigations have been devoted to the case of the electronic ground state, the study of the excited ones turns out to be more complex because of the large number of ionisation channels. Our model, with the consideration of approximate vibronic ionisation potentials could qualitatively describe the experimental results. Concerning the emission of the singlet states, we show that the latter does not influence the emission yields of the states, but its relative phase. Concerning the 3B_2 states, the yield is increased by

a factor ~ 10 and gives the possibility for these states to exhibit a clear signature in the harmonic signal.

Concerning the perspectives of this work, there are admittedly more questions at this point than answers concerning the SO_2 molecule as well as the theoretical development of wavepacket HHG methodology. Let us discuss first about the molecule itself. We present a new picture of the photophysics of the molecule, including consistently the singlet and triplet states. This description could benefit from the study of the rotationally active conical intersection between the electronic ground state and the 1^1A_2 state, providing a radiationless pathway for the deexcitation of the molecule. Moreover numerous Renner-Teller couplings occurring at the linearity of the molecule have been neglected and could be relevant for longer-time dynamics. The inclusion of these different features could lead to interesting behaviour in the dynamics of the system.

But the model developed in this work is as well suitable to study open questions in other fields such as the intriguing Sulfur-mass independent isotope effect. This latter has been observed in sediments before the great oxygenation of the Earth, and is mandatory to understand the history of our planet. Our new mechanisms, which include the triplet states, could give a possible way of research on this effect. I would have been interested to understand the role of the 1^3B_2 state and also the interference patterns in the different isotopologues, which are missing in the recent theoretical work. Moreover the direct photoabsorption to the triplet states could play a role as well.

In the near future we also plan the study of the higher excited electronic states than the ones mentioned in this work, and their computation has been recently finished but not yet used for dynamics. These states are of interest because they provide the first dissociative paths of the molecule after photo photoexcitation. While the lowest one has been already investigated theoretically, the double seams of conical intersection with the higher state have not been addressed and could help in our description and comprehension of the photo-dissociation of the molecule. Available experiments on the subject motivate this perspective [46, 47].

The model developed to describe the HHG experiment in order to study the correlated electron-nuclei dynamics is probably the most "frustrating" part of my work. Not because we do not perfectly obtain com-

parable results with the experiments, which is not the primordial goal of this simple model, but because in my view open questions remain unsolved. The model will greatly benefit from a step-by-step comparison on a simpler system. The numerical solution of the TDSE for SO_2 will certainly not appear in the near future, but a comparison considering simpler systems such as H_2 , H_2^+ ... is possible. Concerning numeric, we showed that standard Quantum Chemistry packages provide enough information in order to compute required quantities to study HHG. It is mandatory, in my opinion to check to quality of the arbitrary truncation of the MRCI wavefunction from our version of Molpro, with for instance a comparison open-source packages such as GAMESS-US. Nevertheless, these additional steps, even if they will be time consuming, do not present difficulties, and will give the possibility to make the model more accurate.

Concerning the model itself, an improvement can be provided thanks to the factorisation of the three step-model, for which each of the steps can be described in a better way, but keeping in mind the numerous nuclear geometries which have to be taken into account. For instance the recombination transition matrix will benefit from a correct description of the continuum states (difficult to incorporate), and a better description of the tunnel ionisation.

Bibliography

- [1] Paul, P. M. *et al.* Observation of a train of attosecond pulses from high harmonic generation. *Science* **292**, 1689–1692 (2001).
- [2] Kienberger, R. *et al.* Steering attosecond electron wave packets with light. *Science* **297**, 1144–1148 (2002).
- [3] Hentschel, M. *et al.* Attosecond metrology. *Nature* **414**, 509–513 (2001).
- [4] Drescher, M. *et al.* X-ray pulses approaching the attosecond frontier. *Science* **291**, 1923–1927 (2001).
- [5] Drescher, M. *et al.* Time-resolved atomic inner-shell spectroscopy. *Nature* **419**, 803–807 (2002).
- [6] Cavalieri, A. L. *et al.* Attosecond spectroscopy in condensed matter. *Nature* **449**, 1029–1032 (2007).
- [7] Uiberacker, M. *et al.* Attosecond real-time observation of electron tunnelling in atoms. *Nature* **446**, 627–632 (2007).
- [8] Remetter, T. *et al.* Attosecond electron wave packet interferometry. *Nat Phys* **2**, 323–326 (2006).
- [9] Boutu, W. *et al.* Coherent control of attosecond emission from aligned molecules. *Nat Phys* **4**, 545–549 (2008).
- [10] Haessler, S. *et al.* Attosecond imaging of molecular electronic wavepackets. *Nat Phys* **6**, 200–206 (2010).
- [11] Wagner, N. *et al.* Extracting the phase of high-order harmonic emission from a molecule using transient alignment in mixed samples. *Physical Review A* **76**, 061403 (2007).
- [12] Itatani, J. *et al.* Tomographic imaging of molecular orbitals. *Nature* **432**, 867–871 (2004).

- [13] Baker, S. *et al.* Probing proton dynamics in molecules on an attosecond time scale. *Science* **312**, 424–427 (2006).
- [14] Wagner, N. L. *et al.* Monitoring molecular dynamics using coherent electrons from high harmonic generation. *Proceedings of the National Academy of Sciences* **103**, 13279–13285 (2006).
- [15] Li, W. *et al.* Time-resolved dynamics in N₂O₄ probed using high harmonic generation. *Science* **322**, 1207–1211 (2008).
- [16] Kanai, T., Minemoto, S. & Sakai, H. Quantum interference during high-order harmonic generation from aligned molecules. *Nature* **435**, 470–474 (2005).
- [17] Wörner, H. J., Bertrand, J. B., Kartashov, D. V., Corkum, P. B. & Villeneuve, D. M. Following a chemical reaction using high-harmonic interferometry. *Nature* **466**, 604–607 (2010).
- [18] Wörner, H. J. *et al.* Conical intersection dynamics in NO₂ probed by homodyne high-harmonic spectroscopy. *Science* **334**, 208–212 (2011).
- [19] Domcke, W., Köppel, H. & Yarkony, D. R. *Conical Intersections: Electronic Structure, Dynamics & Spectroscopy* (World Scientific, Singapore, 2004).
- [20] Domcke, W. & Sobolewski, A. L. Peptide deactivation: Spectroscopy meets theory. *Nat Chem* **5**, 257–258 (2013).
- [21] Barbatti, M. *et al.* Relaxation mechanisms of UV-photoexcited DNA and RNA nucleobases. *Proceedings of the National Academy of Sciences* **107**, 21453–21458 (2010).
- [22] Polli, D. *et al.* Conical intersection dynamics of the primary photoisomerization event in vision. *Nature* **467**, 440–443 (2010).
- [23] Köppel, H., Domcke, W. & Cederbaum, L. S. Multimode molecular dynamics beyond the born-oppenheimer approximation. In Prigogine, I. & Rice, S. A. (eds.) *Advances in Chemical Physics*, 59–246 (John Wiley & Sons, Inc., 1984).
- [24] Köppel, H., Gronki, J. & Mahapatra, S. Construction scheme for regularized diabatic states. *The Journal of Chemical Physics* **115**, 2377–2388 (2001).

- [25] Köppel, H. & Schubert, B. The concept of regularized diabatic states for a general conical intersection. *Molecular Physics* **104**, 1069–1079 (2006).
- [26] Bailey, C. R., Cassie, A. B. D. & Angus, W. R. Investigations in the infra-red region of the spectrum. Part II. The absorption spectrum of sulphur dioxide. *Proceedings of the Royal Society of London. Series A* **130**, 142–156 (1930).
- [27] Watson, W. W. & Parker, A. E. The ultraviolet absorption spectrum of sulfur dioxide. *Physical Review* **37**, 1484–1492 (1931).
- [28] Clements, J. H. On the absorption spectrum of sulphur dioxide. *Physical Review* **47**, 224–232 (1935).
- [29] Asundi, J. H. & Samuel, R. The near ultra-violet absorption bands of SO₂. *Proc. Ind. Acad. Sci. A* **2**, 30–45 (1935).
- [30] Metropolis, N. Vibrational analysis of the absorption system of sulphur dioxide at λ 3400–2600. *Physical Review* **60**, 295–301 (1941).
- [31] Manatt, S. L. & Lane, A. L. A compilation of the absorption cross-sections of SO₂ from 106 to 403 nm. *Journal of Quantitative Spectroscopy and Radiative Transfer* **50**, 267 – 276 (1993).
- [32] Urone, P. & Schroeder, W. H. Sulfur dioxide in the atmosphere: a wealth of monitoring data, but few reaction rate studies. *Environmental Science and Technology* **3**, 436–445 (1969).
- [33] Norrish, R. G. W. & Zeelenberg, A. P. The combustion of hydrogen sulphide studied by flash photolysis and kinetic spectroscopy. *Proceedings of the Royal Society of London. Series A. Mathematical and Physical Sciences* **240**, 293–303 (1957).
- [34] Calvert, J. G. & Jackson, G. E. Triplet sulfur dioxide-carbon monoxide reaction excited with the SO₂(¹A₁)→SO₂(³B₁) "forbidden" band. *Journal of the American Chemical Society* **93**, 2593–2599 (1971).
- [35] Dainton, F. S. & Ivin, K. J. The photochemical formation of sulphinic acids from sulphur dioxide and hydrocarbons. *Trans. Faraday Soc.* **46**, 374–381 (1950).
- [36] Calvert, J. & Pitts, J. *Photochemistry* (John Wiley & Sons, Inc., New York-London-Sydney, 1966).

- [37] Douglas, A. E. The zeeman effect in the spectra of polyatomic molecules. *Canadian Journal of Physics* **36**, 147–149 (1958).
- [38] Merer, A. J. Rotational analysis of bands of the 3800 Å system of SO₂. *Discussions of the Faraday Society* **35**, 127–136 (1963).
- [39] Hillier, I. & Saunders, V. A theoretical interpretation of the bonding, and the photoelectron and ultra-violet spectra of sulphur dioxide. *Molecular Physics* **22**, 193–201 (1971).
- [40] Brand, J. C. D. & Nanes, R. The 3000–3400 Å absorption of sulfur dioxide. *Journal of Molecular Spectroscopy* **46**, 194–199 (1973).
- [41] Hamada, Y. & Merer, A. J. Rotational structure at the long wavelength end of the 2900 Å system of SO₂. *Canadian Journal of Physics* **52**, 1443–1457 (1974).
- [42] Herzberg, G. *Molecular Spectra and Molecular Structure (III): Electronic Spectra and Electronic Structure of Polyatomic Molecules* (Princeton: Van Nostrand, 1969).
- [43] Hecklen, J., Kelly, N. & Partymiller, K. The photophysics and photochemistry of SO₂. *Reviews of Chemical Intermediates* **3**, 315–404 (1980).
- [44] Hecklen, J. *Atmospheric Chemistry* (Academic Press, New York, 1976).
- [45] Calvert, J. G., Su, F., Bottenheim, J. W. & Strausz, O. P. Mechanism of the homogeneous oxidation of sulfur dioxide in the troposphere. *Atmospheric Environment* **12**, 197 (1978).
- [46] Brand, J. & Srikameswaran, K. The 2350 Å band system of sulphur dioxide. *Chemical Physics Letters* **15**, 130 – 132 (1972).
- [47] Sulfur dioxide: Rotational constants and asymmetric structure of the ¹B₂ state. *Journal of Molecular Spectroscopy* **60**, 43 – 56 (1976).
- [48] Katagiri, H. *et al.* Experimental and theoretical exploration of photodissociation of SO₂ via the ¹B₂ state: identification of the dissociation pathway. *Journal of Molecular Structure* **413–414**, 589–614 (1997).

- [49] Snyder, L. E. *et al.* Radio detection of interstellar sulfur dioxide. *The Astrophysical Journal* **198**, L81–L84 (1975).
- [50] Barker, E. S. Detection of SO₂ in the UV spectrum of Venus. *Geophysical Research Letters* **6**, 117–120 (1979).
- [51] Esposito, L. W. *et al.* Sulfur dioxide at the Venus cloud tops, 1978–1986. *Journal of Geophysical Research: Atmospheres* **93**, 5267–5276 (1988).
- [52] Bertaux, J.-L., Widemann, T., Hauchecorne, A., Moroz, V. I. & Ekonomov, A. P. VEGA 1 and VEGA 2 entry probes: An investigation of local UV absorption (220–400 nm) in the atmosphere of Venus (SO₂ aerosols, cloud structure). *Journal of Geophysical Research: Planets* **101**, 12709–12745 (1996).
- [53] Bourassa, A. E. *et al.* Large volcanic aerosol load in the stratosphere linked to asian monsoon transport. *Science* **337**, 78–81 (2012).
- [54] Jessup, K. L., Spencer, J. & Yelle, R. Sulfur volcanism on Io. *Icarus* **192**, 24 – 40 (2007).
- [55] Bertaux, J. L. & Belton, M. J. S. Evidence of SO₂ on Io from UV observations. *Nature* **282**, 813–815 (1979).
- [56] Ballester, G. *et al.* Detection of the SO₂ atmosphere on Io with the Hubble space telescope. *Icarus* **111**, 2 – 17 (1994).
- [57] McGrath, M. A., Belton, M. J., Spencer, J. R. & Sartoretti, P. Spatially resolved spectroscopy of Io's Pele plume and SO₂ atmosphere. *Icarus* **146**, 476 – 493 (2000).
- [58] Kim, S. J. & A'Hearn, M. F. Upper limits of SO and SO₂ in comets. *Icarus* **90**, 79 – 95 (1991).
- [59] Despois, D. Radio line observations of molecular and isotopic species in comet C/1995 O1 (Hale-Bopp). *Earth, Moon, and Planets* **79**, 103–124 (1997).
- [60] Vandaele, A. C., Hermans, C. & Fally, S. Fourier transform measurements of SO₂ absorption cross sections: II.: Temperature dependence in the 29 000–44 000 cm⁻¹ (227–345 nm) region. *Journal of Quantitative Spectroscopy and Radiative Transfer* **110**, 2115–2126 (2009).

- [61] Hermans, C., Vandaele, A. C. & Fally, S. Fourier transform measurements of SO₂ absorption cross sections: I. temperature dependence in the 24 000–29 000 cm⁻¹ (345–420 nm) region. *Journal of Quantitative Spectroscopy and Radiative Transfer* **110**, 756–765 (2009).
- [62] Baroni, M., Thiemens, M. H., Delmas, R. J. & Savarino, J. Mass-independent sulfur isotopic compositions in stratospheric volcanic eruptions. *Science* **315**, 84–87 (2007).
- [63] Gaillard, F., Scaillet, B. & Arndt, N. T. Atmospheric oxygenation caused by methane in volcanic degassing pressure. *Nature* **478**, 229–232 (2011).
- [64] Hattori, S. *et al.* SO₂ photoexcitation mechanism links mass-independent sulfur isotopic fractionation in cryospheric sulfate to climate impacting volcanism. *Proceedings of the National Academy of Sciences* **110**, 17656–17661 (2013).
- [65] Whitehill, A. R. *et al.* Vibronic origin of sulfur mass-independent isotope effect in photoexcitation of SO₂ and the implications to the early Earth’s atmosphere. *Proceedings of the National Academy of Sciences* **110**, 17697–17702 (2013).
- [66] Huzinaga, S. & Yoshimine, M. Abinitio and model potential calculations for the ground state of SO₂. *The Journal of Chemical Physics* **68**, 4486–4489 (1978).
- [67] Kamiya, K. & Matsui, H. Theoretical studies on the potential energy surfaces of SO₂: Electronic states for photodissociation from the \tilde{C}^1B_2 state. *Bulletin of the Chemical Society of Japan* **64**, 2792–2801 (1991).
- [68] Li, A., Suo, B., Wen, Z. & Wang, Y. Potential energy surfaces for low-lying electronic states of SO₂. *Science in China Series B: Chemistry* **49**, 289–295 (2006).
- [69] Dehestani, M. & Mansoori Kermani, M. Theoretical investigation of absorption spectrum of SO₂ molecule: Including S1–S2 vibronic coupling. *Computational and Theoretical Chemistry* **978**, 1–6 (2011).
- [70] Müller, H. & Köppel, H. Adiabatic wave-packet motion on conically intersecting potential energy surfaces. The case of SO₂ ($^1B_1-^1A_2$). *Chemical Physics* **183**, 107–116 (1994).

- [71] Wilkinson, I. *et al.* Excited state dynamics in SO₂. I. Bound state relaxation studied by time-resolved photoelectron-photoion coincidence spectroscopy. *The Journal of Chemical Physics* **140**, 204301 (2014).
- [72] Hockett, P., Bisgaard, C. Z., Clarkin, O. J. & Stolow, A. Time-resolved imaging of purely valence-electron dynamics during a chemical reaction. *Nat Phys* **7**, 612–615 (2011).
- [73] Lewenstein, M., Balcou, P., Ivanov, M. Y., L’Huillier, A. & Corkum, P. B. Theory of high-harmonic generation by low-frequency laser fields. *Phys. Rev. A* **49**, 2117–2132 (1994).
- [74] Lein, M. Attosecond probing of vibrational dynamics with high-harmonic generation. *Phys. Rev. Lett.* **94**, 053004 (2005).
- [75] Schrödinger, E. Quantisierung als eigenwertproblem. *Annalen der Physik* **384**, 361–376 (1926).
- [76] Cvitas, T., Homann, K., Kallay, N., Kuchitsu, K. & Mills, I. *Quantities, Units and Symbols in Physical Chemistry - The Green Book, 2nd edition* (Blackwell Science, 1993).
- [77] Born, M. & Oppenheimer, R. Zur quantentheorie der molekeln. *Annalen der Physik* **389**, 457–484 (1927).
- [78] Szabo, A. & Ostlund, N. S. *Modern quantum chemistry* (Dover publication, INC. Mineola, New York, 1996).
- [79] Levine, I. N. *Quantum Chemistry*. (Prentice Hall, Upper Saddle River, 2008).
- [80] Tannor, D. J. *Introduction to quantum mechanics: a time-dependent perspective* (University Science Books, 2006).
- [81] Von Neumann, J. & Wigner, E. P. über das verhalten von eigenwerten bei adiabatischen prozessen. *The Journal of Physical Chemistry A* **30**, 467 (1929).
- [82] Thiel, A. & Köppel, H. Proposal and numerical test of a simple diabaticization scheme. *The Journal of Chemical Physics* **110**, 9371–9383 (1999).
- [83] Crank, J. & Nicolson, P. A practical method for numerical evaluation of solutions of partial differential equations of the heat-conduction type. *Advances in Computational Mathematics* **6**, 207–226 (1996).

- [84] Beck, M., Jäckle, A., Worth, G. & Meyer, H.-D. The multiconfiguration time-dependent Hartree (MCTDH) method: a highly efficient algorithm for propagating wavepackets. *Physics Reports* **324**, 1–105 (2000).
- [85] Harris, D. O., Engerholm, G. G. & Gwinn, W. D. Calculation of matrix elements for one-dimensional quantum-mechanical problems and the application to anharmonic oscillators. *The Journal of Chemical Physics* **43**, 1515–1517 (1965).
- [86] Heather, R. W. & Light, J. C. Discrete variable theory of triatomic photodissociation. *The Journal of Chemical Physics* **79**, 147–159 (1983).
- [87] Worth, G. A. *et al.* The heidelberg mctdh package: A set of programs for multi-dimensional quantum dynamics. (user’s guide version 8) (2009).
- [88] Dirac, P. A. M. On the annihilation of electrons and protons. *Mathematical Proceedings of the Cambridge Philosophical Society* **26**, 361–375 (1930).
- [89] Frenkel, J. *Wave Mechanics; Advanced General Theory* (Oxford, Clarendon Press, 1934).
- [90] Kosloff, R. & Tal-Ezer, H. A direct relaxation method for calculating eigenfunctions and eigenvalues of the schrödinger equation on a grid. *Chemical Physics Letters* **127**, 223 – 230 (1986).
- [91] Leforestier, C. *et al.* A comparison of different propagation schemes for the time dependent schrödinger equation. *Journal of Computational Physics* **94**, 59–80 (1991).
- [92] Press, W. H., Teukolsky, S. A., Vetterling, W. T. & Flannery, B. P. *Numerical Recipes in FORTRAN; The Art of Scientific Computing* (Cambridge University Press, New York, NY, USA, 1993), 2nd edn.
- [93] Park, T. J. & Light, J. C. Unitary quantum time evolution by iterative Lanczos reduction. *The Journal of Chemical Physics* **85**, 5870–5876 (1986).
- [94] Lanczos, C. An iteration method for the solution of the eigenvalue problem of linear differential and integral operators. *J. Res. Natl. Bur. Stand.* **45**, 255 (1950).
- [95] Krylov, A. N. On the numerical solution of the equation by which in technical questions frequencies of small oscillations of material systems are determined. *Izvestija AN SSSR (News of Academy of Sciences of the USSR)* **VII**, 491–539 (1931).

- [96] Slater, J. C. The theory of complex spectra. *Phys. Rev.* **34**, 1293–1322 (1929).
- [97] Roothaan, C. C. J. New developments in molecular orbital theory. *Rev. Mod. Phys.* **23**, 69–89 (1951).
- [98] Hall, G. G. The molecular orbital theory of chemical valency. viii. a method of calculating ionization potentials. *Proceedings of the Royal Society of London. Series A. Mathematical and Physical Sciences* **205**, 541–552 (1951).
- [99] Werner, H.-J. & Meyer, W. A quadratically convergent multiconfiguration self-consistent-field method with simultaneous optimization of orbitals and CI coefficients. *The Journal of Chemical Physics* **73**, 2342–2356 (1980).
- [100] Werner, H.-J. & Knowles, P. J. A second order multiconfiguration SCF procedure with optimum convergence. *The Journal of Chemical Physics* **82**, 5053–5063 (1985).
- [101] Knowles, P. J. & Werner, H.-J. An efficient second-order MC SCF method for long configuration expansions. *Chemical Physics Letters* **115**, 259–267 (1985).
- [102] Roos, B. O., Taylor, P. R. & Siegbahn, P. E. A complete active space SCF method (CASSCF) using a density matrix formulated super-CI approach. *Chemical Physics* **48**, 157–173 (1980).
- [103] Gerlach, W. & Stern, O. Der experimentelle Nachweis der Richtungsquantelung im Magnetfeld. *Zeitschrift für Physik* **9**, 349–352 (1922).
- [104] Gerlach, W. & Stern, O. Der experimentelle nachweis des magnetischen moments des silberatoms. *Zeitschrift für Physik* **8**, 110–111 (1922).
- [105] Dirac, P. A. M. The quantum theory of the electron. *Proceedings of the Royal Society of London. Series A* **117**, 610–624 (1928).
- [106] Marian, C. M. Spin-orbit coupling in molecules. *Reviews in Computational Chemistry* **17**, **Chapter 3** (2001).
- [107] MOLPRO is a package of ab initio programs written by H.-J. Werner, P. J. Knowles, G. Knizia, F. R. Manby, M. Schütz, P. Celani, T. Korona, R. Lindh, A. Mitrushenkov, G. Rauhut, K. R. Shamasundar, T. B. Adler, R. D. Amos, A. Bernhardsson, A. Berning, D. L. Cooper, M. J. O. Deegan, A. J. Dobbyn,

- F. Eckert, E. Goll, C. Hampel, A. Hesselmann, G. Hetzer, T. Hrenar, G. Jansen, C. Köppl, Y. Liu, A. W. Lloyd, R. A. Mata, A. J. May, S. J. McNicholas, W. Meyer, M. E. Mura, A. Nicklaß, D. P. O'Neill, P. Palmieri, D. Peng, K. Pflüger, R. Pitzer, M. Reiher, T. Shiozaki, H. Stoll, A. J. Stone, R. Tarroni, T. Thorsteinsson, M. Wang.
- [108] Berning, A., Schweizer, M., Hans-Joachim, W., Knowles, P. J. & Palmieri, P. Spin-orbit matrix elements for internally contracted multireference configuration interaction wavefunctions. *Molecular Physics* **98**, 1823–1833 (2000).
- [109] DIRAC, a relativistic ab initio electronic structure program, Release DIRAC13 (2013), written by L. Visscher *et al.* (see <http://www.diracprogram.org>).
- [110] Balint-Kurti, G. G., Dixon, R. N. & Marston, C. C. Time-dependent quantum dynamics of molecular photofragmentation processes. *J. Chem. Soc., Faraday Trans.* **86**, 1741–1749 (1990).
- [111] Heller, E. J. The semiclassical way to molecular spectroscopy. *Accounts of Chemical Research* **14**, 368–375 (1981).
- [112] Zewail, A. H. Laser selective chemistry-is it possible? *Physics Today* **33**, 1–8 (1980).
- [113] Burkey, R. S. & Cantrell, C. D. Discretization in the quasi-continuum. *Journal of the Optical Society of America B* **1**, 169–175 (1984).
- [114] Burkey, R. S. & Cantrell, C. D. Multichannel excitation of the quasi-continuum. *Journal of the Optical Society of America B* **2**, 451–457 (1985).
- [115] Seel, M. & Domcke, W. Femtosecond time-resolved ionization spectroscopy of ultrafast internal-conversion dynamics in polyatomic molecules: Theory and computational studies. *The Journal of Chemical Physics* **95**, 7806–7822 (1991).
- [116] Worth, G. A., Carley, R. E. & Fielding, H. H. Using photoelectron spectroscopy to unravel the excited-state dynamics of benzene. *Chemical Physics* **338**, 220–227 (2007).
- [117] Zanghellini, J., Kitzler, M., Fabian, C., Brabec, T. & Scrinzi, A. An mctdhf approach to multielectron dynamics in laser fields. *Laser Physics* **13**, 1064–1068 (2003).

- [118] Miyagi, H. & Madsen, L. Time-dependent restricted-active-space self-consistent-field theory for laser-driven many-electron dynamics. *Phys. Rev. A* **87**, 062511 (2013).
- [119] Miyagi, H. & Madsen, L. B. Time-dependent restricted-active-space self-consistent-field theory for laser-driven many-electron dynamics. ii. extended formulation and numerical analysis. *Phys. Rev. A* **89**, 063416 (2014).
- [120] Chirilă, C. C. & Lein, M. Influence of nuclear vibration on harmonic generation in molecules. *Journal of Physics B: Atomic, Molecular and Optical Physics* **39**, S437 (2006).
- [121] Chirilă, C. C. & Lein, M. Strong-field approximation for harmonic generation in diatomic molecules. *Phys. Rev. A* **73**, 023410 (2006).
- [122] Falge, M., Engel, V. & Lein, M. Vibrational-state and isotope dependence of high-order harmonic generation in water molecules. *Phys. Rev. A* **81**, 023412 (2010).
- [123] Patchkovskii, S. Nuclear dynamics in polyatomic molecules and high-order harmonic generation. *Physical Review Letters* **102**, 253602 (2009).
- [124] Milosevic, D. B., Bauer, D. & Becker, W. Quantum-orbit theory of high-order atomic processes in intense laser fields. *Journal of Modern Optics* **53**, 125–134 (2006).
- [125] Castiglia, G. *et al.* The influence of the quantum nature of nuclei in high harmonic generation from H_2^+ -like molecular ions. *Laser Physics* **23**, 095301 (2013).
- [126] Corkum, P. B. Plasma perspective on strong field multiphoton ionization. *Phys. Rev. Lett.* **71**, 1994–1997 (1993).
- [127] Morini, F., Hajgató, B., Deleuze, M. S., Ning, C. G. & Deng, J. K. Benchmark dyson orbital study of the ionization spectrum and electron momentum distributions of ethanol in conformational equilibrium. *The Journal of Physical Chemistry A* **112**, 9083–9096 (2008).
- [128] Oana, C. & Krylov, A. Dyson orbitals for ionization from the ground and electronically excited states within equation-of-motion coupled-cluster formalism: Theory, implementation, and examples. *J. Chem. Phys.* **127**, 234106 (2007).

- [129] Oana, C. & Krylov, A. Cross sections and photoelectron angular distributions in photodetachment from negative ions using equation-of-motion coupled-cluster dyson orbitals. *J. Chem. Phys.* **131**, 124114 (2009).
- [130] Löwdin, P.-O. Quantum theory of many-particle systems. I. Physical interpretations by means of density matrices, natural spin-orbitals, and convergence problems in the method of configurational interaction. *Physical Review* **97**, 1474–1489 (1955).
- [131] Dunning, J. T. H. Gaussian basis sets for use in correlated molecular calculations. I. The atoms boron through neon and hydrogen. *The Journal of Chemical Physics* **90**, 1007–1023 (1989).
- [132] Lévêque, C., Komainda, A., Taïeb, R. & Köppel, H. Ab initio quantum study of the photodynamics and absorption spectrum for the coupled 1^1A_2 and 1^1B_1 states of SO_2 . *The Journal of Chemical Physics* **138**, 044320 (2013).
- [133] Xie, C., Hu, X., Zhou, L., Xie, D. & Guo, H. Ab initio determination of potential energy surfaces for the first two UV absorption bands of SO_2 . *The Journal of Chemical Physics* **139**, 014305 (2013).
- [134] Mai, S., Marquetand, P. & González, L. Non-adiabatic and intersystem crossing dynamics in SO_2 . II. the role of triplet states in the bound state dynamics studied by surface-hopping simulations. *The Journal of Chemical Physics* **140**, 204302 (2014).
- [135] Hamada, Y. & Merer, A. J. Rotational structure in the absorption spectrum of SO_2 between 3000 Å and 3300 Å. *Canadian Journal of Physics* **53**, 2555–2576 (1975).
- [136] Weis, B. *Theoretische Untersuchung von Kopplungselekten in Spektren dreiatomiger Moleküle*. Ph.D. thesis, Johann-Wolfgang-Goethe Universität Frankfurt (1991).
- [137] Brand, J. C. D., Jones, V. T. & di Lauro, C. The $^3B_1-^1A_1$ 3880 Å band system of sulfur dioxide: Rotational analysis of the 0-0 band. *Journal of Molecular Spectroscopy* **40**, 616–631 (1971).
- [138] Lévêque, C., Köppel, H. & Taïeb, R. Excited state dynamics in SO_2 . III. an ab initio quantum study of single- and multi-photon ionization. *The Journal of Chemical Physics* **140**, 204303 (2014).
- [139] Zhang, X., Zheng, H., Li, R., Liang, J. & Cui, Z. Ab initio calculations and spectral simulation of the photoionization process. *Journal of Molecular Structure: THEOCHEM* **822**, 122–124 (2007).

- [140] Chang, J.-L. *et al.* Theoretical calculations of C_{2v} excited states of SO_2^+ . *Chemical Physics Letters* **486**, 12–15 (2010).
- [141] Li, W.-Z., Huang, M.-B. & Chen, B.-Z. The $1^2A_1, 1^2B_2$, and 1^2A_2 states of the SO_2^+ ion studied using multiconfiguration second-order perturbation theory. *The Journal of Chemical Physics* **120**, 4677–4682 (2004).
- [142] Palmer, M. H., Shaw, D. A. & Guest, M. F. The electronically excited and ionic states of sulphur dioxide: an ab initio molecular orbital CI study and comparison with spectral data. *Molecular Physics* **103**, 1183–1200 (2005).
- [143] Wang, L., Lee, Y. T. & Shirley, D. A. Molecular beam photoelectron spectroscopy of SO_2 : Geometry, spectroscopy, and dynamics of SO_2^+ . *The Journal of Chemical Physics* **87**, 2489–2497 (1987).
- [144] Wolfram Research, I. Mathematica edition: Version 8.0. *Wolfram Research, Inc.* (2010).
- [145] Manthe, U., Meyer, H.-D. & Cederbaum, L. S. Multiconfigurational time-dependent hartree study of complex dynamics: Photodissociation of NO_2 . *The Journal of Chemical Physics* **97**, 9062–9071 (1992).
- [146] Engel, V. The calculation of autocorrelation functions for spectroscopy. *Chemical Physics Letters* **189**, 76–78 (1992).
- [147] Kullmer, R. & Demtröder, W. Vibronic coupling in SO_2 , and its influence on the rotational structure of the bands in the 300–330 nm region. *Chemical Physics* **92**, 423–433 (1985).
- [148] Brand, J. C. D., Jones, V. T. & di Lauro, C. The $^3B_1-^1A_1$ band system of sulfur dioxide: Rotational analysis of the (010), (100), and (110) bands. *Journal of Molecular Spectroscopy* **45**, 404–411 (1973).
- [149] Lever, A. B. P. *Inorganic Electronic Spectroscopy* (Elsevier, 1984).
- [150] Phillips, P. & Davidson, E. R. Interchange perturbation theory and phosphorescence: application to formaldehyde. *The Journal of Physical Chemistry* **86**, 3729–3733 (1982).
- [151] Kraus, P. M., Baykusheva, D. & Wörner, H. J. Two-pulse field-free orientation reveals anisotropy of molecular shape resonance. *Physical Review Letters* **113** (2014).

- [152] Litvinyuk, I. V. *et al.* Alignment-dependent strong field ionization of molecules. *Physical Review Letters* **90**, 233003 (2003).
- [153] Lee, K. F., Villeneuve, D. M., Corkum, P. B., Stolow, A. & Underwood, J. G. Field-free three-dimensional alignment of polyatomic molecules. *Physical Review Letters* **97**, 173001 (2006).
- [154] Spector, L. S. *et al.* Axis-dependence of molecular high harmonic emission in three dimensions. *Nature Communications* **5** (2014).
- [155] Schmidt, J. A., Johnson, M. S., McBane, G. C. & Schinke, R. Communication: Multi-state analysis of the OCS ultraviolet absorption including vibrational structure. *The Journal of Chemical Physics* **136**, 131101 (2012).
- [156] Schröder, T., Schinke, R., Ehara, M. & Yamashita, K. New aspects of the photodissociation of water in the first absorption band: How strong is excitation of the first triplet state? *The Journal of Chemical Physics* **109**, 6641–6646 (1998).
- [157] Schinke, R., Schmidt, J. A. & Johnson, M. S. Photodissociation of N₂O: Triplet states and triplet channel. *The Journal of Chemical Physics* **135**, 194303 (2011).
- [158] Grebenshchikov, S. Y., Qu, Z.-W., Zhu, H. & Schinke, R. Spin-orbit mechanism of predissociation in the Wulf band of ozone. *The Journal of Chemical Physics* **125**, 021102 (2006).
- [159] Holland, D. M. P. *et al.* An experimental and theoretical study of the valence shell photoelectron spectrum of sulphur dioxide. *Chemical Physics* **188**, 317–338 (1994).
- [160] Norwood, K. & Ng, C. Y. A study of the unimolecular dissociation of SO₂⁺($\tilde{C}, \tilde{D}, \tilde{E}$) using the photoelectron-photoion coincidence method. *The Journal of Chemical Physics* **93**, 6440–6447 (1990).
- [161] Meng, Q. & Huang, M.-B. A CAS study on S-loss and O-loss dissociation mechanisms of the SO₂⁺ ion in the C, D, and E states. *Journal of Computational Chemistry* **32**, 142–151 (2011).
- [162] Yong-Feng, Z. *et al.* Ab initio calculations of the ionization spectrum of SO₂. *Chinese Physics B* **17**, 4163 (2008).
- [163] Li, W.-Z. & Huang, M.-B. C, D, and E electronic states of the SO₂⁺ ion studied using multiconfiguration second-order perturbation theory. *The Journal of Physical Chemistry A* **108**, 6901–6907 (2004).

- [164] Cederbaum, L., Domcke, W., von Niessen, W. & Kraemer, W. A difficult assignment problem: The ionic states of ozone and sulphur dioxide. *Molecular Physics* **34**, 381–396 (1977).
- [165] Zewail, A. H. Femtochemistry: Atomic-scale dynamics of the chemical bond. *The Journal of Physical Chemistry A* **104**, 5660–5694 (2000).
- [166] Stolow, A. & Underwood, J. G. Time-resolved photoelectron spectroscopy of nonadiabatic dynamics in polyatomic molecules. In Rice, S. A. (ed.) *Advances in Chemical Physics*, 497–584 (John Wiley & Sons, Inc., 2008).
- [167] Xue, B., Chen, Y. & Dai, H.-L. Observation of the singlet–triplet pair of the 4p Rydberg state and assignment of the Rydberg series of SO₂. *The Journal of Chemical Physics* **112**, 2210–2217 (2000).
- [168] Suto, M., Day, R. L. & Lee, L. C. Fluorescence yields from photodissociation of SO₂ at 1060–1330 Å. *Journal of Physics B: Atomic and Molecular Physics* **15**, 4165 (1982).
- [169] Kulander, K. C., Schafer, K. J. & Krause, J. L. Dynamics of short-pulse excitation, ionization and harmonic conversion. *Super-intense Laser-Atom Physics, NATO ASI Series* **316**, 95–110 (1993).
- [170] Wörner, H.-J. Private communication .
- [171] Scrinzi, A., Ivanov, M. Y., Kienberger, R. & Villeneuve, D. M. Attosecond physics. *Journal of Physics B: Atomic, Molecular and Optical Physics* **39**, R1 (2006).
- [172] Krausz, F. & Ivanov, M. Attosecond physics. *Rev. Mod. Phys.* **81**, 163–234 (2009).
- [173] Risoud, F., Lévêque, C., Caillat, J., Maquet, A. & Taïeb, R. Quantitative extraction of the emission times of high-order harmonics via the determination of instantaneous frequencies. *Physical Review A* **88**, 043415 (2013).
- [174] Shafir, D. *et al.* Resolving the time when an electron exits a tunnelling barrier. *Nature* **485**, 343–346 (2012).
- [175] Falge, M. *et al.* The time-scale of nonlinear events driven by strong fields: can one control the spin coupling before ionization runs over? *Journal of Physics B: Atomic, Molecular and Optical Physics* **47**, 124027 (2014).

- [176] Sala, M., Saab, M., Lasorne, B., Gatti, F. & Guérin, S. Laser control of the radiationless decay in pyrazine using the dynamic Stark effect. *The Journal of Chemical Physics* **140** (2014).

List of Publications

This thesis has been partially published:

1. C. Lévêque, D. Pelaez-Ruiz, H. Köppel and R. Taïeb *Nature Comms.* **5**, 4126 (2014)
2. C. Lévêque, H. Köppel and R. Taïeb *J. Chem. Phys.* **140**, 204303 (2014)
3. C. Lévêque, R. Taïeb and H. Köppel *J. Chem. Phys. Com.* **140**, 091101 (2014)
4. C. Lévêque, A. Komainda, R. Taïeb and H. Köppel *J. Chem. Phys.* **138**, 044320 (2013)

Additional publications:

1. F. Risoud, C. Lévêque, J. Caillat, A. Maquet and R. Taïeb *Phys. Rev. A* **88**, 043415 (2013)
2. L. Ph. H. Schmidt, J. Lower, T. Jahnke, S. Schössler, M. S. Schöffler, A. Mensen, C. Lévêque, N. Sisourat, R. Taïeb, H. Schmidt-Böcking, and R. Dörner *Phys. Rev. Lett.* **111**, 103201 (2013)
3. E. V. Gromov, C. Lévêque, F. Gatti, I. Burghardt and H. Köppel *J. Chem. Phys.* **135**, 164305 (2011)

Résumé

1 Introduction

L'interaction entre la lumière et la matière est une sonde privilégiée pour étudier et comprendre les atomes, les molécules et les solides. Depuis plus d'un siècle, cette spectroscopie a permis de révéler aux chercheurs de précieuses informations sur l'organisation structurale et énergétique de ces édifices formés d'électrons et nucléons. Pour d'écrire l'évolution de ces particules, les lois de la physique classique échouent, cédant leur place à celle de la mécanique quantique, dans lesquelles la matière perd ses contours, son entité, pour laisser place à son onde de probabilité. Dans ce monde du tout petit, l'énergie, continue à notre échelle, se décompose désormais en niveaux discrets, on dit qu'elle est quantifiée. Dès lors qu'un système quantique est soumis à de la lumière, il peut changer d'énergie sautant entre les différents niveaux, en absorbant, ou émettant, de petits grains d'énergies, les photons. Les différentes transitions donnent accès à l'organisation des énergies électroniques, vibrationnelles, rotationnelles... des molécules. Grâce à l'essor de la technologie des lasers depuis sa réalisation en 1960, il est désormais possible d'initier et de sonder l'évolution dynamique des systèmes quantiques. L'étude du mouvement des noyaux moléculaires a été sujette à une attention particulière à la fin du XXème siècle, lors de l'essor de la "femto-chimie". Pour la première fois il fut possible de "suivre" en temps réel une réaction chimique. Cette avancée majeure, récompensée par le prix Nobel de chimie décerné à A. Zewail en 1999, a naturellement ouvert la voie à une nouvelle quête, celle de l'observation du mouvement des électrons. Pour comprendre l'ampleur du défi que se sont lancé les scientifiques, il faut savoir que ces derniers évoluent entre cent et mille fois plus vite que les noyaux, la femto-seconde laissant ainsi place à l'atto-seconde (10^{-18} s). La conceptualisation de cette échelle de temps est particulièrement ardue, mais un exemple est éloquent : il s'écoule deux fois plus d'atto-secondes en l'espace d'une seconde,

qu'il ne s'est écoulé de secondes depuis la naissance de l'univers, il y a 14 milliards d'années. Ainsi pour observer la dynamique électronique il faut disposer d'un phénomène suffisamment rapide pour mesurer le système. Ce défi fut relevé en 2001, avec la génération de la première impulsion lumineuse d'une durée de quelques centaines d'atto-secondes.

Pour générer de si courtes impulsions, un phénomène d'optique hautement non-linéaire est utilisé, la génération d'harmonique d'ordre élevé (HHG). Ce phénomène est observé lorsqu'un atome ou une molécule est excité par un laser de très haute intensité, arrachant un électron du système et accélérant ce dernier. Lorsqu'un demi-cycle optique plus tard le champ électrique prend la direction opposée, l'électron est ramené vers l'ion parent et peut se recombiner avec celui-ci en émettant un photon, d'une énergie proportionnelle à l'intensité du champ électrique initiateur du processus. Ce phénomène est aujourd'hui utilisé de deux façons distinctes pour étudier les dynamiques atto-seconde. Le rayonnement harmonique émit peut être utilisé pour générer des impulsions lumineuses ultra-brèves, ces dernières étant ensuite utilisées dans des expériences similaires à celle développées ultérieurement pour l'échelle de la femto-seconde. Ce sont des expériences dites "pompe-sonde", dans lesquelles la sonde permet une résolution atto-seconde. La seconde branche de recherche développée utilise les informations contenues dans le rayonnement harmoniques lui-même comme signature du processus physique sous-jacent, ces expériences sont dites "d'auto-sonde", par leur particularité de sonder la dynamique du système entre les instants d'ionisation et de recombinaison.

Le succès de ces deux approches a bouleversé la physique moderne en permettant une observation de nombreux phénomènes physique sur des échelles de temps jamais atteintes, la première méthode s'illustrant par des observations tels que l'ionisation par effet tunnel, la relaxation par émission Auger dans les atomes, l'émission de photoélectrons. La seconde méthode se remarque, quand à sa cohérence, permettant la détermination de l'amplitude mais également de la phase de la fonction d'onde électronique, conduisant dès lors aux premières reconstructions tomographiques d'orbitales moléculaires, jusqu'alors "simple" concept mathématique pour la résolution l'équation de Schrödinger, et conservant une sensibilité aux dynamiques nucléaires. Cette méthode s'impose ainsi comme le candidat idéal pour l'étude des réactions chimiques, dans les quels des modifications importantes de la fonction d'onde électronique et des mouvement nucléaires important sont les acteurs principaux. Le début de ce projet de recherche est ainsi marqué par l'application avec brio de cette méthode pour l'étude de la photodissociation de la molécule Br_2 suivit par celle de NO_2 pour laquelle

une dynamique corrélée entre noyaux et électrons, se produisant au voisinage d'une intersection conique, est expérimentalement sondée.

La présence d'une intersection conique dans la molécule de NO_2 exacerbe d'autant plus l'enjeu de cette étude, car il s'agit d'une situation pour laquelle l'illustre approximation de Born-Oppenheimer ne s'applique pas ceci à cause d'un fort couplage, dit non-adiabatique, desquels résulte une dynamique nucléaire rapide et une superposition d'état électroniques. Les intersections coniques ont connu au cours des dernières décennies une attention particulière de la part des théoriciens et expérimentateurs pour leur rôle prédominant dans un vaste panel de systèmes moléculaires, traversant les différents domaines de la physique moléculaire, chimie et biologie avec leur implication dans la stabilité de l'ADN, permettant une relaxation vibrationnelle, et dans le mécanisme de la vision, par photo-isomérisation du rétinol. Leur description théorique est une tâche ardue qui, aujourd'hui encore, et au cœur du développement des méthodes de simulations allant des descriptions semi-classiques au modèle quantiques, sans possibilité d'une description exacte. Le groupe de chimie théorique de l'Université de Heidelberg fait parti des pionniers dans le développement de méthodes pour leur description avec différents modèles reposant sur le développement en série de Taylor des termes d'interaction entre électrons et noyaux. Ainsi le modèle utilisé dans le cadre de ce travail, dite "méthode de diabatisation régularisée", repose sur cette approche et a déjà montré sa qualité pour décrire certains système moléculaire. Dans cette thèse nous voulons décrire théoriquement la dynamique nucléaire au voisinage d'une intersection conique, et comprendre comment une signature de cette dynamique peut être caractérisée dans les résultats des spectroscopies utilisant la génération d'harmoniques. Un système simple est donc souhaité pour permettre une description précise du processus, mais l'étude de molécules diatomiques est écartée car ils ne permettent pas l'existence d'intersections coniques, obligeant ainsi le choix d'un composé triatomique. Parmi la grande variété de tels systèmes, la molécule de dioxyde de soufre (SO_2) a particulièrement éveillée notre curiosité pour son implication prédominante dans de nombreux domaines de recherche et une production massive de résultats dans la littérature scientifique. L'étude des états électroniquement excités de cette molécule a débuté comme un problème académique dans les années trente, succédant à l'étude des systèmes diatomiques pour lesquels de considérable progrès ont été accomplis grâce au développement de la mécanique quantique. L'étude des propriétés de l'état fondamentale électronique de SO_2 venant d'être accomplie, Watson et Parker ouvre ainsi la voie de la spectroscopie moléculaire dans les états électroniques excités. Avec la résolution

et l'intensité des méthodes utilisées à cette période, le spectre de photoabsorption permet l'observation de la première bande "permise", dénotée ainsi par la suite, mais la complexité de la structure de cette bande, ouvre un grand débat quand à son attribution vibrationnelle et électronique, qui ne sera pas résolue.

Trente ans plus tard, cette molécule connaît un regain d'intérêt pour son implication dans la pollution atmosphérique, provoquant des pluies acides, des difficultés respiratoires ainsi que des dégâts sur les plantes et les matériaux et le rôle de la réactivité des états excités est mis à jour. La présence de la molécule dans l'air est ainsi mise sous haute surveillance, et un effort considérable pour comprendre la photochimie (réaction chimique activée par l'absorption de photons) de SO_2 dans l'atmosphère est déployé, étudiant sa réactivité en présence de dioxygène, de monoxyde de carbone, d'hydrocarbures par exemple. Les questions non-résolues des années trente sont remises au goût du jour, avec l'utilisation de nouvelles méthodes de spectroscopie permettant ainsi à Douglas, par l'intermédiaire de l'effet Zeeman, d'observer la bande dite "interdite" à basse énergie, et de l'attribuer à un état électronique triplet de spin. La symétrie B1 de ce dernier est ensuite déterminée par Merer, grâce à l'analyse rotationnelle du spectre. Les premières études théoriques concernant cette molécule voient également le jour, avec en 1971 la publication des travaux de Hillier et Saunders, déterminant les différents états électroniques d'énergies similaires au spectre expérimental. Ils permettent l'attribution de la première bande "permise" à un état électronique singulet de spin et de symétrie A_2 . Ces résultats, loin de simplifier la compréhension de la molécule exacerbent sa complexité, car une transition entre l'état fondamental et cet état électronique est, en principe, interdite, et ne peut opérer que par l'intermédiaire d'un couplage vibronique fort avec l'état singulet de spin de symétrie B1 prédit théoriquement.

Ce bref résumé de l'histoire de la spectroscopie du dioxyde de soufre montre une richesse et une complexité rare et mouvementée pendant plus de 60 ans, avant l'attribution des états électroniques impliqués dans le spectre de photoabsorption. Ceci fut accompagné de nombreux ouvrages de revue regroupant et classifiant les dernières avancées et les questions encore irrésolues à cette époque. Depuis les années 80, la molécule continue d'intéresser les scientifiques de nombreux domaines, notamment avec la découverte de sa présence dans les milieux interstellaires en 1975, et sa détection dans l'atmosphère de Vénus, Mars et le satellite de Jupiter Io ainsi que dans les comètes, devenant ainsi une molécule d'intérêt pour l'astrophysique. Son importance ne se limite pas aux confins de l'univers, mais intéresse également les géologues pour la prédiction et l'impact environnemental des éruptions volcaniques et les climato paléontologues depuis la découverte de

la séparation indépendante de la masse des isotopes du soufre dans des sédiments datant de l'archéen.

Avec la multiplicité de ces domaines de recherche pour lesquels le dioxyde de soufre est un composé majeur, les études théoriques se sont multipliées à partir des années 90 avec l'évaluation des surfaces d'énergies potentielles (PES) en fonction des différents degrés de liberté vibrationnels de la molécule, fournissant une bonne représentation des différents états électroniques impliqués dans le spectre de photo absorption, ce spectre a été calculé pour la première fois en 2011 avec un accord très limité avec l'expérience et une étude de dynamique de paquet d'onde a été effectuée antérieurement sans discuter du spectre de photo absorption, donnant une compréhension sommaire de la photo physique de la molécule.

Le choix de cette molécule pour nos recherches a été également encouragé par les expériences récentes de I. Wilkinson, A. Stolow and D. Villeneuve de l'université de Ottawa ainsi que de H.-J. Wörner de l'ETH à Zürich. Ils ont réalisé des expériences de type pompe-sonde pour étudier la dynamique vibrationnelle de la molécule dans les états excités, en utilisant et comparant deux sondes différentes, la première étant la spectroscopie de photoémission résolue en temps, pour laquelle la sonde ionise la molécule après un délai avec la pompe et le taux de photoélectrons est mesuré en fonction du temps. Cette méthode, déjà utilisée dans de nombreux systèmes, est connue pour sa sensibilité concernant le mouvement nucléaire et électronique, et dans le cas de SO_2 révèle une signature de la dynamique nucléaire du paquet d'onde dans les états excités. La deuxième méthode expérimentale utilise la génération d'harmonique, et contrairement au cas de NO_2 , "aucune" information concernant la dynamique nucléaire n'est obtenue. Ce cas particulier montre l'importance des études théoriques pour mieux comprendre la génération d'harmonique dans les molécules excités et les limites de cette méthode.

Le but du travail de thèse présenté ici est justement d'établir des éléments de réponses concernant les deux nouvelles méthodes expérimentales utilisées dans le cas de SO_2 et de comprendre la différence entre les résultats obtenus. Pour atteindre cet objectif deux buts sont dégagés, dans un premier temps il faut une description précise de la photo physique de la molécule après une excitation, et comprendre le rôle des différents états électroniques singulets et triplets présents à ces énergies. Le deuxième est de proposer un modèle pour décrire la génération d'harmonique dans le système, pour lequel la dynamique nucléaire doit explicitement être prise en compte.

2 Méthodes théoriques et algorithmes

Cette partie présente les différentes méthodes et approximations qui ont été utilisées pour résoudre l'équation de Schrödinger pour la molécule de dioxyde de soufre. Il s'agit d'une partie importante pour toute étude théorique car la résolution analytique de l'équation de Schrödinger est impossible et des approximations doivent être introduites pour pouvoir la résoudre, les résultats en dépendant directement.

2.1 Traitement quantique des noyaux

Partant de l'équation de Schrödinger décrivant la totalité du système, c'est à dire l'ensemble des électrons et des noyaux, les coordonnées de ces derniers sont séparées dans le cadre de l'expansion de Born-Huang, permettant de scinder le problème en une partie dite électronique, pour laquelle la position des noyaux joue le rôle d'un paramètre et une partie nucléaire décrivant la fonction d'onde associée à ces derniers. Cette approche mène à un jeu d'équations différentielles couplées entre une infinité d'états électroniques ne pouvant pas être résolu numériquement. Pour simplifier la résolution du problème différentes approximations ont été proposées, notamment la célèbre approximation de Born-Oppenheimer, mais aucune ne permet de décrire correctement le système lorsqu'une intersection conique est présente entre différents états électroniques. La position du problème est alors explicitement décrite, et on montre que toutes les approximations de type Born-Oppenheimer ne peuvent être appliquées car elles négligent les couplages non-adiabatiques qui sont induits par l'action de l'opérateur d'énergie cinétique nucléaire sur les fonctions d'onde électroniques paramétrées par les coordonnées nucléaires. Ces derniers s'avèrent non-négligeables lorsque deux états électroniques sont proches énergétiquement, et deviennent même singuliers au voisinage d'une intersection conique.

Pour résoudre ce problème les fonctions d'onde électroniques dites diabatiques ont été introduites et leur concept est rappelé, le point étant mis sur leur définition. On montre ainsi qu'en limitant les variations des fonctions électroniques par rapport aux déplacements nucléaires il est, en théorie, possible d'éviter la divergence des couplages non-adiabatiques, mais pour le cas des molécules de tels états ne sont pas accessibles. L'approximation en états dit quasi-diabatiques qui permettent d'éviter la singularité est alors introduite ainsi que leur obtention dans le cas spécifique des intersections coniques " autorisées par symétrie ". Ce cas spécifique d'intersections coniques est le seul présent dans le cas de SO_2 et fait ainsi l'objet d'une discussion approfondie. Cependant l'obtention d'une telle base d'état électronique qui permet une résolution ultérieure de l'équation

de Schrödinger nucléaire nécessite de la transformation de toutes les grandeurs utiles, telles que le moment de transition, le couplage spin-orbite... calculées dans la base électronique initiale : la base adiabatique. Les différentes transformations sont donc illustrées de façon générale dans cette partie, avant leur utilisation spécifique.

2.2 Méthodes Numériques

La résolution de l'équation de Schrödinger ne pouvant se faire analytiquement, l'utilisation de codes informatiques est aujourd'hui le seul moyen d'étudier théoriquement les processus physiques. Dans notre cas le code développé par le groupe de chimie théorique de l'université de Heidelberg, connu sous l'acronyme MCTDH, a été utilisé. Dans un premier temps la notion de base est introduite, qui permet le passage de l'équation formelle à une forme numérique, et le cas de la représentation variable discrète (DVR) est discutée. Il s'ensuit des considérations sur le coût numérique d'une telle représentation et la mise en parallèle de l'expression de la fonction d'onde nucléaire directement dans la base DVR et le cas de l'approximation Multi-Configuration Time-Dependent Hartree (MCTDH) qui permet de considérablement réduire l'espace de stockage de la fonction d'onde. Notre système étant relativement simple, la première méthode a été principalement utilisée.

Lorsque le problème a été numériquement exprimé, un nouveau jeu d'équations peut être déduit du principe variationnel de Dirac-Frenkel, qui décrit l'évolution temporelle de la fonction d'onde nucléaire. Il s'agit donc de l'homologue de l'équation de Schrödinger dans la base utilisée. Ces différentes équations différentielles couplées doivent ensuite être intégrée numériquement, et le cas de la méthode Short-Iterative Lanczos est présenté. Il s'agit d'une approximation polynomial pour approcher l'action de l'Hamiltonien du système.

2.3 Energies et fonctions propres du problème électronique

La résolution de l'équation de Schrödinger pour les électrons est une étape obligatoire pour envisager la résolution de cette dernière pour les noyaux. Les méthodes utilisées dans notre cas sont dites post-Hartree-Fock, car elles utilisent la fonction d'onde obtenue par la théorie Hartree-Fock (HF), détaillé dans la première partie de cette section, comme point de départ et permettent de corriger les défauts de cette dernière. Le problème principal de la théorie HF est l'absence de corrélation entre les électrons due à la présence d'un champ moyen pour d'écrire leurs interactions mutuelles, conduisant à une surestimation de l'énergie

de répulsion électrostatique entre ces derniers. Un second problème de la méthode est l'impossibilité de décrire des états électroniques pour lesquels différentes configurations électroniques sont prépondérantes. Pour remédier à ces limites, l'utilisation de la méthode MCSCF, associée au concept d'espace actif complet (CAS), a été utilisée. Cette méthode repose sur une description de la fonction d'onde électronique comme une combinaison linéaire de différentes configurations électroniques, permettant ainsi de considérer sur le même pied différentes configurations. De plus la méthode d'interaction de configuration à références multiples (MRCI) est utilisée pour améliorer la description de la corrélation. Les fonctions d'ondes électroniques ainsi obtenues peuvent être utilisées pour calculer le couplage spin-orbite par l'intermédiaire de l'opérateur de Breit-Pauli dans le cadre de la théorie des perturbations.

2.4 Energies et fonctions propres du problème électronique

Une place importante est naturellement dévouée à la description théorique des différentes méthodes de spectroscopies, point central de ce travail de thèse. Dans le cadre d'une approche dépendante du temps le spectre de photoabsorption peut être calculé grâce à la transformée de Fourier de la fonction d'autocorrélation, qui est la projection de la fonction d'onde nucléaire à un instant t sur la fonction d'onde à l'instant initial ($t=0$). En utilisant comme fonction initiale, l'état fondamental de la molécule et en projetant ce dernier sur les états excités par l'intermédiaire du moment dipolaire de transition, une propagation permet d'obtenir la totalité du spectre expérimental, sans inclure explicitement le laser.

2.5 La spectroscopie, une sonde expérimentale importante

Pour pouvoir comparer les résultats expérimentaux à nos simulations, il est nécessaire de calculer les observables adéquates. Dans le cas de la spectroscopie de photoémission résolue en temps, l'énergie cinétique des électrons ionisés doit être calculée. Les travaux ultérieurs de Domcke et Seel ont été utilisés pour décrire notre système. Le cas de la spectroscopie par émission d'harmoniques fait l'objet d'une étude détaillée qui présente le modèle que nous avons développé pour inclure la dynamique nucléaire. L'accent est également mis sur le calcul des éléments de matrice de transition qui repose sur l'approximation de champ fort, qui considère une description du continuum par des ondes planes, négligeant ainsi le potentiel Coulombien de l'ion moléculaire. Dans cette approximation les éléments de matrice de transition peuvent être calculés via

l'utilisation de la transformée de Fourier de la fonction de Dyson. On montre que ce traitement permet d'avoir une évaluation principalement analytique de ces éléments, hormis pour le calcul de la fonction de Dyson.

3 Résultats de structures électroniques

Cette partie est dédiée à la présentation des résultats méthodologiques, c'est à dire résultant de l'application des théories présentées dans la première partie.

3.1 Surface d'énergie potentielle adiabatique

Les surfaces d'énergie potentielle calculées pour décrire le système sont présentées dans cette partie. Pour décrire la première bande "autorisée" du spectre de photo absorption nous avons considéré l'état électronique fondamental (1^1A_1) et les deux premiers états excités (1^1B_1 et 1^1A_2) singulets de spin en fonction des trois degré de liberté vibrationnel de la molécule. La comparaison avec les résultats publiés dans la littérature montre un bon accord général concernant la géométrie obtenue pour les différents points stationnaires des surfaces d'énergie potentielle ainsi que pour les énergies d'excitations. Ainsi pour une excitation verticale (géométrie d'énergie minimale de l'état fondamental) l'état 1^1B_1 est le premier état excité avec une énergie inférieure à celle de l'état 1^1A_2 , mais le minimum de ce dernier est moins énergétique que le celui de l'état 1^1B_1 . Les trois états triplets de spin (1^3A_2 , 1^3B_1 , 1^3B_2) ont également été calculés et comparés avec les résultats disponibles pour vérifier la cohérence de nos résultats.

Les méthodes expérimentales qui ont été utilisées pour sonder la dynamique de la molécule font toutes les deux intervenir l'ionisation du système, dans le cas de la photoémission en tant qu'état final et dans le cas de la génération d'harmoniques en tant qu'état intermédiaire. Pour pouvoir théoriquement modéliser de telles expériences l'évaluation des surfaces d'énergie potentielle des états ioniques de la molécule a également été nécessaire. Trois états ioniques (1^2A_1 , 1^2B_2 et 1^2A_2) sont proches énergétiquement et peuvent jouer un rôle, l'état de première ionisation pour la géométrie de l'état fondamental correspond à une ionisation vers l'état 1^2A_1 , suivie par l'état 1^2B_2 et enfin à plus haute énergie l'état 1^2A_2 de façon similaire aux travaux antérieurs.

3.2 Diabatisation des états couplés par une intersection conique

Pour décrire l'excitation électronique de la molécule dans la gamme d'énergie 3.2-5.5 eV, six états électroniques ont été nécessaires, et dans le cadre de nos travaux sur les nouvelles méthodes de spectroscopie trois états ioniques viennent compléter le tableau. Parmi ces différents états, des intersections coniques autorisées par symétrie sont présentes entre les différents états électroniques. La complexité du spectre de photo absorption a été attribuée antérieurement à l'intersection conique entre les états singulets 1^1B_1 et 1^1A_2 , la méthode de diabatisation est donc particulièrement détaillée pour ces derniers, avec également la comparaison de deux différentes approximations pour la construction des états diabatiques. Le cas des intersections coniques entre les états triplets $1^3A_2/1^3B_1$ et ioniques $1^2A_1/1^2B_2$ est similaire à celui des états singulets, mais sont étudié ici pour la première fois. Les différentes surfaces diabatiques ainsi obtenues peuvent ensuite être utilisées pour la propagation de la fonction d'onde nucléaire.

3.3 Couplage spin-orbite et moment de transition dipolaire

Le passage de la base adiabatique à la base diabatique oblige la transformation des différents termes de couplage calculés dans cette première. Pour décrire de façon précise le rôle du couplage spin-orbite dans le système, nous avons évalué ces derniers entre tous les états singulets et triplets en fonction de la géométrie de la molécule. La dégénérescence des différentes multiplicités de spin des états triplets est ainsi levée et le système comporte dès lors douze états électroniques qui doivent être considérés distinctement. En utilisant une transformation de la base des fonctions de spin, le système peut être découpé en deux sous-systèmes comprenant chacun six états électroniques. Les différents couplages doivent être transformés dans la base diabatique et la méthode systématique utilisée dans notre travail est présentée. Les résultats des calculs des éléments de matrice de transition dans l'approximation des champs forts sont également diabatisés.

4 Spectroscopie de champ faible : spectres de photo absorptions et photoélectrons

4.1 Photo absorption : Les bandes de Clements

La première étape de notre travail s'est concentré sur la description de la dynamique dans les états excités 1^1B_1 et 1^1A_2 . Le système est initialement excité par une transition vers l'état électronique 1^1B_1 car la transition vers l'état 1^1A_2 est interdite par symétrie. Dans la zone de Franck-Condon le paquet d'onde est localisé dans le voisinage de la ligne d'intersections coniques et dès le début de son évolution il va subir un fort couplage non-adiabatique permettant le transfert de 55% du paquet d'onde vers l'état 1^1A_2 en une dizaine de femto secondes (fs), pour atteindre 80% après 60 fs. La présence d'intersections coniques joue donc un rôle prédominant sur la dynamique du paquet d'onde nucléaire, permettant un changement rapide de la configuration électronique de la molécule. Le spectre de photo absorption est également calculé et montre un accord avec son homologue expérimental sans précédent, validant de ce fait la construction de notre modèle. La structure des bandes de Clements est ainsi attribuée à une récurrence dans la fonction d'autocorrélation à 150 fs lorsque le paquet d'onde revient dans la zone de Franck-Condon avec une géométrie similaire à celle de l'instant initial. Cet excellent résultat nous a poussé vers une étude plus approfondie du spectre en proposant une attribution théorique des différentes transitions vibroniques par l'association des nombres quantiques des différents modes de vibration de la molécule. Les 80 transitions entre 3.565 et 4.047 eV ont été minutieusement analysées en calculant les fonctions propres de l'Hamiltonien nucléaire, constatant que pour cette gamme d'énergie la fonction d'onde est majoritairement (>70%) localisée sur l'état 1^1A_2 . On montre également que les bandes de Clements résultent de l'excitation successive du mode de bending (variation de l'angle $O\hat{S}O$) de la molécule, pour différent degré d'excitation des autres modes moléculaire, mais une série est récurrente, présentant quatre nœuds pour l'élongation symétrique et un nœuds pour l'élongation asymétrique de la molécule.

4.2 Considération des états triplets

Les différents états triplets ont été par la suite incorporés au modèle pour comprendre leur rôle dans la dynamique liée à l'excitation. Utilisant la séparation en sous-système de l'Hamiltonien total, seuls les états

triplets présentant un couplage spin-orbite avec les états excités 1^1B_1 et 1^1A ont été pris en compte, ramenant le système à six états électroniques. Cependant l'interprétation des résultats et l'identification des différents processus reste compliquée, ce qui nous conduit à une approche systématique de simplification du système pour comprendre les différents mécanismes de conversion inter-systèmes. En s'appuyant également sur la dynamique du paquet d'onde dans les états singulets et la variation du couplage spin-orbite en fonction de la géométrie moléculaire, on établit les mécanismes de conversion vers les états couplés $1^3A_2/1^3B_1$ et les deux états triplets de symétrie B_2 .

Un résultat clef de cette étude concernant SO_2 est la prédiction du rôle majoritaire des états 1^3B_2 de différentes multiplicités de spin. Depuis la prédiction théorique de l'existence de cet état en 1971, son rôle a pourtant été limité à une perturbation rotationnelle de la bande "interdite".

Le nombre important d'états présents ainsi que les nombreux éléments de couplage spin-orbite, donnent lieu à un phénomène d'interférences entre les différents chemins conduisant à un état triplet donné. Nos différentes simulations montrent que ces interférences sont en fait à l'origine des populations très différentes dans les différents états triplets, suggérant qu'une description quantitative de la conversion inter-système dans les molécules ne peut être obtenue que pour une modélisation complète du système. Celle-ci doit inclure la dépendance du couplage spin-orbite en fonction des coordonnées nucléaires et les différentes multiplicités de spin des états triplets.

L'étude des états triplets couplés avec les états excités s'est avérée très riche, mais la comparaison avec les expériences ne permet pas de reproduire, même sommairement, la bande "interdite" pourtant connue pour émaner de ces états triplets. Pour comprendre cette différence notable, nous avons considéré le second sous-système qui regroupe les états triplets couplés avec l'état fondamental de la molécule. L'interaction, même minime, provoquée par ces couplages perturbe l'état fondamental et montre une partie non-négligeable de la fonction d'onde nucléaire localisée sur les états triplets, donnant naissance à une fonction vibronique fondamentale perturbée. Alors que jusqu'à présent la polarisation de l'excitation n'a pas été considérée car elle n'était permise que perpendiculairement au plan moléculaire, l'état fondamental perturbé peut être excité grâce à toutes les polarisations. Notre étude permet d'établir un lien direct entre l'état perturbé et le spectre expérimental, devenant ainsi une signature de ce dernier. De plus les polarisations permettant l'excitation des bandes de Clements et de la bande "interdite" sont orthogonales, conduisant à un effet antagoniste de

l'orientation de la molécule par rapport à celle-ci. Ainsi, il devient théoriquement possible d'observer le spectre de photo absorption des états singulets et des états triplet séparément en jouant sur la polarisation et l'orientation de la molécule.

4.3 Les spectres de photoélectron

Nos surfaces d'énergie potentielle établissent la présence d'une intersection conique entre les deux états ioniques de plus basse énergie, qui n'a jamais été mentionnée dans les travaux antérieurs qui se sont intéressés aux spectres de photoélectron de la molécule. De façon similaire au spectre de photo absorption, nous avons calculé les spectres de photoélectron grâce à la transformée de Fourier de la fonction d'autocorrélation résultante d'une propagation de paquet d'onde. La première bande du spectre est obtenue en projetant la fonction de l'état fondamentale sur l'état ionique 1^2A_1 en considérant le couplage avec l'état 1^2B_2 . La deuxième bande du spectre expérimentale s'étend énergétiquement sur les deux états ioniques de plus haute énergie. Une simulation considérant l'état 1^2B_2 comme état initial ainsi que sont avec l'état 1^2A_1 permet de reproduire quantitativement la partie de basse énergie de cette bande, montrant l'impact de l'intersection conique entre les états ioniques. La partie de plus haute énergie de cette bande est très bien reproduite lorsque l'état 1^2A_2 est l'état initial, ce dernier n'étant pas couplé aux autres états. Ces résultats montrent ainsi la précision de notre modèle.

5 Spectroscopie de champ fort : Suivre une dynamique temporelle

5.1 Absorption multiple de photons : suivre la dynamique d'un paquet d'onde

Jusqu'à présent la résolution de l'équation de Schrödinger dépendante du temps à été utilisée pour obtenir des observables (spectres de photo absorption et de photoémission) qui en sont indépendantes. La méthode de spectroscopie de photoémission résolue en temps permet de suivre expérimentalement des dynamiques temporelles de la molécule, basées sur un système de type pompe-sonde lors duquel la pompe excite et initie une dynamique vibronique dans les états excités de la molécule, plus particulièrement dans les bandes de Clements, et la sonde ionise la molécule. L'évolution de la quantité de photoélectrons émit par la molécule permet d'obtenir une information quand à la dynamique dans les états excités, avec une variation du signal

présentant une période de 145 fs, similaire au temps caractéristique des bandes de Clements. On a construit un modèle simplifié fondé sur les interprétations expérimentales, et mettant en jeu l'état fondamental, les états excités 1^1B_1 et 1^1A_2 ainsi que les états ioniques 1^2A_1 et 1^2B_2 et un état de Rydberg de la molécule de symétrie B_1 convergeant vers l'état ionique 1^2A_1 et modélisé par ce dernier dans notre étude. Les résultats obtenus par ce modèle sont en bon accord avec l'expérience, confirmant le mécanisme suivant : l'état de Rydberg rend possible une transition résonnante par l'absorption de deux photons de la sonde, de dernier pouvant ensuite être ionisé par l'intermédiaire d'un troisième photon, uniquement lorsque le paquet d'onde est présent dans l'état 1^1B_1 , la transition depuis l'état 1^1A_2 étant interdite par symétrie. Ainsi le transfert périodique de la population entre les deux états excités module le taux d'ionisation en fonction du délai entre la pompe et la sonde et la dynamique peut être suivie expérimentalement.

Mais les résultats expérimentaux sont encore plus riches, établissant la présence d'un état excité supplémentaire intervenant dans la dynamique. En incluant les différents états triplets dans notre modèle mais ne permettant pas leur ionisation, le signal, en plus d'une oscillation périodique, montre une décroissance monotone en fonction du temps, que l'on peut directement relier à la population transférée vers les états 1^3B_2 , qui augmente au cours du temps sans oscillation. Notre modèle n'inclut pas la voie d'ionisation de ces états qui fait intervenir des états électroniques excités de plus haute énergie, mais la relation entre la population des états 1^3B_2 et l'ionisation observée expérimentalement nous permet de confirmer la première observation expérimentale de ces états, et confirme notre description de la molécule.

5.2 Spectroscopie de champ fort : vers une résolution attoseconde

La génération d'harmonique est l'un des grands espoirs pour observer des dynamiques à l'échelle de l'attoseconde. Ces espoirs ont été confirmés pour l'étude des atomes ainsi que certaines dynamiques dans les états ioniques des molécules. Son développement pour sonder des dynamiques dans des états excités a déjà montré le potentiel de cette méthode mais les résultats expérimentaux obtenus pour SO_2 ne laisse pas présager une telle possibilité pour cette molécule. En fait la situation est même pire, car la dynamique observée expérimentalement dans le cas précédent ne donne pas non plus de signature claire. Le modèle que nous avons développé a d'abord été comparé aux modèles utilisant une description classique des noyaux. Les résultats sont très similaires soulignant ainsi la validité de l'approximation classique lorsque l'état fondamental est considéré.

Le modèle a été ensuite utilisé dans le cadre d'une hypothétique dynamique dans l'état électronique fondamental, provoquée par exemple par une excitation Raman. Cette dynamique est ensuite sondée en utilisant une méthode de type pompe-sonde, la sonde étant la génération d'harmoniques. Dans ce cas, la variation simultanée de l'énergie d'ionisation et des éléments de matrice d'ionisation change le profil temporelle de l'intensité des différentes harmoniques émises. Dans ce cas simple, impliquant une dynamique sur un seul état excité, on retrouve une corrélation entre l'évolution temporelle de l'intensité des harmoniques et la dynamique nucléaire. Pour aller plus loin, la dynamique dans les états ioniques a également été considérée, et les interférences entre trajectoires longues et courtes montrent une sensibilité marquée à la phase accumulée par le paquet d'onde lors de son évolution dans les états ioniques, en modifiant le caractère destructif ou constructif des interférences.

Le cas plus compliqué de la dynamique dans les états excités a ensuite été étudié. En approximant l'énergie d'ionisation vibronique du système, nous avons reproduit qualitativement les résultats expérimentaux, qui résultent d'une émission similaire des deux états excités 1^1B_1 et 1^1A_2 , ne permettant pas l'observation de la dynamique nucléaire. Cependant il semble probable que la variation de la population des états 1^3B_2 est observée par une augmentation de l'intensité harmonique grâce à un dipôle de transition plus grand et cela malgré un potentiel d'ionisation plus important.

6 Conclusion et perspectives

Concernant la molécule de dioxyde de soufre, nous avons dessiné au cours de ces trois années de recherche une nouvelle compréhension de la photo physique de la molécule. Avec les nouveaux mécanismes que nous avons établi pour son excitation il est légitime de s'interroger sur leur rôle concernant dans séparation indépendante de la masse des isotopes du soufre car aucun travail n'a considéré l'état 1^3B_2 . De plus, nous nous sommes restreints aux niveaux électroniques de plus faibles énergies, mais nous avons cependant commencé l'étude des deux états électroniques d'énergie supérieure, impliqués dans la deuxième bande du spectre de photo absorption. Ces états permettent la photodissociation de la molécule et n'ont jamais été étudiés par des méthodes de dynamique quantique qui pourrait mettre en évidence le rôle des couplages entre ces deux états. Concernant le modèle développé pour la description de la génération d'harmoniques lors d'une dynamique, ce dernier devrait être testé dans le cadre d'un système simple, comme par exemple le dihydrogène, pour

permettre une comparaison avec des résultats numériques "exacts" et ainsi fournir des informations cruciales sur la qualité des différentes approximations. Les calculs des éléments de matrice de transition ont été fait avec MOLPRO, qui cependant ne permet un accès que partiel à la fonction d'onde électronique au niveau MRCI car il effectue une troncation arbitraire des vecteurs CI, dans la version utilisée ici. Une implémentation de la méthode dans un logiciel "libre" comme GAMESS-US pourrait être particulièrement avantageux pour l'étude d'autres systèmes.